December 2020

Interface Engineering of Materials for Energy and Biological Applications

Ardalan Chaichi

INTERFACE ENGINEERING OF MATERIALS FOR ENERGY AND BIOLOGICAL APPLICATIONS

A Dissertation

Submitted to the Graduate Faculty of the
Louisiana State University and
Agricultural and Mechanical College
in partial fulfillment of the
requirements for the degree of
Doctor of Philosophy

in

The Department of Mechanical Engineering

by
Ardalan Chaichi
B.S., Ferdowsi University of Mashhad, 2014
M.S., Sharif University of Technology, 2016
May 2021

Table of Contents

List of Tables

List of Figures

Abstract

Interface interactions are generally classified into solid-liquid, solid-gas, solid-vacuum, liquid-gas, light-matter and electron-matter categories. Surface morphological studies as well as surface chemical reactions can be studied in various types of complex systems thanks to technological advances in materials characterization methods. By employing interface engineering in different applications, it is possible to control electrical, chemical, mechanical, optical and biological properties of materials. Accordingly, we have applied interface engineering in three different areas of energy materials, biomaterials and surface imaging. As a result, firstly, we have introduced a high intensity light flash-based method on engineered substrates for delamination of reduced graphene oxide to synthesize electrodes for supercapacitor applications. Secondly, we used the produced electrodes for extreme temperature energy storage. In biomaterials sphere, we investigated the effect of cold plasma on prosthetic implants to improve their surface properties. Raman imaging of brain tissue is the last chapter of this dissertation that deals with the application of light-matter interactions at biological interfaces. We have performed in-depth analyses of various experimental methods for each of the aforementioned topics to introduce novel applications of interface engineering in three different areas.

Chapter 1
Introduction

1.1. General Introduction

Despite the existence of vacuum systems in 60s, it was not yet feasible to determine the structure and composition of solid surfaces. During the 80s, first quantitative studies for investigation of solid surfaces in atomic scale manifested which were mainly limited to simple compounds and single crystal structures.(Duke 2003) Nowadays, surface morphological studies as well as surface chemical reactions can be studied ubiquitously in various types of complex systems thanks to technological advances in materials characterization methods. Surface science and engineering is born from the theoretical concepts of physical chemistry and condensed matter physics.(Jain and Agarwal 2011) As an early example of the practical usage of surface science, the scattering phenomena of light and electron on solid surfaces can be mentioned which were employed for surface characterization and structural studies.(Woodruff 2016) Light and electron scattering were used for surface characterization by measuring the intensity and energy of inelastically/elastically scattered photons/electrons and their interaction with matter. Surface and interface engineering of materials have provided a new interdisciplinary research area that can be applicable to numerous real-world applications from electronics to energy storage, biological and novel characterization methods.(Kasemo 2002, Liu, Zhao et al. 2012, Han, Demkowicz et al. 2013, Li, Zhao et al. 2015, Wang, Li et al. 2015)

Interface interactions are generally classified into solid-liquid, solid-gas, solid-vacuum, liquid-gas, light-matter and electron-matter categories.(Ghosh 2009) By employing interface engineering in different applications, it is possible to control electrical, chemical, mechanical, optical and biological properties of materials.(Graetzel, Janssen et al. 2012) Accordingly, this dissertation has been outlined in five chapters. In the first chapter, motivation behind studying the

interface engineering of materials is explained as well as its practical applications in energy, biological and imaging sectors. The second chapter deals with the application of interface engineering in synthesis of multilayered graphene structure for energy storage in supercapacitors followed by a third chapter that discusses the possible solutions for modification of graphene-based supercapacitors at extremely low or high temperatures. In the fourth chapter, application of hand-held atmospheric plasma was investigated as a surface modification approach of prosthetics to alleviate the post-surgery issues accompanied by implanting knee prosthetics. Finally, the fifth chapter describes a novel approach for Raman imaging of biological tissues in order to assess the lipidomic alterations semi-quantitatively.

1.2. Interface Engineering for Improved Energy Storage

Due to the drastic surge in production and release of greenhouse gases into environment, irreversible environmental damages have occurred during the last century.(Gibson, Wilman et al. 2017) Combustion of fossil fuels is the major reason for vast greenhouse gases production including but not limited to industrial, automobile and residential emissions.(Oncel 2017) To alleviate this situation, substantial work needs to be done in decreasing the carbon content products of atmosphere by using clean and renewable energy sources. As a result, significant progress has been made toward utilizing novel clean energy sources such as solar cells,(Yang, Wang et al. 2017) hydrogen production by fuel cells,(Jang, Kim et al. 2019) geothermal sources,(Lin, Yu et al. 2019) wind turbines(Haddad, Ramadan et al. 2019) and so forth. Moreover, substituting electric engines with combustion engines in automobile industry is another huge step forward in reducing the content of carbon products in the atmosphere. Despite the aforementioned attempts to produce clean energy, the next challenge is developing an efficient method for improving the storage capacity of obtained energy.(Mensah-Darkwa, Zequine et al. 2019) Although numerous advances

have been achieved in clean and renewable energy conversion techniques, utilization of sustainable clean energy is only feasible if novel storage approaches are also developed. Automobiles produce the majority of atmospheric carbon products on a daily basis. Therefore, employing of electric vehicles can substantially decrease the amount of carbon footprint and emission of greenhouse gases into atmosphere. Lithium ion batteries have been employed in electric vehicles for energy storage purposes due to rechargeability and high energy density.(Andwari, Pesiridis et al. 2017) However, considerably long charging times, narrow temperature window of operation, high production and maintenance costs and relatively low lifetime have made researchers to investigate new techniques for energy storage in electric vehicles.(Bashash, Moura et al. 2011) On the other hand, supercapacitors offer super-fast charging due to their double layer capacitance. Supercapacitors are able to store higher amounts of energy in comparison with a normal capacitor.(Faggioli, Rena et al. 1999) Supercapacitors possess some of the properties of both batteries and capacitors, while their behavior more resembles a capacitor than a battery. Furthermore, supercapacitors are much more cost efficient with long cycling times and more controllability for extreme temperature applications design.(Zuo, Li et al. 2017) However, their volumetric capacitance is limited compared to batteries because of the lower energy density.(Mensah-Darkwa, Zequine et al. 2019) Therefore, introducing a novel material that comprises the advantages of both batteries and supercapacitors is crucial for electric vehicles. As a result, surface modification was suggested as a practical approach for improving the energy storage properties of materials by introducing novel techniques utilizing nanocomposites, phase change materials, polymers and nanomaterials.(Share, Westover et al. 2016)

Rigorous research has been conducted on using surface enhanced carbon-based materials like graphene, carbon nanotubes and activated carbon as the most desirable candidates for

electrochemical energy storage due to their processability, light weight, high porosity and structural controllability.(Iqbal, Khatoon et al. 2019) High porosity of carbon-based materials is the most significant factor for their unique electrochemical performance that engenders obtaining high energy densities as well as maintaining the high power density. High surface area carbon materials are employed in electrochemical double layer capacitors in which the electric charge stores on the interface of electrode and electrolyte. Amongst the carbon-based electrodes, graphene has been repeatedly reported as the best option due to its 21 μF cm^{-2} intrinsic areal capacitance.(Zhang and Zhao 2009) In general, there are two possible charge storage mechanisms in supercapacitors. The first mechanism is electric double layer capacitance in which the capacitance originates from accumulation of electric charge on the interface of electrode and electrolyte. The second one is called pseudo-capacitance where the capacitance comes from the electro-active species contributing in Faradic reactions. Although it is possible that the two mechanisms occur at the same time, formation of electric double layer is more favorable because of the higher charge/discharge rates as well as longer cycling lifetime.(Zhu, Murali et al. 2011) In electric double layer capacitors, controlling the pore size and specific surface area significantly affects the performance of the electrodes. Therefore, graphene with theoretical surface area of 2630 $m^2 g^{-1}$ has the highest reported specific surface area compared to other carbon-based materials like carbon nanotubes (100-1000 $m^2 g^{-1}$) and activated carbon (<1000 $m^2 g^{-1}$).(Zhang and Zhao 2009) However, in practice, it is not feasible to utilize this entire surface area mainly due to high synthesis cost of single layer graphene. Therefore, researchers started to use multilayer graphene structures which can be produced significantly easier with considerably lower cost. Meanwhile, the most challenging issue was creating a stable delaminated structure of graphene layers to maximize the available surface area of electrodes. Several chemical and mechanical methods were employed to

create such structure of multilayered graphene and reduce agglomeration of graphene layers. However, in most of the studies, the results showed either low volumetric capacitance or poor stability.(Horn, Gupta et al. 2019)

Recently, reduction of graphene oxide (GO) to reduced-graphene (rGO) by laser/high intensity light has become so popular due to the ease of process, high production rate, low cost and good performance of electrodes.(Wan, Wang et al. 2019) However, various factors like the effect of residual oxygen, rGO interlayer spacing and substrate topography on the performance of electrodes were left unexplored. Therefore, we proposed a substrate engineering method for production of rGO by using high intensity light to investigate the effect of aforementioned factors.

Another limitation of current electrochemical energy storage devices is the narrow window of operational temperature that limits their application in many sectors like transportation and aerospace. This issue originates from the lack of temperature resistant electrodes and membranes. Most of the materials used in batteries and supercapacitors disintegrate at higher temperatures (>100 °C) and freeze at lower temperatures (<0 °C).(Hibino, Kobayashi et al. 2015) As a result, the majority of works in this field has been done at room temperature. However, in real-world applications, temperature resistant energy storage devices are needed to operate in a wide range of temperature and retain their properties after exposure to extreme temperatures. Accordingly, we also introduced a fully solid-state supercapacitor by means of our rGO electrodes and a novel polymer blend (poly (arylene ether sulfone) featuring quaternary benzyl pyridinium cations-polybenzimidazole (QPPSf-PBI)) that is capable of operating in a wide temperature range. Both of our electrode material and solid electrolyte polymer blend have proven to be stable at extremely low (<0 °C) and high (>100 °C) temperatures.

1.3. Surface Modification of Prosthetics

Since nineteenth century, prosthetics have been clinically implanted in patients in various parts of body, from knee and hip to coronary stents.(Affatato 2012) From the inception of this phenomena, scientists were continuously searching for novel materials and surface treatment methods to improve the biocompatibility and durability of such implants. However, depending on targeted areas of body, different properties are desired for different prosthetics. For example, a material that is used in coronary stent is intended to suppress the cell growth, while expectations are different for a knee or hip implant.(Munsch 2017) Moreover, sometimes different areas of the same implant should possess different properties depending on its application. For example, knee implants are usually made of two corrosion resistant metallic parts separated with polymeric spacer in between. Owing to numerous treatments and materials development during the last decades, remarkable advances have been achieved to enhance the biocompatibility and durability of prosthetics and reduce the possibility of early infection and rejection of implants. However, the improvement in this sphere is still far from satisfactory due to the complexity of such systems.(Browne and Gregson 1994) This complexity originates from the difficulty of materials selection for prosthetic purposes in which improving one property usually impairs other necessary properties. This is where interface engineering comes into play by enhancing the lifespan and performance of implants while preserving their bulk properties.(Matouskova, Ackermann et al. 2018) Durability of an implant is heavily affected by tribological behavior, corrosion resistance and biocompatibility of the surface of implant. Presurgical surface treatment methods are the most practical approaches for improving the performance of an implant by keeping the bulk properties untouched.(Rodrigues, Fontoura et al. 2019) However, not all the surface treatments can improve the surface properties without affecting the bulk properties and be used in a clinical environment.

In one way, it is possible to categorize surface treatment methods into two groups of thermal and nonthermal techniques. Thermal surface treatment techniques alter the surface properties by increasing the surface temperature drastically. This increase in temperature can negatively affect the bulk properties by changing the tensile, fatigue and toughness properties of the bulk material due to heat transfer.(Singh, Prakash et al. 2019) More specifically, metals and alloys are more susceptible to be damaged by thermal surface treatments due to the high thermal conductivity; meanwhile, many prosthetics are made of metals like stainless steel and titanium alloys. Therefore, introducing a nonthermal technique that can be easily brought into clinics and surgery rooms is considered a huge advancement in prosthetic engineering. Accordingly, we have tested a novel nonthermal handheld plasma treatment technique on knee implants to study the possible surface improvement effects. The temperature of the plasma flame is less than 50 °C meaning it can be used for variety of different materials ranging from alloys to polymers without affecting the bulk properties. Knee implant is a desirable choice for this study due to the usage of two different class of materials (alloys and polymers). Despite using this technique on knee implant, it can be also used in various other prosthetics that is left for future studies.

1.4. Raman Imaging at Biological Interfaces

Inelastic scattering of photons happens due to the difference in frequency of incident and scattered light on matter. Almost 10^{-7} fraction of scattered photons might end up being scattered inelastically. This inelastic scattering of light generates Raman signals which can be categorized into two types: (i) Stokes scattering in which the target molecule absorbs energy and (ii) anti-Stokes scattering in which the energy is lost by target molecule.(Tu and Tu 1982) Raman spectroscopy is remarkably chemical specific due to uniqueness of energy levels for different molecules and chemical bonds. As a result, this technique is used with high confidence for

characterization of molecules and chemical bonds in various fields from materials science to medicine.(Li, Long et al. 2020) Raman spectroscopy has been lately utilized for biomedical purposes due to its capability to provide detailed biochemical information of organs(Huang, Short et al. 2011), tissues(Dybas, Marzec et al. 2016) and cells(Notingher 2007) in molecular level without the need of labeling. Accordingly, Raman spectroscopy has demonstrated promising results for sub-cellular analysis of biological samples with considerably high spatial resolution. Molecular composition changes of cells during experiencing different diseases can be recognized due to the unique fingerprint of biochemicals in this technique. Several studies have proven the application of Raman spectroscopy in detection of biochemical changes for cancer in lung,(Huang, McWilliams et al. 2003) breast,(Haka, Shafer-Peltier et al. 2005) skin,(Lui, Zhao et al. 2012) bladder(Draga, Grimbergen et al. 2010) and esophagus(Huang, Wang et al. 2014) as well as various vascular diseases.(Ward, Barbee et al. 2007) Although numerous studies have been conducted on the application of Raman spectroscopy in biomedical disciplines during the last decades, taking it to next level with visualization of biochemical changes by performing Raman imaging is a novel area to be explored. There are only a small handful of existing molecular imaging techniques including molecular magnetic resonance imaging (MRI), positron emission tomography (PET) and single-photon emission computed tomography (SPECT) which undoubtedly provide precious biochemical information for investigation of mechanisms in various diseases. However, none of the aforementioned techniques is perfect. Figure 1.1 shows the capabilities and limitations of conventional imaging techniques versus Raman imaging in terms of resolution, scan time and effective depth.

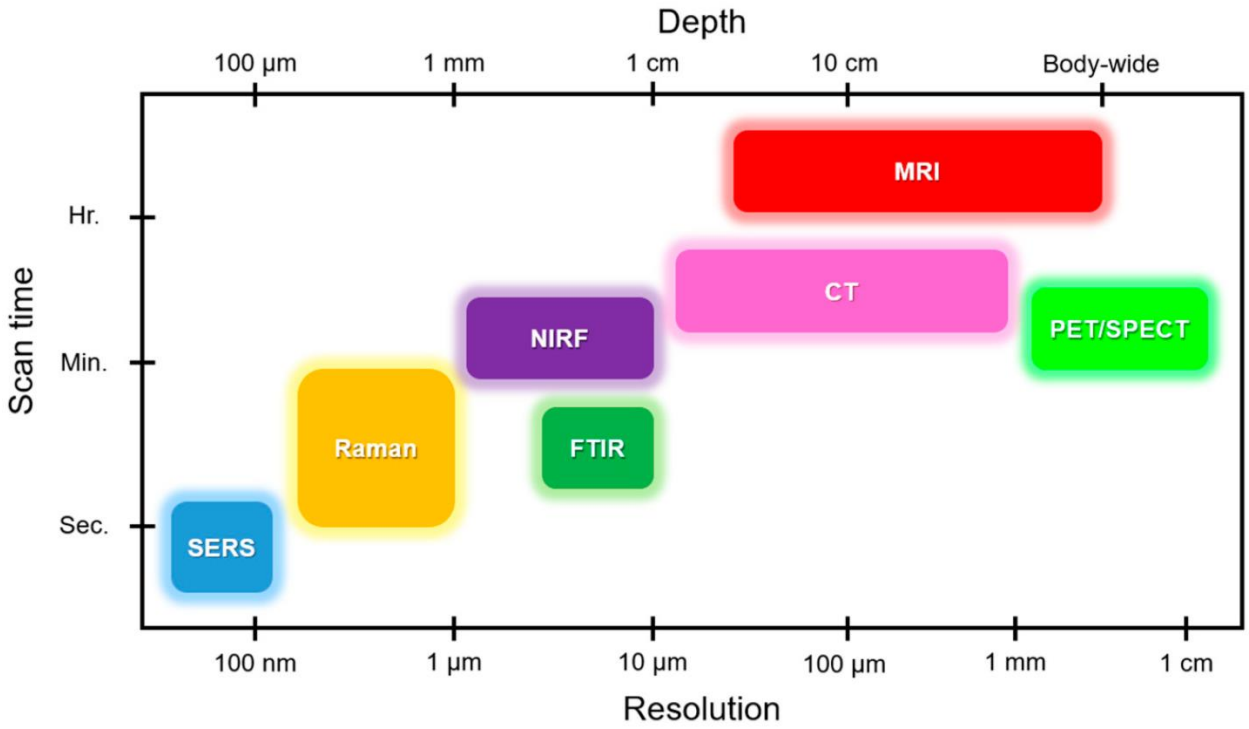

Figure 1.1. Comparison of different imaging techniques which can be potentially employed in biomedicine. MRI: Magnetic resonance imaging, CT: Computed tomography, PET: Positron emission tomography, SPECT: Single-photon emission computed tomography, NIRF: Near infrared fluorescence, FTIR: Fourier-transform infrared spectroscopy, SERS: surface-enhanced Raman scattering.(Chaichi, Prasad et al. 2018)

Raman microscopes for imaging purposes have been recently developed thanks to technological advances that significantly decrease the amount of scanning time for signal acquisition. High spatial resolution, chemical specificity, photostability, label-free detection capabilities, low background signal and multiplexing potentials are the most important properties of Raman imaging.(Stewart, Priore et al. 2012) As a result, we chose Raman imaging technique to track the biochemical changes at biological interfaces using a Raman microscope. More specifically, we employed this technique to measure lipid changes of brain tissues in post-traumatic stress disorder (PTSD) induced rats. Although there is a huge population affected by PTSD worldwide, this is the first report of Raman imaging in this area. By investigating the lipid alterations of brain, novel therapeutic methods can be introduced for PTSD and other behavioral and physiological disorders.

Chapter 2
Interface Engineering of Interconnected Graphene Electrodes

2.1. Introduction

Supercapacitors and batteries are known as two fundamental technologies for electrochemical energy storage purposes. Although batteries provide considerably high energy densities (100-243 Wh kg^{-1}),(Shao, El-Kady et al. 2015, Chee, Lim et al. 2016) they suffer from extremely low power densities (10-100 W kg^{-1})(Xiong, Meng et al. 2014, Shao, El-Kady et al. 2015, Chee, Lim et al. 2016) that result in several hour recharging times. On the other hand, supercapacitors offer fast recharging times (minutes or even seconds), albeit lower energy densities compared to batteries. However, coupling batteries with supercapacitors has been accomplished in practical applications, such as electric automobiles, to benefit from the advantages of both products.(Yan, Fan et al. 2010, Lin, Zhang et al. 2012, Kim, Jung et al. 2013, Wang, Yi et al. 2014, Wu, Feng et al. 2014) Therefore, creating a material for electrochemical energy storage devices that can handle a high energy density as well as maintaining a high power density is contemplated revolutionary.(Gu and Yushin 2014) This combination is not achievable, unless novel architectures are created in micro and nano scale to manipulate the common properties of current materials.(Li and Shi 2012, Xu, Li et al. 2012, Wang, Yi et al. 2014, Qu, Zhao et al. 2015, Sun, Mei et al. 2017) In practical applications, several micro grams of active material per unit area of electrode is required to maintain stable charge/discharge cycles and high reliability. Nevertheless, nano and micro scale engineered materials cannot be simply scaled up to more than one micro gram per unit area due to the drastic decline of charge storage and charge transfer in electrochemical

This chapter was previously published as Ardalan Chaichi, Ying Wang, and Manas Ranjan Gartia. "Substrate engineered interconnected graphene electrodes with ultrahigh energy and power densities for energy storage applications." *ACS applied materials & interfaces* 10.25 (2018): 21235-21245. Reprinted by permission of American Chemical Society.

configurations caused by diffusion constraints.(Huang, Zeng et al. 2012, Yoon, Lee et al. 2014) This limitation can be overcome by providing accessibility for electrolyte throughout the active material which is ignored in the vast majority of studies and publications.(El-Kady, Strong et al. 2012, Chen, Li et al. 2013, Chen, Xue et al. 2013) Being unable to wet the micro pores within active material by electrolyte, decreases the probability of successful double layer formation in porous materials which results in dramatic drop in double layer capacitance as well as the charge/discharge rate.(Luo, Jang et al. 2013, Gu and Yushin 2014) Consequently, carbon based materials, such as activated carbon, nanotubes and graphene, demonstrate much lower double layer capacitance compared to their theoretical values.(Gu and Yushin 2014, Xiong, Meng et al. 2014, Chee, Lim et al. 2016) In addition to the unaffordable price of vertically grown carbon nanotubes, to use carbon nanotubes in practical applications, further addition of conductive polymers is necessary for the formation of a pseudocapacitance pair.(Cote, Cruz-Silva et al. 2009, Basnayaka and Ram 2017) Otherwise, the amount of capacitance achieved by CNT supercapacitors is considerably low and ineffective.(Xiong, Meng et al. 2014, Shao, El-Kady et al. 2015, Chee, Lim et al. 2016) Meanwhile, the formation of pseudocapacitance is unfavorable in many applications because of the high rate of capacitance decay.(Gu and Yushin 2014, Kyerematen, Brousse et al. 2017) On the contrary, highly porous structure of interconnected graphene network with distinguished electron transfer characteristics is capable of providing an ideal architecture for the manufacturing of ultra-high electrical double layer capacitance due to prevailing diffusion limits of ubiquitous carbon based electrodes.(Li and Shi 2012, Zhu, Li et al. 2012, Lee, Park et al. 2013, Zhang, Zhang et al. 2013, Qu, Zhao et al. 2015) The presence of meso and micro porous morphology through the interconnected graphene network increases the capability of charge storage as well as maintaining high power density. Electrochemical capacitance for the

aforementioned structure can even exceed the value for single layer graphene (550 F g^{-1})(Xia, Chen et al. 2009, Goh and Pumera 2010, Zhu, Murali et al. 2011, Chen and Dai 2013, Lee, Park et al. 2013, Wu, Parvez et al. 2013) which has been known as the most ideal type of graphene for energy storage applications. However, interconnected graphene network demonstrates its superior properties while the graphene layers are delaminated and stabilized in this structure. Although the easy accessibility of surfaces and edges on graphene sheets by electrolyte can be considered as the mechanism behind the superiority of this structure over other types of common carbon based materials, the extreme restacking propensity of graphene layers restricts their double layer capacitance.(Lee, Park et al. 2013, Wu, Feng et al. 2014, Pham, Lee et al. 2015) Thus, taking advantage of the entire potential of this material for energy storage devices is limited. The accessibility of graphene edge planes plays a significant role even in the electrochemical capacitance of other types of graphitic materials like nanotubes. There is a direct relation between the number of available graphene edge sites and double layer capacitance for all types of graphitic nanomaterials.(Gu and Yushin 2014, Xie, Yang et al. 2015)

The curved structure of graphene sheets provides a vast wettable surface for the electrolyte that requires to be engineered and manipulated for practical energy storage capacitors. Accordingly, the creation of single layer graphene by various chemical and mechanical methods attracted a lot of interest for energy storage devices.(Simon and Gogotsi 2008, Wang, Shi et al. 2009, Goh and Pumera 2010, Liu, Yu et al. 2010, Zhu, Murali et al. 2011, El-Kady, Strong et al. 2012, Liu 2014, Ke and Wang 2016) Meanwhile, the production of single layer graphene with fairly good quality is extremely expensive and totally impractical for mass production.(Goh and Pumera 2010, Xie, Yang et al. 2015) Therefore, many efforts have been put into creating delaminated interconnected graphene morphologies. Graphene electrodes that were produced by

exfoliation of graphene oxide exhibited the specific capacitance of 100-117 F g^{-1} in 1M H_2SO_4 at the scan rates of 0.01 - 1 V s^{-1}.(Gu and Yushin 2014) The results of this study showed that the capacitance of multi layered graphene can be superior to carbon nanotubes and onion-like carbon.(Gu and Yushin 2014, Chee, Lim et al. 2016) However, it is still lower than carbide derived carbon, activated carbon and zeolite templated carbon.(Gu and Yushin 2014, Wu, Feng et al. 2014) Therefore, endeavors to reduce the agglomeration of graphene layers to achieve higher capacitance, close to the theoretical values, have been started in last few years.(Shao, El-Kady et al. 2015) Reduction of graphene oxide in hydrazine gaseous media was among the first efforts that resulted in specific capacitance of 205 F g^{-1} in 0.3 KOH electrolyte that decreased dramatically after several cycles.(Gu and Yushin 2014) Another approach was to positively charge the graphene surface during reduction procedure by means of p-phenylenediamine (PPD).(Gu and Yushin 2014, Xiong, Meng et al. 2014) However, these methods did not demonstrate favorable results in energy storage applications.(Gu and Yushin 2014, Chee, Lim et al. 2016) Preparation of stabilized graphene in aqueous environment is another technique that benefits from aromatic interaction mechanisms and impressively increased the suspension stability of graphene layers and formation of double layer capacitance (~120 F g^{-1}).(Gu and Yushin 2014) Decreasing the size of graphene segments is another suggested method to reduce the agglomeration of layers and resulted in increased electrochemical capacitance from 82 to 132 F g^{-1} in 1M H_2SO_4 electrolyte.(Xiao, Tan et al. 2013, Gu and Yushin 2014) Curved mesoporous graphene has demonstrated promising specific capacitance (100-250 F g^{-1}) in ionic liquids, albeit, accompanied with poor stability and reliability.(Shao, El-Kady et al. 2015, Chee, Lim et al. 2016) Thermal exfoliation of graphene oxide has been reported to produce electrodes with specific capacitance more than 200 F g^{-1}, although with very poor stability.(Xiao, Tan et al. 2013) Several reports studied the creation of

mesoporous graphene like holey graphene,(Sun, Mei et al. 2017) graphene oxide hydrogels,(Zheng, Yang et al. 2017) nitrogen doped carbon paper(Zhang, Yang et al. 2017) and 3D porous graphene(Wang, Liang et al. 2017) by use of functional groups that demonstrates high pseudocapacitance which is detrimental for many applications mostly because of the low volumetric capacitance.(Cote, Cruz-Silva et al. 2009, El-Kady and Kaner 2013, Wu, Parvez et al. 2013, Wen, Hao et al. 2014, Yu, Goh et al. 2014, Raccichini, Varzi et al. 2015, Wu, Parvez et al. 2015, Basnayaka and Ram 2017, Yang and Bock 2017)

Despite the mentioned advantages of providing higher surface area for electrochemical energy storage, we need to consider that high surface area is not the only factor in this mechanism. Ion accessibility is another important parameter that directly depends on the pore size of the electrode microstructure. Although decreasing the pore size of structure from microns to nanometer usually increases the amount of available surface area, it might become a limiting factor for ion diffusion. In other words, due to the large size of ions in supercapacitor electrolytes, the ions will not be able to diffuse into microporous structures.(In, Kumar et al. 2006, Armand, Endres et al. 2011) Therefore, the amount of stored energy in electrodes decreases, despite providing higher surface area. As a result, it is not only the amount of surface area of the electrode that determines the electrochemical energy storage capabilities, and other factors like the diffusion of ions into those pores should be also considered while designing the electrodes.

Recently, laser and flash reduction of graphene oxide have been employed to prepare carbon based electrodes for electrochemical energy storage applications.(Cote, Cruz-Silva et al. 2009, El-Kady, Strong et al. 2012, Kaniyoor and Ramaprabhu 2012, Han, Wu et al. 2014, Xu, Lin et al. 2014, Yu, Goh et al. 2014, Homenick, James et al. 2016, Kyerematen, Brousse et al. 2017, Liu, Liu et al. 2017, Zhao, Liu et al. 2017) However, in these studies the importance of vital

parameters like interlayer spacing and the effect of supporting substrate topography on the capacitance were not explored. In the current study, we present a novel method for production of highly delaminated graphene network that activates the exceptional potentials of interconnected graphene structure for several energy applications. Controlling the spacing between graphene layers as well as the topography of inactive substrate are significant factors which are capable of exhibiting full potential of layered graphene structure and have been mostly ignored in previous studies.

2.2. Experimental Section

Fabrication of substrate: High quality graphene oxide (GO) (Graphenea Inc., Cambridge, MA) was dispersed in water with the monolayer content of >95% and concentration of 4 mg mL^{-1}. In order to exfoliate agglomerated stacks of GO, the precursor was treated in ultrasonic bath for 30 minutes. Transparent polyethylene terephthalate (PET) was used as substrate for producing the electrochemical electrodes. For creating nano and micro patterns on the plastic substrate, replica molding process was used. Master molds were made by laser interference lithography on quartz substrate and they were silanized for 30 min to become hydrophobic. 2 ml of UV-curable polymer (NOA-61, Sigma Aldrich) were dropped on the surface of master mold with a PET sheet on top of it. Afterwards, it was exposed to UV light with the power of 210 mW cm^{-2} for 1 min. Periodic patterns are formed on PET once the UV-curable polymer is fixed. The plastic is then peeled off gently from the master mold (Figure 2.1).

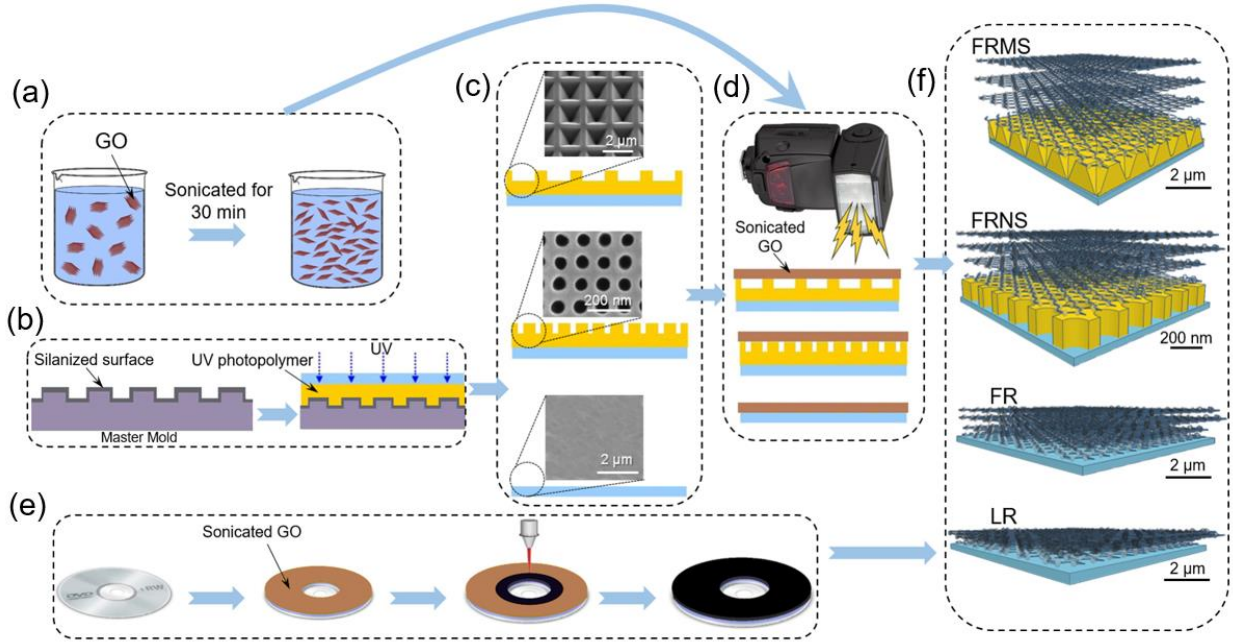

Figure 2.1. Schematic illustration of substrate engineered electrodes for supercapacitor application using flash reduction and laser reduction preparation methods. (a) 20 ml of graphene oxide (GO) dispersed in water (4 mg mL^{-1}) was sonicated for 30 min to exfoliate the GO layers. (b) Nanoimprint lithography was used to produce the nano and micro-patterned substrate. The master mold was silanized for 30 min followed by washing and drying. 2 ml of UV curable polymer were dropped on the silanized master mold and exposed to UV light (210 mW cm^{-2}) for 1 min. (c) The cured polymer on the master mold were peeled using a supporting PET substrate to recover the complimentary structures on the substrate. (d) Exfoliated GO prepared in step (a) was drop cast on the nano and micro patterned substrates. Flash reduction of GO to graphene was performed by the use of a digital camera flash. (e) Exfoliated GO prepared in step (a) was drop cast on a DVD and reduced to graphene using an optical drive. (f) Schematic representation of the interlayer spacing of graphene sheets using different reduction methods and morphology of the substrate. Flash reduced sample on the micro patterned substrate (FRMS) and laser reduced sample on the flat substrate (LR) represent the highest and lowest interlayer spacing of graphene layers, respectively.

Fabrication process of laser and flash reduced graphene electrodes: For the production of flash reduced graphene, 20 ml of GO were drop-cast on the surface of patterned and flat plastic substrates and dried over night at room temperature. A xenon digital camera flash (Neewer PRO i-TTL) was used in air and ambient conditions for reduction of GO to graphene. The flash energy was approximately 0.1-2 J cm^{-2} that was measured by Gentec QE25ELP-S-MB-INT-D0 light measurement system. After flashing, the golden-brown color of GO turns to black which is an evidence for successful reduction of GO to graphene. In order to make laser reduced samples, LG

lightscribe DVD burner employed by means of a regular lightscribe software. Drop-cast GO on PET substrate was glued to the top surface of a lightscribe DVD and burnt in DVD optical drive. Although it takes around 20 min for each cycle, the process should be repeated for at least six times to achieve an acceptable amount of graphene out of GO. Thus, all the laser reduced samples in this study were burnt for eight times. After the preparation of electrodes, three electrode configuration tests were performed in 0.5 M H_2SO_4 electrolyte with Pt and Hg/Hg^+ as working and reference electrodes, respectively. Fabricated electrodes were named LR (laser reduced), FR (flash reduced on flat substrate), FRNS (flash reduced on nano-patterned substrate) and FRMS (flash reduced on micro-patterned substrate).

Electrochemical Experiments: Sandwich type devices were also made out of LR, FR, FRNS and FRMS electrodes by means of microporous membrane and 0.5M H_2SO_4 electrolyte. Electrochemical tests including cyclic voltammetry (CV) and galvanostatic charge/discharge were performed by CHI 600E electrochemical workstation. Electrochemical Impedance Spectroscopy (EIS) measurements were carried out with amplitude of 0.005 V AC in the range of 0.01 Hz to 100 kHz. Volumetric capacitance was calculated using equation 1,(Wen, Hao et al. 2014) where υ, i, ΔV and v are defined as scan rate (V s^{-1}), applied current (A), sweep potential window (V) and volume of active material (cm^3), respectively.

$$C_v = \frac{\int i.dV}{v.\Delta V.\upsilon} \qquad (1)$$

For calculating volumetric capacitance (F cm^{-3}) from the charge/discharge diagrams, equation 2(Wen, Hao et al. 2014) was used.

$$C_v = \frac{-idt}{vdV} \qquad (2)$$

Specific energy density E (Wh cm^{-3}) and power density P (W cm^{-3}) were calculated using equation 3 and equation 4,(El-Kady and Kaner 2013) where t is the discharge time excluding IR drop.

$$E = \frac{C_v \times (\Delta V)^2}{3600} \quad (3)$$

$$P = \frac{E \times 3600}{\Delta t} \quad (4)$$

Conductivity of laser and flash reduced GO was measured by performing cyclic voltammetry (CV) tests in the potential window of -1 to 1 V and scan rate of 0.1 V s^{-1}. The electrical conductivity of GO surface was measured to be 6.38 x 10^{-4} S m^{-1}. After laser and flash reduction, electrical conductivity increased to 1.40 x 10^{3} S m^{-1} and 2.14 x 10^{3} S m^{-1}, respectively.

General Characterizations:

Morphological, Energy-dispersive spectroscopy (EDS) and cross sectional studies were performed by scanning electron microscopy (Quanta 3D DualBeam FEG FIB-SEM). X-ray diffraction diagrams were performed by using Panalytical Empyrean multipurpose diffractometer. In order to study the surface properties, ANASYS atomic force microscope (AFM) has been employed. Renishaw inVia confocal Raman microscope was used to achieve the Raman spectrum of samples. All the spectra were acquired by the excitation wavelength of 532 nm in the range of 500 to 3000 cm^{-1}. For X-ray photoelectron spectroscopy (XPS) analysis, Scienta Omicron ESCA 2SR instrument was employed. It was equipped with a monochromatic Al Kα X-ray source of 1486.7 eV. Altamira AMI-200 was employed for BET experiments. 1 mg of samples were used for surface area measurements and further calculations.

2.3. Results and Discussions

Figure 2.2 schematically shows the formation of interconnected graphene layers on top of flat, nano and micro-structure patterned substrates.

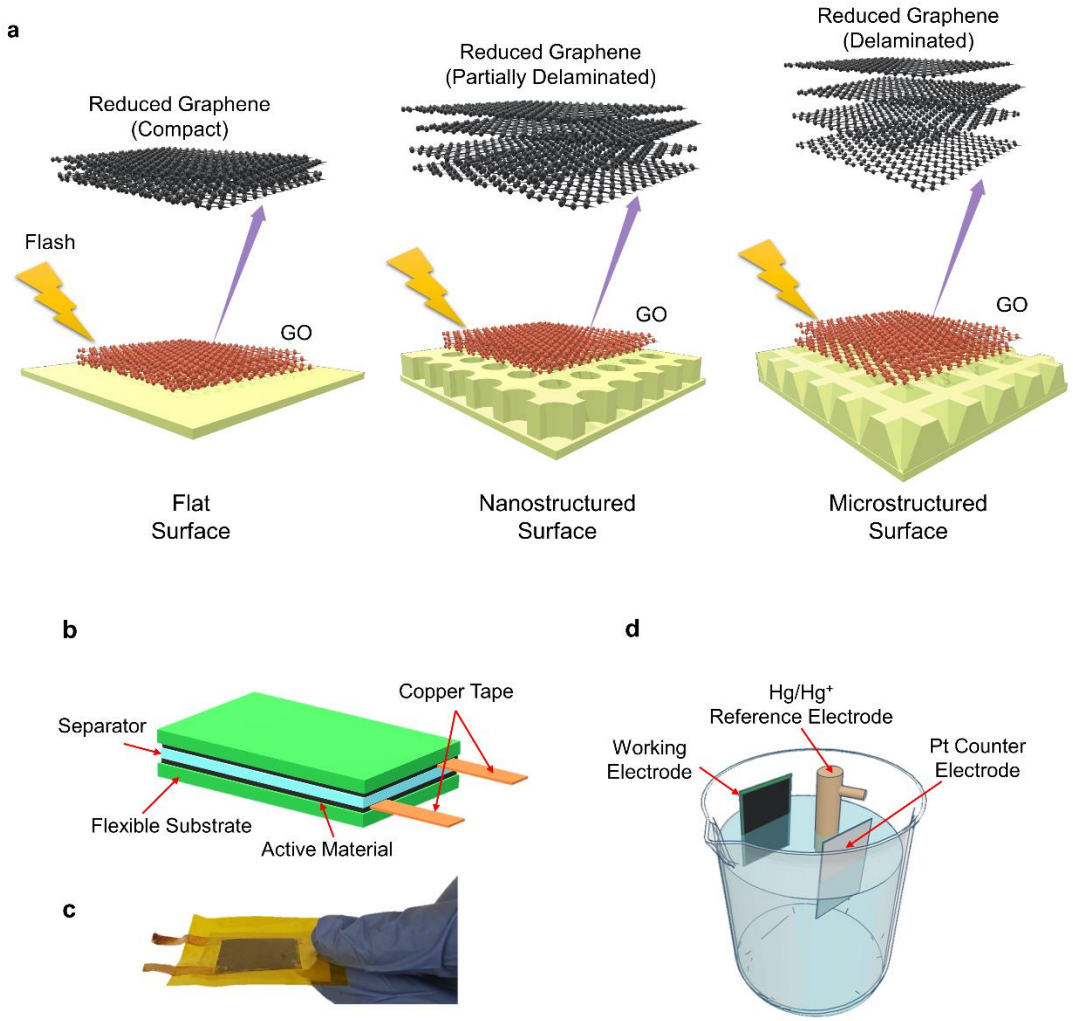

Figure 2.2. Schematic illustration of substrate engineering effect on electrodes for energy applications using flash reduction on flat and patterned substrates. (a) By means of substrate engineering, interlayer spacing of graphene layers increases considerably. Therefore, the diffusion of electrolyte into the interconnected graphene structure is facilitated. (b) Schematic picture of the device made by different electrodes. (c) Real image of the device made by FRMS electrodes. (d) Three electrode configuration used in this study.

A xenon digital camera flash was used to produce the graphene from graphene oxide (GO) (see Figure 2.1 for details). The fabricated electrodes were named FR (flash reduced on flat substrate), FRNS (flash reduced on nano-patterned substrate) and FRMS (flash reduced on micro-patterned substrate). In order to compare the performance of the flash-reduced electrodes, GO was also reduced using lightscribe DVD technique to produce graphene and named LR (laser reduced).

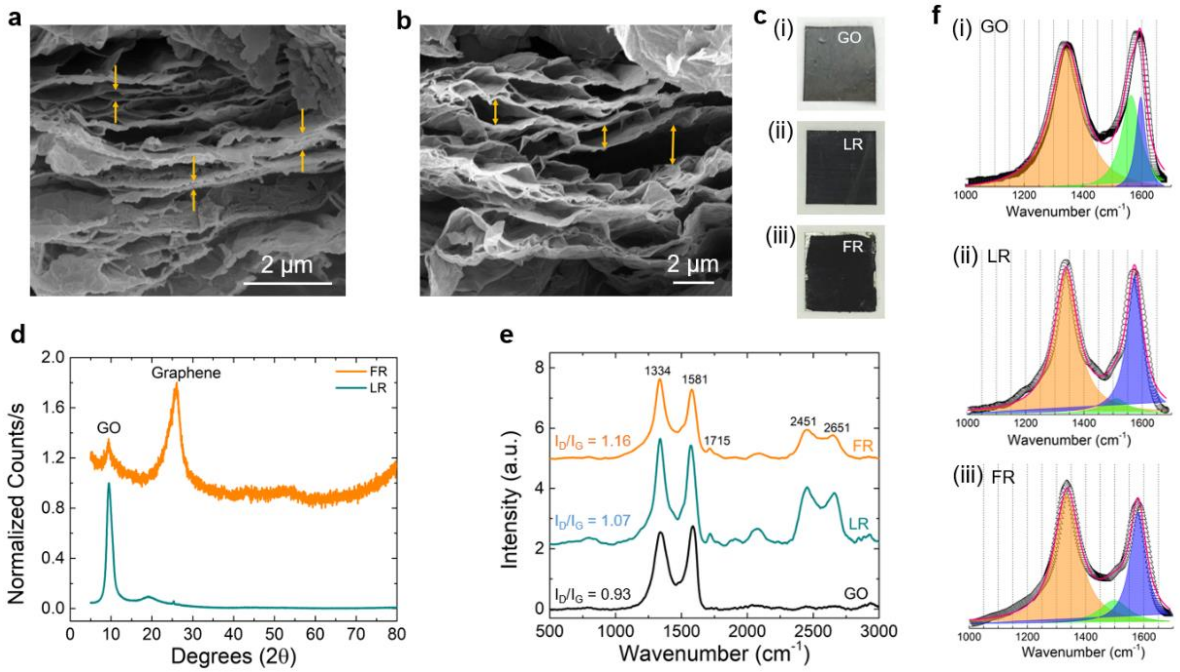

Figure 2.3. Comparison of (a, b) SEM images, (c) bright-field images, (d) XRD analysis and (e, f) Raman spectra of graphene produced by laser reduction and flash reduction methods. (a) SEM image of laser reduced sample shows agglomerated compact layers of graphene sheets with the average interlayer spacing of 0.25 µm. (b) SEM image of flash reduced sample illustrates the delaminated layers of graphene sheets with the mean spacing of 1.76 µm. (c) Bright field images of laser and flash reduced samples apparently show the color change from brown (in GO) to black (in LR and FR) after laser and flash reduction methods. (d) XRD results show a considerable amount of residual GO ($I_{GO}/I_{Graphene} \approx 11.14$) after performing the laser reduction (LR) technique. Meanwhile, the value of residual GO remarkably decreased by an order of magnitude ($I_{GO}/I_{Graphene} \approx 0.77$) by using of flash reduction (FR) method. In order to adhere LR sample to sample holder, a thin layer of Vaseline was used. (e, f) Comparison of the Raman spectra of GO, LR, and FR samples. The D and G-band for each sample is deconvoluted into three peaks.

Figures 2.3a and 3b show the cross-sectional SEM images of LR and FR graphene structure, respectively. We analyzed the distance between graphene layers at ten different places on each sample (Figure 2.4).

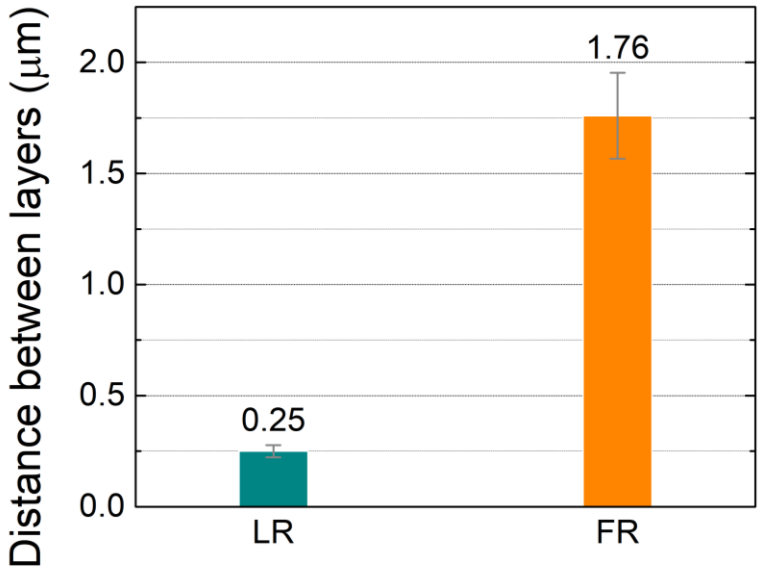

Figure 2.4. Average distance between graphene layers reduced by laser (LR) and flash (FR) based on the analysis of cross-sectional SEM images. The results obtained by image analysis of ten different locations on the cross-sectional images for each sample. Laser reduced sample exhibits a compact structure with the mean interlayer spacing of 0.25 μm. Meanwhile, flash reduced sample shows an average interlayer spacing of 1.75 μm.

The LR sample shows an average spacing of 0.25 μm and the FR sample shows an average spacing of 1.76 μm. Delamination of interconnected multi layered graphene structure benefits electrochemical devices by providing a highly porous architecture that facilitates the wettability of active material and results in rapid ion transfer and enabling more surface for the formation of double layer capacitance. Color change from brown (for GO) to black (for LR and FR) can be considered as the first evidence for the successful conversion of GO to graphene which is shown in Figure 2.3c. We also measured the electrical surface resistance of the device before and after the reduction process. The electrical conductivity of GO surface was measured to be 6.38×10^{-4} S m^{-1} and after reduction (Figure 2.5), the conductivity increased to 1.40×10^{3} S m^{-1} and 2.14×10^{3} S m^{-1} for LR and FR process, respectively.

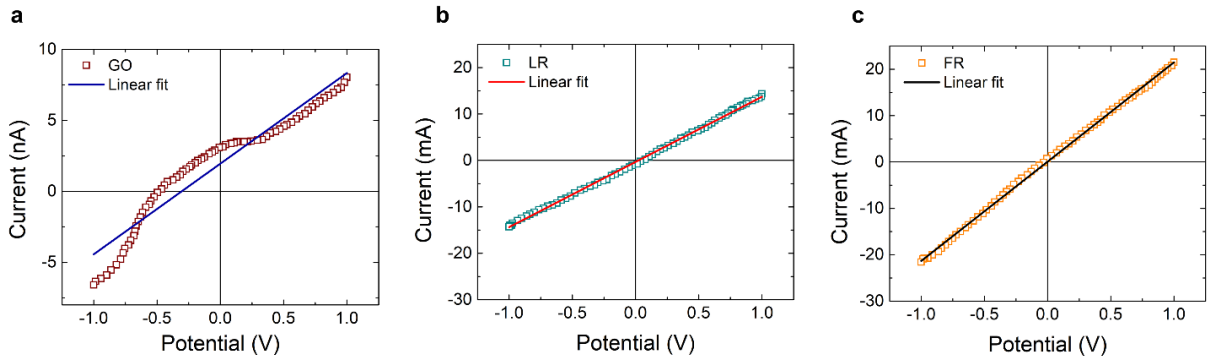

Figure 2.5. Electrical conductivity measurements of (a) GO, (b) LR and (c) FR. The electrical conductivity of GO measured to be 6.38 x 10^{-4} S/m and after reduction, the conductivity increased to 1.40 x 10^{3} S/m and 2.14 x 10^{3} S/m for LR and FR process, respectively.

Another parameter that affects the overall functionality of graphene based supercapacitors is the amount of GO converted to graphene during the conversion process when using GO as the starting material. Figure 2.3d shows the XRD results for the LR and FR samples. A thin layer of Vaseline was used to adhere LR sample to sample holder and keep it flat. The results were compared with the XRD of graphite, graphene, and GO. The XRD pattern of FR shows two characteristic peaks. The broad peak at $2\theta = 26^{o}$ with a *d*-spacing of 3.42 A^{o} is generally associated with the graphitic peak.(Lu, Liu et al. 2012, Johra, Lee et al. 2014, Mishra, Tripathi et al. 2014) The other peak occurred at the same position as that of LR sample's characteristic peak. The XRD pattern of LR shows characteristic peak of $2\theta = 10.09^{o}$ which corresponds to a *d*-spacing of 8.76 A^{o}. This peak is generally associated with graphene oxide.(Lu, Liu et al. 2012, Johra, Lee et al. 2014, Mishra, Tripathi et al. 2014) The oxygen containing functional groups in GO are responsible for the increased d-spacing seen in the XRD of LR samples.(Buchsteiner, Lerf et al. 2006, Lerf, Buchsteiner et al. 2006, Dikin, Stankovich et al. 2007) Some conclusion can be drawn from the intensity ratio of peak of 2θ in the XRD results about which sample has higher oxygen containing functional groups. LR graphene XRD structure shows a considerable amount of residual graphene oxide ($I_{GO}/I_{Graphene} \approx 11.14$, I_{GO}: intensity of GO peak, $I_{Graphene}$: intensity of graphene peak)

compared to FR graphene structure ($I_{GO}/I_{Graphene} \approx 0.77$). This residual GO negatively influences the electrochemical properties of supercapacitors and reduces the amount of capacitance achievable by the device to much lower values. Therefore, the amount of GO conversion should be taken into consideration before using such material in an application regardless of the chosen method for GO reduction. Raman spectrum of laser and flash reduced samples are provided in Figures 2.3e and 3f. First of all, the appearance of 2D peaks at ~ 2651 cm^{-1} in the Raman spectra of LR and FR samples is another evidence of the conversion of GO to graphene (2D peak is absent in the GO Raman spectrum) (Figure 2.3e). The G-band and D-band appears for all the samples. The G-band of LR (1572 cm^{-1}) and FR (1581 cm^{-1}) samples moved to a lower frequency compared to G-band of GO (1585 cm^{-1}) sample. This indicates topological disordering of two-dimensional graphene layers and formation of three-dimensional structures in FR samples. Another indication of three-dimensional structure formation can be derived from the change in I_D/I_G ratio. The I_D/I_G intensity ratio of GO was 0.93 and increased to 1.07 for LR, and further increased to 1.16 for the FR sample. It indicates reduction of the grain size of the sp^2 domains while keeping the aromatic ring intact during the reduction of GO,(Fang, Huang et al. 2017) and the elimination of oxygen functional groups.(Fan, Wang et al. 2010) Similar observations were also reported for reduced GO in previous literatures.(Tung, Allen et al. 2009) The G-band represents in-plane stretching mode vibration of sp^2 sites (double bond carbon atoms) and D-band represents breathing mode vibration of sp^2 sites. More number of phonons participate in the vibration due to decrease in grain size and hence the intensity of G-band decreases. Since the linewidth of D and G peaks are different in all the samples, the 1st order Raman spectra were deconvoluted by three peaks: two of those peaks appeared at D and G-band positions and the third peak is denoted as D*. The D* peak is interpreted as the amorphous sp^3 content (for example, single bond carbon as C-OH).(Vollebregt, Ishihara et

al. 2012, Claramunt, Varea et al. 2015) Figure 2.3f shows the positions of D* band: GO (1563.5 cm^{-1}, FWHM = 80.9 cm^{-1}), LR (1510.4 cm^{-1}, FWHM = 99.8 cm^{-1}), and FR (1498.7 cm^{-1}, FWHM = 127.9 cm^{-1}). According to Claramunt et al.,(Claramunt, Varea et al. 2015)[48] with decrease in oxygen content, the D* peak moves toward lower frequencies (wavenumbers). Compared to GO (1563.5 cm^{-1}), the D* peak moved to a lower frequency for the FR samples (1498.7 cm^{-1}). It provides further confirmation that for FR sample, the oxygen content is decreasing compare to both GO and LR samples.

Further study were performed to understand the effect of supporting substrate on the interlayer spacing and the performance of electrochemical device. Three differently patterned plastic substrates were used to convert GO to graphene using flash reduction technique. For FR specimen that was exposed to flash light on a non-patterned substrate, bottom graphene layers at the interface of active material and substrate are found to be compressed (Figure 2.6a). Delamination of graphene layers occurred only for the top layers, about 2 μm above the substrate. Meanwhile, interconnected graphene structure were found to be highly delaminated right above the substrate when GO was reduced on patterned substrates (nano and micro substrates) (Figures 2.6b, 2.6c). The results can be explained by the fact that nano and micro substrates provide extra space for the expansion of layers and allow escape route for the oxygen gas generated during the GO reduction process. It is noteworthy to mention that the delamination of graphene sheets is more clearly visible when the size of patterns increases from hundreds of nanometers to few microns. Our analysis shows that the average graphene interlayer distance increased from 0.8 μm to 2.2 μm while using micro patterned structure instead of non-patterned structure (Figures 2.6a-c).

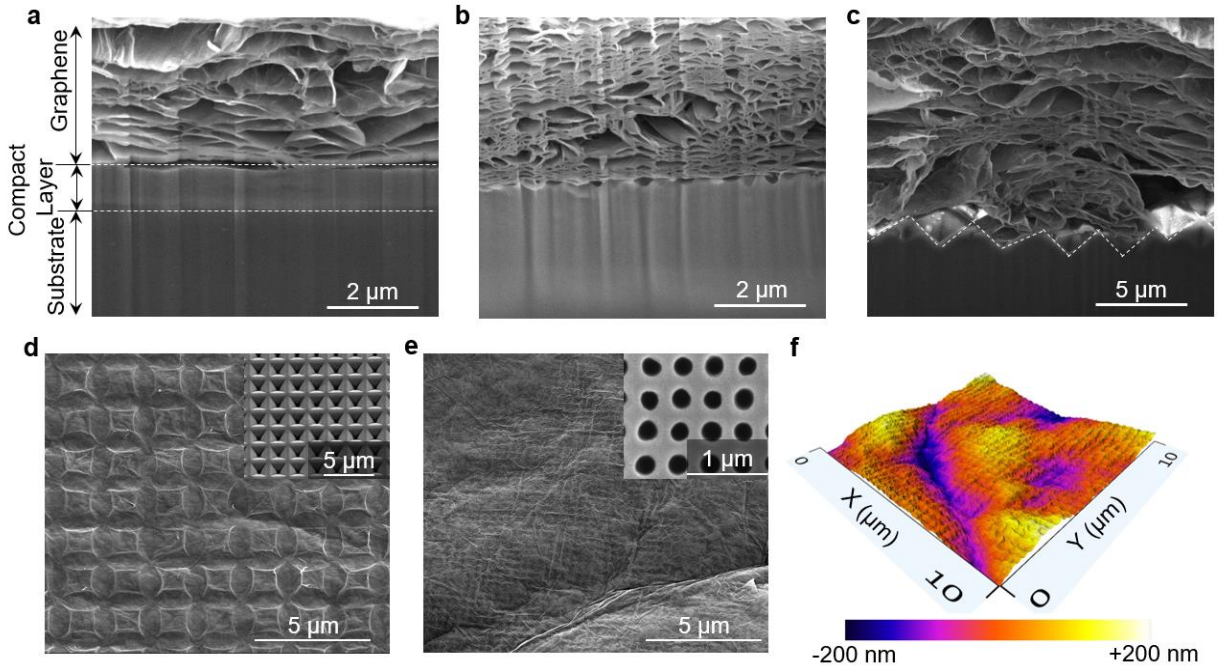

Figure 2.6. Comparison of cross sectional and top view SEM images of electrodes produced using flash reduction method on flat, nano and micro structure substrates showing the effect of substrate engineering. (a) SEM image of flash reduced on flat (FR) sample shows a compact layer of graphene sheets. (b) SEM images of flash reduced on nano structure (FRNS) electrode illustrate that the thickness of graphene compact layers considerably decreased, but the bottom layers are not still as delaminated as top layers. (c) SEM images of flash reduced GO on micro structure (FRMS) electrode show the uniformly delaminated layers of graphene from bottom to top. (d) SEM image of GO on microstructured substrate before the reduction process. The inset shows the geometry of the inverse pyramid structure of the substrate with pitch of 2 µm, pit length of 1.5 µm and pit depth of 2.1 µm. (e) SEM image of GO on nano substrate before the reduction process. The inset shows the geometry of the periodic nanohole structure of the substrate with pitch of 350 nm, hole diameter of 180 nm and hole depth of 0.5 µm. (f) AFM analysis confirms the formation of a nanostructured pattern on GO before reduction on nanostructured substrate.

Figures 2.6d, 2.6e and 6f show the surface of drop-cast GO which was in contact with micro and nano patterned substrates. Accordingly, the periodic structures are clearly visible by means of SEM and AFM microscopes. The inset of Figure 2.6d and Figure 2.6e show the SEM of micro and nano structure. The microstructure is inverse pyramid shaped with pitch of 2 µm and depth of 1.2 µm. The nanostructure is nanohole periodic structure with pitch of 350 nm, hole diameter of 180 nm and hole depth of 500 nm.

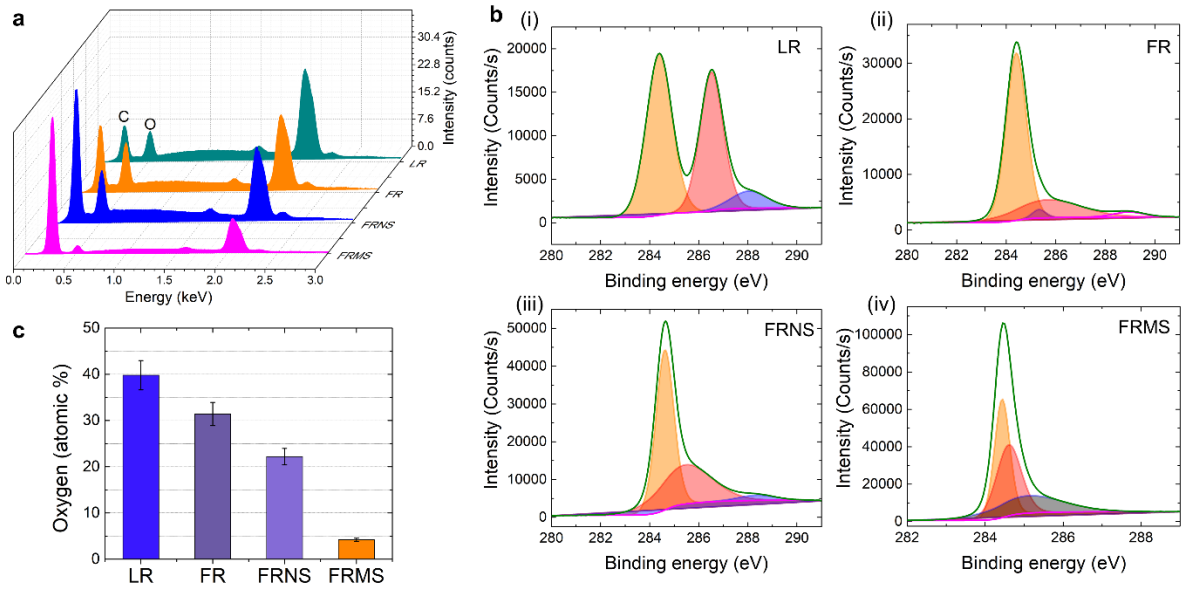

Figure 2.7. EDS analysis and XPS spectra of C 1s in LR, FR, FRNS and FRMS electrodes. (a) EDS analysis shows a dramatic difference in the oxygen and carbon content of samples. (b) XPS results for (i) LR, (ii) FR, (iii) FRNS and (iv) FRMS electrodes confirm the enhanced conversion of GO to graphene while using flash reduction method on patterned substrates. Deconvolution of the XPS peak in to four peaks showed the different oxygen containing functional groups. (c) LR electrode shows the highest amount of residual oxygen (39.8 %) and FRMS sample represents the lowest value (4.2 %). The amount of residual oxygen decreases dramatically from LR to FRMS sample.

Figure 2.7a illustrates the X-ray energy dispersive spectrum (EDS) analysis results obtained for different type of samples inside the SEM to determine the amount of residual oxygen which is directly correlated to residual GO (also see Figure 2.8). For all the samples three prominent peaks were observed. The peak at around 0.270 keV is assigned to C, the peak at 0.521 keV is assigned to O, and the peak at 2.06 keV is due to the Pt (used in SEM to reduce charging effect during imaging). From the analysis, LR specimen showed the highest value of residual oxygen (39.8 at.%) (Figure 2.7c). The flash reduction of GO on micro patterned substrate (FRMS) dramatically decreases the residual oxygen to 4.2 at.%. Thus, the presence of micro and nano structure on substrate surface during GO reduction process, enhances oxygen depletion which results in an expanded interconnected network of graphene.

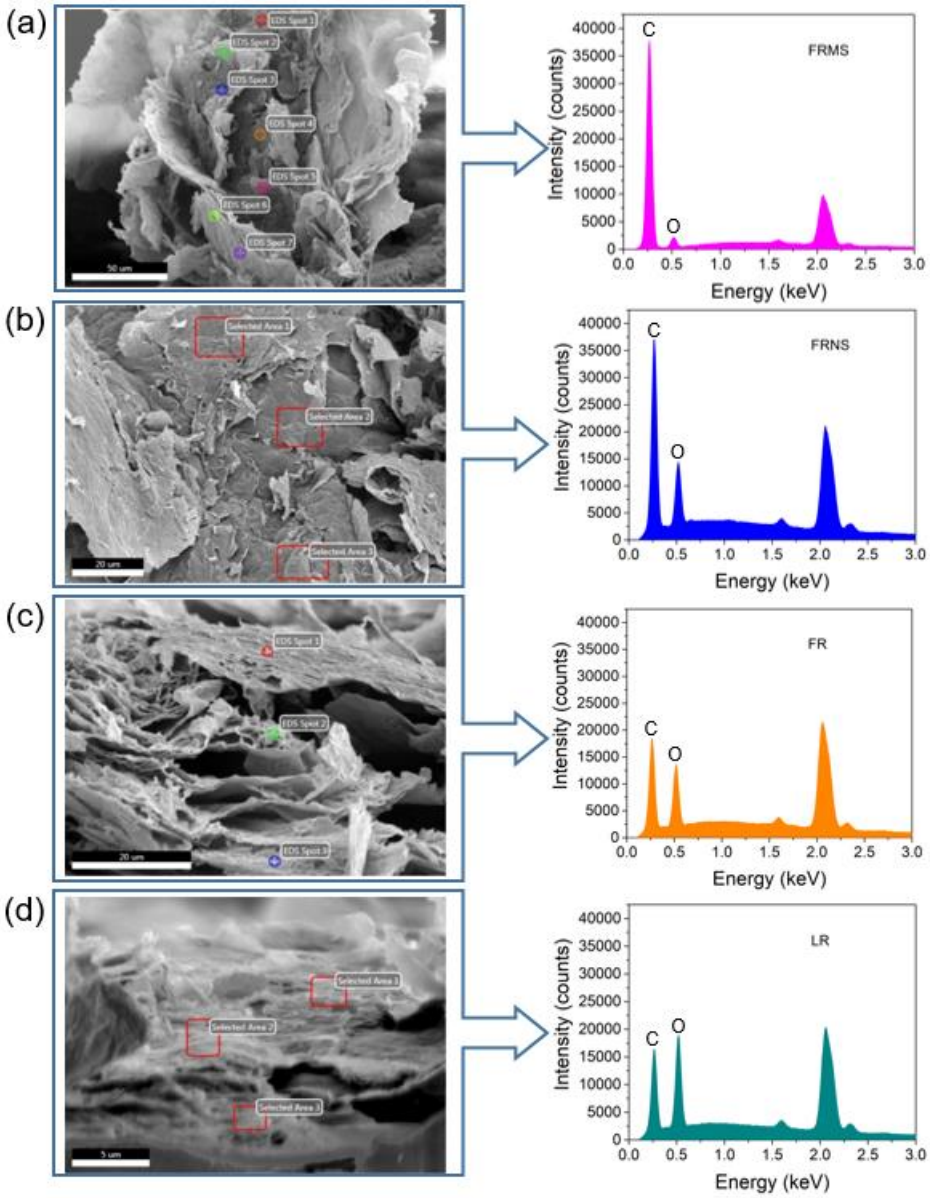

Figure 2.8. X-ray energy dispersive spectra results for (a) FRMS, (b) FRNS, (c) FR and (d) LR. The least amount of residual oxygen is observed for FRMS samples due to the sufficient room provided for the escape of oxygen produced during the reduction process of GO to graphene. The residual amount of oxygen increases for FRNS, FR and LR samples, respectively. Therefore, the production method and substrate engineering drastically affect the quality of electrodes.

In order to provide further evidence about the difference in the oxygen content, high-resolution XPS C 1s spectrum analysis has been performed for all the samples. By means of this technique, surface chemical properties of carbon and oxygen atoms can be investigated. The XPS C 1s spectra for LR, FR, FRNS and FRMS samples were shown in Figure 2.7c (i)-(iv) respectively.

All the spectrum were deconvoluted into four distinct peaks (FRNS and FRMS showed only three peaks). Distinctive peak shapes and identities clearly demonstrate different surface properties among LR, FR, FRNS and FRMS samples. The XPS peak positions and the corresponding bond assignment are as follows: LR sample has peak at 284.38 eV (C=C), 286.54 eV (C-OH, C-O-C), 287.35 eV (O-C=O), and 288.06 eV (C=O); FR sample has peak at 284.39 eV (C=C), 285.33 eV (C-C, sp^3 C), 285.77 eV (C-O), 288.96 eV (O-C=O); FRNS has peak at 284.6 eV (C=C), 285.54 eV (C-C), 288.47 eV (O-C=O); FRMS has peak at 284.4 eV (C=C), 284.61 eV (C=C) and 285.18 eV (C-C, sp^3 C). The assignment of the bonds are in agreement with the literature values.(Yang and Bock 2017) Yang et al. reported previously that laser reduction method of graphene oxide is not capable of removing oxygen-containing functional groups efficiently.(Yang and Bock 2017) Remarkably, FRMS process removed most of the oxygen containing functional groups compared to other synthesis methods. From XPS analysis, oxygen content of LR, FR, FRNS and FRMS samples were found to be 34.3, 29.9, 15.9 and 4.9 at.%, respectively, which are in close agreement with the values found from the EDS analysis (Figure 2.7c). The decrease in oxygen content in FRNS and FRMS samples demonstrate that employing flash reduction technique on nano and micro structured substrates leads to enhanced conversion of GO to graphene. We also performed FTIR-ATR on GO, LR, FR, FRNS and FRMS samples to compare the amount of residual oxygen content. As can be seen in Figure 2.9, using flash reduction on patterned substrates engenders a considerable reduction of oxygen species.

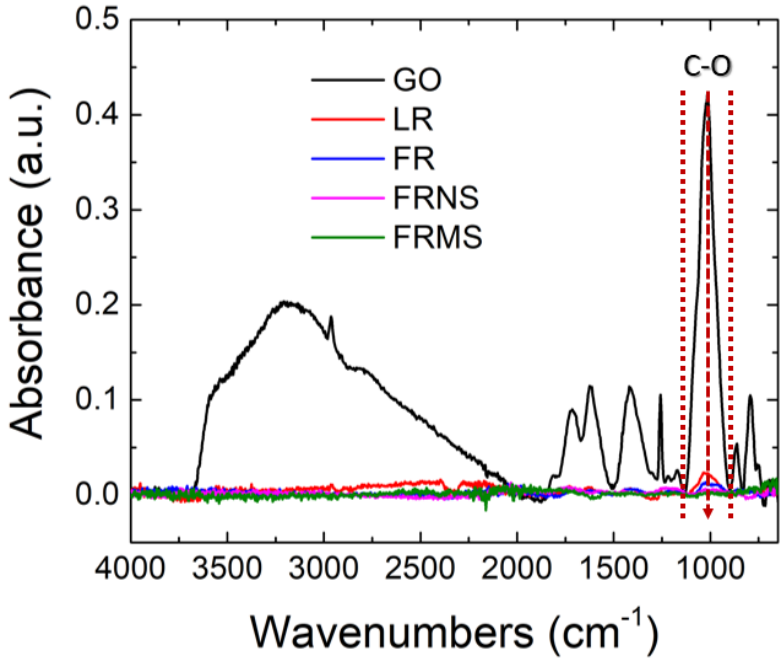

Figure 2.9. FTIR-ATR spectrum of GO, LR, FR, FRNS and FRMS results shows the considerable reduction of oxygen species after using of patterned substrates.

In order to understand the effect of morphological changes of graphene layers on the electrochemical behavior of electrodes, cyclic voltammetry (CV) tests were performed on the samples. Figure 2.10 and Figure 2.11 demonstrate the results obtained from electrochemical response of LR, FR, FRNS and FRMS samples.

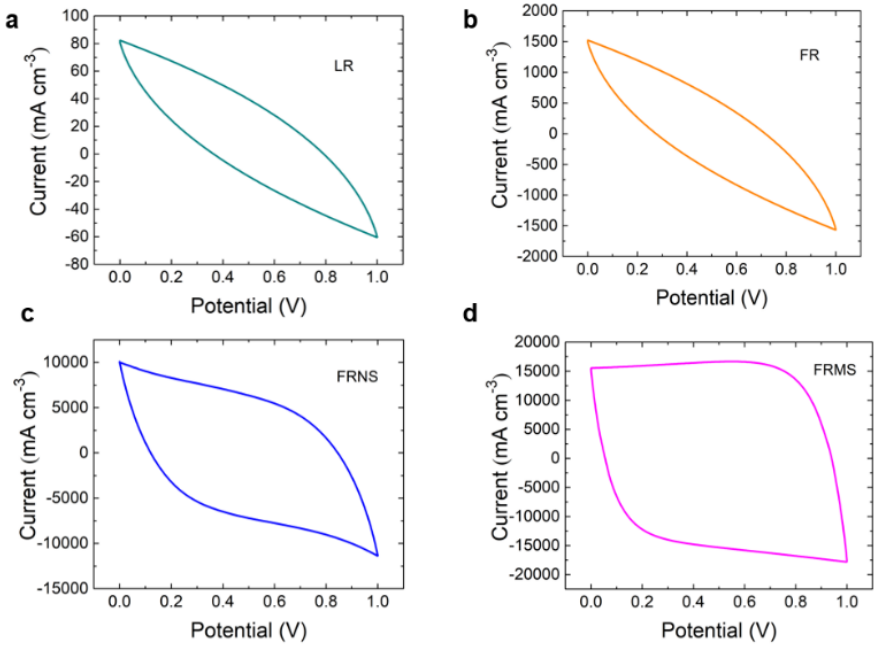

Figure 2.10. Cyclic voltammetry (CV) curves of (a) LR, (b) FR, (c) FRNS and (d) FRMS samples at scan rate of 100 mV s^{-1}. The integrated area of each cycle is correlated with the value of capacitance and increases from LR to FRMS electrode by orders of magnitude. FRMS CV curve reveals a rectangular shape that confirms the swift current response by voltage change.

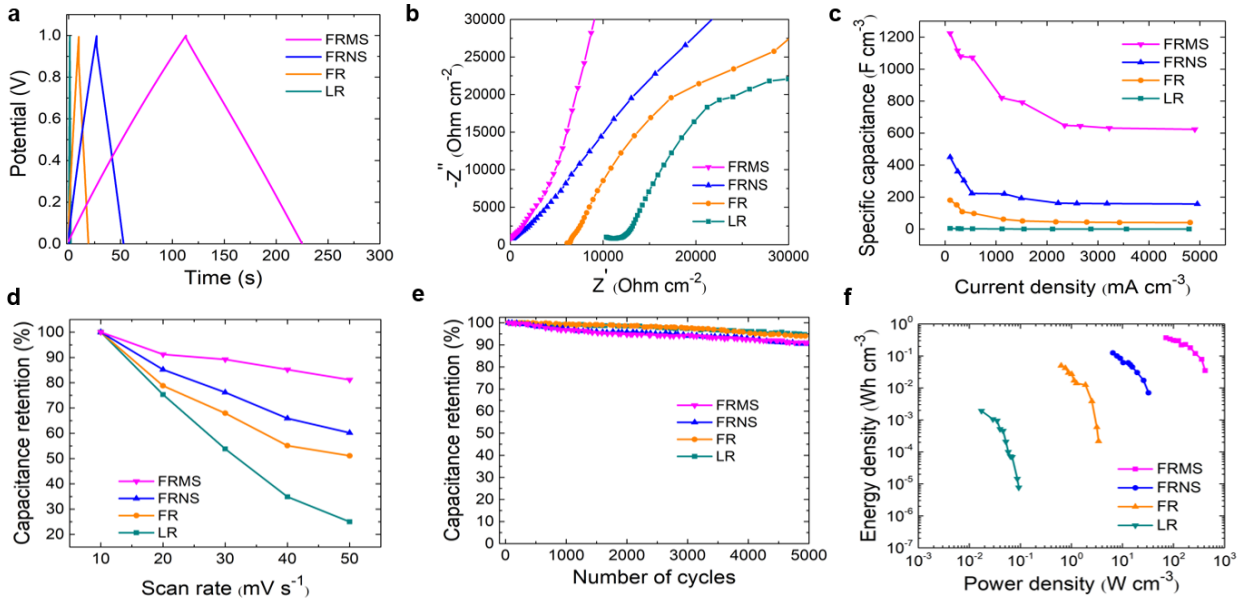

Figure 2.11. Electrochemical performance of LR, FR, FRNS and FRMS electrodes. (a) Galvanostatic charge/discharge curves at the current density of 100 mA cm^{-3}, shows a dramatic difference in the discharge time of various electrodes. (b) Nyquist plot shows the complex plane plot of impedance for four different electrodes. (c) Plot showing the volumetric capacitance evolution as a function of the current density. (d) Evolution of specific capacitance vs. scan rate (e) Reliability plot. (f) Ragone plot.

The CV curves (Figure 2.10) were reported for a scan rate of 100 mV s^{-1} and normalized by the volume of the film (see Figure 2.12 for volume measurement details).

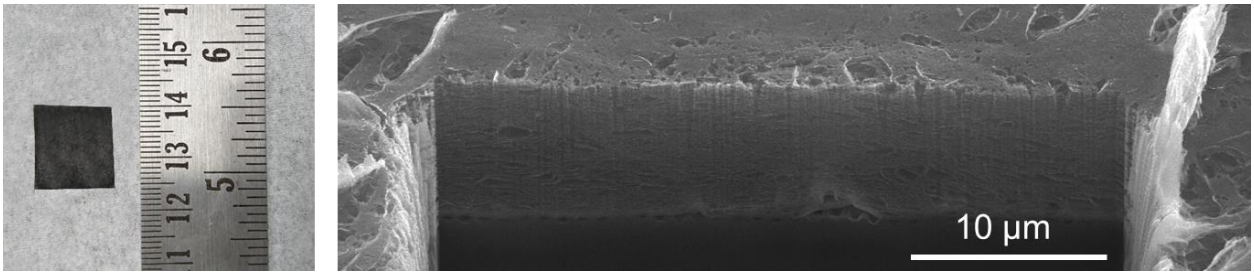

Figure 2.12. Measurement of effective area and thickness of electrodes by means of top view images and cross sectional SEM microscopy. The area was measured by AutoCAD software package. In order to estimate the thickness of rGO in samples, focused ion beam (FIB) was employed to create a pit in random locations and take cross sectional SEM images.

The rectangular symmetric shape of the CV curve for FRMS indicates formation of electric double layer (EDL) capacitor. The increase of specific current (current per unit volume) for FRMS device with increase of scan rate from 10 mV s^{-1} to 300 mV s^{-1} (Figure 2.13) indicates fast charge propagation within the electrode. Further, LR sample showed a peak current density of 80 mA cm^{-3}.

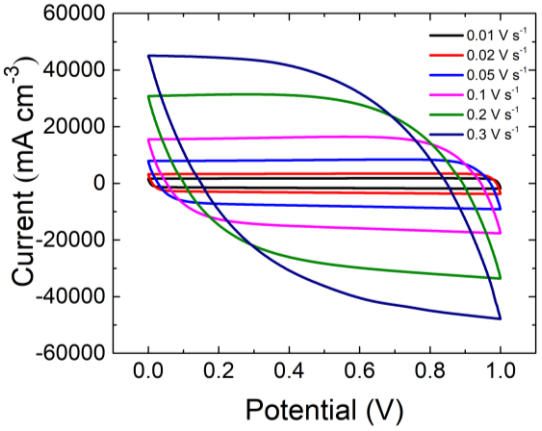

Figure 2.13. Cyclic voltammetry (CV) tests of FRMS device in several scan rates. The increase of specific current (current per unit volume) in this device with increase of scan rate from 0.01 V s^{-1} to 0.3 V s^{-1} indicates fast charge propagation within the electrode.

The FRMS sample showed two-order of magnitude higher current density (15,000 mA cm^{-3}) compared to LR devices. The volumetric capacitance is estimated using two methods: (1) from

the integration of CV curves, and (2) from the galvanostatic charge/discharge curve. The volumetric capacitance of LR, FR, FRNS and FRMS electrodes were calculated using the relation(Wen, Hao et al. 2014) $C_v = \frac{\int I.\mathrm{d}V}{\mathcal{V}.\Delta V.\nu}$, where C_v = volumetric capacitance (F cm^{-3}), I = voltammetric current (A), $\mathcal{V}$ = volume (cm^3) of the device, ΔV= sweep potential window (V) and ν= scan rate (V s^{-1}). The volumetric capacitance of LR, FR, FRNS and FRMS electrodes were found to be 3.7 F cm^{-3}, 178.7 F cm^{-3}, 441.5 F cm^{-3} and 1205.2 F cm^{-3}, respectively. The galvanostatic charge/discharge (GC) curves were performed at a constant current density of 100 mA cm^{-3} and shown in Figure 2.11a. The triangular shape of the GC curve indicates fast ion transport and efficient EDL formation within the supercapacitor electrodes. The volumetric capacitance of the different supercapacitor designs were calculated from the galvanostatic charge/discharge values using the equation(Wen, Hao et al. 2014) $C_v = \frac{I}{\mathcal{V}(-dV/dt)}$. The volumetric capacitance obtained by charge/discharge curves were estimated to be 3.8 F cm^{-3} (LR), 180.7 F cm^{-3} (FR), 450.1 F cm^{-3} (FRNS) and 1224.4 F cm^{-3} (FRMS). The volumetric capacitance values estimated by the two methods are in agreement with each other. The IR drop (voltage drop at the start of each discharge curve) was measured to be ~ 0.01 V at 100 mA cm^{-3}indicating very low resistance for all the devices. The corresponding results for three-electrode test were shown in Figure 2.14.

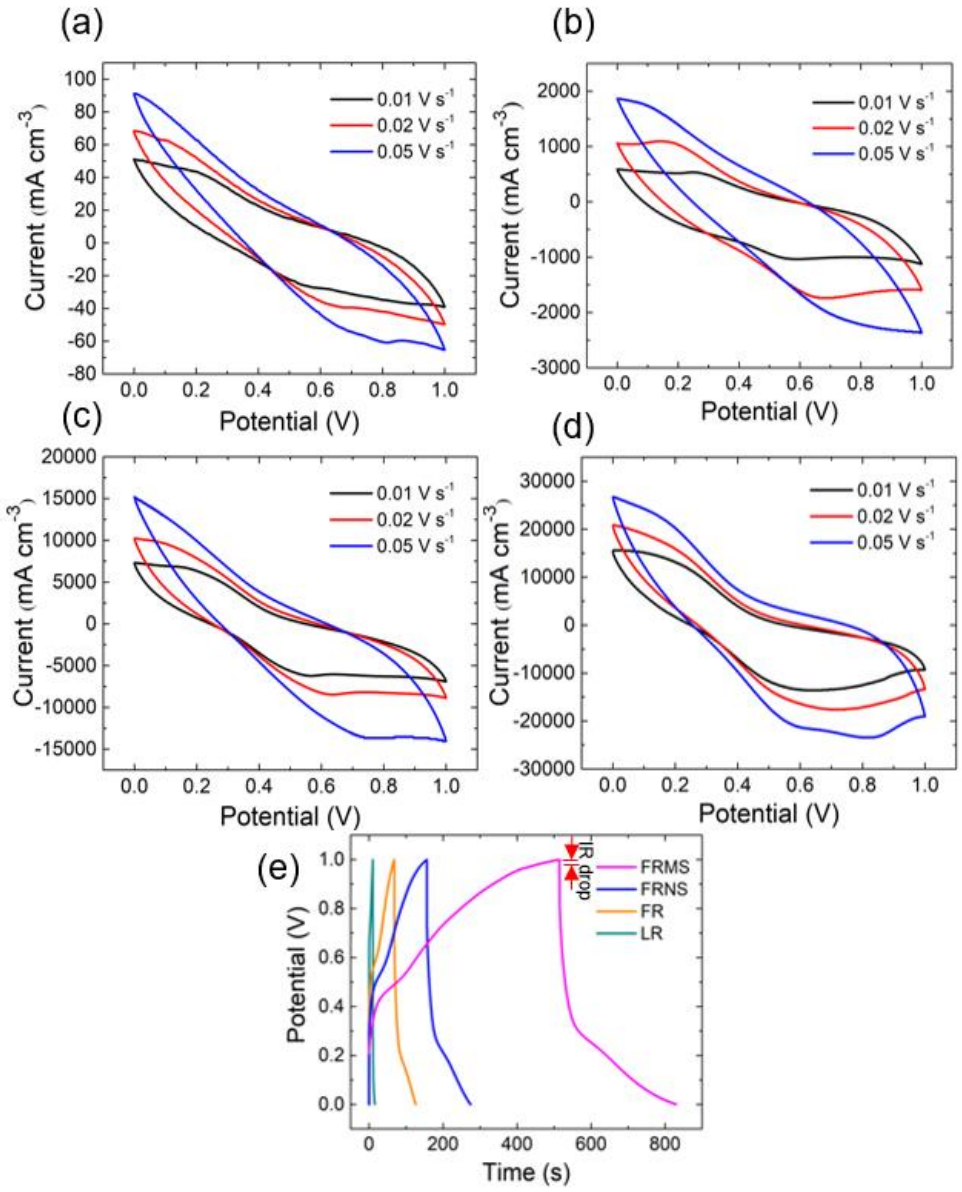

Figure 2.14. Cyclic voltammetry (CV) and galvanostatic charge/discharge curves at the current density of 100 mA cm^{-3} in three electrode cell. CV profiles of (a) LR, (b) FR, (c) FRNS and (d) FRMS are showed in three scan rates of 0.01, 0.02 and 0.05 V s^{-1}. The integrated area of each cycle is correlated with the value of capacitance and increases from LR to FRMS electrode by orders of magnitude. (e) Charge/discharge curves show a dramatic difference in the discharge time of various electrodes. FRMS electrode illustrates the highest double layer capacitance.

From both CV and charge/discharge diagrams, order of magnitude differences in volumetric capacitance values were observed for the FRMS devices, mainly due to the removal of residual oxygen containing functional groups and the increase in the interlayer spacing originated from adopting different synthesis method. Therefore, such major improvements can be obtained

from exact same precursors by solely manipulating and engineering the electrode materials. Figure 2.11a shows that 324x higher volumetric capacitance can be obtained from flash reduction of GO (FRMS devices) compared to laser scribing (LR devices) by just manipulating the geometry of the supporting substrate. Furthermore, reducing GO by laser scribe drive takes several hours for producing acceptable amount of graphene, while much higher quality graphene structure can be produced in less than a second by flash reduction technique.

Utilizing patterned substrates (FRNS and FRMS) instead of a flat surface (FR) also provided high specific capacitance. The specific capacitance was calculated using the equation: $C_S = \frac{I}{m(-dV/dt)}$, where *m* is the active mass within the device. The active mass was calculated using two methods: (1) by weighing the sample after GO reduction and subtracting the weight of the substrate, (2) using SEM to calculate the volume and estimating the mass using the density of graphene. The specific capacitance of FRMS was calculated to be 680.2 F g^{-1} at a current density of 100 mA cm^{-3}, which is higher than the theoretical value of 552 F g^{-1} reported for single layer graphene (it should be noted that the theoretical value is calculated from the single-layer graphene intrinsic capacitance(Xia, Chen et al. 2009) value of ~ 21 µF cm^{-2}, and specific surface area of graphene(Stoller, Park et al. 2008, Liu, Yu et al. 2010, Zhu, Murali et al. 2010, Zhu, Murali et al. 2011, Chen and Dai 2013) ~ 2630 m^2 g^{-1}). Due to the use of reduced GO and existence of residual oxygen in the samples, pseudocapacitance and double layer capacitance both contribute to the total capacitance value.(Shao, El-Kady et al. 2015, Chee, Lim et al. 2016) As a result, the achieved capacitance for FRMS sample is higher than the theoretical value. Correspondingly, interconnected graphene network produced by a low-cost material like GO, provides quite higher specific capacitance than a single layer graphene which has been presumed to possess the highest electrochemical capacitance among different types of graphene. Further, micro structure patterned

electrode (FRMS) demonstrated 172% higher volumetric capacitance compared to the nano structured graphene electrode (FRNS). This can be explained by the ~ 51% higher inter layer spacing of graphene sheets and ~ 14.5x greater conversion of GO to graphene on FRMS samples compared to FRNS. BET results showed that FRMS sample has specific surface area of 1262.3 m^2 g^{-1}, which is about four-fold higher ion accessible area compared to 355.8 m^2 g^{-1} found for GO samples (Figure 2.15).

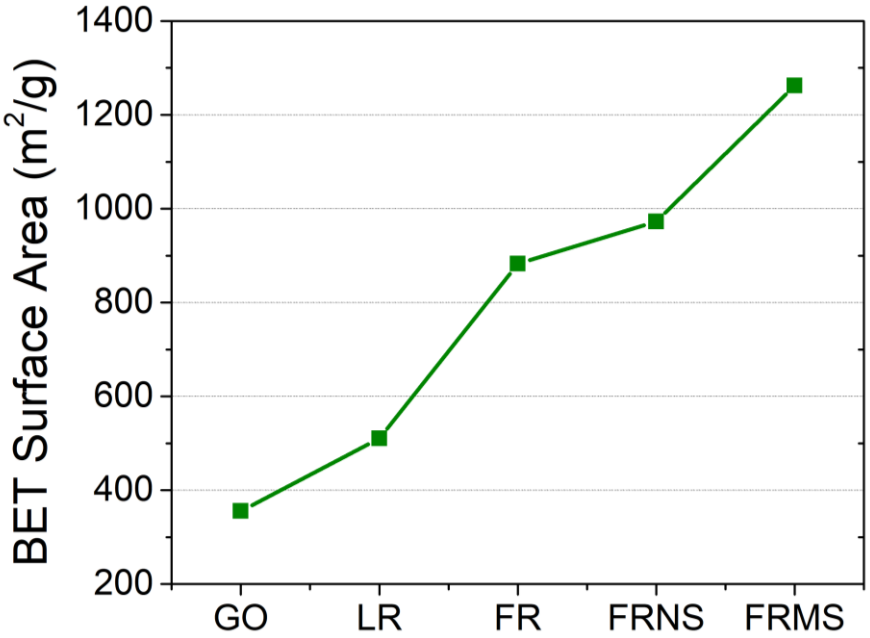

Figure 2.15. BET surface area measurements. The plot shows a dramatic increase in BET surface area of samples from 355.8 m^2 g^{-1} (GO) to 1262.3 m^2 g^{-1} (FRMS). This can explain the higher double layer capacitance of FRMS samples in comparison with other electrodes.

A further confirmation of fast ion transport in FRMS device is supported by the electrochemical impedance spectroscopy (EIS) results shown in Figure 2.11b. At low frequency the curve for FRMS showed large slope with sharp (90^o) rise, indicating high accessible surface area in the graphene film. At higher frequency, the intercept of the Nyquist plot can be utilized to measure the internal and charge transfer resistance. The FRMS device showed the least internal resistance among the different tested designs and found to be 5.8 Ω cm^{-2} compared to 10340 Ω cm^{-2} measured for LR. In addition, the FRMS showed quite small charge transport resistance with an

almost invisible semicircle, demonstrating the superiority of the device by retaining capacitive behavior even at higher frequencies. Further, the angle of the lower frequency region with respect to the horizontal axis signify the capacitive behavior of the electrode (higher the angle, more capacitive in nature). The near vertical shape of the EIS curve for FRMS device indicates superior capacitive behavior compared to other electrode design. Finally, the time constant, τ_0, (which is the time needed to discharge all energy with > 50% efficiency(Taberna, Simon et al. 2003, Pech, Brunet et al. 2010) is calculated from the impedance phase angle vs. frequency curve to be 20.9 s (LR), 821.4 ms (FR), 615.6 ms (FRNS), and 1.75 ms (FRMS) (Figure 2.16).

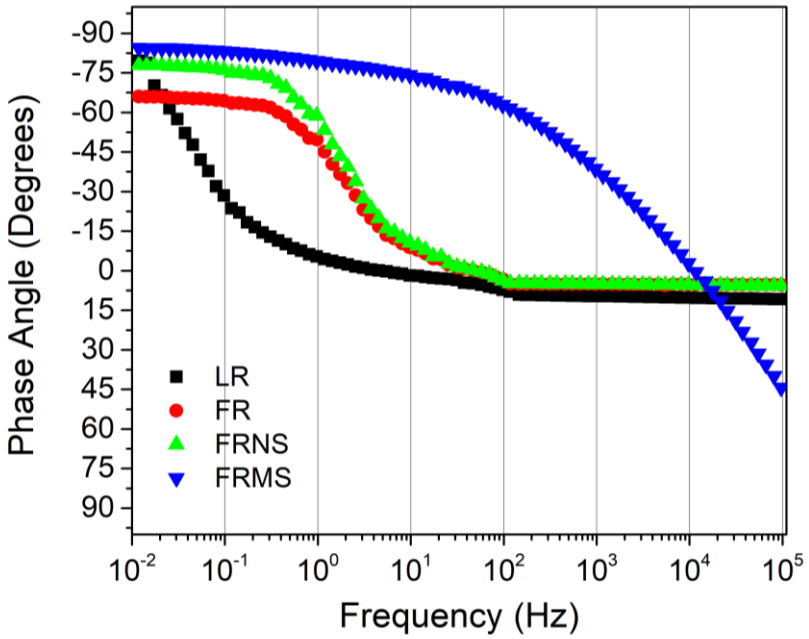

Figure 2.16. Phase angle vs. frequency plot achieved by impedance spectroscopy. The measured time constant (τ_0) is 20.9 s, 821.4 ms, 615.6 ms, and 1.75 ms for LR, FR, FRNS and FRMS samples, respectively. Accordingly, FRMS device has the lowest relaxation time among the tested devices.

This shows that the FRMS device is also suitable for deriving instantaneous power and the relaxation time is lower than other reported values such as activated carbon (700 ms),(Pech, Brunet et al. 2010) onion-like carbon (26 ms),(Kyerematen, Brousse et al. 2017) interdigital graphene/CNT electrodes (4.8 ms).(Beidaghi and Wang 2012)

Further, we investigated the volumetric capacitance of all the devices as a function of current density and shown in Figure 2.11c. The specific capacitance decreases with current density. The FRMS device retains more than 50% of its capacitance when operated at an ultrahigh current density of 4,900 mA cm^{-3}. The highest volumetric capacitance of the FRMS electrode was 1224.4 F cm^{-3}, obtained at a current density of 100 mA cm^{-3}; the volumetric capacitance was decreased to a value of 648.3 F cm^{-3} when the current density was increased to 2346 mA cm^{-3}. The lowest volumetric capacitance for the FRMS was still much higher than the highest value obtained from other samples (Figure 2.11c). The retention of capacitance as a function of scan rate is shown in Figure 2.11d. The volumetric capacitance for the laser reduced sample (LR) dropped dramatically to 25 % of its initial capacitance value by increasing the scan rate from 10 to 50 mV s^{-1} (slope ≈ -17.1% / mV s^{-1}). However, volumetric capacitance for flash reduced samples (FR, FRNS and FRMS) decreased with a milder slope (≈ -4.4% / mV s^{-1}). Interestingly, specific capacitance of FRMS sample retained more than 80 % of its initial capacitance value at higher scan rate of 50 mV s^{-1}. The higher diffusion rate of ions in FRMS sample which is caused due to the high electrolyte wettability of electrodes, is most likely responsible for maintaining the high volumetric capacitance at high scan rates. The capacitance retention of electrodes after being subjected to 5000 charge/discharge cycles is shown in Figure 2.11e. FRMS electrode was able to retain 91 % of its initial capacitance after 5000 cycles. However, it is observed that the flash reduced samples (FR, FRNS and FRMS) lose their initial capacitance slightly faster than laser reduced electrode. This is mostly due to the decrease in interlayer spacing of graphene layers after 5000 cycling that reduces the accessible surface area and affects the capacitance retention of active material. However, it could be easily prevented for on-chip and practical energy storage applications by utilizing appropriate designs and use of solid electrolytes.

In order to further evaluate the electrochemical performance of the supercapacitor devices and bulk electrodes, the energy density (E) and power density (P) were calculated from the charge discharge curve using the relationship: $E = \frac{1}{2}CV^2, C = I/(-dV/dt), P = E/t$, where t = time. Figure 2.11f shows the Ragone plot for different types of interconnected graphene structures used in this study considering the volume of the active materials at the electrode (calculated from the three electrode tests). It shows that increasing the spacing between graphene layers and increasing the amount of GO to graphene conversion, improves both the energy density and the power density of the electrodes. Moreover, the power density and energy density achievable by FRMS electrodes are roughly three order of magnitude higher than that of LR electrodes. By use of flash reduction instead of laser, energy density was increased from 2 mWh cm^{-3} (LR) to 370 mWh cm^{-3} (FRMS). Similarly, the power density increased five order of magnitudes for the FRMS device compared to the LR device from 0.09 W cm^{-3} (LR) to 416.6 W cm^{-3} (FRMS). In fact, as shown in Figure 2.11c, most reported carbon-based supercapacitors shows energy densities <50 mWh cm^{-3}.

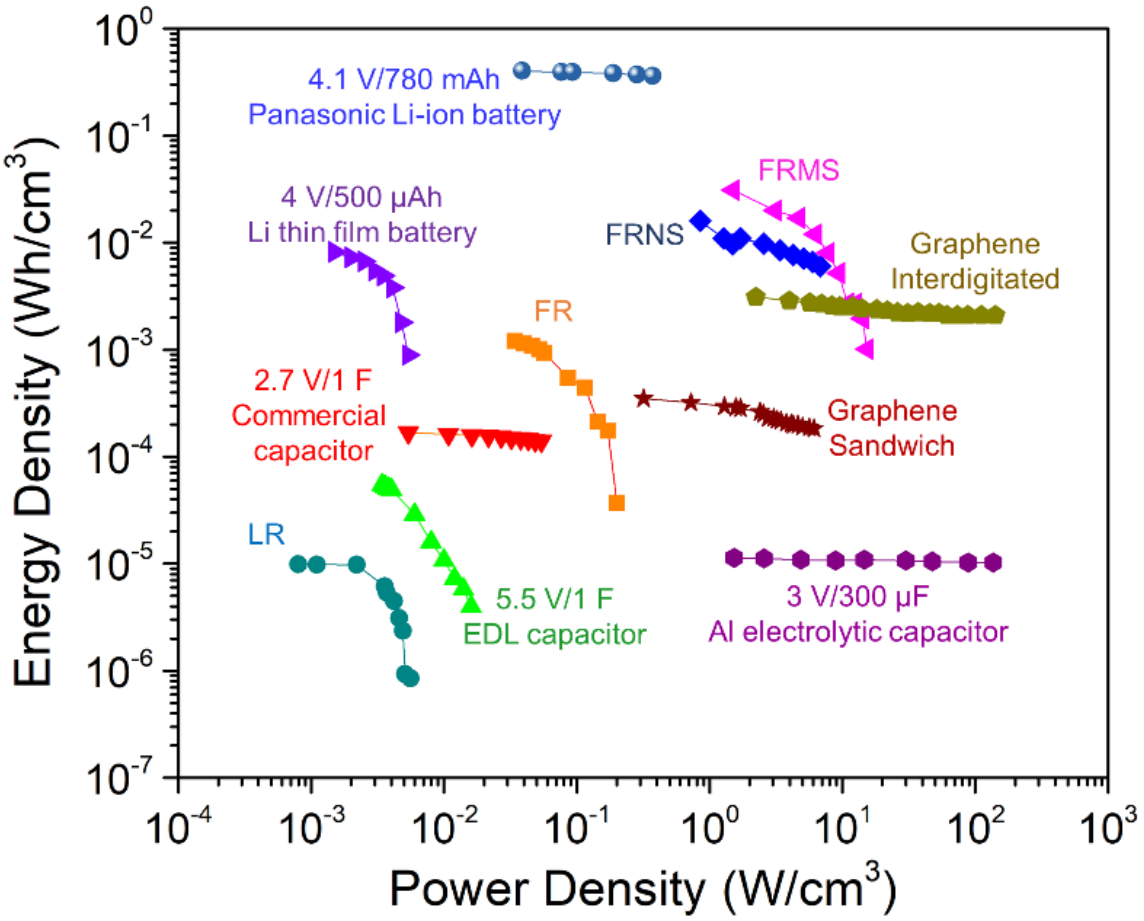

Figure 2.17. Comparison of FRMS electrode properties with several commercial and conventional energy storage devices.

Figure 2.17a shows the Ragone plot comparing the different thin-film based energy storage devices. The data includes result from our own devices, commercial supercapacitors tested under the same dynamic conditions [Maxwell Technologies Ultracapacitors (2.7 V/1 F), Cornell Dubilier EDL Supercapacitor (5.5 V/1 F)], and various literature data for batteries [Li thin film battery (4 V/500 µAh),(Pech, Brunet et al. 2010) Panasonic Li-ion battery (4.1 V/780 mAh)(Nagasubramanian, Jungst et al. 1999) as well as supercapacitors [electrolytic (3 V/300 µF),(El-Kady, Strong et al. 2012) graphene-based sandwiched capacitor,(El-Kady and Kaner 2013) graphene-based interdigitated capacitors.(El-Kady and Kaner 2013) FRMS thin-film sandwich-type device showed energy densities of up to 31 mWh/cm^3, which is four times higher

than Li thin-film battery (8 mWh cm^{-3}), and four order of magnitude higher than the aluminum electrolytic capacitors (0.0114 mWh cm^{-3}). Further, the energy density of FRMS device is approximately 88 times higher than the state of the art graphene-based sandwich supercapacitors.(El-Kady and Kaner 2013) However, these energy densities are still order of magnitude less than the value obtained by the bulk electrodes (Panasonic Li battery, 403 mWh cm^{-3}). In addition, the power density of the FRMS device (15.3 W cm^{-3}) is 41 times higher than the bulk Li-ion battery (0.37 W cm^{-3}), three order of magnitude higher than the Li thin-film battery (0.005 W cm^{-3}), and two times higher than the state of the art graphene-based sandwich supercapacitors (6.1 W cm^{-3}). Although, the power density of FRMS sandwich-type device is lower than the power density of interdigitated devices (141.8 W cm^{-3}), the device was discharged at much shorter time (1.75 ms) compared to the interdigitated supercapacitor (19 ms). Further, the high power densities are generally observed at lower energy densities. For example, the power density of 137 W cm^{-3} for the aluminum electrolytic capacitor was observed at 0.01 mWh cm^{-3}, and for the in-plane graphene micro-supercapacitor,(Wu, Parvez et al. 2013) the power density of 495 W cm^{-3} was observed at an energy density of 0.14 mWh cm^{-3}. However, the power density of 15.3 W cm^{-3} was observed the FRMS devices even at a higher energy density of 1 mWh cm^{-3}. Finally, our devices outperformed most of the existing bulky as well as thin film based micro-supercapacitors designs reported over the past years. The combination of results provided in this paper with recently published designs and studies open up new horizons for practical applications of graphene based structures in countless energy applications and introduce a serious competition for Li-ion batteries.

2.4. Conclusion

In summary, a novel method for taking advantage of the full potential of graphene based structures through substrate engineered interconnected layers in energy applications has been successfully accomplished. Improved performance in the volumetric capacitance, energy density and power density of graphene based electrodes has been achieved by adjusting the graphene layer inter-spacing and improved diffusion of ions. Furthermore, it is presented that the GO conversion value to graphene is an important consideration while using it as precursor, due to its influence on the electrochemical characterization of electrodes. By controlling the value of GO conversion and interlayer spacing of graphene network, high specific capacitance of 680.2 F g^{-1} was obtained. Likewise, on these electrodes extremely high energy density of 370 mWh cm^{-3} was obtained along with a high power density of 416.6 W cm^{-3}. Above all, these modifications are applied by means of flash reduction process of GO and patterning of transparent PET substrate. Thus, the whole process is cost efficient, faster and amenable to scale-up for practical electrochemical energy storage applications.

Chapter 3
Application of Interface Engineered Graphene Electrodes at Extreme Temperatures

3.1. Introduction

Supercapacitors are well-known for low equivalent internal series resistance, high cycling stability as well as providing high power density.(Kumar, Choudhary et al. 2018, Raza, Ali et al. 2018, Strauss, Marsh et al. 2018) These properties are responsible for the ever-increasing interest in supercapacitors for a wide-range of energy storage purposes (e.g., biomedical devices, starting electric vehicles, etc.).(Chen, Qin et al. 2019) To increase the utility of these devices for consumer and aerospace applications, there is a need for producing supercapacitors with lower form factor and that operate over a wide temperature range. Introducing graphene-based supercapacitors redefined their applications by producing flexible, thin and light energy storage devices that can fit into various multifunctional electronics.(Meng, Zhao et al. 2013, Xie, Liu et al. 2014) However, most supercapacitor and batteries technologies operate in a narrow temperature range and are not suited for both low and high temperature operation.(Xu, Yuan et al. 2019) The temperature limitation for supercapacitor is primarily related to the electrochemical properties of materials, which are a strong function of temperature.(Masarapu, Zeng et al. 2009, Asbani, Douard et al. 2019, Yang, Ng et al. 2019) As a result of the materials limitation, most of the reported literature on supercapacitors only report device operation at room temperature. Hence, there are very few studies that report supercapacitor devices that operate at both high and low temperatures.(Vellacheri, Al-Haddad et al. 2014, Zang, Zhang et al. 2017, Newell, Faure-Vincent

This chapter was previously published as Ardalan Chaichi, Gokul Venugopalan, Ram Devireddy, Christopher G. Arges, and Manas Ranjan Gartia. "A Solid-State and Flexible Supercapacitor that Operates Across a Wide Temperature Range." *ACS Applied Energy Materials* (2020). Reprinted by permission of American Chemical Society.

et al. 2018) Furthermore, only a small subset of these studies showed cycling properties of these devices at extreme temperatures because the device performance measurements at the temperature extremes is challenging.(Zang, Zhang et al. 2017)

In order to realize a supercapacitor technology tolerant of extreme temperatures, it is paramount to select functional materials under the temperature range desired. The major components that makeup a supercapacitor consists of an electrolyte, electrodes, current collectors, and packaging. Among these, electrode and electrolyte functionality have limited temperature range and thus are the main liming factors for enabling supercapacitor technology that performs over a wide-temperature range.(Kim, Kim et al. 2015, Zequine, Ranaweera et al. 2016) Despite some attempts to increase the operating temperature range of electrode materials, working temperature of activated carbon and onion-like carbon is still constrained to -10 to 100 °C and -50 to 80 °C, respectively.(Zhang and Zhao 2009, Nègre, Daffos et al. 2016, Zeiger, Jäckel et al. 2016) Reduced graphene oxide (rGO) electrodes, on the other hand, provide functionality in the temperature range (-40 to 200 °C) for supercapacitor applications.(Zang, Zhang et al. 2017) Hence, rGO is a suitable electrode material for fabricating a wide-temperature range supercapacitor, but a robust electrolyte that is functional at both extremely low and high temperatures has been elusive.

Supercapacitor electrolytes are usually categorized into liquid electrolytes (ionic, organic and aqueous liquids) and solid-state electrolytes (mainly polymer or particle gels). Solid-state electrolytes potentially perform better at both extremely high temperatures (> 100 °C) and low temperatures (< 0 °C).(Lv, Liu et al. 2018) Additionally, solid-state electrolytes offer the prospect to mitigate problems associated with liquid electrolytes such as shunt currents and fire hazards. Plus, they enable a thinner and flexible design.(Niu, Zhou et al. 2015) However, the main limitation of using solid-state electrolytes relates to their lower conductivity (100 to 1000 times lower)

compared to liquid electrolytes.(Zhu, Yang et al. 2015, Tiruye, Muñoz-Torrero et al. 2016) Therefore, overcoming the ionic conductivity hurdles of solid-state electrolytes is needed to realize supercapacitors that operate effectively over a wide temperature range.

Most solid-state electrolytes for supercapacitors utilize a polymer or particle gel host. The viscous nature of these materials hinders device flexibility and do not provide good ionic conductivity. A less explored option as a solid-state electrolyte for supercapacitor devices are ion-exchange membranes (e.g., proton exchange membranes (PEMs) and anion/hydroxide exchange membranes (AEMs)).(Rosli, Sulong et al. 2017, Arges and Zhang 2018) PEMs and AEMs have been deployed in various electrochemical processes, such as fuel cells,(Kusoglu and Weber 2017, Arges and Zhang 2018) but these membrane variants for these applications do not traditionally contain any excess electrolyte that can flow in and out of the membrane making them undesirable for supercapacitor applications. Furthermore, their ability to provide ionic conduction is strongly correlated to high levels of hydration for counterion ion dissociation from tethered ionic groups to the polymer backbones.(Kusoglu and Weber 2017, Arges and Zhang 2018) Enabling anhydrous proton conduction in PEMs for fuel cells that operate in the temperature range of 120 to 180 °C was achieved over 25 years employing phosphoric acid-doped PBI.(Li, Jensen et al. 2009) These PEMs, H_3PO_4-PBI, has been implemented in solid-state, high temperature (25 to 150 °C) supercapacitors,(Rathod, Vijay et al. 2009, Kim, Kim et al. 2015, Soavi, Bettini et al. 2016, Staiti and Lufrano 2016, Wei, Wang et al. 2018) but they have not been evaluated at temperatures below 25 °C (even frigid temperatures of less than 0 °C) and their performance cannot be evaluated above 180 °C as the H_3PO_4 starts to evaporate from PBI.(Lee, Spendelow et al. 2016, Lee, Maurya et al. 2018, Lee, Choe et al. 2019) Our group has recently extended the temperature range of anhydrous PEMs through the use of polycation-PBI polymer blend doped with H_3PO_4.(Venugopalan, Chang

et al. 2019) The polycation in the blend was Udel® poly (arylene ether sulfone) featuring quaternary benzyl pyridinium cations (QPPSf). The H_3PO_4-QPPSf-PBI showed a considerably high in-plane proton conductivity (up to 290 mS cm^{-1} at 220 °C) as well as superior mechanical properties (11.9 MPa at break and 25% elongation), while also endowing long-term thermal stability at 220 °C.(Venugopalan, Chang et al. 2019) In this work, we not only show that the solid-state electrolyte membrane (SSEM) of H_3PO_4-QPPSf-PBI blend can extend the temperature range to 220 °C for an all solid-state, flexible supercapacitor with rGO electrodes, but this SSEM also fosters proton conduction as low as -70 °C. Therefore, the polycation-PBI SSEM incorporated with rGO electrodes has resulted in a supercapacitor technology for applications necessitating a wide temperature range.

3.2. Materials and Methods

3.2.1. Preparation of Solid-State Electrolyte

Chloromethylated poly(arylene ether sulfone) (CMPSf) was made via a Friedel-Crafts reaction following the procedure reported by Arges *et al*. (Arges, Parrondo et al. 2012) An example reaction is as follows: 10 g of Udel® poly(arylene ether) sulfone (PSf) was dissolved in 500 ml of chloroform in a round bottom flask. Once the PSf dissolved, 6.8 g of paraformaldehyde. Afterwards, 30 mL of chlorotrimethylsilane was added to the samples in a sealed bulb. 525 μL of $SnCl_4$, the Lewis acid catalyst, was added to the sealed bulb. The degree of functionalization (DF) (i.e., chloromethyl groups per repeat unit) was monitored during the reaction by withdrawing a sample from the flask. The withdrawn solution was cooled to room temperature and precipitated in 5:1 volume ratio methanol. The precipitate was collected via vacuum filtration and dried and then analysed via ^1H NMR. When the desired DF values for the CMPSf was attained, the whole reaction solution was cooled to room temperature followed by precipitation in methanol (5:1

volume ratio). The precipitate was collected via vacuum filtration and air dried in the fume hood. The solid was redissolved in chloroform (5wt %) and then precipitated in methanol (5:1 volume ratio) to remove impurities. The solid was collected via vacuum filtration and then vacuum dried at room temperature. The DF value of the purified CMPSf was determined via ^{1}H NMR.

The preparation of the blended membrane was recently reported in our work.(Venugopalan, Chang et al. 2019) A brief description of the method is given here: CMPSf was dissolved in N,N-dimethylacetamide (DMAc) to attain a 5 wt% solution. A similar 5 wt% solution of PBI in DMAc was prepared. Equal volume ratios of PBI and CMPSf solutions were mixed to prepare a solution blend. The mixed solutions were sonicated for half an hour and then drop casted on a levelled glass plate in oven at 120 °C for 6 hours. The dried membranes were peeled off from the glass plates and were immersed in pyridine solution (1M in reagent alcohol) at 40 °C for 16 hours to convert the chloromethylated groups to quaternary benzyl pyridinium chloride groups. The resulting membranes were washed with DI water and blot dried with the thickness of about 36-50 μm. The membranes were then immersed in 85 wt% phosphoric acid at the temperature of 120 ºC for six hours. The membranes were then blot dried to remove the excess acid. The thermal stability, ion-exchange capacity, ^{1}H NMR of QPPSf, and mechanical properties of the membranes were reported in our previous work.(Venugopalan, Chang et al. 2019)

In-plane proton conductivity (κ_{H+}) measurements were performed using galvanostatic impedance spectroscopy with a Gamry 3000 AE potentiostat over a frequency range of 1 MHz to 1 Hz using a 0.1 mA perturbation in a four-point conductivity probe (platinum wires and meshes in a PTFE housing). The κ_{H+} (mS cm^{-1}) of the membranes were found using:

$$\kappa_{H^+} = \frac{\mathrm{L}}{\mathrm{R \times D \times W}} \qquad (1)$$

where L (cm), R (mΩ), D (cm) and W (cm) are defined as distance between the electrodes, resistance of the membrane, thickness of the membrane and width of the membrane, respectively. The κ_{H+} was measured in a temperature-controlled oven (-70 to 220 °C). Three different thermal cycles performed for three individual membrane samples. During each cycle, the conductivity was measured from -70 to 220 °C at different points. The membranes were equilibrated at 25 °C before proceeding to the next cycle (-70 to 220 °C). Thermal gravimetric analysis (TGA) of undoped, H_3PO_4 doped QPPSf-PBI membranes and rGO electrodes were performed under nitrogen using Pyris 1 TGA (TA instruments). The samples were initially heated to 100 °C and equilibrated at that temperature for 10 minutes. Afterwards, samples were heated with the rate of 10 °C min^{-1} up to 700 °C. The phase transition in H_3PO_4 doped QPPSf-PBI membrane was recorded using DSC Q-10 with heating rate of 10 °C min^{-1} from 60 °C to -40 °C under nitrogen atmosphere.

3.2.2. Preparation of rGO Electrodes

High quality water-dispersed graphene oxide (GO) was purchased from Graphenea Inc., Cambridge, MA with GO concentration of 4 mg mL^{-1} and monolayer content of >95 %. For proper exfoliation of the GO, water-dispersed GO was sonicated for 30 minutes in a sonication bath. Afterwards, the GO solution was drop-cast on the surface of a Teflon® sheet and dried at room temperature overnight. The reason for using Teflon® sheet is to prevent the adherence of reduced graphene oxide (rGO) to the temporary substrate. Neewer PRO i-TTL xenon camera flash was employed for reduction of GO to rGO under ambient conditions. Gentec QE25ELPS-MB-INT-D0 light energy meter was used to measure the energy of camera flash which was in the range of 0.1-2 J cm^{-2}. A small explosion sound was heard after flashing the GO and the produced rGO easily detached from the Teflon® surface afterwards. Color change from brown to black was indicated successful GO to rGO conversion. Sandwich type devices were made by packing the electrodes

and membrane by means of temperature resistant Kapton® tape. Copper tape was used for collecting and passing charge from electrodes.

3.2.3. Electrochemical Tests on the Device

Electrochemical tests were performed on sandwich type devices made of rGO flash reduced electrodes and QPPSf-PBI electrolyte. GAMRY 1010E potentiostat was employed to perform the electrochemical impedance spectroscopy (EIS), cyclic voltammetry (CV) and galvanostatic charge discharge (GCD). Kryo 560-16 controlled rate freezer was used to cool down the temperature from 25 to -70 °C. VWR standard oven was employed to test the device at high temperatures (up to 220 °C). Before all the temperature dependent tests, the device was held at the desired temperature for 10 min to reach the temperature equilibrium. EIS experiments were performed in the range of 100 kHz to 1 Hz. From CV curves, areal capacitance was calculated from equation 2:

$$C_v = \frac{\int i.dV}{v.\Delta V.v} \qquad (2)$$

In which, ΔV is the potential window (V), i is the current (A) and v is the area of the active material (cm^{-2}). From GCD plots, areal capacitance was measured by using the following equation:

$$C_v = \frac{-idt}{vdV} \qquad (3)$$

In which, t is value of discharge time. Energy (E) and power (P) density values obtained by equation 4 and 5:

$$E = \frac{C_v \times (\Delta V)^2}{3600} \qquad (4)$$

$$\mathrm{P} = \frac{\mathrm{E} \times 3600}{\Delta \mathrm{t}} \qquad (5)$$

3.2.4. Materials Characterization

Scanning electron microscope images were obtained by Quanta 3D DualBeam FEG FIBSEM with working distance of 10.2 mm and accelerating voltage of 5 kV. Fourier-transform infrared spectroscopy (FTIR) and Raman spectroscopy were performed by Thermo Nicolet Nexus 670 ATR-FTIR (total # of scans = 64) and Renishaw inVia confocal Raman microscope, respectively. Laser 532 nm was used for Raman spectroscopy of samples in the range of 500-3000 cm^{-1} and exposure time of 10 s.

3.3. Results and Discussion

Figure 3.1 illustrates the sandwich type device made by flash reduced rGO electrodes and the 50:50 H_3PO_4-QPPSf-PBI. The inset of the Figure 3.1 shows the chemical structure of the H_3PO_4-QPPSf-PBI. This polycation-PBI blend for the SSEM was prepared using a process disseminated in our previous work (see Figure 3.2).(Venugopalan, Chang et al. 2019)

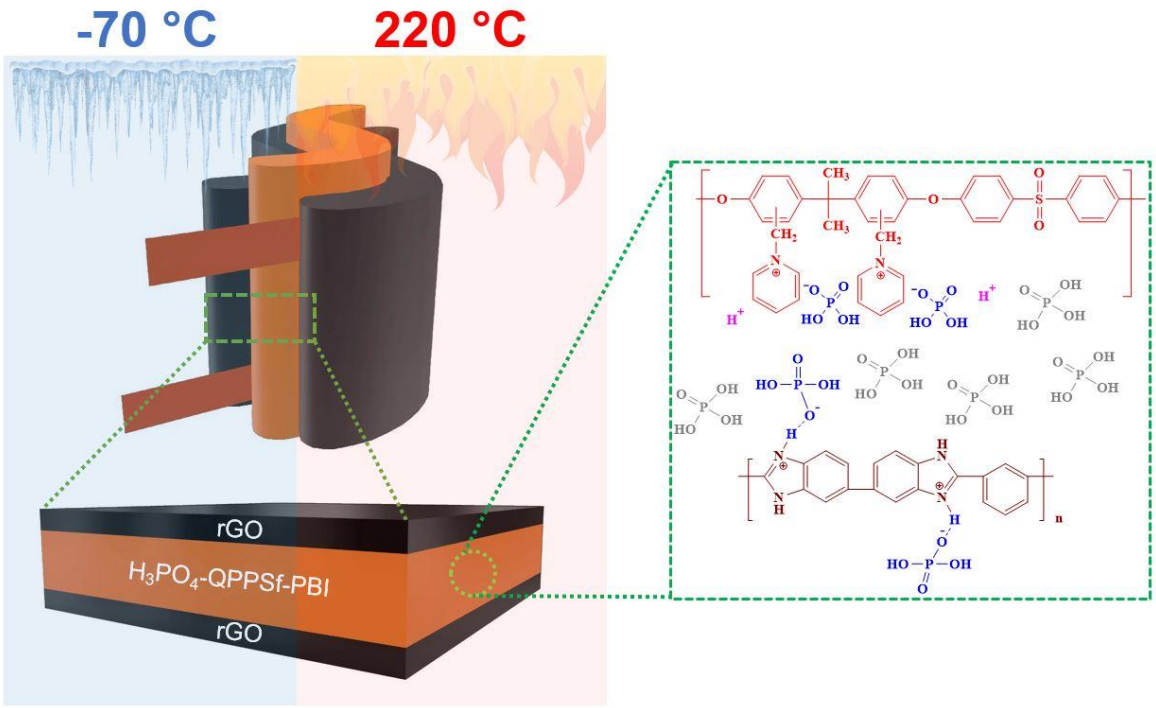

Figure 3.1. Schematic of the sandwich type supercapacitor design featuring rGO electrodes and H_3PO_4-QPPSf-PBI based solid-state electrolyte membrane (SSEM). Chemical structure of the H_3PO_4-QPPSf-PBI SSEM is given in the inset.

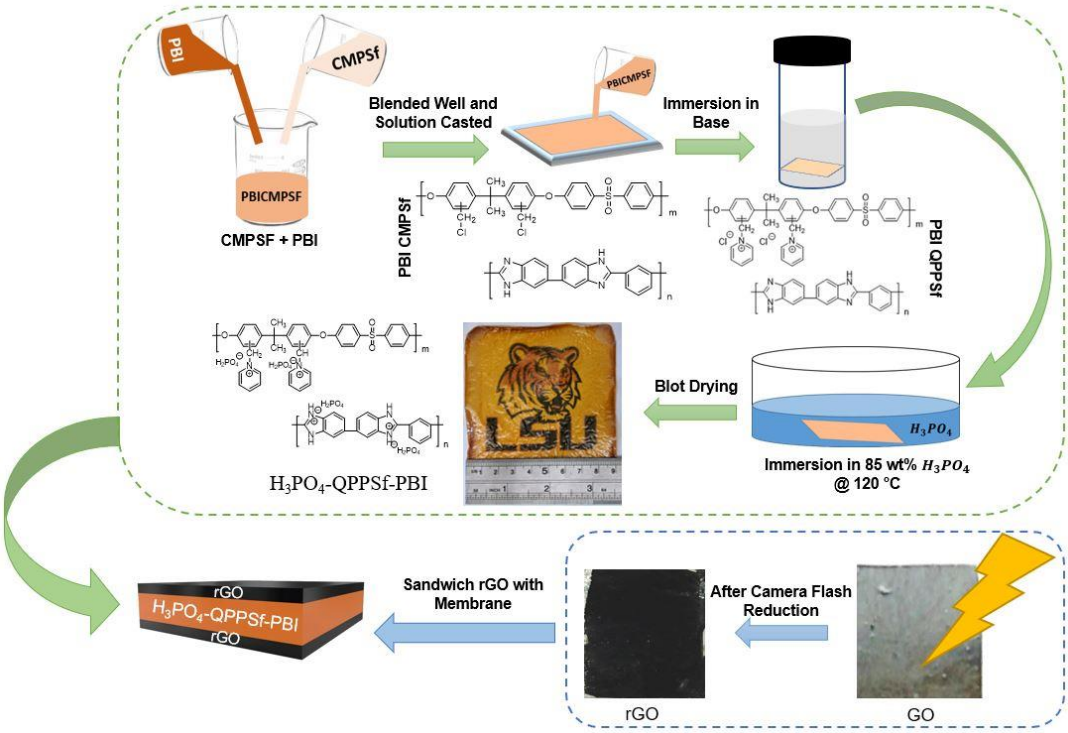

Figure 3.2. Synthesis and fabrication methods of membrane, rGO and the supercapacitor. Color change from brown to black confirms producing of rGO from GO. The 50:50 PBI-QPPSf blend was the best ratio for the two blended polymers to yield the optimal membrane conductivity, mechanical properties, and thermal stability.

Briefly, the polycation, Udel® poly(arylene ether sulfone) with quaternary benzyl pyridinium, was synthesized by first performing Friedel-Crafts chloromethylation of commercially available Udel® poly(arylene ether sulfone).(Palakkal, Rubio et al. 2018) The chloromethylated polymer dissolved in N,N-dimethylacetamide (DMAc, 5 wt%) was blended at a 50:50 ratio with commercially acquired PBI in DMAc (5 wt%, PBI Performance Products).(Palakkal, Rubio et al. 2018) The blended polymer solutions were drop casted to prepare a free-standing membrane with thickness varying from 36 to 48 μm. The membrane was then immersed in 1 M pyridine (reagent alcohol solvent) to convert the chloromethyl groups to quaternary benzyl pyridinium chloride groups. The final step imbibed H_3PO_4 into the polymer matrix by soaking in 85 wt% $H_3PO_{4(aq)}$ at 120 °C for 6 hours. In our previous work (Venugopalan, Chang et al. 2019) varying blends of H_3PO_4-QPPSf-PBI were prepared, and the 50:50 blend yielded the highest conductivity and best

mechanical and thermal stability. Hence, the 50:50 H_3PO_4-QPPSf-PBI blend was evaluated as a SSEM for supercapacitor device studies.

3.3.1. Materials Characterization of the Membrane and the Electrodes

Prior to device studies, Raman spectroscopy (Figure 3.3a) and ATR-FTIR (Figure 3.3b) identified the different chemical moieties in the H_3PO_4-QPPSf-PBI membrane and the non-acid doped QPPSf-PBI membrane.

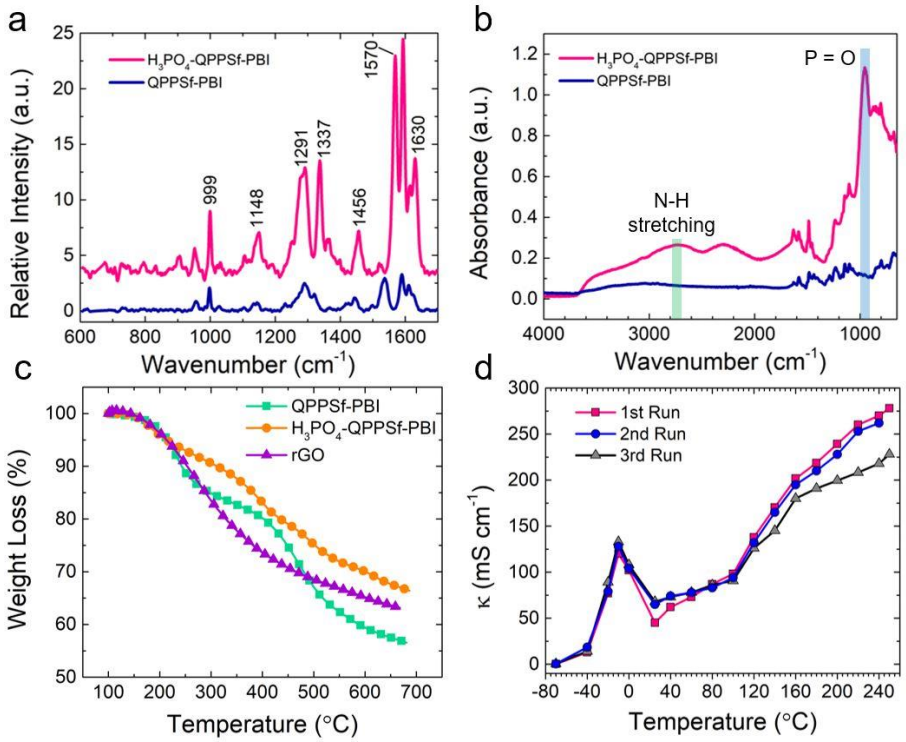

Figure 3.3. (a) Raman spectra of QPPSf-PBI with and without H_3PO_4. (b) ATR-FTIR spectra of QPPSf-PBI with and without H_3PO_4. Both Raman and FTIR spectra show the charged ionic moieties (e.g., pyridinium, imidazolium, and H_3PO_4) in the SSEM. (c) TGA curves for the pristine and H_3PO_4 imbibed QPPSf-PBI membranes and rGO electrode material. Each of these materials are thermally stable up to 220 °C. (d) In-plane proton conductivity of the H_3PO_4 imbibed QPPSf-PBI membrane in the temperature range of -70 to 220 °C.

The peak at 1539 cm^{-1} in the Raman spectra in the non-acid doped SSEM was ascribed to the imidazole group present in PBI, while the peak at 1610 cm^{-1} corresponded to the C-N^+ stretching in the pyridinium moiety. The FTIR peak at 2924 cm^{-1} was attributed to the methylene group that tethered the cation to the poly (arylene ether sulfone) backbone and the methyl groups

in the iso-propyl moiety in the poly (arylene ether sulfone) backbone. The FTIR peak at 1487 cm^{-1} came from the C-H stretching the arylene rings and the pyridinium cation.(Deimede, Voyiatzis et al. 2000, Zeis 2015) After immersing the membrane in H_3PO_4, the peak at 1539 cm^{-1} in the Raman spectra shifted to 1570 cm^{-1} because the H_3PO_4 protonated the imidazole in PBI to yield imidazolium.(Deimede, Voyiatzis et al. 2000, Zeis 2015) A broad FTIR peak in the range 2400-3000 cm^{-1} for the acid-doped in the SSEM was ascribed to the N-H stretching in the protonated PBI. Furthermore, a significant vibration at 956 cm^{-1} in the FTIR was observed and was attributed to the P=O in H_3PO_4.(Deimede, Voyiatzis et al. 2000, Zeis 2015)

Table 3.1 reports the properties of the H_3PO_4-QPPSf-PBI SSEM.(Venugopalan, Chang et al. 2019) The acid uptake of membrane was 220% and the ion-exchange capacity (IEC) of the non-acid doped SSEM (on a base group basis) was 4.1 mequiv g^{-1}. Normalizing the acid uptake to the IEC resulted in a H_3PO_4 level per base moiety (nH_3PO_4 B^{-1}) of 7.9. The H_3PO_4-QPPSf-PBI SSEM gave an ultimate tensile strength of 11.9 MPa at 25% elongation at break. The excellent toughness of the membrane, and its ability to be moderately stretched, made it a good candidate for electrochemical devices that need some degree of flexibility like wearable electronics.

Table 3.1. Different properties of phosphoric acid doped QPPSf-PBI.

Sample	H_3PO_4 uptake (%)	IEC_{H3PO4} (mequiv g^{-1})	nH_3PO_4 B^{-1}	Ultimate tensile strength (MPa)[a]	Elongation at break (%) [a]
QPPSf-PBI	220	2.2	7.9	11.9	25

[a] Measurements conducted at ambient conditions: 25 °C and ~50% relative humidity

The thermal stability of the acid-doped and undoped SSEM was assessed with thermogravimetric analysis (TGA). The TGA curves are presented in Figure 3.3c. The undoped membrane exhibited two stages of weight loss. The first region between 220-275 °C was due to the degradation of the pyridinium group and the second weight loss region between 450-700 °C derived from degradation of the polymer backbone. The H_3PO_4 doped membranes displayed an

initial weight loss in the temperature range of 100-160 °C and this was attributed to residual water evaporation. The second weight loss in the temperature range of 160-250 °C was due to minor evaporation of H_3PO_4 and condensation of H_3PO_4 to triphosphoric acid, pyrophosphoric acid, or polyphosphoric acid and some quaternary benzyl pyridinium degradation.(Samms, Wasmus et al. 1996, Venugopalan, Chang et al. 2019) The other weight loss regions observed from 300-700 °C were ascribed to polymer backbone degradation. The interaction of phosphate anions with the pyridinium cations prevents the bulk of H_3PO_4 from evaporating between 160-250 °C from the QPPSf-PBI polymer host.(Venugopalan, Chang et al. 2019) With respect to stability, the H_3PO_4-QPPSf-PBI SSEM retained 85% of its in-plane proton conductivity at 220 °C for 96 hours. This stability test showed the initial proton conductivity drop within 24 hours was due to excess acid evaporation followed by no changes in proton conductivity over the next 72 hours. The thermally stability data provided confidence that the H_3PO_4-QPPSf-PBI SSEM would be an effective electrolyte candidate for supercapacitor devices in the temperature range of 25-220 °C.

An important PEM property is its ability to foster adequate proton conductivity across a wide-temperature range. Figure 3.3d presents the proton conductivity of the H_3PO_4-QPPSf-PBI SSEM from -70 to 220 °C. For the temperature range between 25 to 220 °C, the proton conductivity increase was commensurate with rising temperature values. As the temperature increases, the structural diffusion of protons in the hydrogen bonded network becomes greater. Surprisingly, the H_3PO_4-QPPSf-PBI SSEM displayed higher conductivity at -20 °C versus 25 °C.(Venugopalan, Chang et al. 2019) The ionic conductivity measurements were performed under ambient laboratory settings and it is known that residual water in H_3PO_4 disrupts the hydrogen bonded network hindering facile ionic conductivity.(Schechter, Savinell et al. 2009, Venugopalan, Chang et al. 2019) Therefore, cooling the environment down to -20 °C reduced/eliminated the

partial pressure of water in the environment and this resulted in an increase in the SSEM's proton conductivity when compared to the value at 25 °C. It is worth noting that pure H_3PO_4 is a solid at room temperature, but this acid imbibed into the polycation-PBI host depresses its freezing point enabling proton conductivity as high as 50 mS cm^{-1} at -20 °C. Reducing the temperature from -20 to -70 °C severely compromises proton conductivity. The reduction in proton conductivity below -20 °C could be realized from the differential scanning calorimetry (DSC) for H_3PO_4 doped QPPSf-PBI (Figure 3.4). Figure 3.4 shows two peaks, one at 0 °C and other at -15 °C.

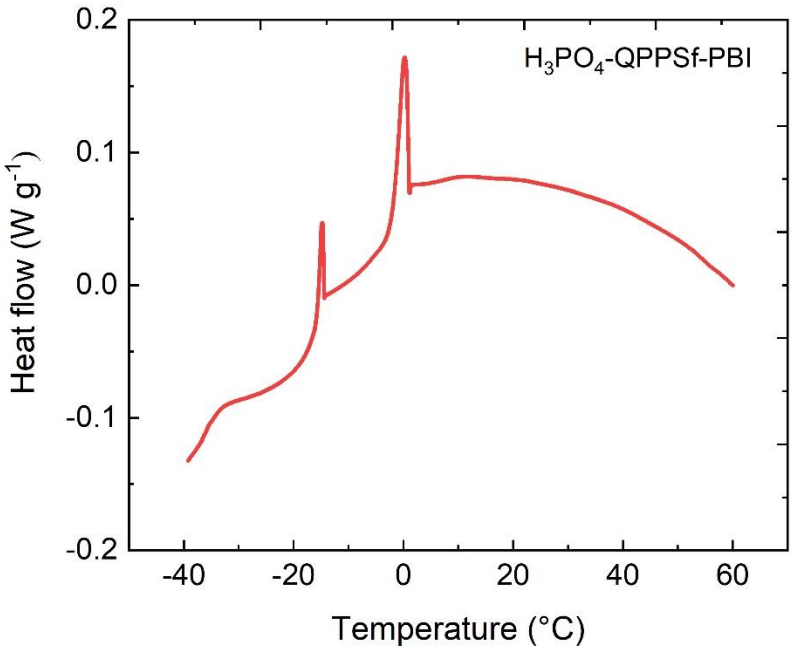

Figure 3.4. DSC of H_3PO_4-QPPSf-PBI. Two peaks were observed at 0 °C and -15 °C. The peak at 0 °C was due to residual water freezing within the sample. The other peak was due the freezing of H_3PO_4 in the sample.

The former peak could be corroborated to the reduction in partial pressure of water in the environment, whereas the latter peak was observed due to complete immobilization of phosphate anion due to crystallization.

The proton conductivity at -70 °C is 0.01 mS cm^{-1}. Although this value is at least a 4-order magnitude reduction of the maximum proton conductivity observed, the value of 0.01 mS cm^{-1}

for conductivity still rivals some lithium salt containing polymer electrolytes for lithium ion batteries.(Teran, Tang et al. 2011) It will be shown later on that the supercapacitor device can still operate at the extreme low temperature of -70 °C with the H_3PO_4-QPPSf-PBI SSEM despite the high ohmic penalty. Finally, it is important to note that this proton exchange membrane displayed repeatable conductivity values (n=3 repeat traces plotted in Figure 3.3d) when evaluating the temperature across the range of -70 to 220 °C. During each cycle, the temperature was ramped up from room temperature to 220 °C and cooled to -70 °C and ramped up to 220 °C. EIS measurements were performed at different temperature points. In-plane proton conductivity loss and stability of the membranes in the temperature range was assessed by performing cycling tests.

The data presented in Figure 3.3d and Table 3.1 signify that the H_3PO_4-QPPSf-PBI SSEM offers excellent proton conductivity over a wide-temperature range (over 50 mS cm^{-1} from -25 to 220 °C), while being thermally stable at the elevated temperature of 220 °C and mechanically robust. The molecular origins behind the exceptional conductivity of the H_3PO_4 doped polycation-PBI membrane was assigned to: i.) the cationic groups on the polycation promote greater hydrogen bonding frustration as they do not accept a proton like PBI and ii.) the presence of PBI in the blend allows for greater H_3PO_4 uptakes – which is not the case for most polycation membranes that are typically used in AEMs. Furthermore, the cations in the polycation create electrostatic interactions that are an order magnitude stronger with phosphate type anions over the acid-base interactions in H_3PO_4-PBI.(Lee, Spendelow et al. 2016) Thus, the stronger electrostatic interactions can extend the upper temperature range of the membrane without concern of H_3PO_4 evaporation. Now that the proton exchange membrane can withstand temperatures greater than 180 °C (and up to 220 °C) by mitigating H_3PO_4 evaporation, the increased temperature value to 220 °C promotes structure proton diffusion and higher ionic conductivity. With regard to the below room temperature proton

conductivity, there is no literature available on H_3PO_4 doped polycations and sparse reports on H_3PO_4-PBI. As previously stated, pure H_3PO_4 is a solid at room temperature. Mixing this acid with the polycation-PBI polymer host disrupts the hydrogen bonded network in H_3PO_4 preventing it from becoming a solid at low temperatures. With this effect, it is possible to maintain structure proton diffusion within the SSEM and proton conductivity at depressed temperatures.

With the properties H_3PO_4-QPPSf-PBI SSEM established, it is important to focus on the electrode properties used in the supercapacitor demonstrations across the wide-temperature range. Figure 3.5a provides a cross-sectional SEM image of flash reduced rGO. As showed in our previous work,(Chaichi, Prasad et al. 2018) graphene sheets are delaminated due to the camera flash reduction process.

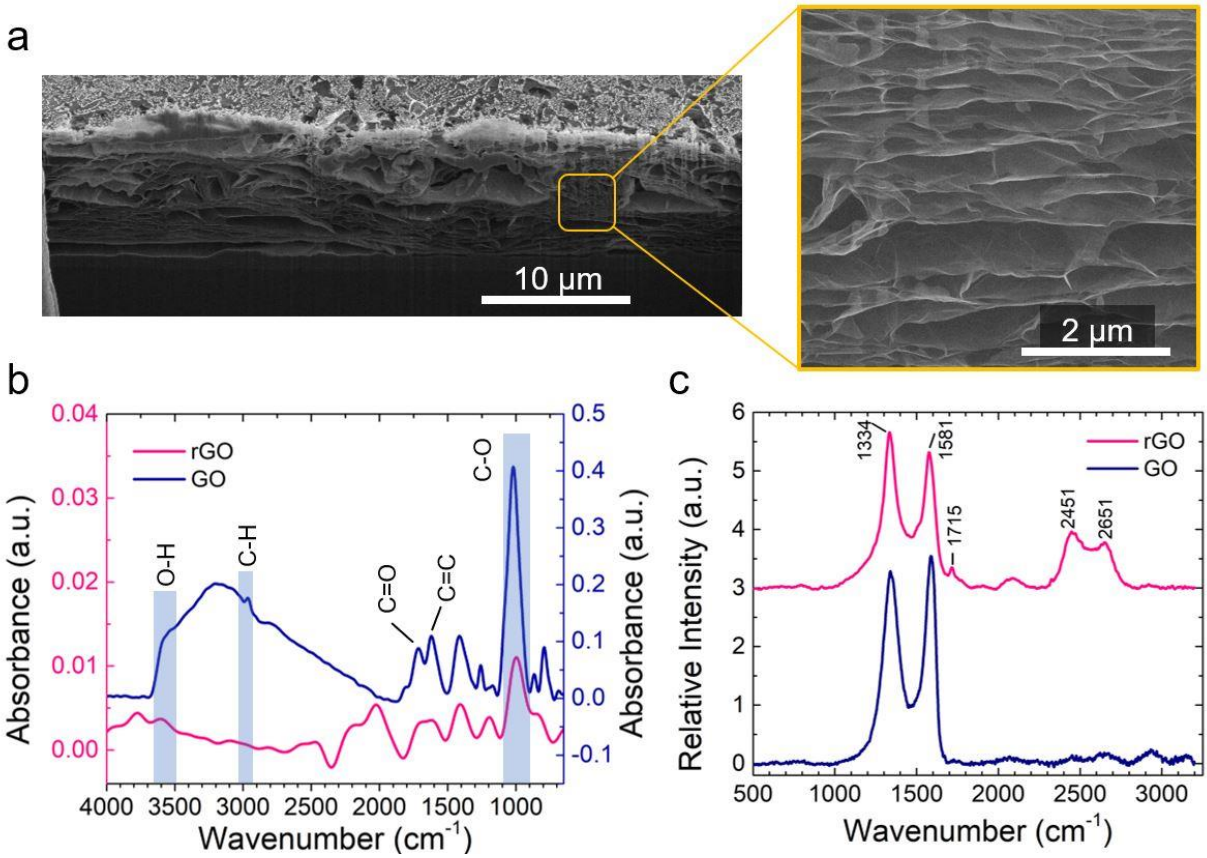

Figure 3.5. (a) Cross-sectional SEM image of rGO electrodes. (b) ATR-FTIR results (c) Raman spectra of GO and rGO and this spectroscopic technique also substantiated multilayered graphene as evident by the 2D peak at 2651 cm^{-1}.

The color of the surface changed from brown to black indicating production of rGO from GO (Figure 3.2). By flashing the GO, oxygen atoms escape the layered structure of graphene oxide accompanied by producing a small explosion sound. This micro-explosion increases the inter-layer distance between the produced multilayered graphene structures.(Chaichi, Prasad et al. 2018) As a result, the high surface area of rGO is activated and this is an important property for electrochemical charge storage. More details about reduction of graphene oxide via flash reduction method is explained elsewhere.(Chaichi, Prasad et al. 2018) Figure 3.5b shows the ATR-FTIR spectrum obtained from GO and rGO. A strong hydroxyl group stretching peak is observed at 3412 cm^{-1} for GO, but this signal is almost eliminated after flash reduction.(Sharma, Sharma et al. 2017) At 1713 cm^{-1}, C=O carbonyl stretching peak has a much higher intensity in GO compared to rGO.(Ossonon and Bélanger 2017) The peak at 1020 cm^{-1} shows the existence of oxygen in the multilayered graphene structure.(Sharma, Sharma et al. 2017) As can be seen, the intensity of this peak decreases by ~ 40X after the flash reduction of GO and thus provides further evidence for the successful conversion of GO to rGO via flash reduction method.

Raman spectra (Figure 3.5c) provided additional evidence of GO conversion to rGO using the flash reduction process. The doublet peak located at 2651 cm^{-1} corresponded to the existence of multilayered graphene and supported the reduction of GO to rGO. The G band in Figure 3.5c shifted slightly from 1585 to 1581 cm^{-1} after the flash reduction and this shift derives from the formation of a 3D structure by delamination of graphene layers and topological disordering.(Krishnamoorthy, Veerapandian et al. 2012) I_D/I_G ratio has also changed from ~0.93 in GO to ~1.16 in rGO sample demonstrating the removal of oxygen species in the reduced sample.(Krishnamoorthy, Veerapandian et al. 2012) Shifting of D^* band from 1563 cm^{-1} (for GO) to 1499 cm^{-1} (rGO) also showed a decrease in the amount of oxygen content after the flash

reduction. The spectra in Figures 3.5b and 3.5c unequivocally demonstrate the production of rGO electrodes from GO using the flash reduction method and the electron micrograph in Figure 3.5a demonstrates that the reduction process results in porous, layered electrodes.

3.3.2. Room-Temperature Electrochemical Tests

Figure 3.6a is a picture of an assembled all-solid-state and flexible supercapacitor with rGO as working electrodes and H_3PO_4-QPPSf-PBI SSEM. The measured current and capacitance values from all device electrochemical experiments were normalized to the geometric area of the device. Figure 3.6b shows the CV curve of rGO-50:50 H_3PO_4-QPPSf-PBI SSEM at 10, 50, 100 and 1000 mV s^{-1} scan rates at room temperature (20 to 22 °C).

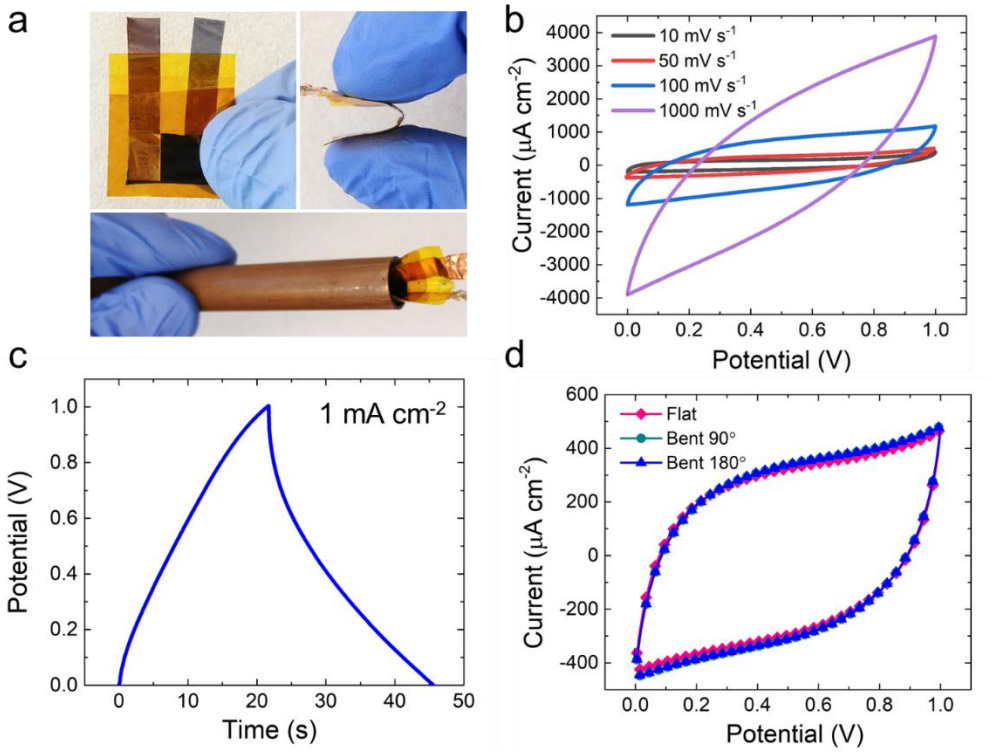

Figure 3.6. (a) Optical image showing the solid-state and flexible supercapacitor device made of rGO electrodes and H_3PO_4-QPPSf-PBI SSEM. (b) CV curve of the device obtained at 25 °C and at scan rates of 10, 50, 100 and 1000 mV s^{-1}. (c) Galvanostatic charge-discharge (GCD) plot at current density of 1 mA cm^{-2}. (d) Flexibility test of the supercapacitor devices (assessed by CV) performed at bending angles of 0° (flat), 90°, and 180°.

Inspection of the CV curves reveals the formation of a double-layer capacitance because the traces are symmetric in shape and are largely rectangular across the potential range.We assert that excess H_3PO_4 in the polymer host is responsible for ions that can be stored in the electrochemical double layer (EDL) of rGO electrodes. There was no imbibing of acid into the electrodes during fabrication of the capacitor device. Hence, the only source of ions that could be adsorbed in the EDL hailed from the SSE membrane. Our previous research(Venugopalan, Chang et al. 2019) has showed that not all of the imbibed acid in the polymer blend membrane is anchored through electrostatic interactions and some of the excess acid can leach out of the membrane. As observed with most electrochemical capacitors featuring carbon electrodes, increasing the scan rate results in larger current response and a bigger rectangular area. For example, 400 μA cm^{-2} was produced at a scan rate of 10 mV s^{-1} and 3900 μA cm^{-2} was generated at a scan rate 1000 mV s^{-1}. The value of areal capacitance was determined at a current density of 1 mA cm^{-2} from the galvanostatic charge-discharge (GCD) plot (Figure 3.6c) and found to be 3 mF cm^{-2} at room temperature. The symmetric and linear shape of GCD curve also shows the double layer capacitance nature of the device. The slight deviations from the perfect double layer capacitance shape in CV and GCD curves may originate from inevitable impurities of the system (residual oxygen) and surface reactions (redox reactions due to residual oxygen). The energy density and power density values of the supercapacitor at room temperature ranged from 0.83-2.79 mW h cm^{-2} and 90-125 mW cm^{-2}, respectively. Because a mechanically robust SSEM was adopted, the supercapacitor device could be bent up to 180° while retaining its original CV shape (Figure 3.6d). These results confirm the outstanding electrochemical properties of this all-solid-state device which is also fully flexible.

3.3.3. Extreme-Temperature Electrochemical Tests

After analyzing the general electrochemical properties of the supercapacitor at ambient conditions, electrochemical properties of supercapacitor were measured across a wide temperature range. Figure 3.7a shows the CV plot of supercapacitor at scan rate of 50 mV s^{-1} in the temperature range of -70 °C to 25 °C. The inset for Figure 3.7a highlights that the device still operated at -70 °C. The current density attained by the device continued to drop when cooling the capacitor from 25 °C to -70 °C. Figure 3.7b presents the CV curves of the supercapacitor device in the elevated temperature range of 25 to 220 °C. The CV traces in both Figures 3.7a and 7b were fairly symmetrical when operated across the voltage range of 0 to 1 V.

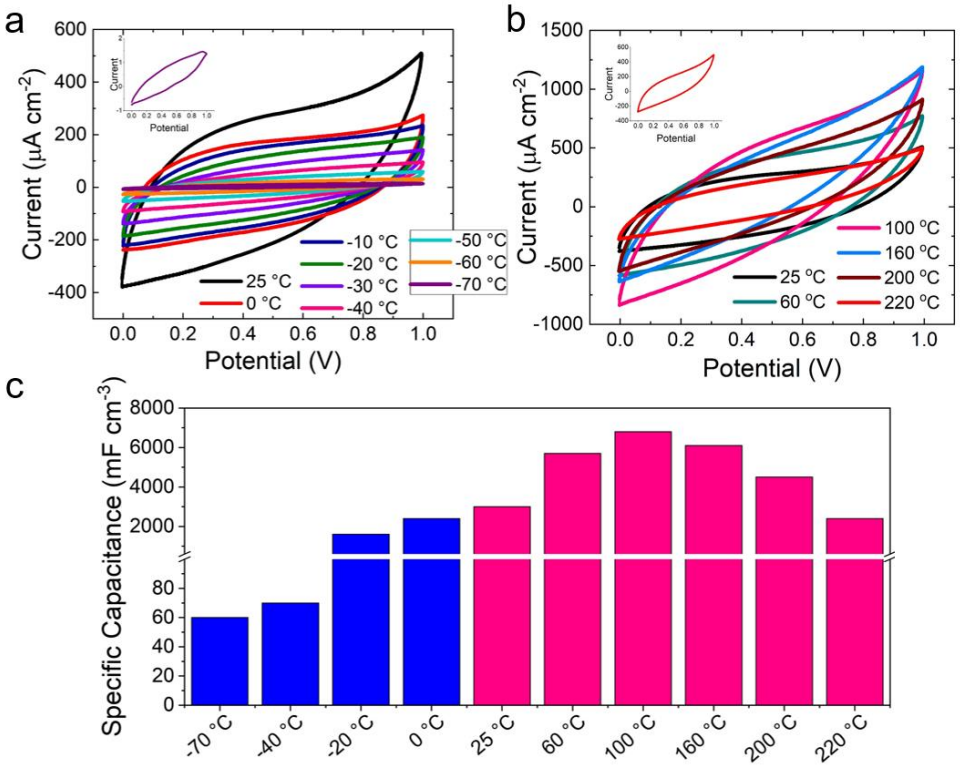

Figure 3.7. Electrochemical properties of the solid-state supercapacitor at different temperature values. (a) CV of supercapacitor at scan rate of 50 mV s^{-1} in the temperature range of -70 to 25 °C. (b) CV of supercapacitor in the range 25 to 220 °C. (c) The calculated values of specific capacitance determined from the CV plots at a scan rate of 50 mV s^{-1}. The maximum capacitance of the device was measured to be 6800 mF cm^{-3} and it was obtained at 100 °C.

The current response of the supercapacitor with the SSEM continued to increase when ramping the temperature from 25 °C to 160 °C. The CV curve at 100 °C and 160 °C were almost similar. Increasing the temperature beyond 160 °C resulted in smaller current responses at 200 °C and 220 °C. The resultant device capacitance values from the CV curves in Figures 3.7a and 3.7b were plotted as a function of temperature in Figure 3.7c. There are two key takeaways from Figure 3.7c: i.) the maximum capacitance was observed at 100 °C and the value at 160 °C was pretty close to the value at 100 °C and ii.) the supercapacitor's capacitance value was on the same order of magnitude in the temperature range of -20 °C to 220 °C. Cooling the capacitor below -20 °C still resulted in a device that still operated but with a capacitance value that was about two orders in magnitude smaller. Despite the reduction of capacitance value below -20 °C, it is still higher than the recently published works for solid-state supercapacitors at low temperatures.(Zhao, Liu et al. 2017, Newell, Faure-Vincent et al. 2018)

To better understand why the supercapacitor displayed the highest capacitance at 100 °C and 160 °C and a dramatic reduction in capacitance at temperatures below -20 °C, electrochemical impedance spectroscopy (EIS) was performed to delineate the ohmic and diffusion resistance of ions in the electrodes as function of temperature. Figure 3.8a-c show the EIS of the supercapacitor with a SSEM at different temperatures.

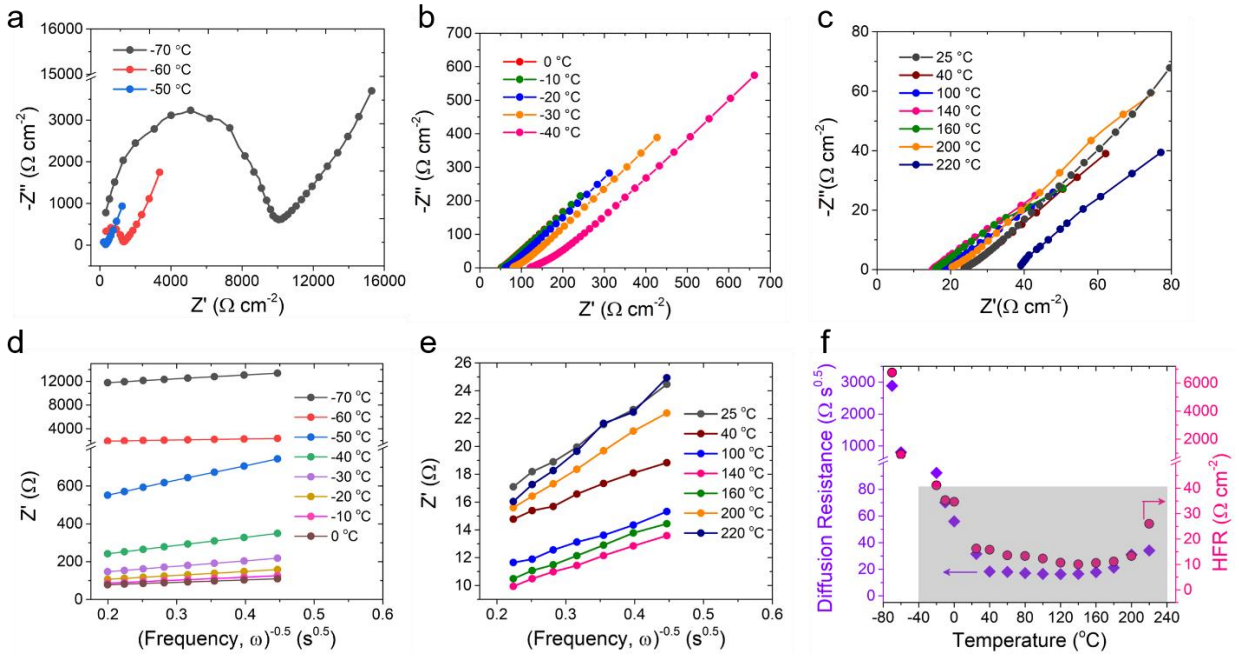

Figure 3.8. Nyquist plots from EIS experiment at (a, b) low to room temperature range (-70 °C to 25 °C), (c) high temperature range (40 °C to 220 °C). Z' vs. inverse square root of frequency from the EIS experiments to calculate the diffusion resistance is plotted at (d) low temperatures, and (e) high temperature ranges; (f) Diffusion resistance and high frequency resistance (HFR) values vs. temperature. The supercapacitor showed low to intermediate diffusion resistance from -40 °C to 220 °C (shaded region). The plots also display a diffusion-controlled charge-storage mechanism in the electrodes. The formation of the semi-circles observed in (a) signifies that a charge-transfer resistance may be present when decreasing the temperature at or below -50 °C.

The Nyquist plots exhibited linear tails starting over the entire frequency range illustrating a diffusion-controlled mechanism for charge storage in the temperature range of -40 to 220 °C. The high frequency resistance (HFR) and the diffusion resistance were extracted from the Nyquist plots by fitting an electric circuit equivalent model to the data. The HFR occurred at where the Nyquist trace cross the x-axis. The diffusion resistance was determined from the slope of the real resistance (Z') versus reciprocal of the square root of frequency ($\omega^{-0.5}$) in the linear regime of the Nyquist plot (Figure 3.8d, e). Figure 3.8f plots the HFR and diffusion resistances as a function of temperature. The higher capacitance values that were commensurate with increasing temperature from 25 °C to 100 °C originated from improved structural proton diffusion in the SSEM that ultimately enhanced the conductivity of the SSEM leading to a lower HFR value. Plus, the

improved conductivity also reduced the diffusion resistance of H_3PO_4 in the rGO electrodes. Between the temperature ranges of 100 °C to 160 °C, the diffusion resistance started to increase in Figure 3.8f. At 180 °C, the HFR also started to increase when increasing the temperature to 220 °C. The larger individual resistance values accounted for the decrease in capacitance observed above temperatures of 160 °C. At elevated temperatures, the migrated excess H_3PO_4 to the rGO electrodes may start to evaporate as there are no cationic groups to anchor them to the electrode – unlike the SSEM.(Lee, Spendelow et al. 2016, Venugopalan, Chang et al. 2019) Furthermore, a fraction of the phosphoric acid undergoes dehydration at temperatures above 160 °C forming triphosphoric, pyrophosphoric, or polyphosphoric acid. These bigger acids may cause a small drop in SSEM ionic conductivity and as a result a higher HFR value. Plus, these bigger acids cannot migrate as easy from the SSEM host into the rGO electrodes resulting in a larger diffusion resistance.

At temperatures below -40 °C, a drastic increase in the HFR and diffusion resistance is observed (Figure 3.8). Since the proton conductivity is inversely proportional to the HFR, we will expect less available ions for the double layer formation. Therefore, the increase in resistances at low temperature conditions are leading to much lower capacitance values (i.e., below 1 mF cm^{-2}) compared to higher temperatures. Another reason for the rapid rise of diffusion resistance is attributed to the freezing of the H_3PO_4 in the polymer host restricting structural H_3PO_4 diffusion. Interestingly, semi-circles appeared in the Nyquist plot at -50 °C, -60 °C and -70 °C. These semi-circles indicated that a charge-transfer resistance may be occurring at these low temperatures. The origin of the apparent charge-transfer elements, which can be represented by a capacitor and a constant phase element in parallel, is currently unknown and will be the focus of future investigations. If the semi-circles are related to an electron-charge transfer process, such as

corrosion of the electrodes or oxidation/reduction of oxygen, electrolyte, or water, it is unclear at the moment why this process would occur at -50 to -70 °C and not at greater temperatures. One possibility to explain the observation beyond a formal charge-transfer process may be related to the freezing of the electrolyte causing a poor interface between the electrode-electrolyte. This poor interface may be abrupt and could potentially be explained by a resistor and constant phase element in parallel. The molecular behavior of supercapacitors as such low temperatures is relatively un-explored and will be investigated in greater detail in the future.

Figure 3.9a presents the cycling stability of the device at 220 °C, 25 °C, and -70 °C. The supercapacitor device retains 92% of its initial capacitance at room temperature after 5000 cycles. Inspection of reports in the peer-reviewed literature revealed that most high and low temperature supercapacitor studies do not perform cycling assessments at extreme temperatures.

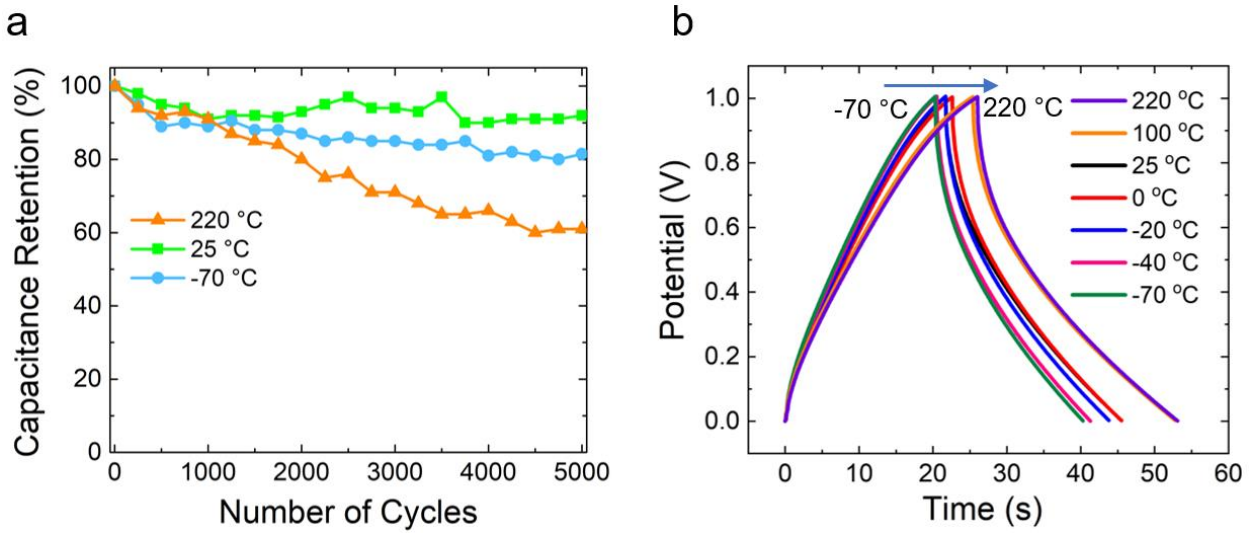

Figure 3.9. (a) Cycling stability of the device at -70 °C, 25 °C, and 220 °C after 5000 cycles. (b) Galvanostatic charge-discharge (GCD) curves at a current density of 1 mA cm^{-2} and at temperature ranges of -70 to 220 °C. The device was held for 1 hour at individual temperatures in the temperature range of -70 to 220 °C and the GCD was measured after the 1-hour exposure, at room temperature. The symmetrical shape of GCD plot is maintained even after exposing the device to extremely low (-70 °C) and high temperatures (220 °C).

Surprisingly, the supercapacitor device maintained 81.5% of its capacitance at -70 °C after 5000 cycles. The device also retained more than 91% of its capacitance after 1000 cycles at 220

°C. However, capacitance retention reduced to 61% after 5000 cycles at the same temperature. The conversion of H_3PO_4 to polyphosphoric acids at 220 °C may be responsible for the capacity of the fading over time. Overall, the SSEM capacitance device with rGO electrodes displayed better than expected cycling stability and future efforts are underway to improve device performance and cycling retention.

In another stability assessment (Figure 3.9b), the supercapacitor device was held for 1 hour at individual temperatures in the temperature range of -70 to 220 °C and the GCD was measured after the 1-hour exposure, at room temperature. The curves in Figure 3.9b convey symmetrical shapes of the GCD curves after the temperature hold confirming device stability for at least 1 hour at the various temperatures. Comparison of the GCD diagrams at the different temperatures showed better stability of the supercapacitor devices at low temperatures (≤ 0 °C) than higher ones (≥ 100 °C). These results complement the cycling stability data generated in Figure 3.9a. It is noteworthy to mention that the specific capacitance of the device obtained by GCD curves after holding the device at different temperatures showed almost the same values (~3 mF cm^{-2}).

Figure 3.10a reports capacitance retention of the device as a function of discharge current density in the range of 1 to 100 mA cm^{-2}. Charge storage in supercapacitors occurs by the formation of double layer capacitance at the interface of electrode and electrolyte.

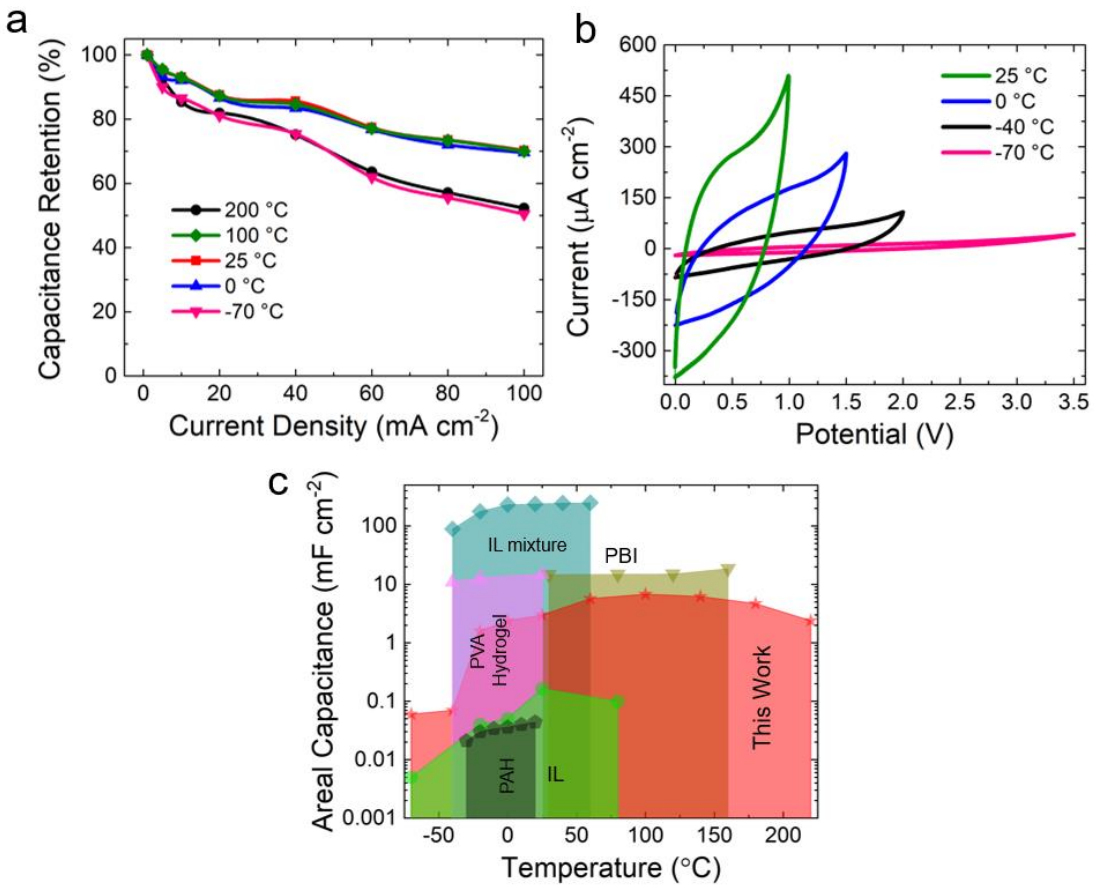

Figure 3.10. (a) Capacitance retention of the device as a function of different current densities at different temperatures. (b) CV curves show an increase in working potential window of the device from 1 to 3.5 V by decreasing the temperature from 25 to -70 °C. (c) Comparison of areal capacitance vs. operating temperature range for this work with the literature data. The present work showed that the supercapacitor is working under a wide operating temperature ranges.

The electrochemical double layer is formed by diffusion of ions from electrolyte to the interface of electrode/electrolyte. It is crucial to examine the charge storage properties of the device at different temperatures. To this end, capacitance retention of the device at different temperatures was obtained by applying current densities in the range of 1 to 100 mA cm^{-2} (Figure 3.10a). By deviating from room temperature and increasing the applied current density, specific capacitance of the device decreases. This difference is negligible at lower current densities. However, it becomes more evident at higher current densities due to ohmic losses. Accordingly, diffusion of the ions from electrolyte to electrode/electrolyte interface is limited at very high or low

temperatures because at high temperatures polyphosphoric acids do not migrate well and at low temperatures the acid electrolyte is mostly a solid. Figure 3.10b shows the increase in working potential window of the device from 1 to 3.5 V by decreasing the temperature from 25 to -70 C. This can be explained by suppressing the occurrence of possible Faradaic reactions at high potentials by lowering the temperature. Faradaic reactions are restricted both thermodynamically and kinetically at extremely low temperatures. The occurrence of these Faradaic reactions mainly originates from redox reactions occurring due to the residual oxygen in the system. In our previous work,(Chaichi, Prasad et al. 2018) we have shown the existence of residual oxygen in rGO electrodes which is mainly responsible for undesirable redox reactions.

Overall, the supercapacitor device developed herein with H_3PO_4-QPPSf-PBI SEM and rGO electrodes displayed energy storage capability across a large temperature range (-70 °C to 220 °C). In fact, to the best of our knowledge, this is widest temperature range a supercapacitor device. Figure 3.10c compares the areal capacitance vs. operating temperature range of our device and other similar recently published works. Accordingly, the supercapacitor with the SSEM in this work shows competitive areal capacitance and the largest temperature operation range compared to ionic liquid (IL) electrolytes and polyampholyte hydrogels,(Zhao, Liu et al. 2017, Newell, Faure-Vincent et al. 2018) Although the areal capacitance for polyvinyl alcohol (PVA) gel based electrolytes (Nègre, Daffos et al. 2016, Rong, Lei et al. 2018) is higher than what is reported in this work, the operating temperature of a supercapacitor with a polyvinyl alcohol (PVA) gel based electrolytes is limited to the temperature range of -40 to 60 °C. Additionally, H_3PO_4 doped PBI electrolyte only operates from room temperature to 160 °C.(Kim, Kim et al. 2015) The wide operating temperature range of our device makes it possible to tolerate harsh environmental conditions in the range of -70 to 220 °C. Furthermore, a radar plot (Figure 3.11) summarizes all

the different electrochemical properties of this device at a glance. The ability of the device to operate over a wide-temperature range is necessary for numerous applications that vary from wearable electronics to transportation and aerospace.

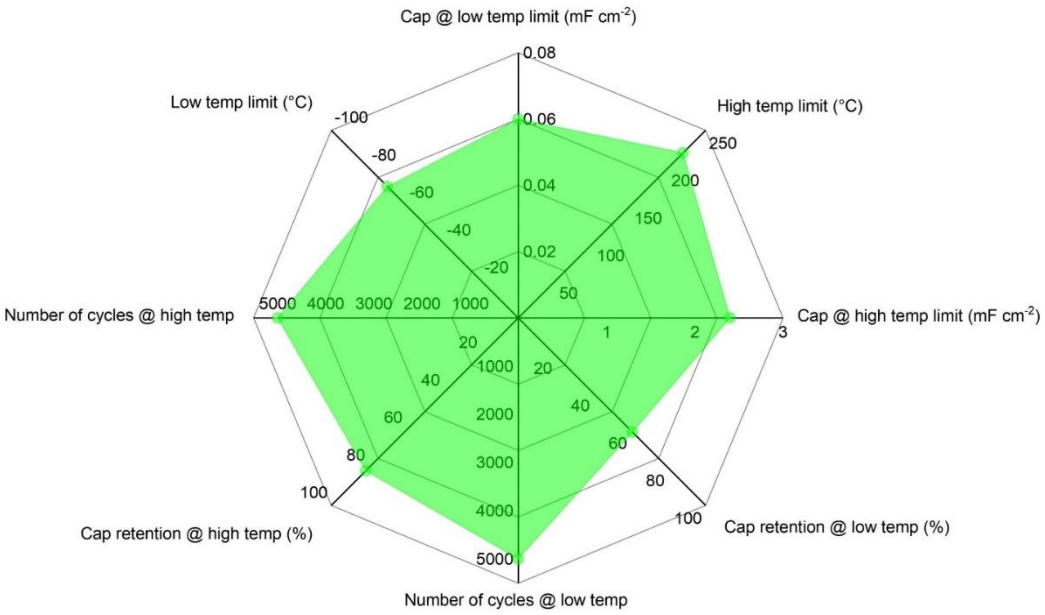

Figure 3.11. Radar plot that shows different electrochemical properties of the supercapacitor device discussed in this report. This device operates over a wide temperature range of -70 to 220 °C. The combination of these features is required in several energy sectors.

3.4. Conclusions

In this work, a solid-state and flexible supercapacitor was realized for extreme temperature applications by means of a novel polymer blend membrane and flash reduced graphene oxide electrodes. Raman and FTIR studies confirmed the formation of rGO from GO and revealed the various chemical species of the membrane. H_3PO_4 imbibed QPPSf-PBI blended membranes showed impressively high conductivity of 278 mS cm^{-1} at 220 °C. Outstanding performance and thermal resistance of the device was confirmed by several electrochemical tests over a wide temperature range of -70 to 220 °C. Our device showed maximum capacitance of 6800 mF cm^{-3} at 100 °C. Energy density and power density were measured to be in the range of 0.83 to 2.79 mW h cm^{-2} and 90 to 125 mW cm^{-2}, respectively. Formation of double layer capacitance was observed

at both extremely low (-70 °C) and high (220 °C) temperatures. Working potential window of the device increased from 1 to 3.5 V by decreasing the temperature from 25 to -70 °C. This device maintained 92% of its initial capacitance at room temperature after 5000 cycles. Furthermore, 81.5% of initial capacitance was preserved at -70 °C after 5000 cycles as well as 91% of its capacitance after 1000 cycles at 220 °C. Additionally, our supercapacitor demonstrated excellent flexibility by retaining its original CV curve shape after being bent up to 180°. As a result, the fully solid-state and flexible supercapacitor successfully operates in the temperature range of -70 to 220 °C as well as outperforming most of the current state of art solid-state supercapacitors at room temperature. Merging the aforementioned properties reveals new horizons for extreme temperature supercapacitors for challenging energy storage applications such as in aerospace, transportation and micro-electronics.

Chapter 4
Interface Engineering of Prosthetic Biomaterials

4.1. Introduction

Joint and disc replacement via knee and hip, are growing considerably due to the increasingly aging population as well as the higher demand for an active lifestyle in the elderly population.(Carr and Goswami 2009, Clary and Maletsky 2017, Kunčická, Kocich et al. 2017) However, the longevity of implants is significantly limited by wear performance, corrosion, biocompatibility and post-surgery infection.(Sharkey, Hozack et al. 2002, McEwen, Barnett et al. 2005, LaCour, Komistek et al. 2016) These factors are correlated to each other and effectively addressing any of them can dramatically improve the quality of prosthetic performance and lifespan. To this end, presurgical measures should be taken to maximize the performance of joint and disc implants.(Raphel, Holodniy et al. 2016) Thermal stabilization, electron beam and gamma irradiation are the most conventional approaches employed for enhancement and engineering of biomaterials.(Kulkarni, Mazare et al. 2014, John, Jaganathan et al. 2016) However, these methods are accompanied with drawbacks such as degradation of bulk properties (toughness, fatigue and tensile strength) but do improve the surface features and characteristics.(Wu, Li et al. 2015) This degradation in bulk properties could cause catastrophic failure in some implants under high cyclical loads or extreme loading conditions, such as knee prosthesis.(Clary and Maletsky 2017) Additionally, more recent techniques like Ar plasma modification require thermal stabilization that tends to negatively affect bulk properties.(Kostov, Nishime et al. 2014) Furthermore, the

---

This chapter was previously published as Ardalan Chaichi, Alisha Prasad, Lijesh Kootta Parambil, Shahensha Shaik, Ali Hemmasian Ettefagh, Vinod Dasa, Shengmin Guo, Michelle Osborn, Ram Devireddy, Michael M. Khonsari and Manas R. Gartia. "Improvement of Tribological and Biocompatibility Properties of Orthopedic Materials Using Piezoelectric Direct Discharge Plasma Surface Modification." *ACS Biomaterials Science & Engineering* 5.5 (2019): 2147-2159. Reprinted by permission of American Chemical Society.

conventional plasma coating methods are not cost efficient and require extremely large machinery, rendering them inappropriate for clinical applications. During the last decade, nonthermal plasma has been widely investigated mostly because of the associated antimicrobial effects and surface sterilization capabilities.(Guo, Huang et al. 2015, Lunov, Zablotskii et al. 2016) However, most studies on this subject have been performed on polymeric materials while the tribological behavior of nonthermal plasma treated surfaces has remained uninvestigated. Piezoelectric direct discharge (PDD) plasma is categorized as a novel nonthermal plasma generating method in which the cold plasma is produced due to a direct discharge in a piezoelectric transformer.(REGULA, IHDE et al. 2017) In this method, a compact hand-held device can be used to produce cold plasma (< 50 ºC) without the requirement of external gas cylinders. Similar devices are suitable for healthcare and clinical applications due to the safety and ease of operation. Yet there are still no published studies that thoroughly examine the potential surface enhancements of PDD for prosthetic applications.

Ti6Al4V is an extensively employed material in highly corrosion resistant and biocompatible α-β titanium alloy with high strength-to-weight ratio.(Yadroitsev, Krakhmalev et al. 2014, Wang, He et al. 2017, Ataee, Li et al. 2018) However, poor wear properties of this alloy under cyclic loadings restrict its effectiveness as an implant in high-load bearing areas like in the knee and hip.(Chandramohan, Bhero et al. 2017, Ren, Liu et al. 2017, Wang, Xiong et al. 2017) As a result, researchers are working on a wide variety of surface enhancements and coatings to mitigate this issue. Gallardo-Moreno et al.(Gallardo-Moreno, Pacha-Olivenza et al. 2009) have shown that the formation of titanium oxide on the surface of Ti6Al4V improves the physico-chemical properties of this alloy for biomedical applications. Accordingly, creation of a thin oxide

layer on Ti6Al4V can significantly improve its biocompatibility as well as the wear resistance properties.

GUR1020, on the other hand, is an ultra-high molecular weight polyethylene (UHMWPE) in prosthetic applications due to its high biocompatibility, high toughness and ease of fabrication methods.(Sobieraj and Rimnac 2009, Enqvist, Ramanenka et al. 2016, Hunt and Joyce 2016) These properties degrade over cyclic loading conditions because of poor wear resistance.(Utzschneider, Harrasser et al. 2009, Mimaroglu and Unal 2015) Therefore, the lifespan of polyethylene implants is limited to less than ten years after surgery.(Musib 2011) Subsequently, the implant needs to be replaced with a new one to prevent infection and potential pain caused by the worn-out debris of the prosthesis. Hence, several coating methods (such as γ irradiation, ion irradiation and plasma surface modification) have been proposed to extend the longevity of polyethylene implants by improving the tribological properties.(Cho, Lee et al. 2005, Visco, Torrisi et al. 2010, Gilman, Piskarev et al. 2017) However, these methods are impractical at the clinical level due to the complexity and size of machinery, safety issues, and detrimental effects on bulk properties of the prosthesis.

In this study, we have investigated the potential surface modification of Ti6Al4V and polyethylene by means of a hand-held PDD plasma generator to scrutinize surface changes through the treatment process and their effect on tribological, corrosion and biological properties. This study explores new horizons for clinical applications of nonthermal plasma research and pioneers the introduction of a practical surface treatment method that can be utilized prior to prosthetic surgeries in a clinical setting.

4.2. Materials and Methods

4.2.1. Materials

High strength grade-5 Ti6Al4V (ASTM B348) rods (dia. 1.3 cm) were purchased from McMaster-Carr (1901 Riverside Pkwy). The rods were then machined into smaller pellets with a thickness of 3 mm for further characterization and biocompatibility experiments. Titanium pins were also machined from the same rod to be used in tribological tests. Medical grade polyethylene UHMWPE - Compression molded rods with diameter of 5 cm were purchased from Total Plastics Int'l Life Sciences (7508 Honeywell Fort Wayne). The chemical structure of polyethylene is shown in Figure 4.1. GUR1020 is a linear polyethylene with very good aberration and mechanical properties due to considerably higher density (937 kg/m^3) and molecular weight (3.5×10^6 g/mol) compared to standard polyethylene (due to longer polymer chain length). GUR1020 is produced from powder by means of compression molding and extrusion processing methods. GUR1020 is one of the very common materials in orthopedic implants mainly due to its special mechanical and biocompatibility properties. Pellets and discs were machined from the GUR1020 rod for further characterization, tribological and biological tests, as detailed below.

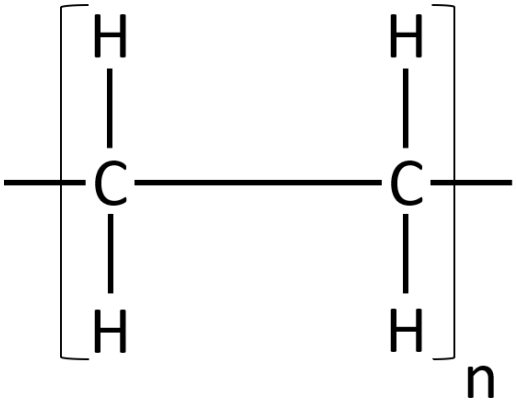

Figure 4.1. Chemical structure of polyethylene.

4.2.2. PDD Plasma Generator

Relyon Plasma Piezobrush PZ2 (12 V DC, 30 W) hand-held device was purchased from Relyon Plasma GmbH (Osterhofener Straße 693055 Regensburg, Germany) and used for surface plasma treatment of samples. Although the device is capable of using external gas cylinders (like Ar, He, O_2, etc.) (Table 4.1), we investigated the used of ambient air to facilitate the easy transition to a clinical setting. The ambient air was fed into the PDD device via a feeding fan on back of the device. The temperature of generated plasma was always less than 50 ºC and all the treatments were performed at room temperature with a relative humidity of 30-50 %. The distance between the plasma generator and surface was kept constant at 5 mm ± 1 mm. All the experiments were performed on treated samples right after the plasma exposure without any delays.

Table 4.1. Various reactive species during plasma treatment.

External gas cylinder-based plasma	**Atmospheric plasma**
Ar plasma: $Ar + e \rightarrow Ar^* + e$	$O_2 + e \rightarrow 2O + e$
He plasma: $He + e \rightarrow He^* + e$	$N_2 + e \rightarrow 2N + e$
N_2 plasma: $N_2 + e \rightarrow 2N + e$	$O + N \rightarrow NO$
O_2 plasma: $O_2 + e \rightarrow 2O + e$	$O + NO \rightarrow NO_2$
$O_2 + e \rightarrow {}^1O_2 + e$	$O + O_2 \rightarrow O_3$
CO_2 plasma: $CO_2 + e \rightarrow CO + O + e$	$O_3 + N \rightarrow NO + O_2$
$CO + e \rightarrow C + O + e$	

4.2.3. Characterization Tests

A Krüss (Hamburg, Germany) drop shape analyzer was utilized for contact angle measurements and wettability studies. Distilled water (2 µl) was used to measure the contact angle between surface and liquid. For aging experiments, water contact angle of the 20 min plasma treated samples was measured at different time points for both GUR1020 and Ti6Al4V materials.

Microhardness measurements were performed by Ratnakar Vickers hardness tester with a tetragonal pyramid diamond tip (vertex angle of 136º) under the loading of 100 g and holding time of 30 seconds. Thermo Nicolet Nexus 670 ATR-FTIR equipped with a DTGS detector, a Globar source and Smart iTR diamond ATR accessory, and Renishaw inVia confocal Raman microscope (laser: 532 nm) were used to analyze the characteristics of GUR1020 before and after plasma exposure. Scienta Omicron ESCA 2SR X-ray photoelectron spectroscope (XPS) was utilized for surface analysis of Ti6Al4V and GUR1020 which was equipped with a monochromatic Al Kα X-ray source (1486.7 eV). An ion gun (Ar gas) with beam energy of 3 keV, emission current of 3.8 µA, filament current of 10 µA and angle of 45º was used for surface etching. The Stopping and Range of Ions in Matter (SRIM) software package was employed to estimate ion etching depth in the matter; the same parameters of the experimental setup were applied to simulations. A PANalytical Empyrean multipurpose diffractometer was utilized to perform X-ray diffraction (XRD) experiments with X-ray wavelength of 0.154 nm in the 2θ range of 10º to 90º.

4.2.4. Tribological Tests

To understand the variation in the tribological performance of GUR1020 and Ti6Al4V with the plasma treatment, experiments were performed on a pin-on-disc setup (Figure 4.2). In this test setup, the stationary Ti6Al4V pin was slid over the rotating GUR1020 disc in the presence of phosphate-buffered saline (PBS). The pin and disc were rigidly affixed to the pin and disc holders, respectively. The details of the setup are provided in Figure 4.2. To simulate the walking motion, the disc was subjected to an oscillatory motion of 24º angle at an oscillatory speed of 60 rpm and a load of 30 N (1 MPa pressure). In this work, we have used nine different conditions (0:0, 10:0, 20:0, 0:10, 10:10, 20:10, 0:20, 10:20 and 20:20) for surface treatment of the samples (five samples

for each condition) to investigate the effect of different exposure times on the tribological behavior of this system (polymeric disc and metallic pin).

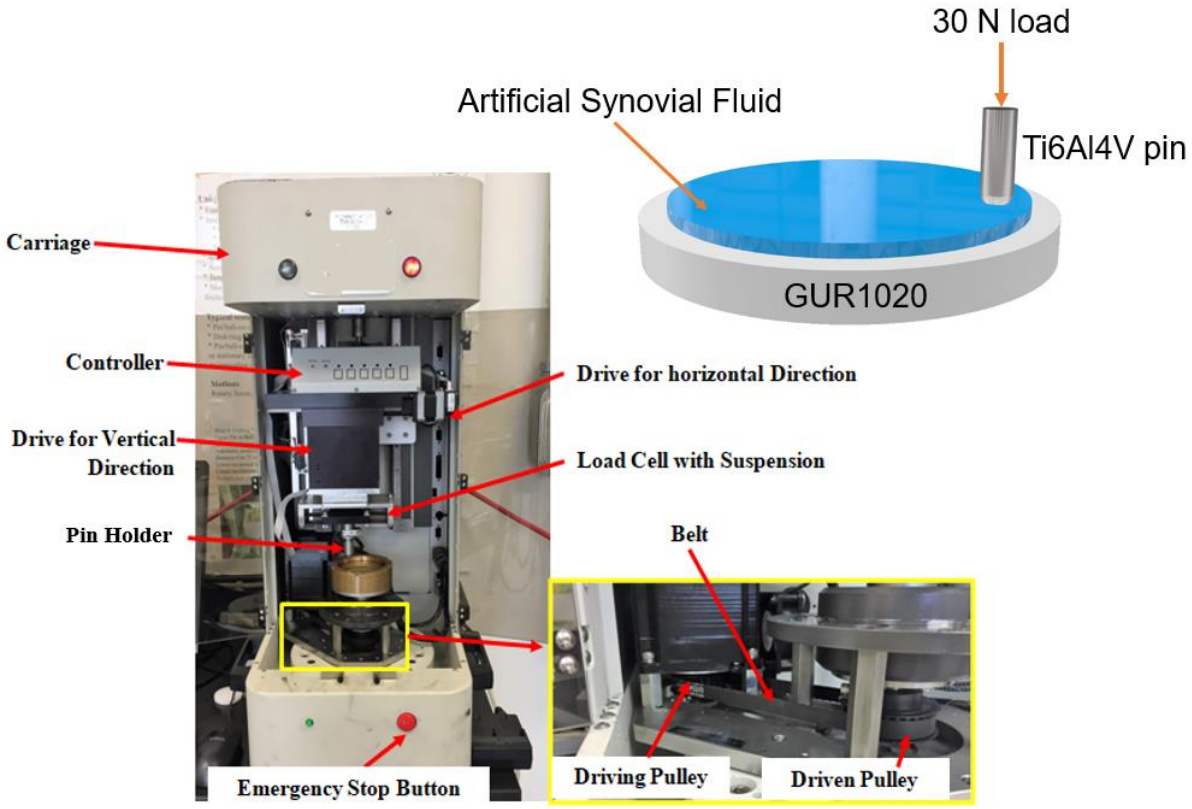

Figure 4.2. The pin-on-disk setup used for conducting of tribological experiments. Artificial synovial fluid was used as the lubricant to simulate the real *in vivo* conditions. The amount of load (30 N) was chosen according to the weight of an average person.

The first number for each experiment indicates the plasma exposure time (min) for GUR1020 disc and second number indicates the plasma exposure time (min) for Ti6Al4V pin. All experiments were performed at the same radius of contact. To check the repeatability, experiments were performed twice. Nine different specimens were developed by treating both pin and disc with plasma for 0, 10, 20 min. The specimens were evaluated by measuring (i) wear volume rate from the measured wear depth values and (ii) friction coefficient values. Wear volume (w_v) can be determined by:(Molinari, Straffelini et al. 1997, Kalin and Vižintin 2000)

$$w_v = \pi R^2 \delta \qquad (1)$$

where, R is the radius of pin (m) and δ is the wear depth (m). The surface roughness of the specimen was measured using a 3D profilometer [Bruker (Model 831-775) with a 5X objective].

4.2.5. Corrosion Tests

Three electrode cell corrosion experiments were performed by employing a CHI-604C instrument equipped with a saturated calomel electrode (SCE) (reference electrode), a platinum electrode (counter electrode), and Ti6Al4V (working electrode), which was molded by cold epoxy. The exposed area of all samples to the electrolyte media were ~ 1 cm^{-2}. Phosphate buffered saline (PBS) was chosen as the solution with naturally dissolved oxygen at 37 °C. Tafel curves were plotted in the potential range of -1 to 2 V vs. saturated calomel electrode (SCE) (1.67 mV/s). Samples were polished with sand papers (grit size 320-1000) prior to the tests. The variation of corrosion potential with time was measured immediately after the immersion of the samples for 20 minutes.

4.2.6. Cell Study

Cell culture (Adipose derived stem cells (ASCs) to osteogenic stem cells (OSCs) differentiation): ASCs isolated from subcutaneous adipose tissue were purchased and cryopreserved for cell culture practice. A frozen batch of ASCs were suspended in stromal growth medium StromaQual™ (LaCell LLC, LA, USA) containing a mixture of 10% DMSO and 90% FBS. The cells were thawed in a 37°C water bath until it liquefied. The ASCs were then suspended in a growth medium with serum and cultured until passage 1 and plated in 12-well plates at a density of 1×10^4 cells/cm^2. In our case passage 1 cells mean the resuspended cryopreserved cells after culture have reached 90 % confluency. The cells were incubated in an incubator at 37°C, with 5% CO_2 for 24-36 hours and checked until confluency. After reaching 90% confluency, the cells were inoculated only on one side of the surface of the polymer and titanium discs and resuspended

in osteogenic medium for 21 days (media (OsteoQual™ (LaCell LLC, LA, USA) were replaced every 3 days). The controls were suspended in stromal medium. The schematic representation of the osteogenic stem cell study timeline is provided in Figure 4.3.

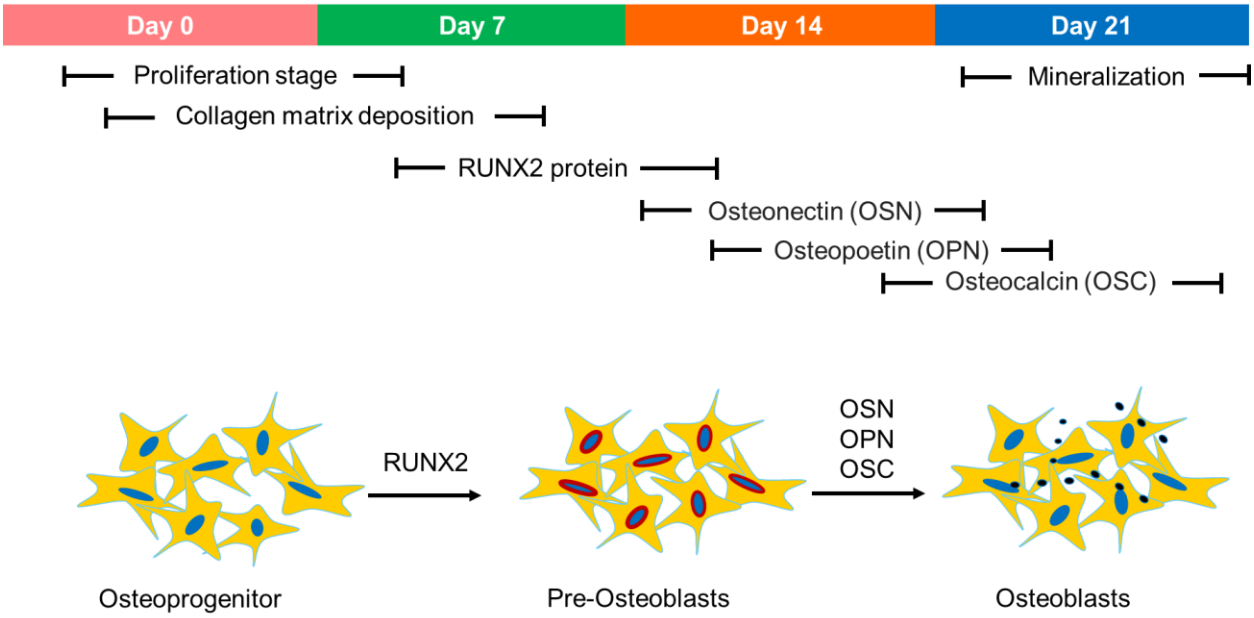

Figure 4.3. Schematic representation of the osteogenic stem cell study timeline.

Cell viability: The cell viability was determined based on the Live/Dead cell assay by staining the cells with fluorescent dyes calcein AM/ propidium iodide with final concentrations at 2 and 3 μM respectively. live (green) and dead (red) cell numbers were counted by means of a fluorescent microscope (Zeiss SteREO Lumar.V12) with excitation/emission filter at 550/565 nm.

Immunohistochemistry: Cells were characterized after fixation with 4 % paraformaldehyde followed by permeabilization with 0.2% TritonX-100. Phalloidin and 0.2% fish skin gelatin was used for immunofluorescence as well as CF™488A (Biotium, USA), RUNX 2 mouse antibody sc-390351 AF594 (Abcam, USA), and Osteocalcin mouse antibody sc-74495 AF594 (Abcam, USA) for 45 min at 4°C. On day 7 & 14 Phalloidin and RUNX 2 stains were used to and characterize the cytoskeleton and pre-osteoblasts. On day 21 cells were stained with Phalloidin and Osteocalcin to characterize the cytoskeleton and mature osteoblasts. All cells were

counterstained with 2 µg/mL of 200 µL Hoechst (Thermo Fisher Scientific, USA) in PBS for 1-2 minutes to identify the nucleus. Images were captured at 10X magnification using confocal microscopy (Leica TCS SP8 Confocal Microscope with WLL) at $\lambda_{460/490}$ for Hoechst, $\lambda_{488/510}$ for Phalloidin, and $\lambda_{594/650}$ for RUNX2 and Osteocalcin respectively. Alizarin red S (Sigma Aldrich, USA) staining was also conducted to identify calcium containing cells on day 21 differentiated cells. Images were captured at 10X magnification using a bright field microscope.

Gene Expression: The osteogenic gene expression was evaluated by RNA isolation, and quantitative reverse transcription-polymerase chain reaction (qPCR) experiment to identify RUNX2, Osteopontin, and Osteonectin on day 14 and 21 respectively. Purelink RNA kit (Life Technologies, CA, USA) was used for isolation of RNA. By means of nanodrop spectrophotometer, RNA samples were quantified. High capacity cDNA synthesis kit (Applied biosciences, CA, USA) was used for synthesis of the first strand cDNA. ABI-7900 qPCR machine was used for SYBR green and qPCR. The primer sequences for osteogenic genes are described in Li et al.(Li, Zanata et al. 2016) The primer sequence for GAPDH gene designed in our previous work(Shaik, Wu et al. 2018) were used. The fold change in gene expression was calculated and normalized to GAPDH for osteogenic genes by $2^{-(\Delta\,\Delta Ct)}$ method.(Livak and Schmittgen 2001)

X-ray computed tomography (µCT) images of the implants were obtained with a SCANCO Medical AG (Switzerland) model µCT 40 system using a voltage of 55 kVp, a current of 145uA and a voxel size of 10um. Scanning was conducted to check the spreading of cells on the implants at 1°C/min using a SKYSCAN 1074 Portable X-ray Microtomograph (Bruker, NJ, USA). The 3D images were constructed using Avizo 5.0 software. Cells were fixed with 4 % paraformaldehyde and stained with 0.01 % osmium tetroxide for 24 hours, followed by washing three times with PBS before scanning.

4.3. Results and Discussion

4.3.1. Characterization

Figure 4.4a shows the plasma hand-held device in-action coating a polyethylene pellet. Figures 4.4b and 4.4c demonstrate the contact angle measurement results of Ti6Al4V and polyethylene. Plasma treatment of surface reduced the water contact angle from 79.2º to 13.1º for Ti6Al4V and from 91.8º to 38.1º for polyethylene samples. Accordingly, both metal and polymer proved to become considerably hydrophilic due to plasma exposure (~ 6X reduction in contact angle for metallic, and ~ 2.5X reduction in contact angle for polymer sample).

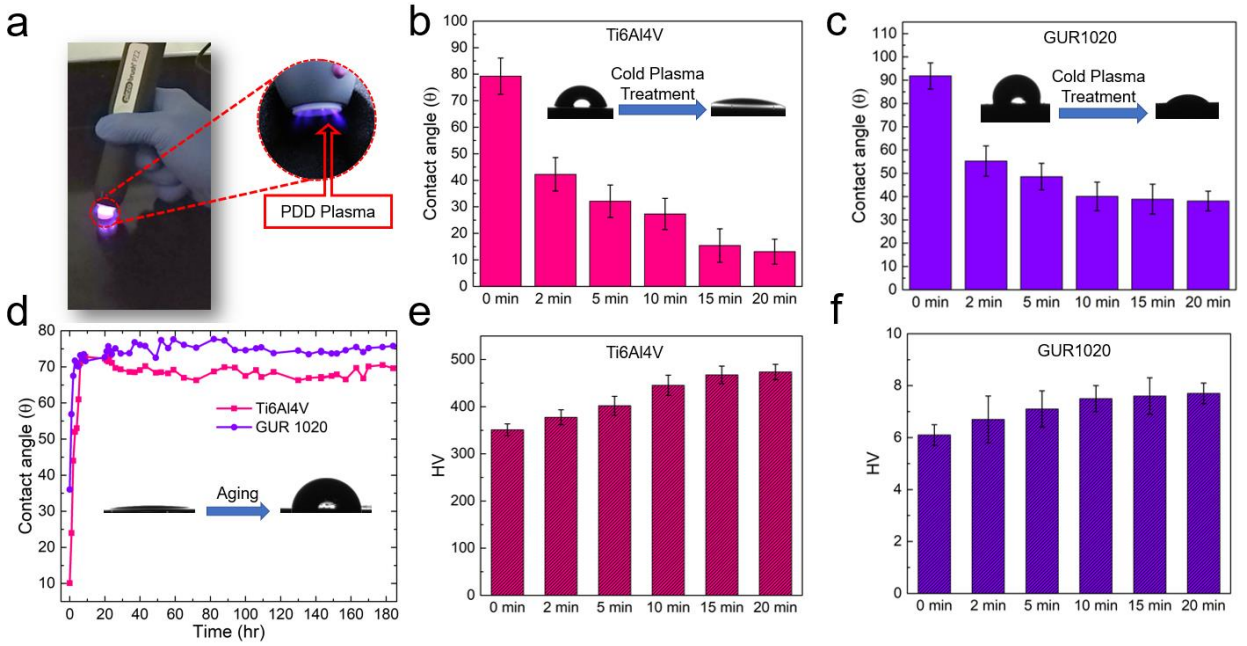

Figure 4.4. Contact angle and microhardness measurements of treated and untreated samples for six different time intervals. (a) Illustration of GUR1020 pellet surface treatment by means of handheld PDD plasma generator. (b) Water contact angle decreases by increasing the plasma exposure time for Ti6Al4V. (c) Plasma treatment improves the hydrophilicity of GUR1020 sample. (d) Aging experiment shows the formation of a temporary and a permanent coating due to plasma exposure. (e) The value of microhardness increases by increasing the exposure time for Ti6Al4V. (f) Microhardness of the GUR1020 sample increases due to plasma exposure. Each test was repeated at least 10 times and each exposure experiments were performed on a separate sample.

Furthermore, contact angle becomes almost constant after 20 min of plasma exposure which indicates the treatment saturation point for metal and polymer. The lifespan of coating was

measured by conducting the aging experiment (Figure 4.4d). As a result, two stages were observed during the “aging process”. The first stage illustrates the existence of a temporary coating that degrades after about 10 hours of aging. The second stage shows a permanent coating that does not degrade over time. Therefore, all the experiments, including biocompatibility tests, were performed right after the plasma exposure without any further delays. Figures 4.4e and 4.4f show the microhardness measurements conducted on Ti6Al4V and polyethylene ($p<0.01$). Accordingly, microhardness of Ti6Al4V and polyethylene increased by approximately 35 % and 26 %, respectively, compared to untreated surfaces. Likewise, the saturation point was observed after 20 min of plasma treatment.

The increment in hydrophilicity and microhardness values can be justified by the results obtained from FTIR and Raman spectroscopy analyses. Figure 4.4a illustrates the ATR-FTIR results of polyethylene sample.

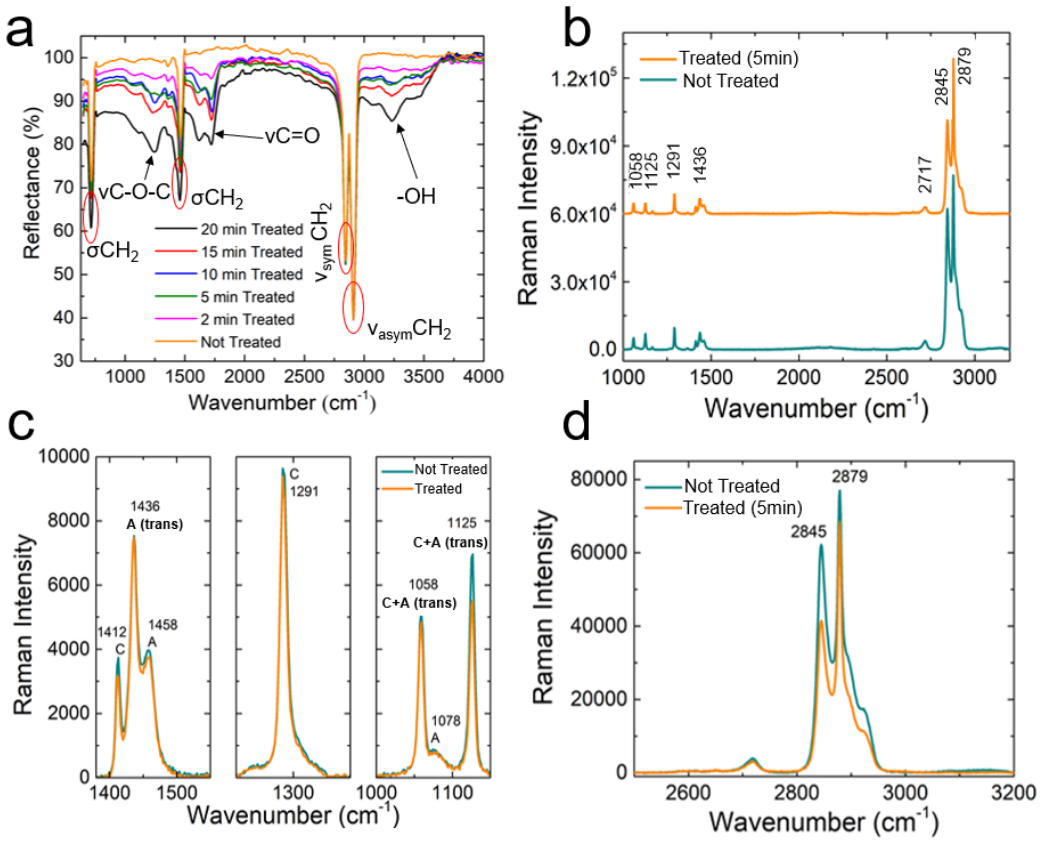

Figure 4.5. Vibrational spectroscopy of treated and untreated GUR1020. (a) FTIR spectra of GUR1020 after different exposure times shows the formation of new chemical groups. (b) Raman spectrum of treated and untreated polymer in the range of 1000-3250 cm^{-1} with 532 nm laser shows the typical peaks of GUR1020. (c) Analysis of Raman spectrum in fingerprint region for treated and untreated polymer shows the variation of peak intensity due to plasma exposure. (d) Analysis of Raman spectrum in high wavenumber region for the polymer sample shows an increase in crystallinity of the treated sample.

Different vibrational modes and bonding groups are assigned in Figure 4.5a to show the changes that occurred during the surface modification at different time intervals. Typical polyethylene bands can be observed at 713 cm^{-1} (σCH_2; ν: stretching mode), 1456 cm^{-1} (σCH_2; σ: scissoring mode), 2844 cm^{-1} ($\nu_{sym}\, CH_2$) and 3233 cm^{-1} ($\nu_{asym}CH_2$). The signal intensity of σCH_2 groups have changed slightly due to the plasma treatment. However, there is no considerable intensity change for $\nu_{sym}CH_2$ and $\nu_{asym}CH_2$ groups. On the other hand, the remarkable increase in intensity of νC-O-C (1244 cm^{-1}) and νC=O (1722 cm^{-1}) bands is evidence of the plasma effect on the surface of the polymer. Moreover, the number of -OH (3230 cm^{-1}) species dramatically

increased on the surface as a result of plasma treatment. Figures 4.5b, 4.5c and 4.5d show the Raman spectra of GUR1020 before and after treatment. Typical polyethylene bands are observed at 1058 cm^{-1} (ν_{asym}C-C), 1125 cm^{-1} (ν_{asym}C-C), 1291 cm^{-1} (τCH_2) (τ: twisting mode), 1436 cm^{-1} (σCH_2), 2845 cm^{-1} ($\nu_{sym}\, CH_2$) and 2879 cm^{-1} ($\nu_{asym} CH_2$). From the width and intensity changes of 2845 cm^{-1} and 2879 cm^{-1} bands, it can be concluded that the crystallinity of the polymer has increased after the surface modification. Accordingly, the formation of reactive oxygen species and crystallinity improvement are two fundamental reasons for the enhancement of hydrophilicity and hardness on the polymer surface.

To accurately monitor the surface evolution of the samples, XPS studies were conducted for Ti6Al4V and GUR1020. Figure 4.6a and 4.6b show the deconvoluted C 1s XPS spectrum. Accordingly, C-C peak was observed at 284 eV for polyethylene before and after the treatment. Meanwhile, C-O, C=O and COOH peaks also appeared at 286 eV, 287.6 eV and 288 eV after performing the surface treatment.

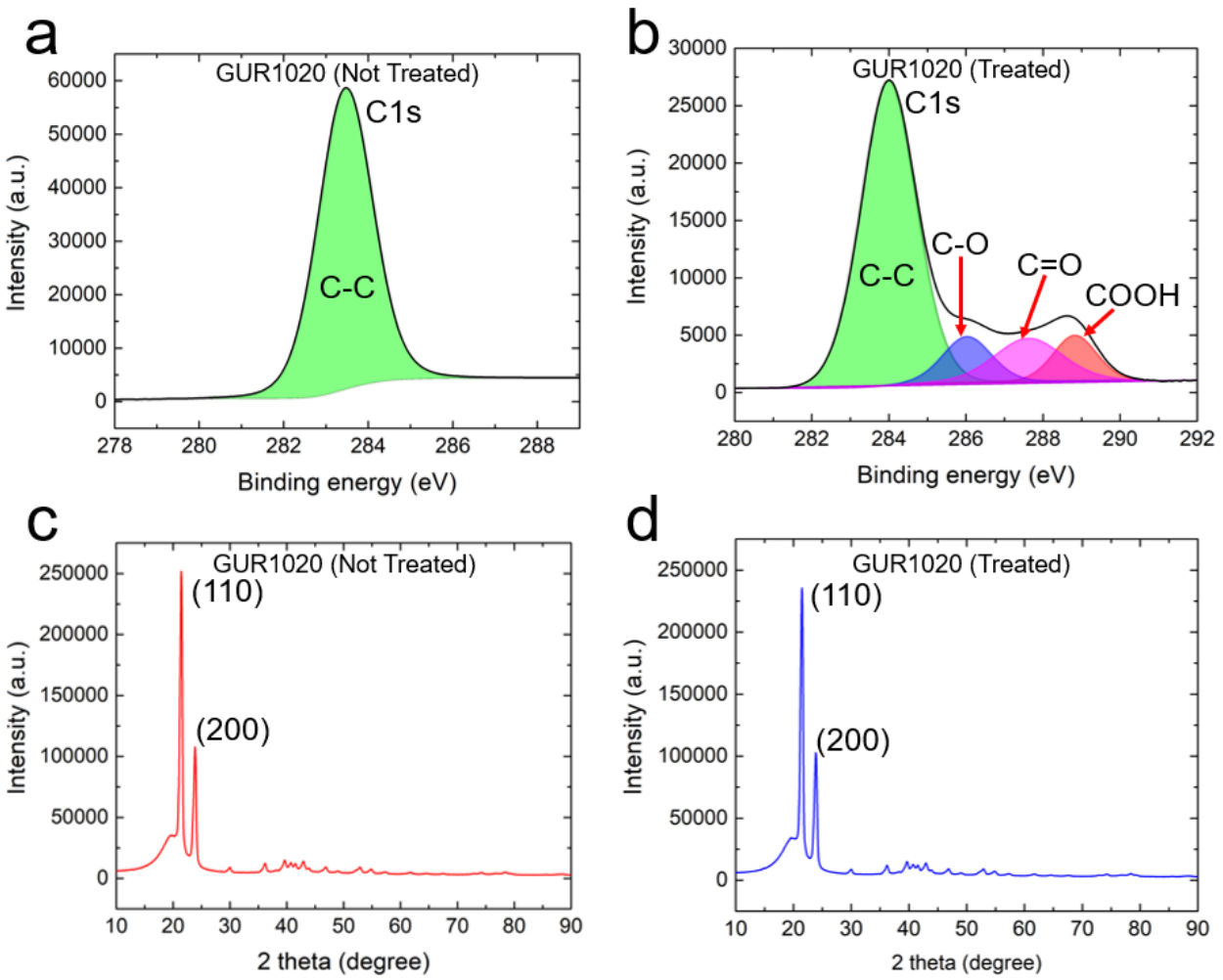

Figure 4.6. XPS (a, b) and XRD (c, d) analyses of the polymer sample. (a, b) XPS results confirm the formation of new chemical groups after plasma exposure. (c, d) XRD results show that the bulk properties are constant before and after plasma exposure.

On the other hand, XRD analysis was performed to demonstrate that the bulk properties of samples have not been changed due to the surface modification. From Figure 4.6c and 4.6d, (110) and (200) crystal planes of polyethylene appeared at 2θ values of 21.5º and 23.8º, respectively, for both treated and untreated samples. In addition, interplane spacing (d_{hkl}) was measured by means of equation 2 (Bragg's equation).

$$d_{hkl} = \frac{n\lambda}{2\sin\theta} \qquad (2)$$

where, n, λ (0.154 nm) and θ are defined as level of diffraction, X-ray wavelength and Bragg angle, respectively. The interplane spacing for both treated and untreated samples were 0.41 Å (for (110)

plane) and 0.37 Å (for (200) plane). Accordingly, XRD spectra of polyethylene did not change after the treatment. Therefore, it can be concluded that the bulk properties are constant, and this method of plasma surface treatment only changes the surface properties of the polymer.

XPS spectra of Ti 2p in treated and untreated Ti6Al4V are shown in Figures 4.7a and 4.7b. As can be seen, Ti $2p_{3/2}$ and Ti $2p_{1/2}$ peaks are located at 453 eV and 459 eV, respectively.

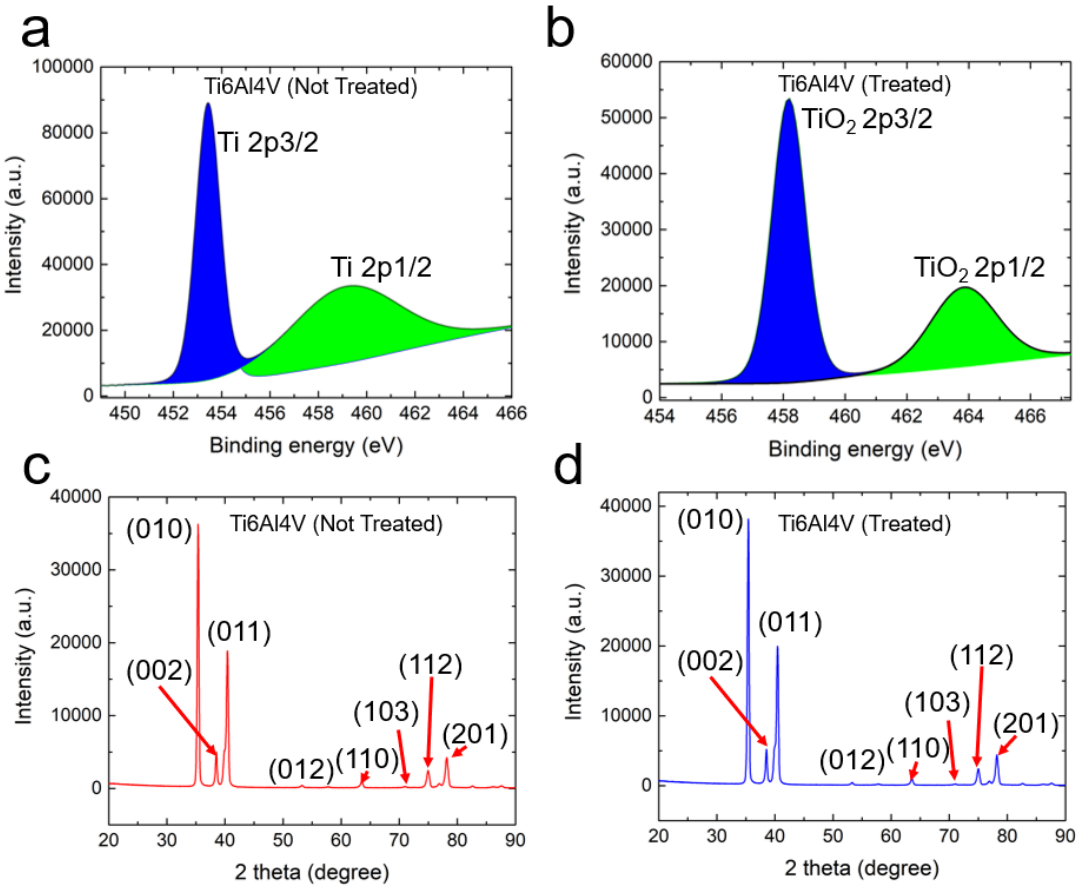

Figure 4.7. XPS (a, b) and XRD (c, d) analyses of the metallic sample. (a, b) Formation of TiO_2 due to plasma treatment, is illustrated by XPS analysis. (c, d) XRD results confirm that the bulk properties of Ti6Al4V are constant before and after plasma exposure.

After the plasma treatment, O_2 species formed on the surface and the TiO_2 $2p_{3/2}$ and TiO_2 $2p_{1/2}$ peaks shifted to 458 eV and 464 eV, respectively. Moreover, the distance between $2p_{3/2}$ and $2p_{1/2}$ peaks has changed from 6 eV in untreated sample to 7 eV in the treated sample. The aforementioned evidences demonstrate the formation of titanium oxide on the surface of Ti6Al4V

due to surface treatment. However, XRD results (Figures 4.7c and 4.7d) do not show any significant change in the bulk properties of Ti6Al4V before and after the surface treatment. According to Figure 4.7c and 4.7d, the most prominent 2θ peaks for both treated and untreated Ti6Al4V appear at 35.4º and 40.4º which are assigned to (010) and (011) planes, respectively. Moreover, intraplane spacing was also the same (~ 0.25 Å for (010) and ~ 0.22 Å for (011) plane) for both types of samples regardless of the surface treatment.

To realize the effective depth of PDD plasma on metal and polymer specimens, time dependent Ar ion etching was employed along with XPS analysis to quantify the depth of penetration. Firstly, Ar etching depth was measured by means of SRIM simulation package (details are elaborated in experimental section). Figure 4.8a illustrates the simulation results for Ar ion etching of polyethylene (3D results are provided in Figure 4.9).

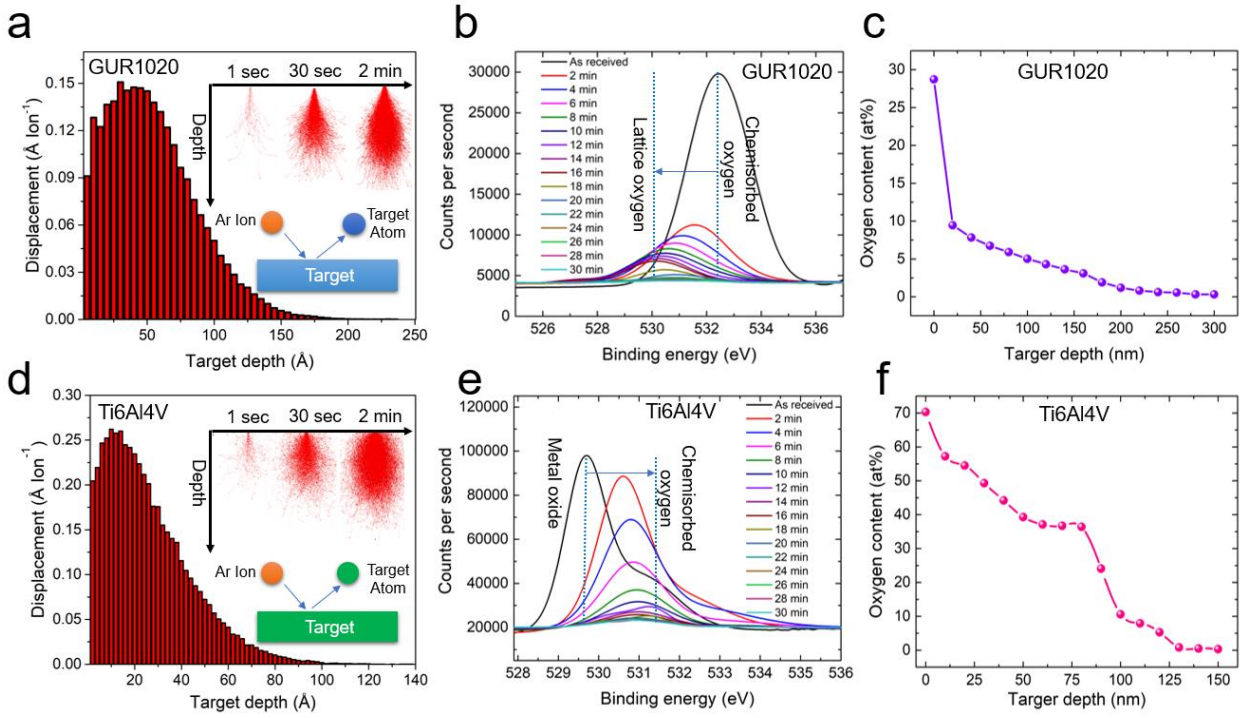

Figure 4.8. SRIM simulations coupled with experimental XPS results for depth analysis of plasma coating on polymer and metal substrates.

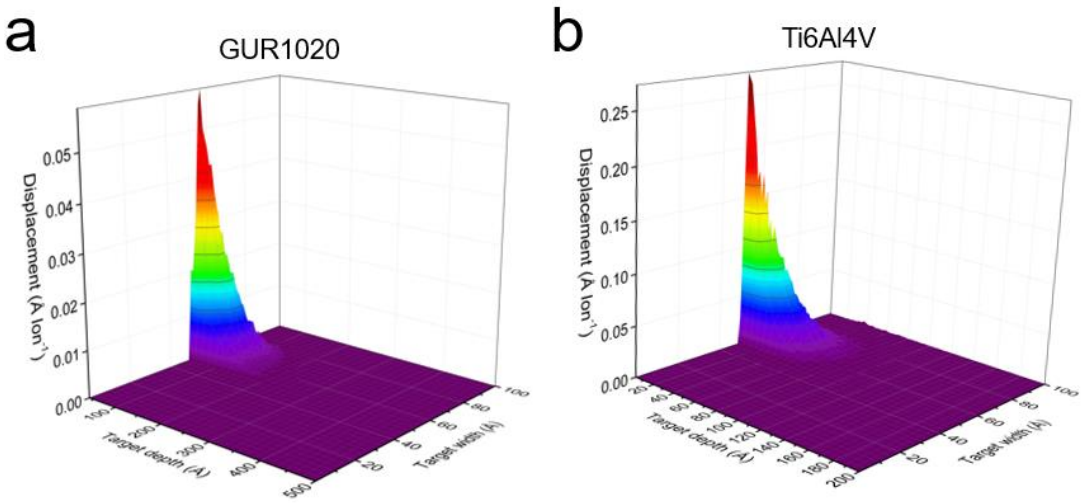

Figure 4.9. 3D images of SRIM simulation. Coupling SRIM simulations with XPS results in different depth reveals the approximate depth of plasma surface modification.

Accordingly, the effective depth of etching was measured to be ~ 20 nm for every 2 minutes of etching. Figure 4.8b shows the O 1s XPS spectrum of plasma treated sample within 30 min of etching with 2 min intervals. Figure 4.8b shows O 1s peak is shifting to left (lower values) from 532.4 eV to 530.1 eV and the intensity of peak has been decreased as well by increasing the etching time. The decreasing peak intensity shows the decrease in oxygen content. The shift in peak position of O 1s shows that different species of oxygen and partial species of oxygen are being produced. By comparing the SRIM and XPS results, the effective depth of plasma penetration for polyethylene was measured to be ~ 220 nm (Figure 4.8c). Furthermore, the same method was performed to calculate the effective depth of plasma treatment for Ti6Al4V sample (Figure 4.8d). From Figure 4.8e, O 1s peak for Ti6Al4V shifted to right (higher values) from 529.7 eV to 531.3 eV and the peak intensity decreased with the increase of etching time. Accordingly, effective depth of PDD plasma for surface modification of Ti6Al4V was measured to be ~ 130 nm (Figure 4.8f).

4.3.2. Tribological Behavior

The obtained wear depth data for Ti6Al4V and GUR1020 are plotted in Figure 4.10a, 4.10b and 4.10c for different treatment times. The wear volume rate is calculated from the measured wear depth values from Figure 4.10a, 4.10b and 4.10c and utilizing equation 1. Similar to wear depth data, the obtained friction coefficient values are plotted in Figure 4.10d, 4.10e and 4.10f. From Figure 4.10, it can be observed that transient wear prevailed until the sliding time of 1800 s and that steady state wear was observed afterwards. Therefore, in the present work the wear volume rate was calculated for the steady state wear region, and the determined values for different plasma exposure times are plotted in Figure 4.11a.

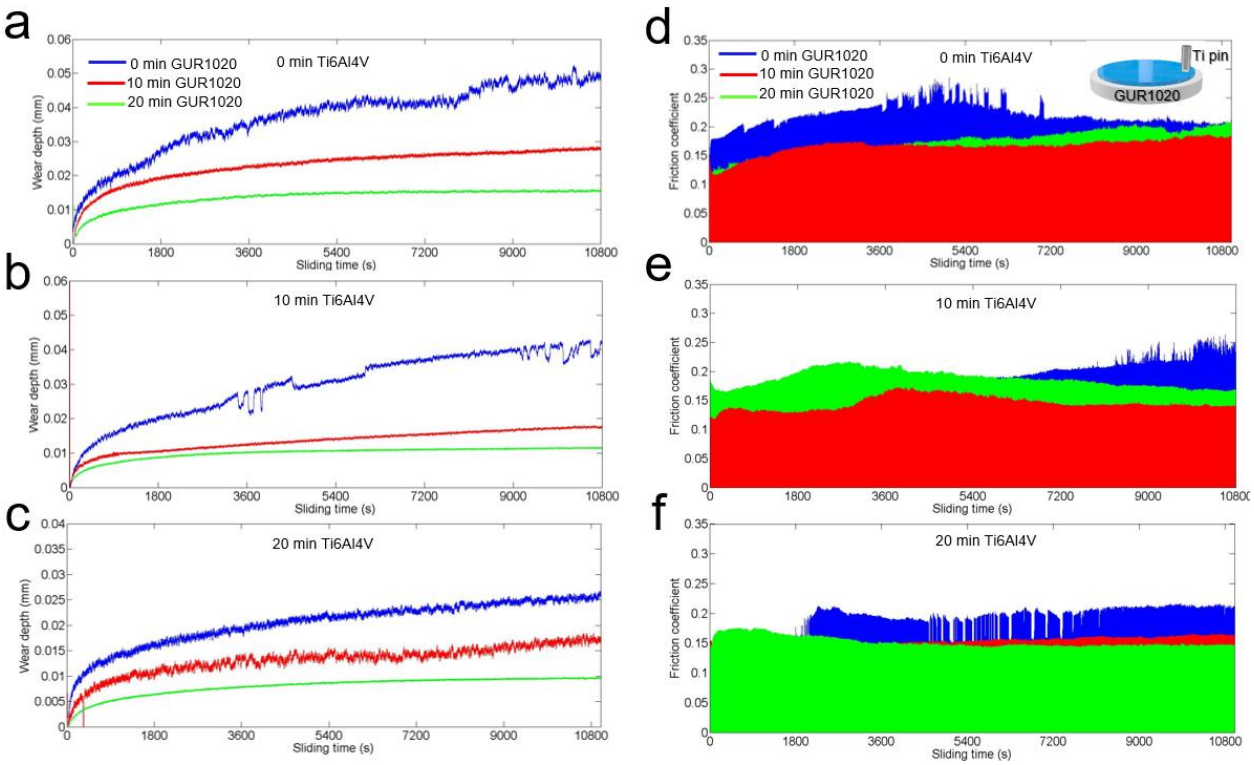

Figure 4.10. Tribological results for several cases with different plasma exposure times on the metal pin and polymer disc. (a, b, c) Wear depth vs. sliding time for various plasma exposure times shows the improvement of tribological properties by applying the plasma treatment (d, e, f) Friction coefficient vs. sliding time shows the reduction of friction after plasma treatment of the surfaces.

To obtain the variation in wear volume rate with plasma treatment, wear volume rate ratio ($w_{untreated}/w_{treated}$) is calculated by dividing the wear volume obtained for untreated samples by wear volume rate for plasma treated samples (with different treatment times). The obtained values are plotted in Figure 4.11b.

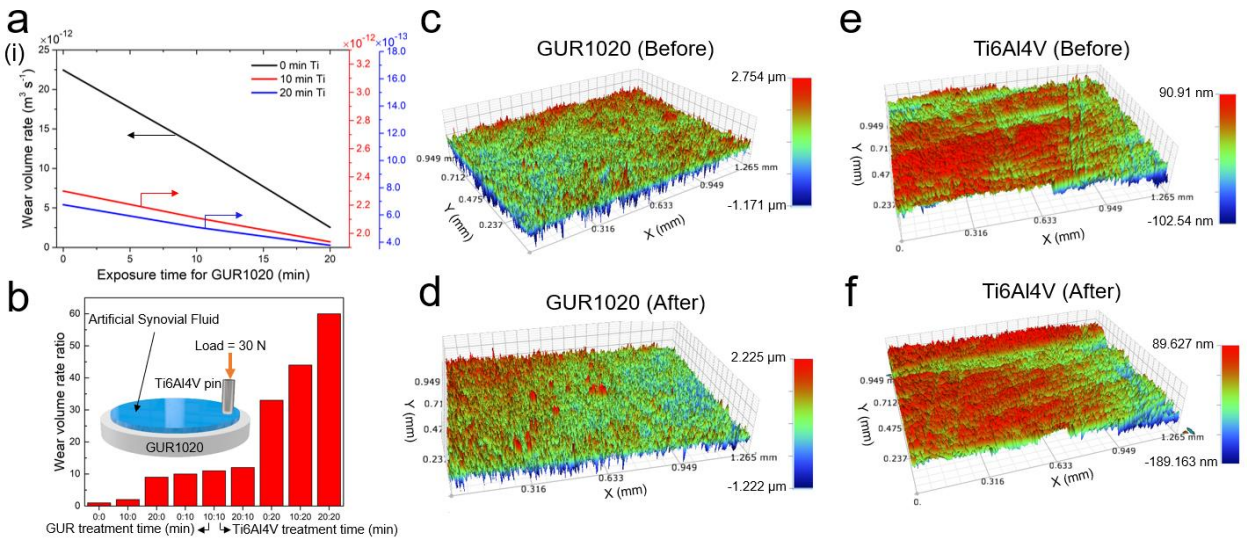

Figure 4.11. Tribological analysis of polymer and metal substrates before and after plasma treatment. (a) The significant reduction of wear volume due to plasma exposure confirms the improvement of tribological properties. (b) Wear volume ratio for different cases shows the remarkable tribological improvements due to the surface treatment. (c, d, e, f) 3D surface profiles of polymer and metal samples shows that the roughness of surface was slightly changed after the plasma exposure.

From this Figure, when both the polyethylene disc (GUR1020) and pin (Ti6Al4V) are treated for 20 min each, the amount of wear rate was reduced by ~ 60X compared to the untreated case. Comparing case 20:0 (GUR 20 min; Ti6Al4V 0 min) and case 0:20 (GUR 0 min; Ti64 20 min), it can be concluded that surface plasma treatment is more effective in reducing wear when the metallic part (Ti6Al4V) is treated with plasma. It is now hypothesized that the reduction in wear with plasma treatment leads to better tribological properties due to the presence of an oxide layer. The presence of an oxide layer on the surface of Ti6Al4V and GUR1020 was already discussed in the previous section. As shown in Figures 4.8c and 4.8f, the magnitude of maximum oxygen percentage (Ti6Al4V: 70 %; GUR1020: 28 %) and its availability with depth is more than

2.5X in the case of Ti6Al4V compared to polyethylene. Likewise, the oxide layer formation on the surface of the specimen can be indirectly determined by contact angle measurements (Figure 4.4b, 4.4c and 4.4d). The reduction in the contact angles indicates the presence of the oxide layer as well as the change in surface properties (hydrophobic to hydrophilic). This type of surface treatment enhances the wear properties by providing better wettability on the surface. In addition, the increase in microhardness as well as the enhanced wettability improve the tribological properties and reduce the wear volume. Therefore, it can be concluded that the presence of surface oxides, the formation of a hydrophilic layer and an increase in microhardness results in wear reduction. According to Figure 4.11d, 4.11e and 4.11f, the value of the friction coefficient does not vary considerably by increasing the plasma treatment time on polyethylene. Therefore, it can be concluded that the surface treatment of polyethylene has a noticeably lower influence on the tribological behaviour of the Ti6Al4V-GUR1020 system. Meanwhile, the friction coefficient value decreases dramatically by applying the PDD plasma treatment on Ti6Al4V surface. As a result, the best tribological properties are achieved when both metallic and polymeric parts are exposed to plasma. Statistical results of the tribological tests are also provided in Figure 4.12. Accordingly, a good repeatability for tribological tests can be observed.

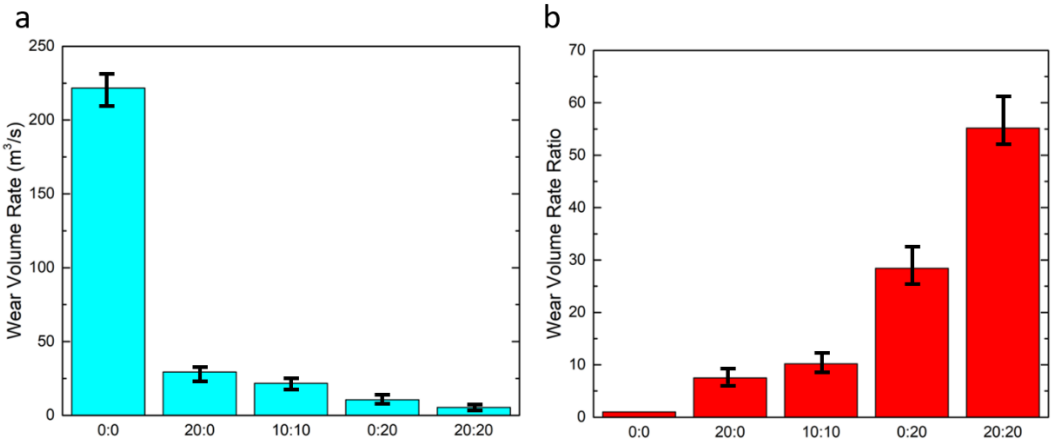

Figure 4.12. The amount of (a) wear volume rate (m^3/s) and (b) wear volume rate ratio in five different conditions ($p<0.01$).

Figures 4.11c and 11d illustrate the surface 3D profile of polyethylene samples before and after plasma treatment. The average roughness for polyethylene before and after treatment was measured to be ~ 179.8 μm and ~ 181 μm, respectively. Furthermore, the maximum height difference between the peaks and valleys of the surface were ~ 3.9 μm and ~ 3.7 μm for untreated and treated samples, respectively. Figures 4.11e and 11f show, for the Ti6Al4V sample, that average roughness was ~ 63 nm for the untreated sample and ~ 57 nm for the treated sample. Additionally, the maximum peak-valley height difference of samples was ~ 203 nm (untreated) and ~ 179 nm (treated). Accordingly, the average roughness of samples decreased by ~ 5 % for polyethylene and ~ 13 % for Ti6Al4V. Although the slight decrease in surface roughness might have some effect on the enhancement of tribological properties, this is not a significant factor in this system compared to surface chemistry, wettability and hardness.

4.3.3. Corrosion Behavior

Corrosion resistance is a significant factor for biological materials: a poor corrosion resistance increases the risk of implant rejection. It is well-known that Ti and its alloys form a surface oxide layer which improves the corrosion resistance.(Fazel, Salimijazi et al. 2015, Durdu, Usta et al. 2016, Vaithilingam, Goodridge et al. 2016) In order to evaluate the corrosion behavior of the samples before and after the surface treatment, open circuit potential (OCP) and Tafel curves were obtained and are presented in Figure 4.13.

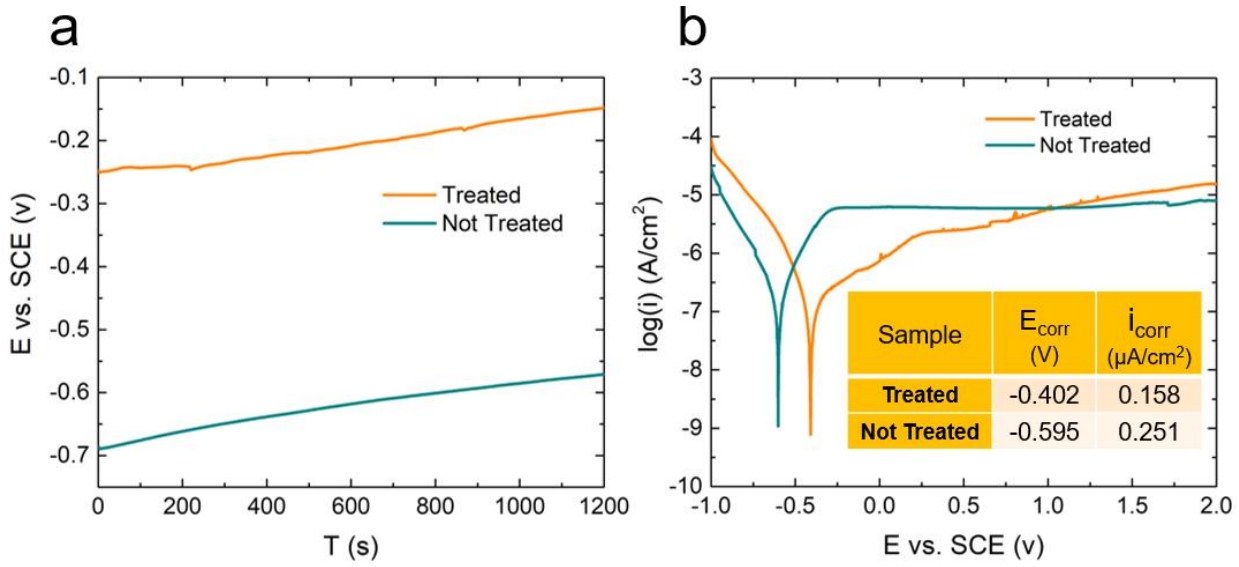

Figure 4.13. Corrosion behavior of Ti6Al4V before and after surface modification. (a) Potential vs. time diagram shows the formation of TiO_2 passive layer after surface modification. (b) Current vs. potential diagram illustrates the enhancement of corrosion behavior of the metallic substrate due to surface treatment by shifting i_{Corr} to smaller values.

Based on the OCP curve (Figure 4.13a), it is clear that in both samples, the anodic reaction is prevented with the same mechanism while the potential of both samples increased with time. But the treated sample is more stable thermodynamically. In other words, despite almost the same slope of both curves, the initial potential for the treated sample is more positive, meaning that the surface has become more noble due to the treatment. This may be due to the pre-formed oxide film on the surface after the surface treatment, as confirmed by characterizing experiments in the previous sections.

Tafel curves for untreated and treated samples (Figure 4.13b) clearly indicate a decrease in corrosion rate and a more noble potential. For the treated sample, the Tafel curve is shifted to the lower values of current density (0.158 $\mu A/cm^2$) and more positive values of potential (-0.402 V). The related measured parameters from the polarization curves are attained by Tafel extrapolation. As mentioned before, the surface treatment forms an oxide layer on the surface, and this layer acts as a protective coating on the surface, thereby maintaining the excellent corrosion resistance of the

alloy, and improving it by 37%. As a result, it can be concluded that the nonthermal plasma surface treatment increases the lifetime of the alloy in body fluid has no negative effect on the corrosion properties of Ti6Al4V. Statistical analysis of the corrosion studies are provided in Figure 4.14, which showed good reproducibility.

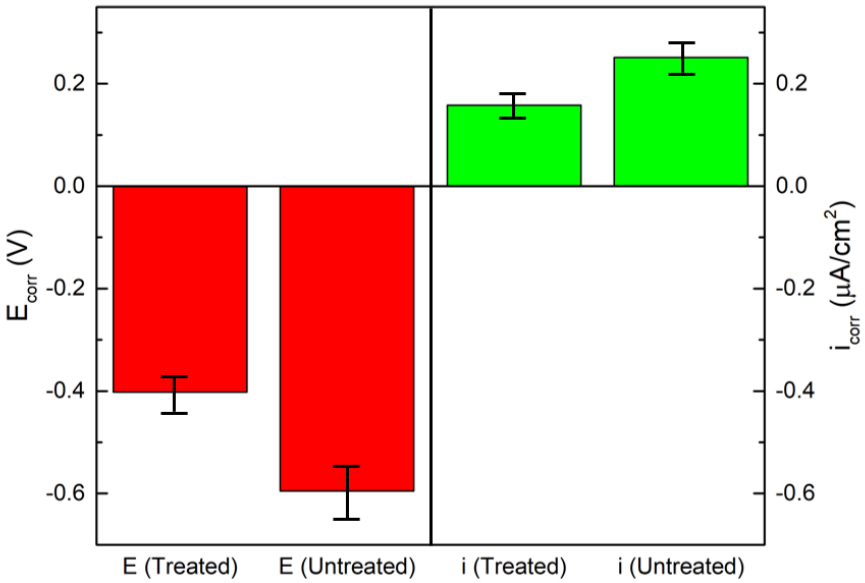

Figure 4.14. Statistical analysis of corrosion experiments for E_{corr} and i_{corr} of the treated and untreated samples ($p<0.01$).

4.3.4. Cell Study

The osteogenic stem cell study timeline as shown in Figure 4.3 was followed. We evaluated the osteogenic stem cells study at three times points: day 7, day 14 and day 21 respectively. Figure 4.15 shows the fluorescence images of day 7, 14, 21 and their controls respectively. F-actin filaments were observed on all days with different morphology. The nucleus colocalization protein RUNX2, and also a pre-osteoblast marker was observed on day 7 cells. According to literature, RUNX2 is likely to occur from day 7-16, however there might be differences based on age of the donors.(Kar, Molla et al. 2019) The protein Osteocalcin, a mature osteoblast marker, was observed on day 21 cells.

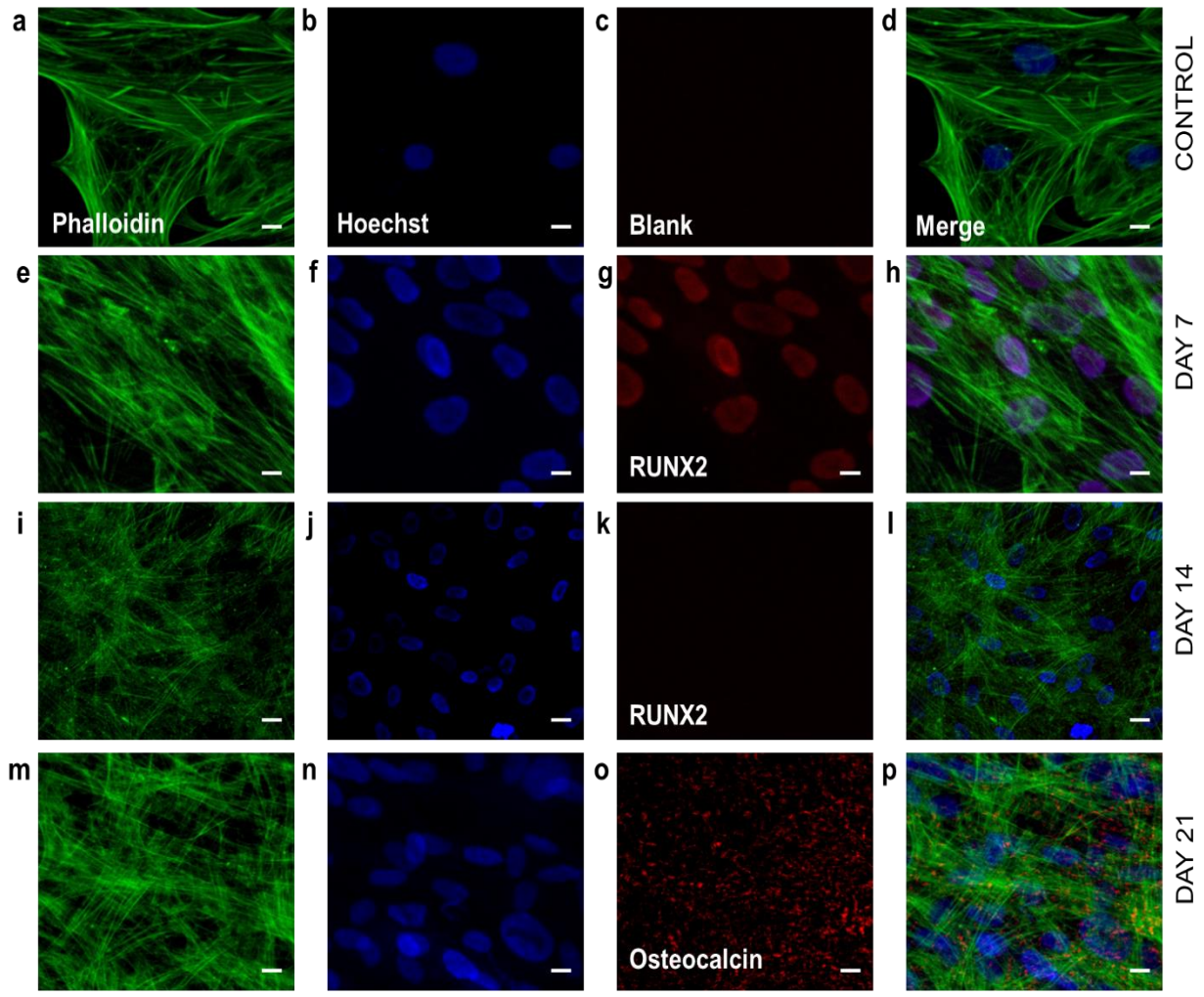

Figure 4.15. Representative immunofluorescence confocal microscope images of stem cells. Column 1 (a,e,i,m) Phalloidin; Column 2(b,f,j,n) Hoechst; Column 3 (individual as labelled); Column 4 (d,h,l,p) Merged. (a-d) Control (e-h) Day 7 osteogenic differentiated stem cells (i-l) Day 14 osteogenic differentiated stem cells (m-p) Day 21 osteogenic differentiated stem cells. Scale bar: 1 µm.

Further we also evaluated the calcium containing cells on day 21 differentiated cells by Alizarin red S Staining. Figure 4.16a, 4.16b show the representative images of osteogenic stem cells and controls acquired using a bright filed microscope at 10 X magnification.

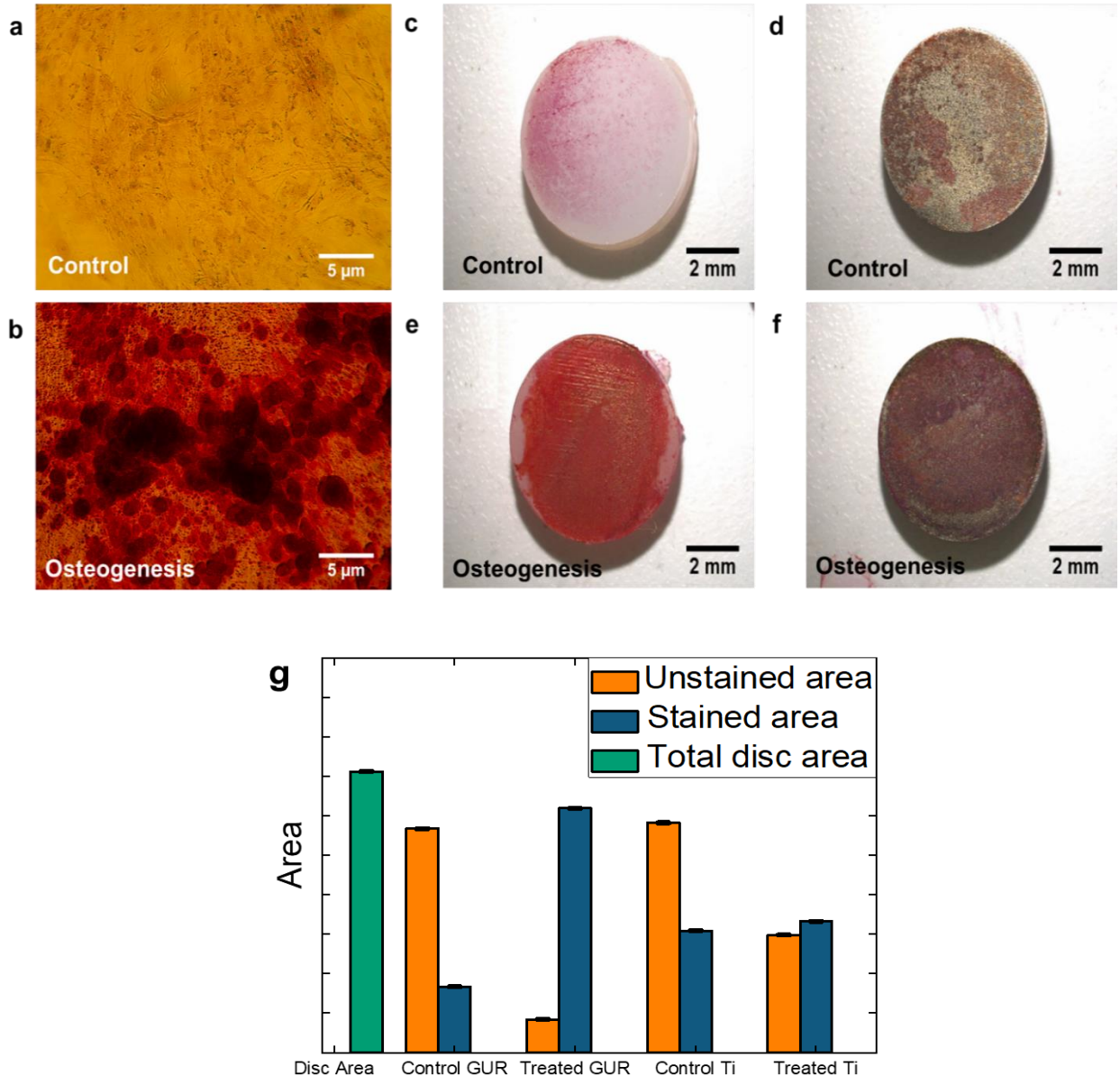

Figure 4.16. Alizarin red S Staining of Day 21 stem cells (a) Control (b) Osteogenic differentiated stem cells. Images were acquired at 10x magnification. Scale bar: 5 µm (c) Control GUR (d) Control Ti (e) Treated GUR (f) Treated Ti. Scale bar: 2 mm (g) Bar chart showing stained and unstained area for implants (c-f).

We also evaluated the osteogenic potential on the treated implants and their respective controls as shown in Figure 4.16c-16f and the respective area of Alizarin red stained and unstained area distribution calculated using ImageJ is shown in Figure 4.16g. The quantitative analysis from images acquired were done by image segmentation and thresholding using ImageJ software.

Figures 4.17 and 4.18 show the demonstration of ImageJ analysis to measure region of interest (ROI) in histological samples. From the results, it was found that the treated polymer and titanium has higher amount of calcium deposits in comparison to the non-treated ones.

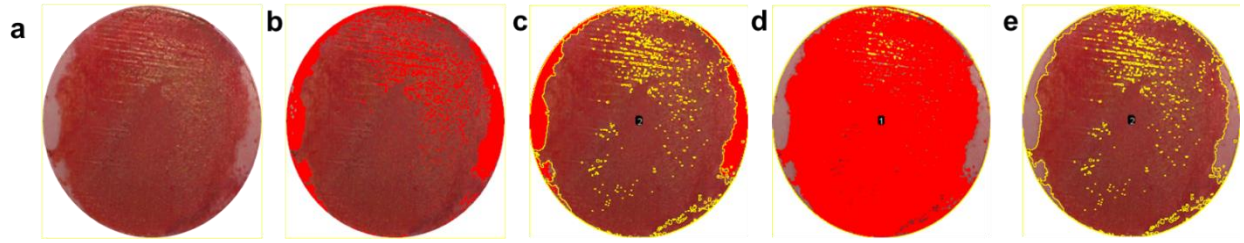

Figure 4.17. Demonstration of ImageJ to measure region of interest (ROI) in histological samples (a) Original image (b) White/Unstained area (c) Selection of White/Unstained area (d) Red/Stained area (e) Selection of Red/Stained area.

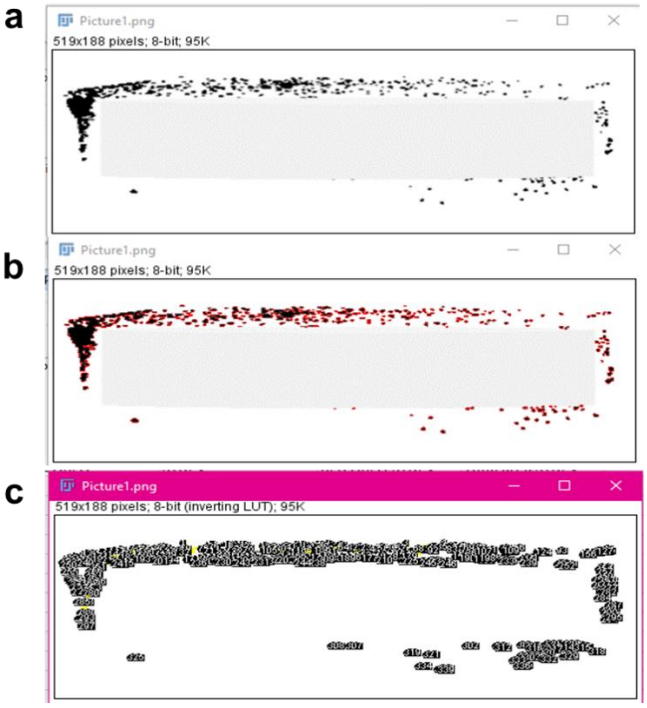

Figure 4.18. Demonstration of ImageJ to measure region of interest (ROI) (a) Original image (b) Selected area (c) Counting cells on the µCT images.

Figure 4.19a shows the schematic representation of the cell study on the implants and Figure 4.19b shows the cell viability determined based on the Live/Dead cell assay.

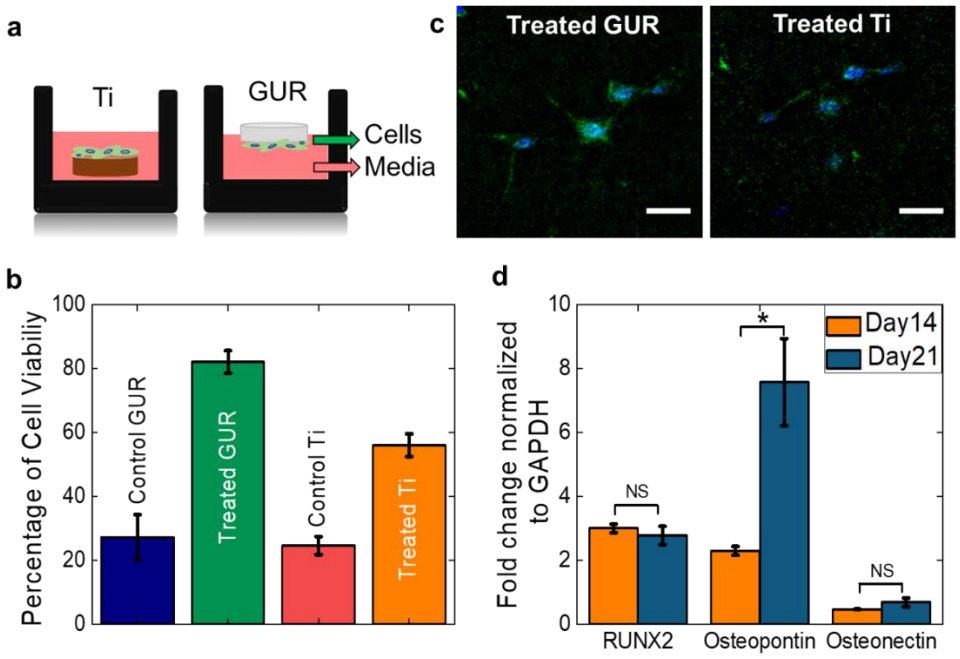

Figure 4.19. (a) Schematic representation of cell study on the implants. (b) Percentage of Cell viability on implants (c) Representative fluorescence images on treated implants. Scale bar 0.5 μm (d) qPCR Osteogenesis– expression of osteogenic genes RUNX2, Osteopontin, and Osteonectin on day 14 and 21 respectively. * indicates as ($p < 0.05$) as statistically significant. NS is not significant ($p > 0.05$).

From the results, it was observed that the percentage of viable cells after 20 mins of plasma exposure was 82 % for treated GUR and 56 % for treated Ti, whereas it was significantly lower for the control ranging from 24% to 27 % in control GUR and control Ti respectively. One tailed, paired students T-test analysis between the plasma treated groups revealed a strong statistical significance with $p<0.01$. These results can be corroborated from the physicochemical results mentioned in the characterization section, showing that plasma treatment creates a hydrophilic layer and enhances the surface properties. Additionally these results are in accordance with literature results, which support that plasma treated implants induce better cellular compatibly,(Somayajula 2008, Kubinova, Zaviskova et al. 2017) likely due to the antimicrobial NO_x generation produced by plasma treatment.(Pavlovich, Ono et al. 2014, Xu, Shen et al. 2017) Figure 4.19c, shows the representative cell images, where the actin filaments are stained green and

the nucleus is stained blue. The gene expression data as shown in Figure 4.19d further supports that the cells were differentiated into osteogenic stem cells showing the presence of RUNX2, Osteopontin, and Osteonectin genes on days 14 and 21 respectively. RUNX2 and Osteonectin were expressed in nearly same levels on day 14 and 21. Osteopontin on the other hand showed elevated gene expression with 4-fold higher gene expression on day 21 in comparison to day 14. One tailed, paired students t-test- was used to perform statistical analysis of the obtained data.

In order to show the 3D stem cell integration, X-ray μCT scans were performed after 21 days of cell culture on the surfaces. Figure 4.20 shows the μCT scan results for the control and treated polymeric and metallic substrates. Three dimensional (isometric view and side view) images as well as top surface images showed better osteogenic stem cell integration to GUR and Ti6Al4V surfaces after plasma treatment compared to untreated control surfaces. Moreover, it can be seen that plasma treated implants are covered with both a monolayer and multilayer of cells. The control untreated surfaces showed substantially less stem cell proliferation compared to treated ones.The 3D images of the top and cross-sectional constructs were in accordance with the fluorescence cell image results supporting the hypothesis of improved performance with plasma treatment.

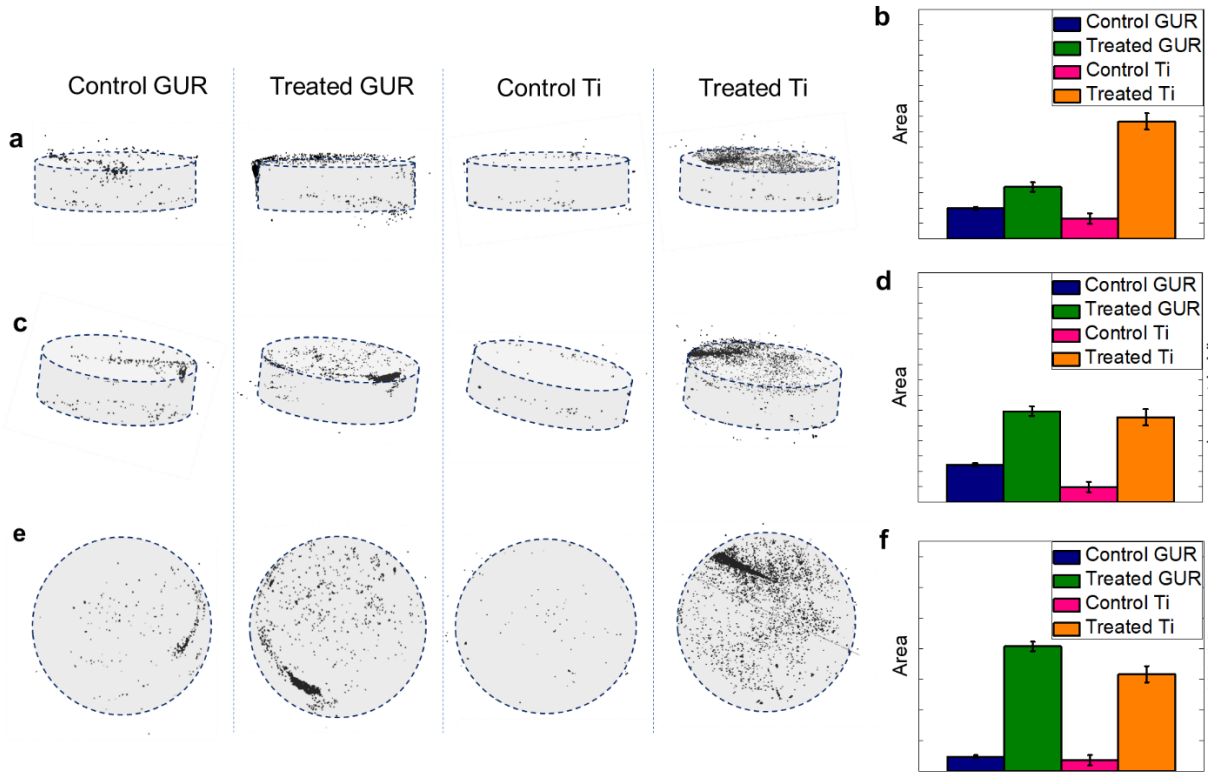

Figure 4.20. X-ray micro computed tomography (µCT) images for control and treated implants (GUR and Ti) showing better cell adhesion for treated surfaces. The gray surfaces are the implant samples, and the black dots are the cells. µCT images showing the cells covering the implants in (a) side view, (c) isometric view and (e) top view for both control and treated surfaces for GUR and Ti samples. The corresponding percentage cell coverage area are presented in (b) side view, (d) isometric view and (f) top view.

4.4. Conclusion

The effect of a novel non-thermal plasma coating (PDD) generated by a hand-held device was investigated on polyethylene and Ti6Al4V sample surfaces by utilizing contact angle measurements, microhardness, ATR-FTIR, Raman spectroscopy, XPS, XRD, tribological studies, corrosion studies and biocompatibility examination. The results showed that the hydrophilicity of both polymeric and metallic substrates increased after the plasma exposure. The formation of new oxygen species as well as an increase in crystallinity of the polymer was confirmed by FTIR and Raman spectroscopy. Furthermore, it was observed that formation of a thin oxide layer on top of

Ti6Al4V enhances the wear properties, corrosion behavior and biocompatibility of the samples. From tribological assessments, wear volume rate ratio was improved by approximately 60X after 20 min of plasma treatment in Ti6Al4V and polyethylene samples. According to biocompatibility results, the plasma treated surfaces showed better osteogenic stem cell integration as confirmed by cell viability, fluorescence and μCT imaging experiments.

Chapter 5
Raman Imaging at Biological Interfaces

5.1. Introduction

Lipids play an important role in the brain through their homeostasis to maintain the integrity of the cell membranes and control the signaling through the membranes.(Piomelli, Astarita et al. 2007, Müller, Reichel et al. 2015) Changes in brain lipids have been correlated with many neurological diseases(Chan, Oliveira et al. 2012, Prasain, Wilson et al. 2015) such as Alzheimer's disease,(Tajima, Ishikawa et al. 2013, Naudí, Cabré et al. 2015) Parkinson's disease,(Ruipérez, Darios et al. 2010, Cheng, Jenner et al. 2011) and schizophrenia.(Orešič, Seppänen-Laakso et al. 2012, Wood, Filiou et al. 2014) Structurally, brain tissues are composed of about 5-15% lipids that may account for 50% of the dry weight of the brain.(Hamilton, Hillard et al. 2007) Mass spectrometry has been the gold standard for lipidomics analysis and has been accurately applied to cells tissues and whole organisms.(Rohner, Staab et al. 2005, Seeley and Caprioli 2011, Brügger 2014, Soltwisch, Kettling et al. 2015) Most classical lipidome analysis requires extraction and homogenization of the sample, which results in a loss of spatial localization. Immunohistochemistry based methods preserve the spatial information. However, this is a targeted method, and the target lipids must be known in advance to select an appropriate antibody for staining. Also, the number of dyes available for staining the lipids are limited. Further, multiplexing is difficult with the histochemical approach. For example, only one or two antibodies can be applied simultaneously on the same sample.

This chapter was previously published as Ardalan Chaichi, Syed Mohammad Abid Hasan, Nishir Mehta, Fabrizio Donnarumma, Philip Ebenezer, Kermit K. Murray, Joseph Francis, and Manas Ranjan Gartia. "Label-free lipidome study of paraventricular thalamic nucleus (PVT) of rat brain with post-traumatic stress injury by Raman imaging." *Analyst* (2020). Reprinted by permission of Royal Society of Chemistry.

Both matrix-assisted laser desorption/ionization (MALDI) based mass spectrometry and Raman spectroscopy can alleviate many of the limitations listed above. Raman spectroscopy has additional advantages over MALDI such as Raman spectroscopy is non-destructive, and no matrix is needed. In addition, Raman spectroscopy requires minimal sample preparation. Raman spectroscopy has become a ubiquitous method for molecular level analysis of various biological samples such as brain,(Desroches, Jermyn et al. 2015, Jermyn, Mok et al. 2015, Talari, Movasaghi et al. 2015, Surmacki, Ansel-Bollepalli et al. 2017) heart,(Ohira, Tanaka et al. 2017, Timchenko, Timchenko et al. 2018, Yang, Zhao et al. 2018) kidney,(de Sousa Vieira, Bispo et al. 2016, Saatkamp, de Almeida et al. 2016, Haifler, Pence et al. 2018) lipids,(Wu, Volponi et al. 2011, Czamara, Majzner et al. 2015) and proteins(Tuma 2005, Rygula, Majzner et al. 2013, Huang, Pandey et al. 2018) due to the non-invasive and label-free nature of it. Among these, Raman spectroscopy of lipids has attracted particular attention in the field because of the strong Raman scattering of lipids provided by long nonpolar acyl chains in their structure.(Czamara, Majzner et al. 2015) It is well-established that lipids play significant role in different cellular functions such as transport in cell membranes, signaling and energy storage.(Oliveira, Chan et al. 2016) Therefore, the Raman signal obtained from the lipid bands of cells could be utilized as pathological biomarkers. Although there are similarities in the Raman spectrum of different lipids, individual lipids possesses unique spectra depending on numerous factors including geometry, phase, solubility, saturation, and polymorphism.(Kochan, Maslak et al. 2015) Lipids have Raman bands in both the fingerprint (400-1800 cm^{-1}) and higher wavenumber group frequency regions (2400–3800 cm^{-1}).(Santos, Caspers et al. 2016) The most typical characteristics of lipids which originate from hydrocarbon chains manifest themselves in 1200-1050 cm^{-1} (C-C stretch), 1250-1300 cm^{-1} (CH_3 scissor and twist) and 1400-1500 cm^{-1} (CH_2 scissor and twist) ranges.(Movasaghi, Rehman

et al. 2007) At higher wavenumbers, strong Raman bands appear in the 2800-3100 cm^{-1} region which is assigned to C-H stretching of lipids.(Czamara, Majzner et al. 2015)

Post-traumatic stress disorder (PTSD) is considered a prevalent psychiatric disorder caused by exposure to repeated or single life-threatening events such as individuals involved in traffic accidents, combat veterans and rape victims.(Bovin, Marx et al. 2016) PTSD patients relive traumatic event by sudden remembrance of traumatic memories or flashbacks originating from the extreme horror and feelings of helplessness caused by the traumatic event. People with PTSD develop psychiatric disorders and symptoms such as severe depression, substance abuse, cognitive impairments, and persistent anxiety.(De Jongh, Resick et al. 2016) Controlled biological investigations of PTSD in human subjects are mostly restricted due to ethical and logistical issues. Thus, indirect neurobiology studies on post-traumatic stress injured brains have become conventional by means of translational animal model approaches.(Ebenezer, Wilson et al. 2016, Ronzoni, del Arco et al. 2016) As a result, many studies have been carried out by exposing animals to acute or chronic stress conditions to study their physiology and behavior changes which provide valuable knowledge under conditions similar to that experienced by traumatized human subjects. Although traumatic memories can develop into PTSD, it is not the only influential factor involved in constructing an effective animal model due to multidimensional nature of this disease.(Seetharaman, Fleshner et al. 2016) Accordingly, various animal models such as predator stress, inescapable shocks, single prolonged stress, and unpredictable variable stress have been developed to ensure the occurrence of severe fear stress and production of human-like biological and behavioral symptoms in animals.(Deslauriers, Toth et al. 2018)

It is well-known that severe stress exposure negatively affects various parts of brain which are responsible for emotional responses, memory, and decision-making functions.(Shin, Rauch et

al. 2006, Levkovitz, Fenchel et al. 2015, Manjoch, Vainer et al. 2016, Cohen, Matar et al. 2018) Numerous morphological and functional deteriorations in various regions of their brain including the hippocampus, prefrontal cortex, amygdala and thalamus have been observed in animal models exposed to prolonged stress conditions.(Shin, Rauch et al. 2006, Herman and Tasker 2016) Since physiological and behavioral symptoms of PTSD in brain and their connection is crucial to thoroughly comprehending this type of disorder. However, most of the studies in this field have been directed toward the hippocampus and prefrontal cortex regions and the other parts are frequently neglected due to complexity.(Van Rooij, Kennis et al. 2015, Morey, Haswell et al. 2016, Nelson and Tumpap 2017, van Rooij, Stevens et al. 2018) The paraventricular nucleus of the thalamus (PVT) is one of the stress sensors in mammalian brains that has been recently examined for its correlation to post-traumatic stress disorders.(Penzo, Robert et al. 2015) According to recent studies,(Hsu, Kirouac et al. 2014, Kirouac 2015) both psychological and physical stressors can affect and activate this region. Meanwhile, the correlation between adaptive behavioral responses due to severe stress and PVT region of brain is still tangled. PVT is a part of the thalamic nuclei located at the midline and intralaminar region and it is commonly assumed to participate in the arousal system.(Penzo, Robert et al. 2015) According to neuroanatomical investigations,(Hsu, Kirouac et al. 2014, Kirouac 2015, Penzo, Robert et al. 2015) PVT collects autonomic and arousal projections of the brainstem and nervous system. These studies have experimentally demonstrated PVT activation by arousal and stress stimulators. Furthermore, it was recently shown that drug addiction behaviors are also associated with this region of brain.(Millan, Ong et al. 2017) In addition, substance addiction projections to the prefrontal cortex, amygdala, and nucleus accumbens are likely to originate from the PVT region.(Zhou and Zhu 2019)

Despite the large population of patients affected by PTSD worldwide, there are no available reports regarding the application of Raman spectroscopy or imaging for this type of brain disorder. In order to understand the biochemical effects of PTSD on different regions of the brain which are controlling vital functions, it is substantially important to monitor the lipid alterations in those regions.(Oliveira, Chan et al. 2016) Accordingly, novel therapeutic approaches can be developed to suppress these stress-induced changes. Recent studies illustrate the importance of stress-induced lipid metabolism analysis and their huge impact on unravelling the functions of brain regions.(Müller, Reichel et al. 2015, Réus, Abelaira et al. 2015) As a tangible example, it has been reported that prolonged stress stimulates an important lipid enzyme (phospholipase A2) which directly influences inflammatory responses by altering cellular lipid signaling.(Oliveira, Chan et al. 2015) Furthermore, stress-induced lipid modulations affect the PVT region by altering arachidonoylglycerol and diacylglycerol levels.(Herman and Tasker 2016) Additionally, ceramide level changes have also been observed in the brain due to prolonged stress conditions.(Oliveira, Chan et al. 2015)

There is a growing interest in discovering novel therapeutics for the treatment and molecular imaging methods for PTSD. We present new findings regarding the use of Raman spectroscopy imaging for measuring lipid changes in the brain. Specifically, we describe an approach for analyzing changes in the lipid levels in the PVT region of the brain tissue by obtaining 2D images of the formalin fixed brain sections from PTSD induced and control rats. We have used both unbiased PCA analysis and targeted approaches using lipid standards to identify lipid classes. We have validated the Raman imaging results with MALDI MS data. We anticipate that similar studies can be accomplished in other regions of brain to better understand the impact of stress-induced modulations on behavioral and physiological responses in PTSD.

5.2. Materials and Methods

5.2.1. Biochemicals and Reagents

To build a Raman reference library, purified lipid standards such as phosphatidylinositol (P6636-1G), phosphatidylserine (P7769-25MG), phosphatidylethanolamine (P1348-25MG), cholesteryl palmitate (C6072-1G), cholesterol (C8667-1G), galactocerebroside (C4905-10MG), glyceryl tripalmitate (T5888-1G), phosphatidic acid (P4013-100MG) and sphingomyelin (S0756-100MG) were purchased from Sigma-Aldrich (St. Louis, Missouri). Other lipids such as sulfatide (Avanti # 131305) and ganglioside (Avanti # 860053) were purchased from Avanti Polar Lipids (Alabaster, Alabama).

5.2.2. Brain Tissue Sample Preparation

Naive adult male Sprague-Dawley rats (n = 12) (Harlan Laboratories, Indianapolis, IN) weighing 325-350 g with age of 10 weeks were used for this study. The animals were fed *ad libitum* and kept under standard laboratory conditions (temperature: 20^{o}C, humidity: 23 - 42%). Alternating dark and light cycles (lasting 12 h each) was maintained. All animal handling procedures was approved by the Institutional Animal Care and Use Committee (IACUC) of the Louisiana State University School of Veterinary Medicine.

We used an acute predator exposure model(Zoladz, Fleshner et al. 2012, Wilson, Ebenezer et al. 2014, Wilson, McLaughlin et al. 2014, Ebenezer, Wilson et al. 2016, Ogundele, Ebenezer et al. 2017) to induce traumatic stress in the animal. In this model, rats were exposed periodically to a cat (adult, 7 years old, Harlan Laboratories, Indianapolis, IN) followed by rotating the rats into different cages to eliminate any social support and to induce chronic psychological stress. The experiments continued for 31 days and the rats were exposed to the cat on day 1 and day 11 for 1 h. The first exposure was performed during the daylight cycle (07:00 – 19:00), while the second

exposure was performed during the night cycle (19:00 – 07:00). Between Day 1 to Day 31, the rats were subjected to random cage rotation to make sure that no rat was housed with the same set of rats on consecutive days or more than four times within the experimental period. Also, it is important to note that during the exposure period, the cat was not allowed to touch the rats by putting the rats in Plexiglas containers. Further, during the cage rotation periods care was taken not to allow any cat or cat material near the cages. The control group (n = 6) were not subjected to exposure to cat or cage rotation and were kept in the same cages from Day 1-Day 31.

The behavioral test for anxiety was performed on all the rats using an elevated plus maze (EPM) experiment (EB-Instruments, Bioseb, Tampa Bay, FL).(Wilson, Ebenezer et al. 2014, Wilson, McLaughlin et al. 2014, Ebenezer, Wilson et al. 2016) In these experiments the rats were allowed to roam freely for 5 min. and their movement were captured using an overhead camera (BioEPM3C, EB-Instruments, Tampa Bay, FL). From the captured video, the number of entries into each arm as well as the total time spent in the open vs. closed arms were extracted. Compared with the control rats, the stressed rats avoided the open arm. The rats exposed to the cat showed a decrease in the time spent at the open arm and an increase in the time spent at the closed arm.(Zoladz, Fleshner et al. 2012, Wilson, Ebenezer et al. 2014, Wilson, McLaughlin et al. 2014, Ebenezer, Wilson et al. 2016, Ogundele, Ebenezer et al. 2017) Further, the rats developing stress were identified through a label-free *in vivo* electron paramagnetic resonance (EPR) test.(Ebenezer, Wilson et al. 2016) The stressed rats showed an elevated level of reactive oxygen species (ROS) in their brains compared to the control rats.(Ebenezer, Wilson et al. 2016)

The rats from the control and PTSD groups were humanely euthanized via inhalation of carbon dioxide. Immediately after, transcardial perfusion was performed using 10 mM phosphate-buffered saline (PBS) solution. To fix the tissue, this step was followed by transcardial perfusion

with 4% phosphate-buffered paraformaldehyde (PB-PFA) solution. We immediately harvested the whole brain using cranial dissection. The brains were cryosectioned into 40 µm thick slices that were kept in 1X PBS at 4 °C. The tissue sections containing the paraventricular nucleus of the thalamus (PVT) region were found by using the rat brain stereotaxic coordinates in the Bregma number regions of -1.20 mm to -3.6 mm (Figure 5.1).

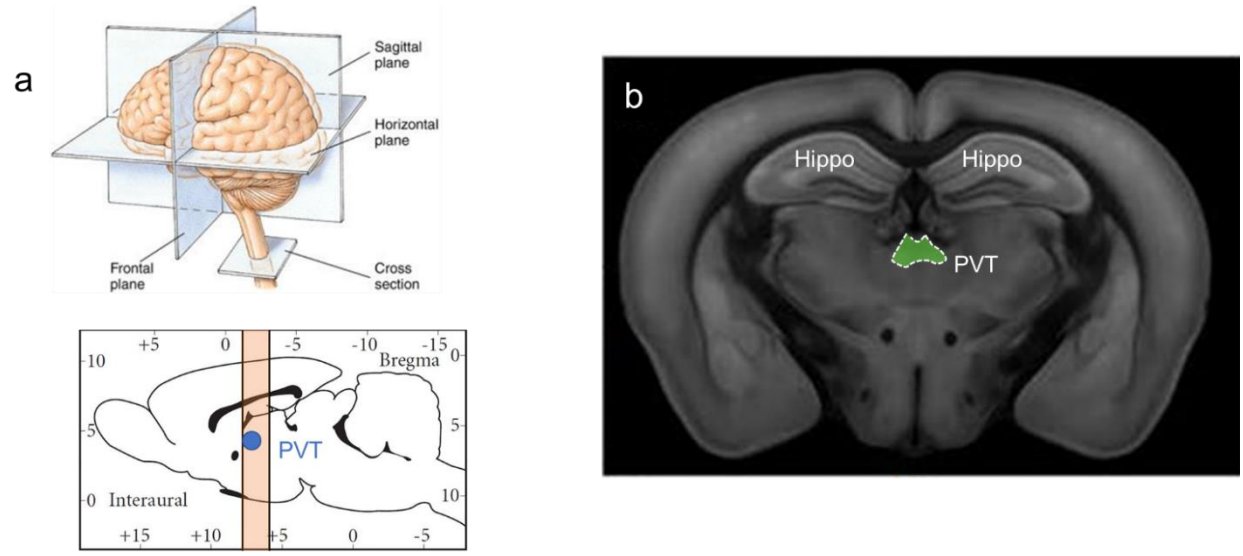

Figure 5.1. Paraventricular nucleus of the thalamus (PVT) region inside rat brain. The tissue section containing the PVT region using the rat brain stereotaxic coordinates in Bregma number region of -1.20 mm to -3.6 mm.

5.2.3. Histology

Hematoxylin and Eosin (H&E) staining protocol was followed for the histology observations. First, the nuclei were stained with alum hematoxylin. After rinsing, the samples were dipped in acidified alcohol (1 ml concentrated HCl with 400 ml 70% ethanol). Afterwards, samples were rinsed again and stained with eosin for 2 min. Finally, they were dehydrated and mounted on standard 75 mm x 25 mm microscope slides.

5.2.4. Raman Spectroscopy and Microscopy

The Raman spectra of pure lipids in powder form were obtained with a Renishaw inVia Reflex Raman Spectroscope with a 785 nm laser with an exposure time of 20 s and 100% power.

All the Raman spectra from brain samples were obtained under PBS (1X) immersion conditions with an exposure time of 10 s, step size of 20 µm, objective lens of 50X (long-working distance) and with high confocality. The machine was calibrated using the silicon peak at 520 cm^{-1}.

5.2.5. Data Processing and Statistical Analysis

All the Raman spectra were baseline corrected by Renishaw's WiRE 4.4 (Windows-based Raman Environment) software. Preprocessing of the data and the subsequent principal component analysis were performed by Origin 2018 (OriginLab, Northampton, MA). The Min-Max normalization approach was applied to the datasets and smoothing was performed by means of the Savitzky-Golay method. Direct classical least squares analysis (DCLS) method was used to generate the mapping data. ImageJ 1.8 software was used for the quantification of Raman mapping based imaging data. Figures 5.2-5.4 demonstrate the steps for quantification of the Raman maps by means of pixel intensity and distribution. Accordingly, all the images were first converted into 8-bit format. The weighted mean value of brightness (pixel value) as well as the regarding histogram data were then calculated for all the pixels in an ROI by using the "Measure" function under the "Analyze" tab of ImageJ software. This value is chosen as a representative for the relative concentration of lipids (Figures 5.2 and 5.3). A color thresholding method was used to determine the distribution of lipids. Based on the inspection of all the images, a brightness value of 111 (in order to have a good contrast) was selected as a threshold in all the images. By keeping the threshold constant, we analyzed the distribution of lipids in each Raman map (Figure 5.4).

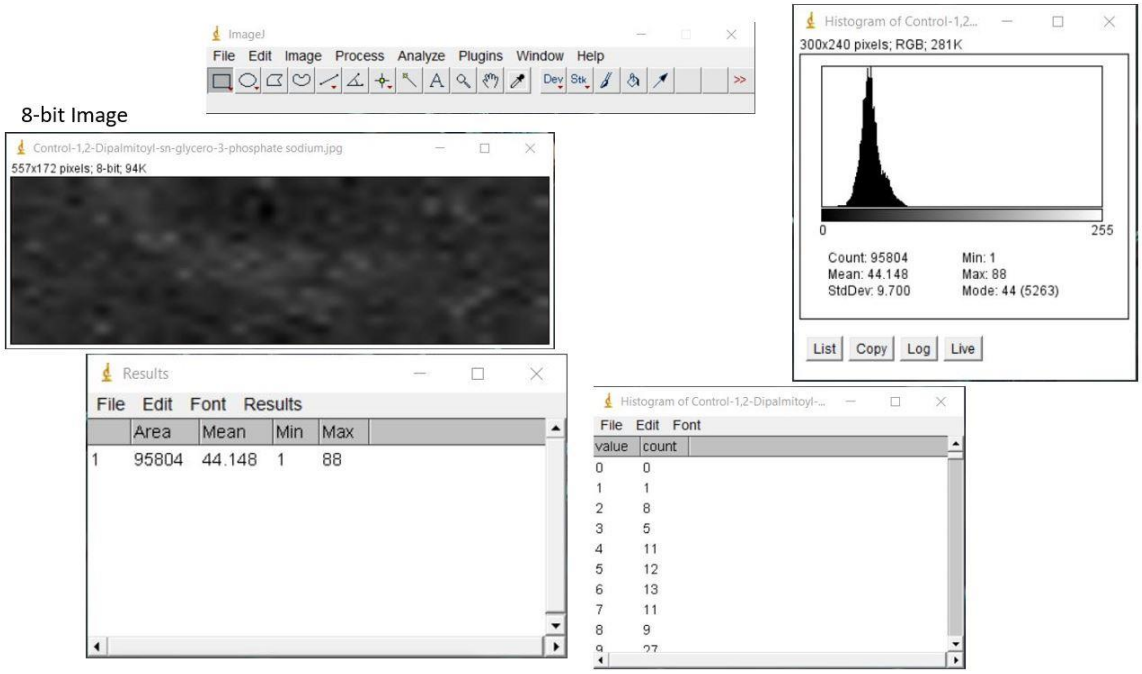

Figure 5.2. The method used for quantification of Raman maps by means of brightness intensity values. 8-bit image should be used for calculation of weighted mean value.

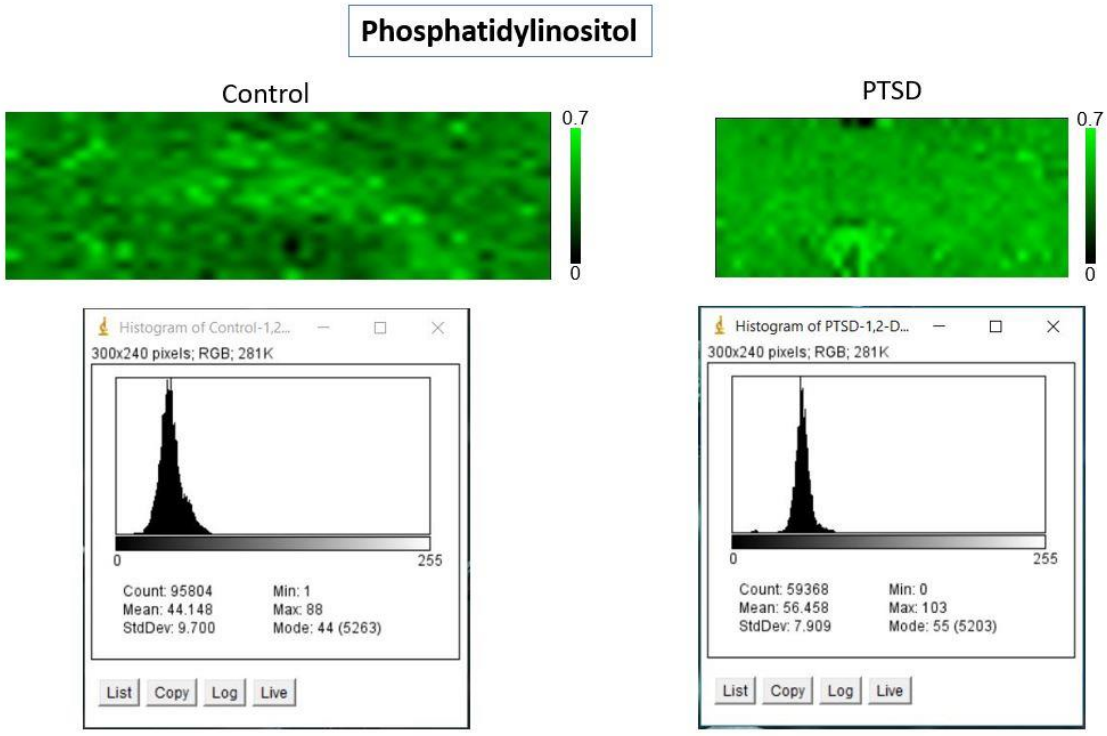

Figure 5.3. Quantification of phosphatidylinositol base on pixel value method for control and PTSD samples. Weighted mean value can be obtained from pixel values of the 8-bit image.

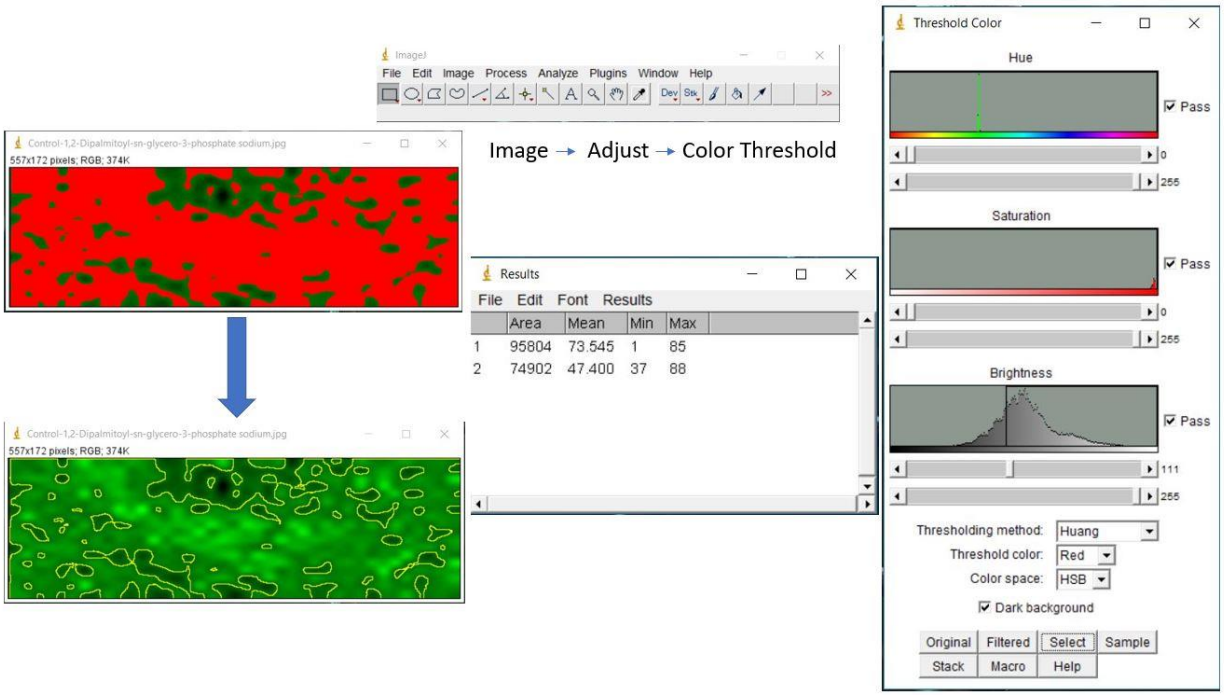

Figure 5.4. Calculating the areal distribution percentage base on thresholding method. Selected area (red) shows the region with higher pixel value than a certain threshold.

The Raman spectral data were analyzed using principal component analysis (PCA).(Molony, McIntyre et al. 2018, Ditta, Nawaz et al. 2019, Marzi, Brauchle et al. 2019, Spiers, Marzi et al. 2019) Multivariate analysis using the "Principal Component Analysis for Spectroscopy" toolbox of Origin 2018 was used to perform the PCA. The spectral differences among the data sets were described by the principal components (PC). Each of the Raman spectra is described as a point on a score plot when selecting two or more PCs. Finally, the clustering of the data on the score plot and their vibrational fingerprint assignment is obtained by the loading plot.

5.2.6. MALDI Analysis

A matrix assisted laser desorption/ionization (MALDI)-TOF/TOF mass spectrometer (UltrafleXtreme, Bruker Daltonics, Billerica, MA, USA) was utilized for mass spectrometry imaging (MSI) in positive ion mode. Brain slices were mounted on an indium tin oxide (ITO)

coated slides (UniversityWafer, Inc.). Super-DHB (Millipore-Sigma), 2, 5-dihydroxybenzoic acid (DHB, Sigma-Aldrich), and α-cyano-4-hydroxycinnamic acid (Millipore-Sigma) were used as the matrix.(Karas, Ehring et al. 1993) The matrix was prepared by dissolving super-DHB (1:1 ratio) in methanol and water solution containing 0.1 vol% of trifluoroacetic acid, to a final concentration of 10 mg/mL. Tissue sections were dried in a vacuum chamber for about 7 minutes. Afterwards, matrix was uniformly deposited on the tissue by means of pneumatic nebulizer (nitrogen gas pressure= 70 kPa; liquid flow rate= 100 μL/min). Lamp heating was used to dry the matrix on the surface of the tissue. All the MS data were smoothed by B-spline fit. A custom code, 'Decimator.vi' written in LabVIEW VI (National Instruments) was utilized for baseline subtraction, averaging, decimation, and de-noising of the obtained data. Bruker FlexAnalysis 3.0 software and MSiReader,(Robichaud, Garrard et al. 2013, Bokhart, Nazari et al. 2017) an open-source Matlab package, were employed for data analysis after baseline subtraction. Peak assignments were done by using the available databases on lipidmaps.org. MALDI images were analyzed by using the same method used for Raman images, as described above.

5.3. Results and Discussion

5.3.1. Raman Spectra for the PTSD and Control Tissue

Figure 5.5 shows an overview of this study from the animal model to output data. A predator exposure/psychosocial stress regimen was utilized to develop PTSD in the rat. For verification of PTSD induction, behavioral analysis, neurotransmitter changes, and oxidative stress analysis were performed as described in the previous study.(Ebenezer, Wilson et al. 2016)

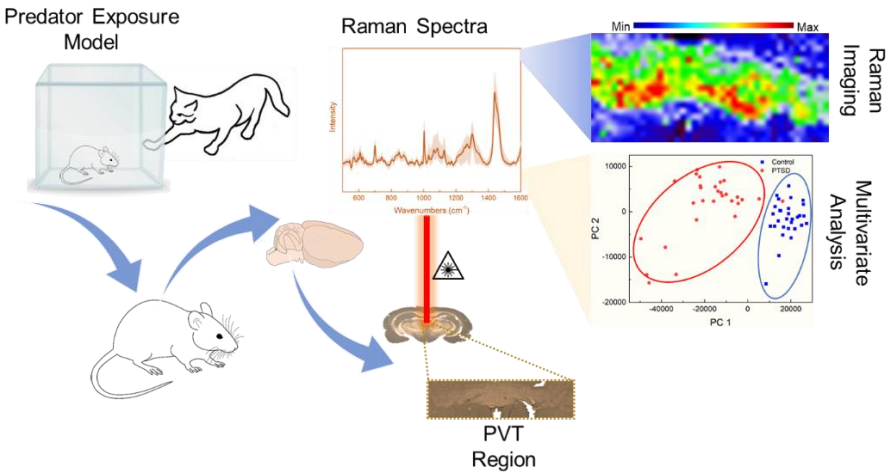

Figure 5.5. Schematic showing the design of experiment. Brain tissue from control and PTSD rats was obtained. Multivariate statistical analyses were performed on the Raman spectra and Raman images to identify the biochemical changes in the paraventricular nucleus of the thalamus (PVT) region of the brain.

In order to demonstrate the location of the PVT region in rat brain, Figure 5.6 shows H & E (Figure 5.6a, b), bright field (Figure 5.6c, d) and Raman (Figure 5.6e, f) images of the control and PTSD brain tissues.

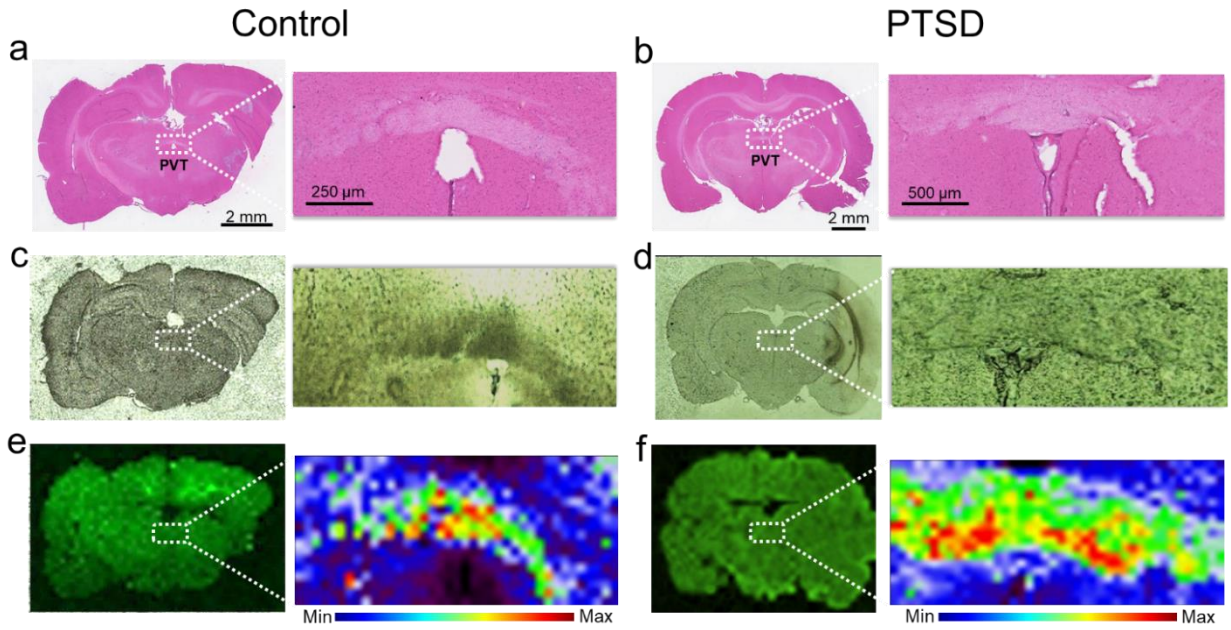

Figure 5.6. Histology and Raman imaging of brain tissues. Raman map is shown at 1002 cm^{-1} collected using a λ = 785 nm laser

Magnified PVT region is shown next to the image of full brain slice. The PVT region is visible with a white color in H & E images and a darker color in bright field images. Raman images (Figure 5.6e, f) were plotted at the peak position of 1002 cm^{-1} for control and PTSD samples. This peak is the most abundant peak in most of the biological samples. It is assigned to the aromatic ring C-C stretching mode and usually demonstrates the existence of phenylalanine amino acid.(Movasaghi, Rehman et al. 2007) Accordingly, the PVT region is distinguishable from the surrounding area due to different contrast in all the three imaging methods.

Figure 5.7a and 5.7b show the magnified view (12 X) of H & E images showing the PVT region and the different neuron cell structures inside and outside of the PVT.

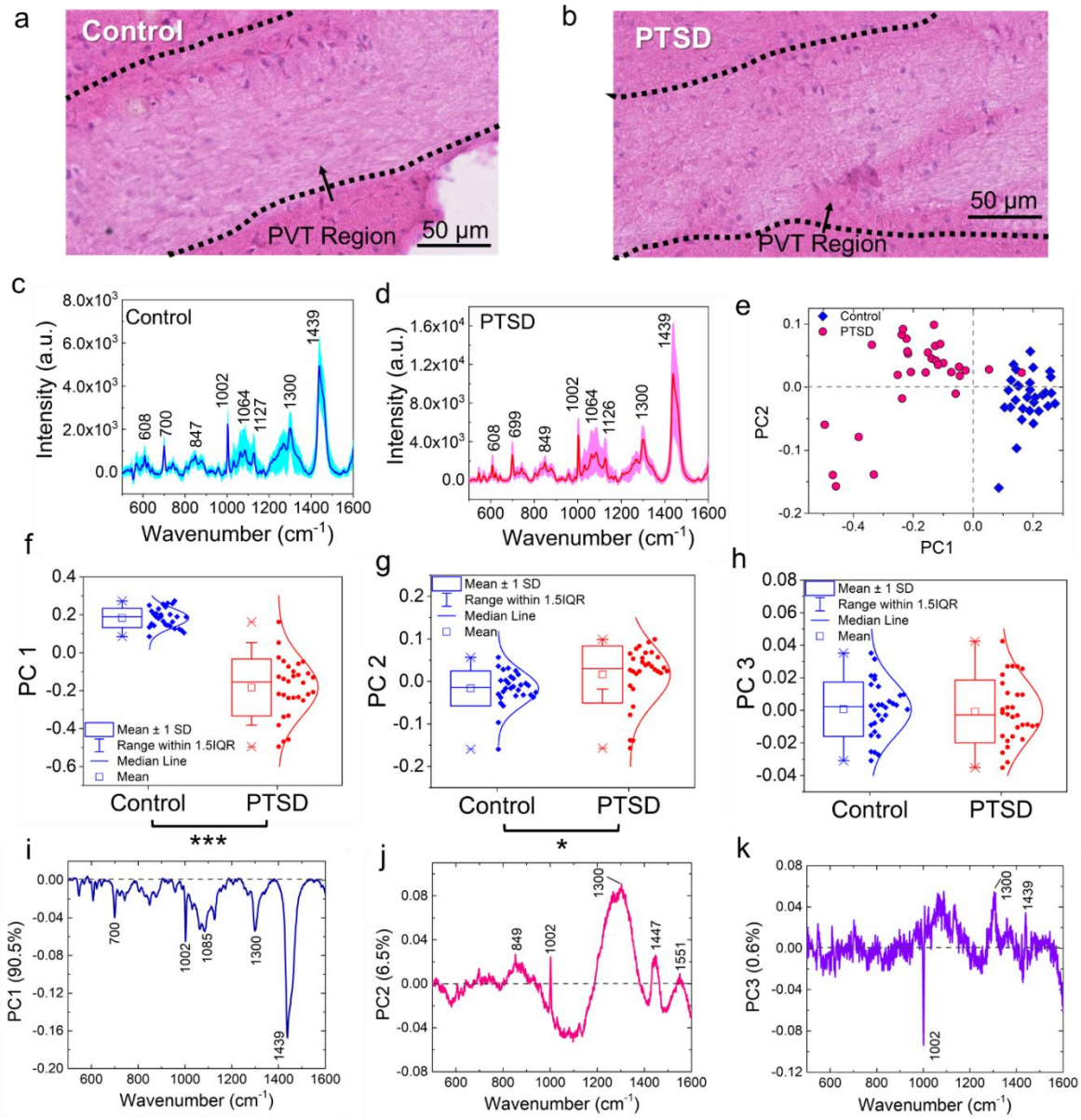

Figure 5.7. Raman spectroscopy, multivariate analysis, and associated histology images of the PVT region. Representative H&E image of the PVT region for the (a) Control, (b) PTSD rat. The corresponding mean Raman spectra of (c) Control, (d) PTSD brain tissue. The standard deviation of all the spectra is shown as shaded color for each sample. (e) PCA score plot showing the separation between PTSD and control tissue sample along PC 1. The distribution of score values for (f) PC 1, (g) PC 2, and (h) PC 3. The corresponding loading plots highlighting the significant peaks responsible for the separation in the score plot for (i) PC 1, (j) PC 2, and (k) PC 3. $*P < 0.05$, $**P < 0.01$, $***P < 0.001$, total number of spectra, n = 30.

Accordingly, no morphological change was observed in the aforementioned region. To probe the biochemical changes, Raman experiments were performed on the same region. Raman

spectra of control (Figure 5.7c) and PTSD (Figure 5.7d) samples illustrate the biochemical changes in the brain in the PVT region due to the applied stress. The diagrams are achieved by plotting 30 different spectra inside the dotted area for each sample. The average value is highlighted by darker colors for both datasets. Raman bands of the brain spectra are assigned to cholesterol (608 cm^{-1}), methionine (700 cm^{-1}), DNA/RNA (847 cm^{-1}), phenylalanine (1002 cm^{-1}), acyl chains (C-C stretch; 1064 cm^{-1}), proteins (C-N stretch; 1127 cm^{-1}), lipids (CH_2 twist; 1300 cm^{-1}), lipids (CH_2 bend; 1439 cm^{-1}).(Czamara, Majzner et al. 2015) The Raman peak positions did not change significantly in the PTSD brain samples compared to control samples (the assignment of all the Raman peaks are in Table 5.1).

Table 5.1. Peak positions of Raman spectrum for control and PTSD samples. Peak positions are mostly remained unchanged or negligibly changed.

Raman band (cm^{-1})		**Assignment**			
Control	**PTSD**	**DNA/RNA**	**Proteins**	**Lipids**	**Carbohydrates**
543	545			CE	
568	569			PI	
593	592			PS	
608	608			FC, Glycerol	
622	622	Z-DNA, dG (ν(C-C)$_{ring}$)	Phe (t(C-C))		
643	642		Stretching C-S, tyrosine twisting C-C		
700	699			Cholesterol, cholesterol ester	
725	722	Adenine base/DNA			
741	740				
761	760		Tryptophan, d (ring)		
806	804	OPO backbone stretching			
847	849		Tyrosine, C-C stretching		

(Table cont'd.)

Raman band (cm^{-1})		Assignment			
Control	**PTSD**	**DNA/RNA**	**Proteins**	**Lipids**	**Carbohydrates**
914	914				Glucose
927	926	OPO backbone stretching			
959	957			Cholesterol	
987	986		C-C		C-O ribose
1002	1002		Phenylalanine, C-C skeletal		
1031	1031		d(C-H), phenylalanine		
1064	1064	C-O stretching	C-C & C-N stretching	C-C & C-O stretching	C-C & C-O stretching, OCH in-plane deformation
1085	1084			Phospholipids	
1127	1126	C-O stretching	C-N stretching	C-C stretching	C-C & C-O stretching
1158	1156		In-plane vibrations of the conjugated C=C-C		
1173	1172		C-H bending, tyrosine		
1208	1206		Amide III		
1220	1219	(PO_2), nucleic acids			
1267	1267	RNA C-C stretching			
1300	1300			CH_2 bending	
1439	1439			CH_2 and CH_3 deformation vibrations	

However, we found a consistent modulation of Raman intensities between control and PTSD samples. Therefore, we utilized principal component analysis (PCA) method to reveal any possible biochemical changes in the PTSD brain samples. Significant changes were identified by the PCA and scatter plot that were able to discriminate both sample groups, PTSD and control.

5.3.2. Raman Fingerprint Spectra Discriminates PTSD and Control

Figure 5.7e shows the score plot from the first two principle components based on 30 spectra chosen from PTSD (pink) and control (blue) tissue samples. The score plot demonstrates a clear segregation and distinct clustering of data obtained from different sample groups. Figure 5.8 also shows the 3D view of the PCA analysis including the scatter plots from these first three PCs and it can distinguish the two sample groups as well. Figures 5.7f-5.7h show the box plot of the distribution of spectral data for the two groups. The spectral data of the PTSD samples were significantly shifted ($P < 0.001$) to the negative PC 1 range (median= -0.15) compared to control (median = 0.18; Figure 5.7f). Likewise, substantial changes ($P < 0.05$) were observed in the PC 2 (Figure 5.7g) data distribution by shifting the median value from -0.14 in the control to 0.03 in the PTSD. However, the changes in PC 3 (Figure 5.7h) were not significant ($P > 0.05$).

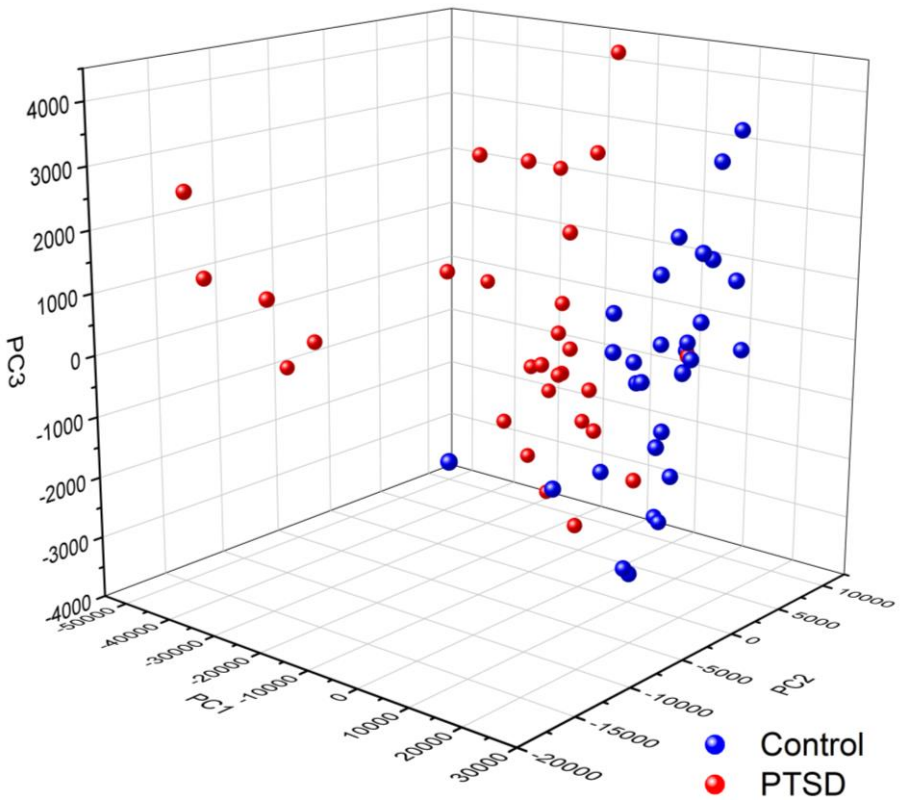

Figure 5.8. 3D view of PCA analysis. Scattered plot from the first three PCs can distinguish the two sample groups.

To find the biochemical components in each spectral variation, loading plots (Figures 5.7i, 5.7j, 5.7k) of the spectra obtained from the PVT region from PTSD and control are presented. The loading plots demonstrate the major spectral differences of the PCs. The overall contribution from the first three PCs is ~97.6 %. Characteristic peaks of each dataset are provided for PC 1, PC 2 and PC 3 (Figures 5.7i, 5.7j, 5.7k). These characteristic peaks indicate the differences in the various Raman datasets. The loading plot for PC 1 (Figure 5.7i) was obtained from PTSD and control samples and represents 90.5 % of the spectral variation includes the Raman peaks from all biomolecules types (lipids, proteins, RNA and DNA). For example, 700 (methionine C-S *trans*), 1002 (phenylalanine C-C aromatic ring stretch), 1085 (phosphodiester groups in nucleic acids), 1300 (lipid CH_2 twist) and 1438 cm^{-1} (lipid CH_2 bend) are the prominent peaks for PC 1; 849 (amino acid stretch), 1002, 1300 and 1447 (proteins and lipids CH_2 bending) cm^{-1} are the most distinctive bands for PC 2 (Figure 5.7j). Moreover, the third compound of PC (Figure 5.7k) which contains only 0.6 % of the spectral variation, can differentiate between proteins (1002 cm^{-1}, negative value) and lipids (1300 cm^{-1}, positive value). As can be seen, some of the most significant distinctive characteristics were observed in the lipid bands. As a result, a considerable change in the concentration of lipids can be derived from the Raman spectra of PTSD brain compared to the control sample. The in-depth discussion of lipid alterations is provided in the following.

5.3.3. Raman Spectroscopic Comparison of Lipids Relevant to Brain Tissue

In order to track the lipid concentration changes in the rat brain due to acute stress exposure, Raman spectra of the eleven most common lipids in brain(Wells and Dittmer 1967, Macala, Yu et al. 1983, Krafft, Neudert et al. 2005, Oliveira, Chan et al. 2016) were acquired by collecting the Raman signal from pure reference lipid samples by means of the 785 nm excitation laser. As can

be seen in Figures 5.9a-5.9e, different lipids have different Raman spectra which distinguish them from the other lipids.

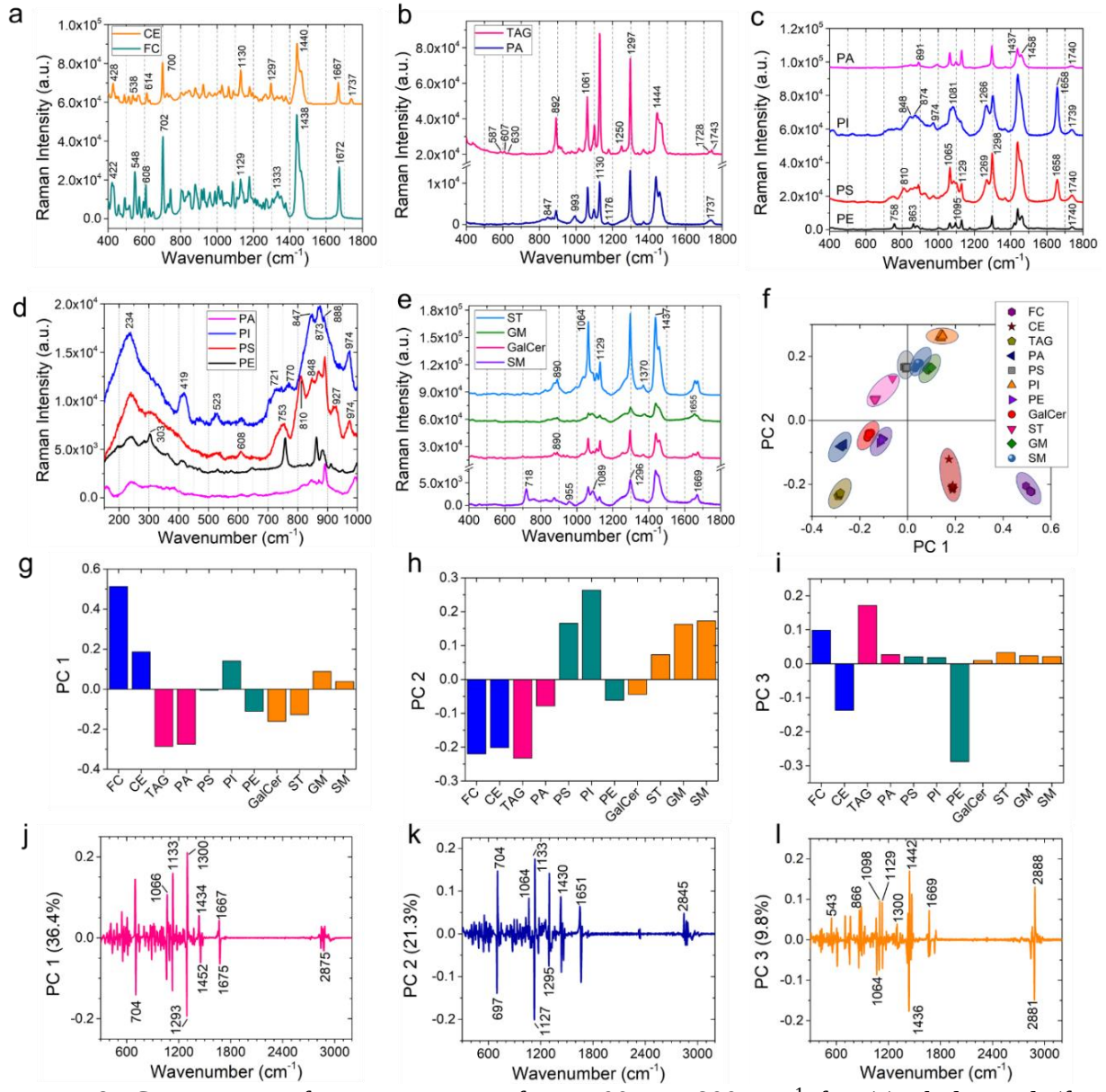

Figure 5.9. Comparison of Raman spectra from 400 to 1800 cm^{-1} for (a) cholesterol (free cholesterol, FC), and cholesteryl palmitate (cholesterol ester, CE); (b) glyceryl palmitate (triacylglyceride, TAG), and phosphatidic acid (PA); (c) phosphatidylinositol (PI), phosphatidylserine (PS), and phosphatidylethanolamine (PE); (d) the Raman spectra of phospholipids in the low wavenumber range of 200 – 1000 cm^{-1}; (e) comparison of Raman spectra from 400 to 1800 cm^{-1} for sulfatide (ST), ganglioside (GM), galactocerebroside (GalCer), and sphingomyelin (SM). (f) Multivariate analysis showing one-way PCA scatter plot of the first two principal components. (g, h, i) and (j, k, l) their corresponding loading plots are shown for PC 1, PC 2, and PC 3, respectively.

The spectral region from 400 – 1800 cm^{-1} shows the fingerprint region for each lipid. The peaks in the wavenumber region 2700 – 3500 cm^{-1} are due to the CH, and OH stretch (Figure 5.10).

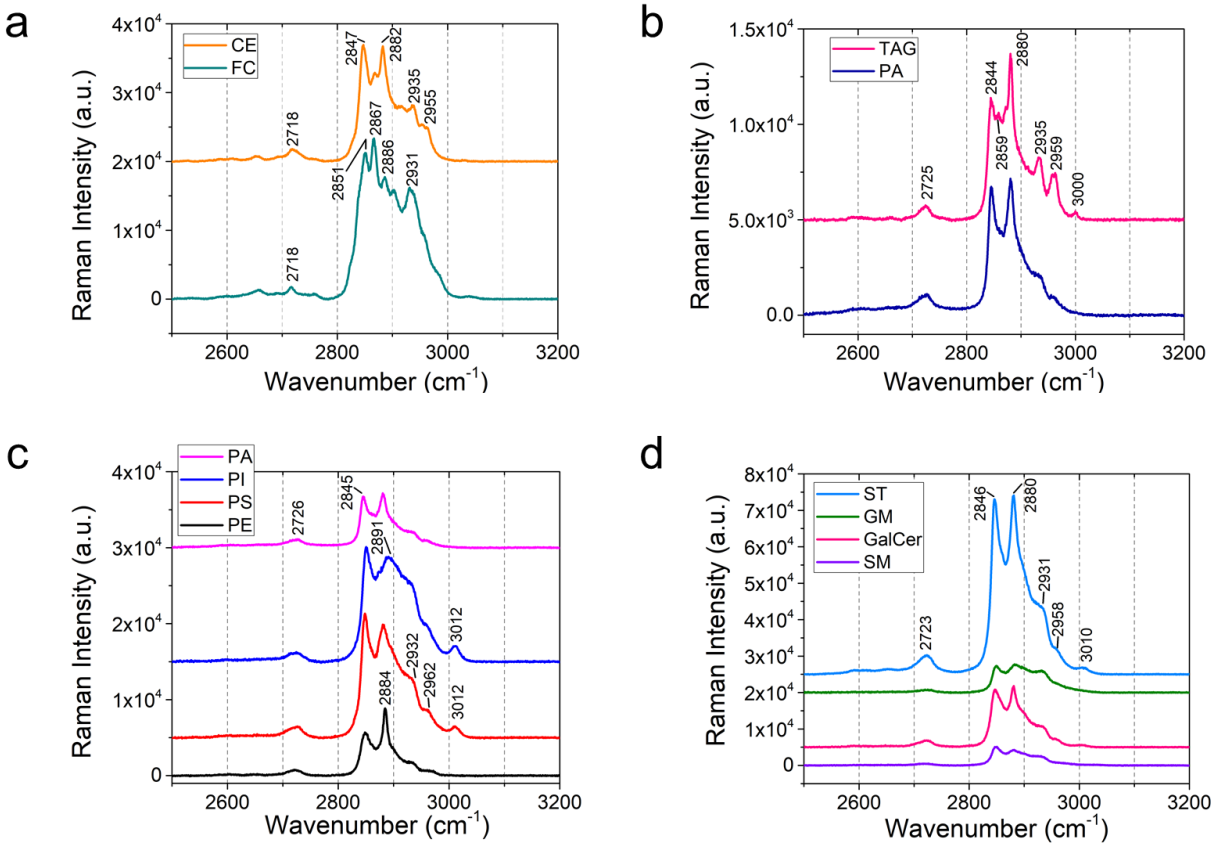

Figure 5.10. High-wavelength region of Raman spectra for different lipids. The high wavenumber region 2700 – 3500 cm^{-1} are due to the stretching vibration of CH, and OH groups.

For instance, peaks from 2845 – 2868 cm^{-1} are due to the $=CH_2$ symmetric stretch, 2870 – 2904 cm^{-1} are from the $=CH_2$ asymmetric stretch, peaks from 2905 – 2940 cm^{-1} are due to the $-CH_3$ symmetric stretch, 2941 – 2970 cm^{-1} are from the $-CH_3$ asymmetric stretch, and the Raman peaks from 3000 – 3015 cm^{-1} are due to the unsaturated =CH bond stretch.(Czamara, Majzner et al. 2015) Figure 5.9a shows the comparison of cholesterol (FC) and cholesteryl palmitate (or cholesterol ester, CE) (the molecular structure is in Figure 5.11).

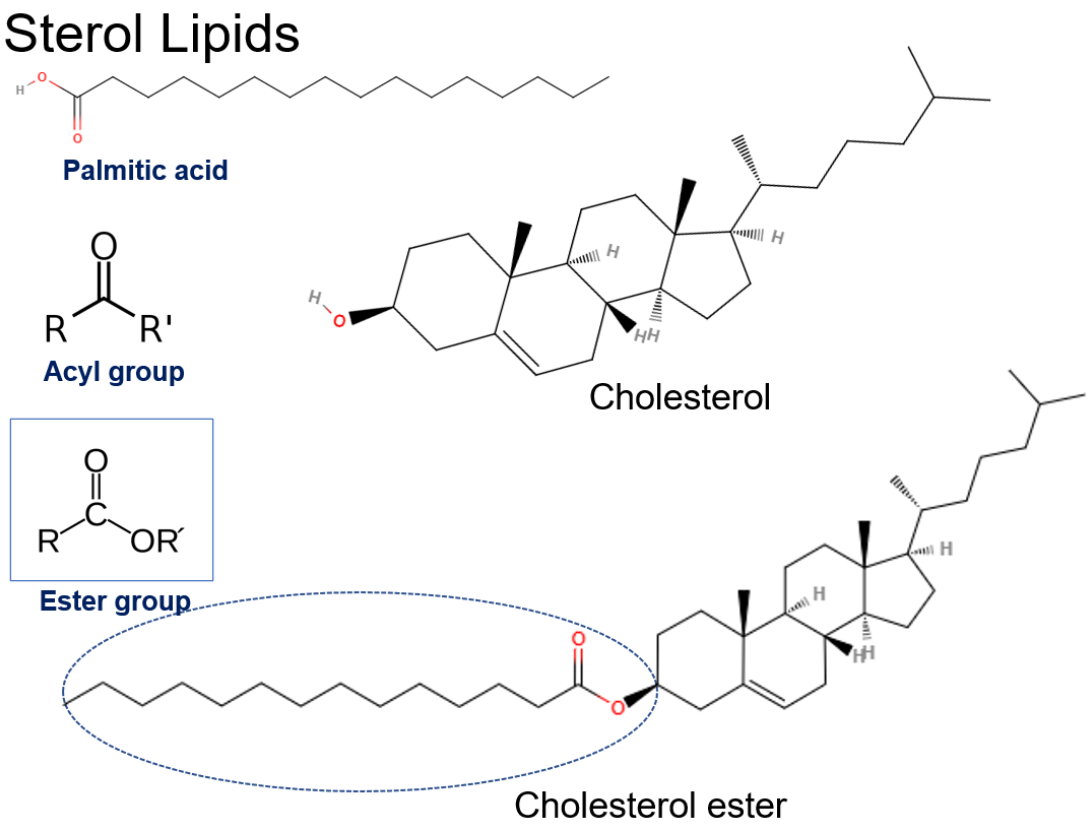

Figure 5.11. Comparison of cholesterol (FC) and cholesteryl palmitate (or cholesterol ester, CE) molecular structures. The Raman band due to ester group at 1737 cm^{-1} is absent in cholesterol. Spectral band at 1065, 1130, and 1297 cm^{-1} are due to palmitic acid group in the cholesterol ester.

The Raman band due to ester group at 1737 cm^{-1} is absent in cholesterol. Spectral band at 1065, 1130, and 1297 cm^{-1} are due to palmitic acid group in the cholesterol ester.(Krafft, Neudert et al. 2005) The intense band at 1440 cm^{-1} is due to acyl group (CH_2 or CH_3 scissor). Further, the following band shift was observed from cholesterol to cholesterol ester: 422 to 428, 548 to 538 (CH_2 bend), 608 to 614 (ester group), and 1672 to 1667 cm^{-1} (C=C stretch).

Next, Figure 5.9b compares glyceryl palmitate (or triacylglyceride, TAG) and phosphatidic acid (PA) (Figure 5.12). They share quite similar structures with one palmitic acid chain in TAG replaced by a phosphate group for PA.

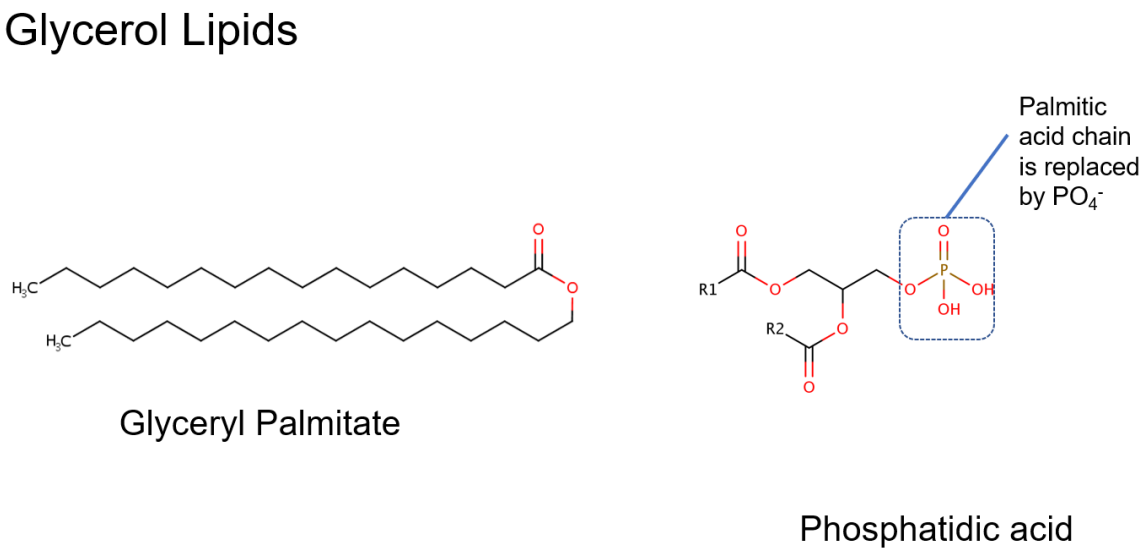

Figure 5.12. Comparison of glyceryl palmitate (or triacylglyceride, TAG) and phosphatidic acid (PA) molecular structures. They share quite similar structure with one palmitic acid chain in TAG is replaced by a phosphate group for PA.

The band due to ester group appears at 1737 cm^{-1} for PA. The ester band for TAG splits into two at 1728 and 1743 cm^{-1} indicating that they are in a different surrounding environment compared to PA. The three small bands at 587, 607, and 630 cm^{-1} are due to glycerol.(Schrader 1989) The band due to stretching of P-O vibration of PO_4 group is at 993 cm^{-1}.(Frost, Weier et al. 2004) The intense bands at 1061 (C-C stretch), 1130 (C-C stretch), 1297 (CH_2 twist), and 1444 cm^{-1} (CH_2/CH_3 scissoring) are due to fatty acid chains. Figure 5.9c, d show the comparison of different phospholipids.

Phospholipids

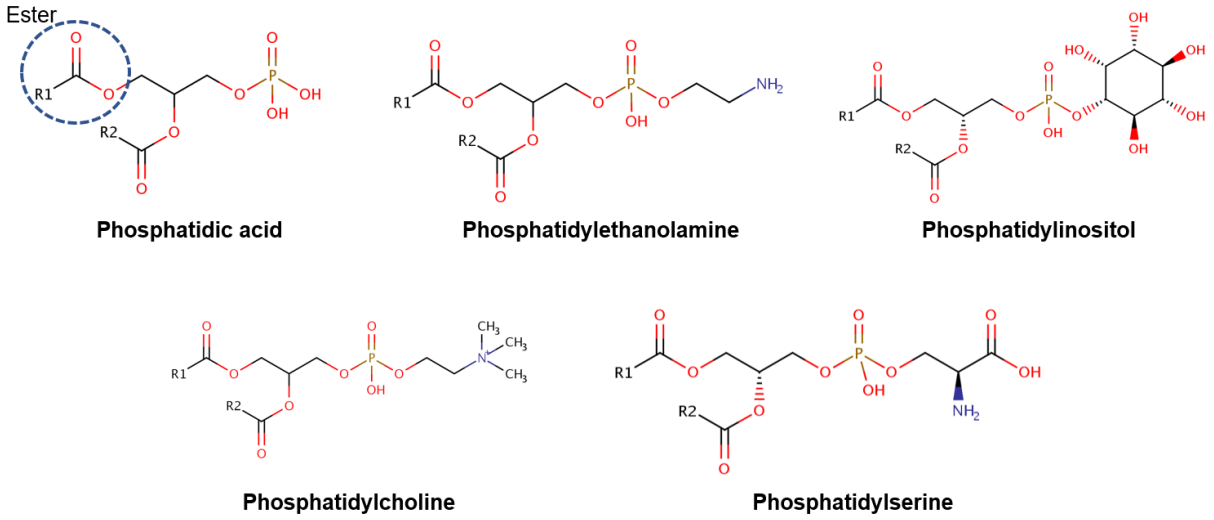

Figure 5.13. Molecular structure of different phospholipids (PE, PI, PC, PS). Raman bands of phospholipids share features similar to that of phosphatidic acid.

As shown in Figure 5.13, the parent group of phospholipids (PE, PI, PC, PS) is the phosphatidic acid (PA). Therefore, the Raman bands of phospholipids share features similar to that of phosphatidic acid. The band for phosphatidylethanolamine (PE) at 758 cm^{-1} is assigned to ethanolamine (Figure 5.9c, Figure 5.14).

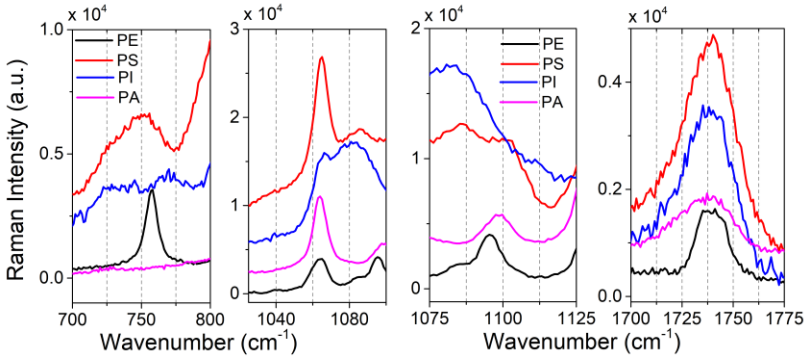

Figure 5.14. Raman Spectra of phospholipids (PE, PI, PC, PS) in the fingerprint region. The band for phosphatidylethanolamine (PE) at 758 cm^{-1} is assigned to ethanolamine. the band at 1095 cm^{-1} of the PE Raman spectrum is due to phosphodioxy groups PO_2^- (stretching of P-O bond).

Similarly, the band at 1095 cm^{-1} of the PE Raman spectrum is due to phosphodioxy groups PO_2^- (P-O stretch). At low wavenumbers between 200 -1000 cm^{-1}, distinct differences among

phospholipids were observed (Figure 5.9d). Phosphatidylinositol (PI) shows peaks at 234, 419, 523, 721, 770, 847, 873, 888, and 974 cm^{-1}; Phosphatidylserine (PS) shows peaks at 234, 524, 608, 753, 810, 848, 873, 888, 927, and 974 cm^{-1}. The PI and PS have bands at 1658 cm^{-1} (C=C stretch) which are absent in PA and PE. All the phospholipids have band for ester (1739 cm^{-1}) and acyl chains (1065, 1130, 1298, 1437 cm^{-1}; Figure 5.14).

Figure 5.9e compares the Raman spectra obtained from sphingolipids (see Figure 5.15 for the molecular structures). Sphingolipids are composed of lipids, a ceramide backbone, and glucose rings with or without linker groups; the linker group for galactocerebroside (GalCer) is galactose, sulfate containing monosaccharide for sulfatide (ST), and oligosaccharides for ganglioside (GM).

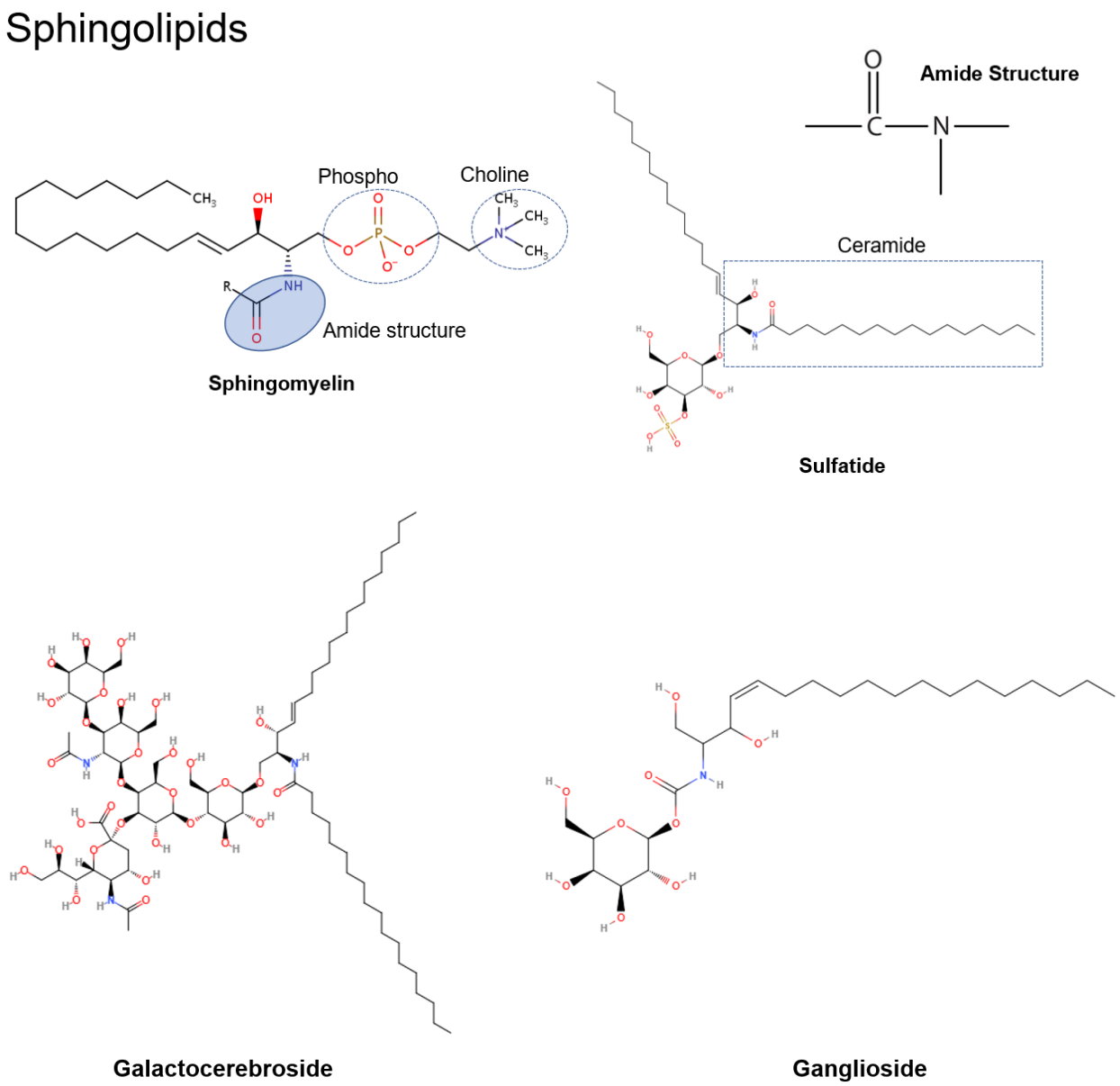

Figure 5.15. Comparison of the molecular structure of sphingolipids. Sphingolipids are composed of lipids, a ceramide backbone, and glucose rings with or without linker groups; the linker group for galactocerebroside (GalCer) is galactose, sulfate containing monosaccharide for sulfatide (ST), and oligosaccharides for ganglioside (GM).

As seen in Figure 5.15 and 5.16 (also Figure 5.9e), Raman signature of lipids (at 1064, 1129, 1298, 1437 cm^{-1}), ceramide backbone (1657, 1671 cm^{-1}; C=C stretch), and sugar chain (1370 cm^{-1}; Figure 5.16) is clearly present. Figure 5.16 also shows that the area under the peak at 1370 cm^{-1} is the highest for ganglioside (GM) and lowest for sphingomyelin (SM).

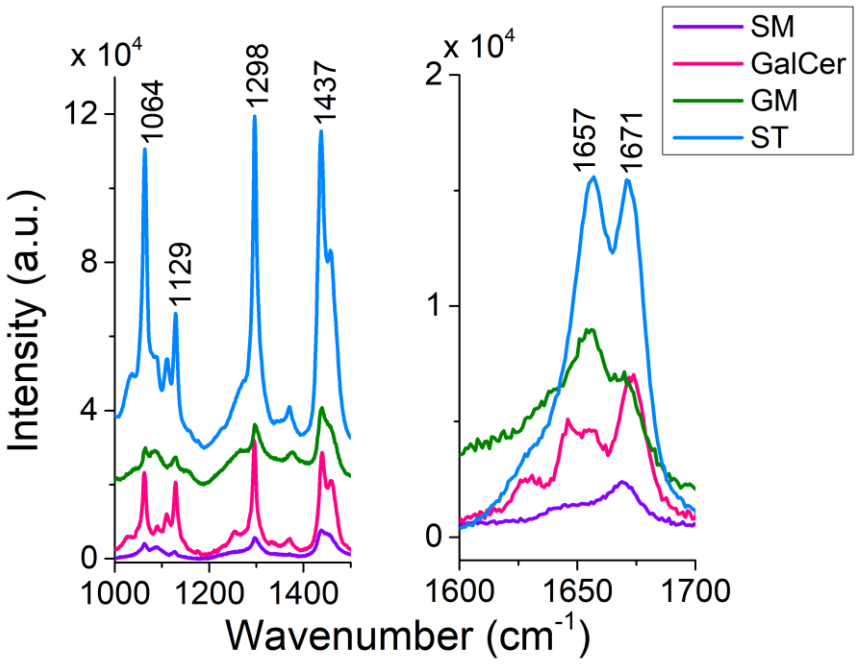

Figure 5.16. Raman spectra of sphingolipids at fingerprint region. Raman signature of lipids (at 1064, 1129, 1298, 1437 cm^{-1}), ceramide backbone (1657, 1671 cm^{-1}; C=C stretching), and sugar chain (1370 cm^{-1}).

This agrees well with the molecular structure of GM, which has the maximum saccharide content (Figure 5.15) and that of SM, which has no glucose group. Further, we observed that the peak ratio of 1370 (sugar chain) to 1297 cm^{-1} (fatty acid) is the highest for GM. The Raman peak at 890 cm^{-1} (C-O-O skeletal mode) is present in all the sphingolipids except SM as SM does not have any C-O-O group (Figure 5.17). The sulfate band in ST is characterized by 614 and 995 cm^{-1} (Figure 5.18).(Ben Mabrouk, Kauffmann et al. 2013) Finally, sphingomyelin is composed of a phosphatidylcholine (PC) residue, which is characterized by Raman peaks at 718 and 875 cm^{-1} (Figure 5.9e, 5.19). Another key difference between the backbone of phospholipids and ceramide structure is the amide bond (1669 cm^{-1}; Figure 5.9e, 5.19) in the ceramide backbone instead of the ester band (1739 cm^{-1}) of phospholipids.

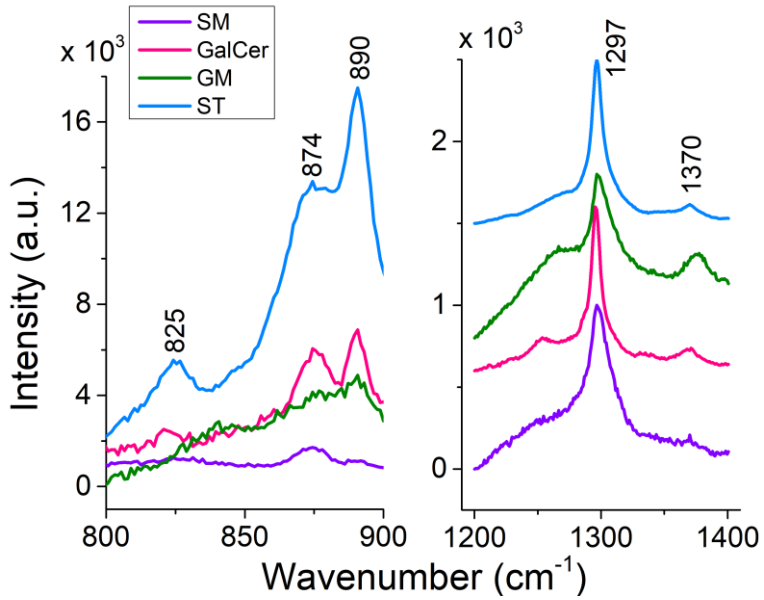

Figure 5.17. Raman spectra of sphingolipids at fingerprint region. The Raman peak at 890 cm^{-1} (C-O-O skeletal) mode is present in all the sphingolipids except SM as SM does not have any C-O-O group.

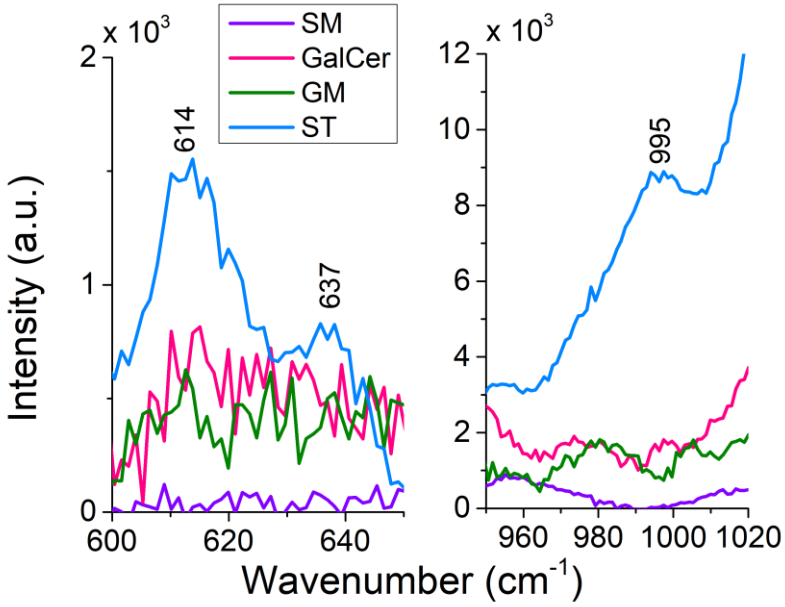

Figure 5.18. Raman spectra of sphingolipids at fingerprint region. The sulfate band in ST is characterized by 614 and 995 cm^{-1}.

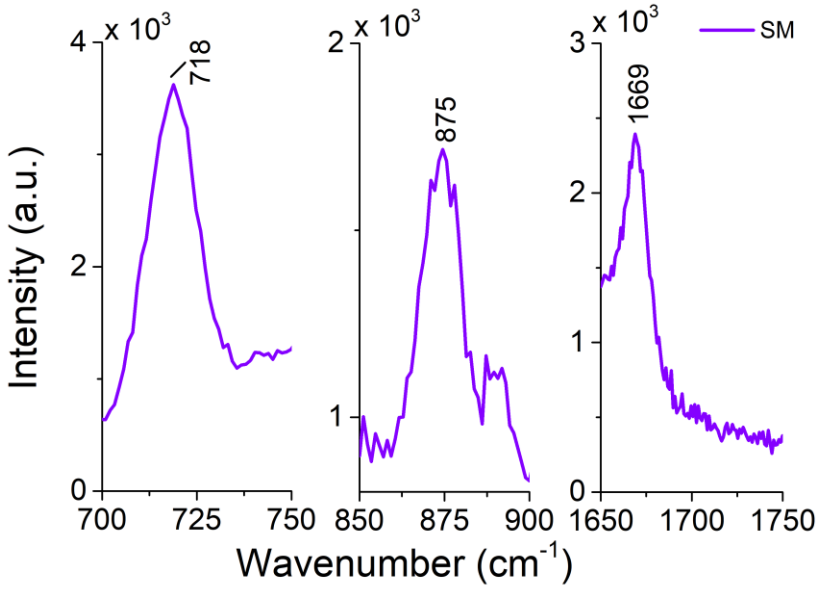

Figure 5.19. Raman spectrum of sphingomyelin. Sphingomyelin is composed of a phosphatidylcholine (PC) residue, which is characterized by Raman peaks at 718 and 875 cm^{-1}.

Further, we utilized one-way multivariate statistical analysis coupled with the PCA approach to separate different populations of lipids. PCA analysis was performed on the 11 most common lipids found in brain tissue. Figure 5.9f represents the PCA scatterplot results obtained from the first-derivative of the Raman data in various data sets of lipid spectra. The 95% confidence ellipse of the clustered group PCA distribution is also shown in the plots. The PCA analysis of the raw data did not cluster different classes of lipids separately and overlap among classes can be seen (Figure 5.20a). However, after normalization, smoothing, and taking the 1st derivative of the data, considerable separation among different lipid clusters was observed in the PCA results (Figure 5.20b-d). Meanwhile, the second-derivative did not further improve separation of lipid clusters. Therefore, it can be concluded that the first-derivative provides the best PCA results for our data set (Figure 5.9f).

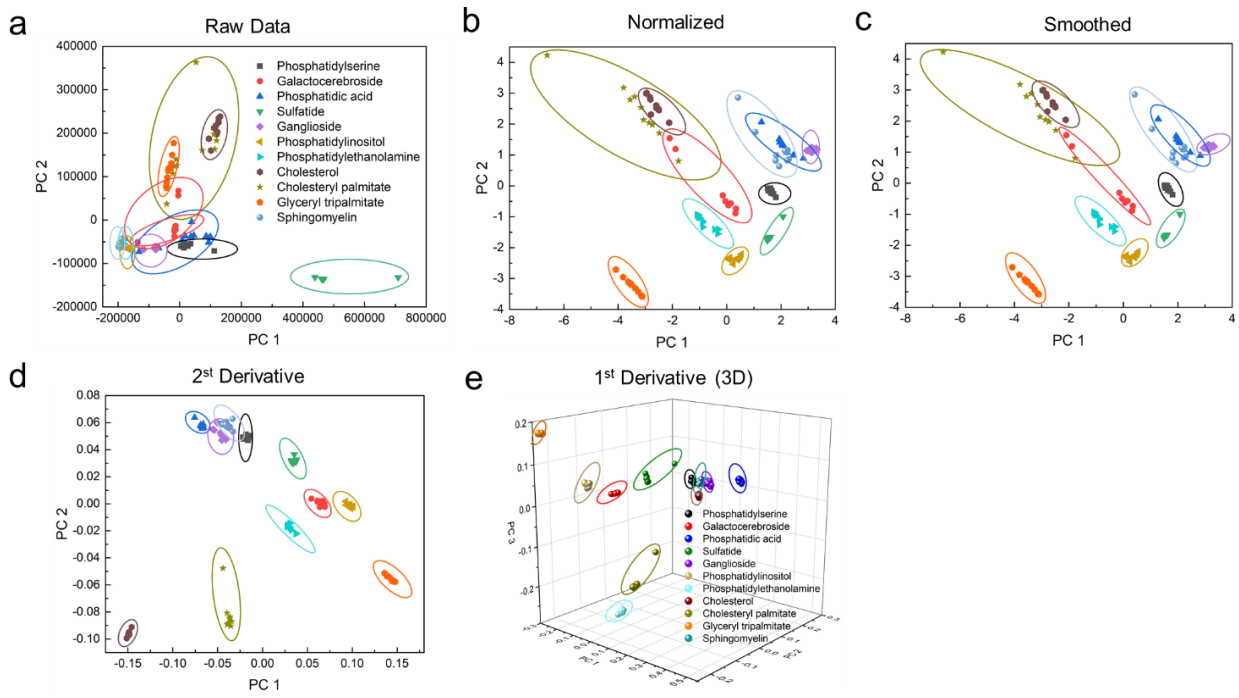

Figure 5.20. PCA analysis of the most common lipids in brain tissue for (a) raw data, (b) normalized data, (c) smoothed data and (d, e) derivatives of data. PCA analysis on raw data does not distinguish the lipids very well. Meanwhile, after normalization, smoothing and taking the derivatives of the data, a well distinguishability is observed in the PCA results.

To include more variance among the data sets, PC 3 of the first-derivative was also calculated to plot the 3D PCA result (Figure 5.20e). Figures 5.9g-5.9i show the PC values of first-derivative for different lipids. Each bar shows the mean value of the data. By performing ANOVA on the PC 1 data set, it can be seen that the PC 1 value for every lipid is significantly different ($P< 0.001$) from the other lipids (see Table 5.2). Similarly, the same significant difference ($P< 0.001$) was also observed for PC 2 data set except for phosphatidylserine vs. sphingomyelin, phosphatidylserine vs. ganglioside, and ganglioside vs. sphingomyelin (see Table 5.2). Furthermore, the PC 3 data also showed significant differences ($P< 0.001$) for most of the lipids (see Table 5.2). The corresponding loading plots of PC 1, PC 2, and PC 3 show the major peaks responsible for the clustering of the data set (Figure 5.9j, 5.9k, 5.9l). The percentage variance described by PC 1, PC 2, and PC 3 was 36.4%, 21.3%, and 9.8%, respectively. Analysis of the

loading plots showed that the prominent Raman peaks of the lipids show the most variance at 704 (characteristic band for cholesterol), 1133 (acyl chain, palmitic and fatty acids), 1300 (lipid CH_2 twist mode) and 1293 (methylene) cm^{-1} peak positions. As a result, it can be concluded that Raman spectra of the most abundant lipids in the brain are statistically different from each other. Therefore, we can use statistical methods to compare the lipid concentration in control and PTSD samples.

Table 5.2. ANOVA with Levene test for Homoscedasticity for the Raman spectra of the lipids.

Comparisons significant at the 0.001 level are indicated by *.**				
Lipid Comparison	**Difference Between Means**	**95% Confidence Limits**		
Glyceryl tripalmit - Cholesterol	0.073252	0.066209	0.080294	***
Glyceryl tripalmit - Sulfatide	0.138848	0.131805	0.145891	***
Glyceryl tripalmit - Phosphatidic acid	0.145274	0.138231	0.152317	***
Glyceryl tripalmit - Ganglioside	0.148326	0.141284	0.155369	***
Glyceryl tripalmit - Sphingomyelin	0.150536	0.143493	0.157579	***
Glyceryl tripalmit - Phosphatidylserine	0.151309	0.144266	0.158352	***
Glyceryl tripalmit - Phosphatidylinosit	0.153514	0.146471	0.160557	***
Glyceryl tripalmit - Galactocerebroside	0.161893	0.154850	0.168936	***
Glyceryl tripalmit - Cholesteryl palmit	0.308696	0.301653	0.315739	***
Glyceryl tripalmit - Phosphatidylethano	0.459798	0.452755	0.466841	***
Cholesterol - Glyceryl tripalmit	-0.073252	-0.080294	-0.066209	***
Cholesterol - Sulfatide	0.065596	0.058554	0.072639	***
Cholesterol - Phosphatidic acid	0.072022	0.064980	0.079065	***
Cholesterol - Ganglioside	0.075075	0.068032	0.082117	***
Cholesterol - Sphingomyelin	0.077284	0.070242	0.084327	***
Cholesterol - Phosphatidylserine	0.078057	0.071015	0.085100	***
Cholesterol - Phosphatidylinosit	0.080262	0.073219	0.087305	***

(Table cont'd.)

Comparisons significant at the 0.001 level are indicated by ***.				
Lipid Comparison	**Difference Between Means**	**95% Confidence Limits**		
Cholesterol - Galactocerebroside	0.088641	0.081599	0.095684	***
Cholesterol - Cholesteryl palmit	0.235444	0.228401	0.242487	***
Cholesterol - Phosphatidylethano	0.386546	0.379504	0.393589	***
Sulfatide - Glyceryl tripalmit	-0.138848	-0.145891	-0.131805	***
Sulfatide - Cholesterol	-0.065596	-0.072639	-0.058554	***
Sulfatide - Phosphatidic acid	0.006426	-0.000617	0.013469	
Sulfatide - Ganglioside	0.009478	0.002436	0.016521	***
Sulfatide - Sphingomyelin	0.011688	0.004645	0.018731	***
Sulfatide - Phosphatidylserine	0.012461	0.005418	0.019504	***
Sulfatide - Phosphatidylinosit	0.014666	0.007623	0.021709	***
Sulfatide - Galactocerebroside	0.023045	0.016002	0.030088	***
Sulfatide - Cholesteryl palmit	0.169848	0.162805	0.176891	***
Sulfatide - Phosphatidylethano	0.320950	0.313907	0.327993	***
Phosphatidic acid - Glyceryl tripalmit	-0.145274	-0.152317	-0.138231	***
Phosphatidic acid - Cholesterol	-0.072022	-0.079065	-0.064980	***
Phosphatidic acid - Sulfatide	-0.006426	-0.013469	0.000617	
Phosphatidic acid - Ganglioside	0.003052	-0.003990	0.010095	
Phosphatidic acid - Sphingomyelin	0.005262	-0.001781	0.012305	
Phosphatidic acid - Phosphatidylserine	0.006035	-0.001008	0.013078	
Phosphatidic acid - Phosphatidylinosit	0.008240	0.001197	0.015283	***
Phosphatidic acid - Galactocerebroside	0.016619	0.009576	0.023662	***
Phosphatidic acid - Cholesteryl palmit	0.163422	0.156379	0.170465	***
Phosphatidic acid - Phosphatidylethano	0.314524	0.307481	0.321567	***
Ganglioside - Glyceryl tripalmit	-0.148326	-0.155369	-0.141284	***
Ganglioside - Cholesterol	-0.075075	-0.082117	-0.068032	***
Ganglioside - Sulfatide	-0.009478	-0.016521	-0.002436	***

(Table cont'd.)

Comparisons significant at the 0.001 level are indicated by ***.				
Lipid Comparison	**Difference Between Means**	**95% Confidence Limits**		
Ganglioside - Phosphatidic acid	-0.003052	-0.010095	0.003990	
Ganglioside - Sphingomyelin	0.002210	-0.004833	0.009252	
Ganglioside - Phosphatidylserine	0.002983	-0.004060	0.010025	
Ganglioside - Phosphatidylinosit	0.005188	-0.001855	0.012230	
Ganglioside - Galactocerebroside	0.013567	0.006524	0.020610	***
Ganglioside - Cholesteryl palmit	0.160370	0.153327	0.167412	***
Ganglioside - Phosphatidylethano	0.311472	0.304429	0.318515	***
Sphingomyelin - Glyceryl tripalmit	-0.150536	-0.157579	-0.143493	***
Sphingomyelin - Cholesterol	-0.077284	-0.084327	-0.070242	***
Sphingomyelin - Sulfatide	-0.011688	-0.018731	-0.004645	***
Sphingomyelin - Phosphatidic acid	-0.005262	-0.012305	0.001781	
Sphingomyelin - Ganglioside	-0.002210	-0.009252	0.004833	
Sphingomyelin - Phosphatidylserine	0.000773	-0.006270	0.007816	
Sphingomyelin - Phosphatidylinosit	0.002978	-0.004065	0.010021	
Sphingomyelin - Galactocerebroside	0.011357	0.004314	0.018400	***
Sphingomyelin - Cholesteryl palmit	0.158160	0.151117	0.165203	***
Sphingomyelin - Phosphatidylethano	0.309262	0.302219	0.316305	***
Phosphatidylserine - Glyceryl tripalmit	-0.151309	-0.158352	-0.144266	***
Phosphatidylserine - Cholesterol	-0.078057	-0.085100	-0.071015	***
Phosphatidylserine - Sulfatide	-0.012461	-0.019504	-0.005418	***
Phosphatidylserine - Phosphatidic acid	-0.006035	-0.013078	0.001008	
Phosphatidylserine - Ganglioside	-0.002983	-0.010025	0.004060	
Phosphatidylserine - Sphingomyelin	-0.000773	-0.007816	0.006270	
Phosphatidylserine - Phosphatidylinosit	0.002205	-0.004838	0.009248	
Phosphatidylserine - Galactocerebroside	0.010584	0.003541	0.017627	***
Phosphatidylserine - Cholesteryl palmit	0.157387	0.150344	0.164430	***

(Table cont'd.)

Comparisons significant at the 0.001 level are indicated by ***.				
Lipid Comparison	**Difference Between Means**	**95% Confidence Limits**		
Phosphatidylserine - Phosphatidylethano	0.308489	0.301446	0.315532	***
Phosphatidylinosit - Glyceryl tripalmit	-0.153514	-0.160557	-0.146471	***
Phosphatidylinosit - Cholesterol	-0.080262	-0.087305	-0.073219	***
Phosphatidylinosit - Sulfatide	-0.014666	-0.021709	-0.007623	***
Phosphatidylinosit - Phosphatidic acid	-0.008240	-0.015283	-0.001197	***
Phosphatidylinosit - Ganglioside	-0.005188	-0.012230	0.001855	
Phosphatidylinosit - Sphingomyelin	-0.002978	-0.010021	0.004065	
Phosphatidylinosit - Phosphatidylserine	-0.002205	-0.009248	0.004838	
Phosphatidylinosit - Galactocerebroside	0.008379	0.001337	0.015422	***
Phosphatidylinosit - Cholesteryl palmit	0.155182	0.148139	0.162225	***
Phosphatidylinosit - Phosphatidylethano	0.306284	0.299242	0.313327	***
Galactocerebroside - Glyceryl tripalmit	-0.161893	-0.168936	-0.154850	***
Galactocerebroside - Cholesterol	-0.088641	-0.095684	-0.081599	***
Galactocerebroside - Sulfatide	-0.023045	-0.030088	-0.016002	***
Galactocerebroside - Phosphatidic acid	-0.016619	-0.023662	-0.009576	***
Galactocerebroside - Ganglioside	-0.013567	-0.020610	-0.006524	***
Galactocerebroside - Sphingomyelin	-0.011357	-0.018400	-0.004314	***
Galactocerebroside - Phosphatidylserine	-0.010584	-0.017627	-0.003541	***
Galactocerebroside - Phosphatidylinosit	-0.008379	-0.015422	-0.001337	***
Galactocerebroside - Cholesteryl palmit	0.146803	0.139760	0.153845	***
Galactocerebroside - Phosphatidylethano	0.297905	0.290862	0.304948	***
Cholesteryl palmit - Glyceryl tripalmit	-0.308696	-0.315739	-0.301653	***
Cholesteryl palmit - Cholesterol	-0.235444	-0.242487	-0.228401	***
Cholesteryl palmit - Sulfatide	-0.169848	-0.176891	-0.162805	***
Cholesteryl palmit - Phosphatidic acid	-0.163422	-0.170465	-0.156379	***
Cholesteryl palmit - Ganglioside	-0.160370	-0.167412	-0.153327	***

(Table cont'd.)

Comparisons significant at the 0.001 level are indicated by ***.				
Lipid Comparison	**Difference Between Means**	**95% Confidence Limits**		
Cholesteryl palmit - Sphingomyelin	-0.158160	-0.165203	-0.151117	***
Cholesteryl palmit - Phosphatidylserine	-0.157387	-0.164430	-0.150344	***
Cholesteryl palmit - Phosphatidylinosit	-0.155182	-0.162225	-0.148139	***
Cholesteryl palmit - Galactocerebroside	-0.146803	-0.153845	-0.139760	***
Cholesteryl palmit - Phosphatidylethano	0.151102	0.144060	0.158145	***
Phosphatidylethano - Glyceryl tripalmit	-0.459798	-0.466841	-0.452755	***
Phosphatidylethano - Cholesterol	-0.386546	-0.393589	-0.379504	***
Phosphatidylethano - Sulfatide	-0.320950	-0.327993	-0.313907	***
Phosphatidylethano - Phosphatidic acid	-0.314524	-0.321567	-0.307481	***
Phosphatidylethano - Ganglioside	-0.311472	-0.318515	-0.304429	***
Phosphatidylethano - Sphingomyelin	-0.309262	-0.316305	-0.302219	***
Phosphatidylethano - Phosphatidylserine	-0.308489	-0.315532	-0.301446	***
Phosphatidylethano - Phosphatidylinosit	-0.306284	-0.313327	-0.299242	***
Phosphatidylethano - Galactocerebroside	-0.297905	-0.304948	-0.290862	***
Phosphatidylethano - Cholesteryl palmit	-0.151102	-0.158145	-0.144060	***

5.3.4. Raman Identifies Differences in Lipid Signature in PTSD and Control Brain Tissues

In order to compare the amount of lipid distribution in control and PTSD samples, we used direct classical least squares analysis (DCLS) method.(Zhang, Henson et al. 2005, Gordon and McGoverin 2011, Bohndiek, Wagadarikar et al. 2013) According to this model, the mixture spectrum can be modeled as a linear mixture of various reference spectra. The DCLS model is useful when reference spectra are available from pure samples. Accordingly, we first acquired the Raman signal from the PVT region of both control and PTSD specimens. Afterwards, the Raman spectra of pure lipids (Figure 5.9a-e) were used to quantify each lipid in terms of relative

concentration and distribution. Figures 5.21, 5.22 and 5.23 illustrate the Raman maps of eleven commonly found lipids in the PVT region of the rat brain (the bars beside each image indicate the value of the correlation coefficient between the corresponding lipid and brain spectra).

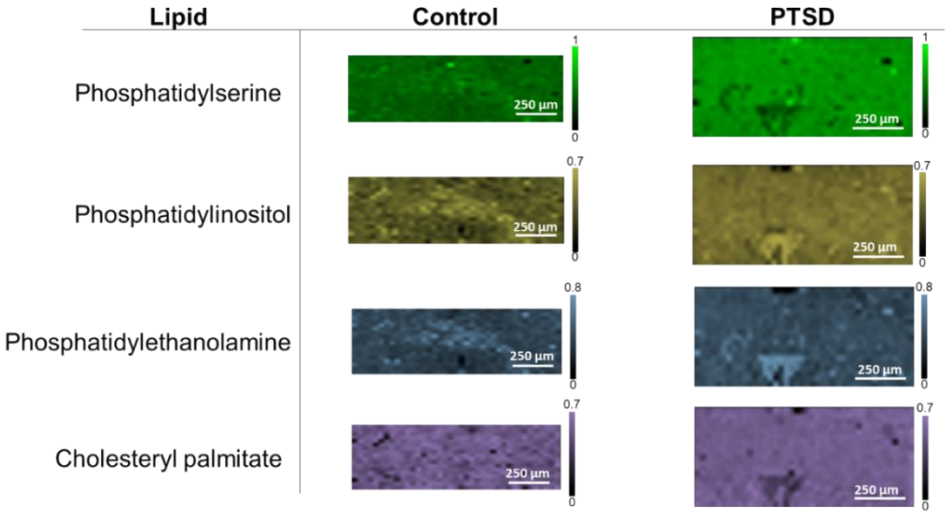

Figure 5.21. Raman maps of phosphatidylserine, phosphatidylinositol, phosphatidylethanolamine and cholesteryl palmitate in PVT region of the rat brain. The bars beside each image indicate the value of correlation coefficient between the corresponding lipid and brain spectra.

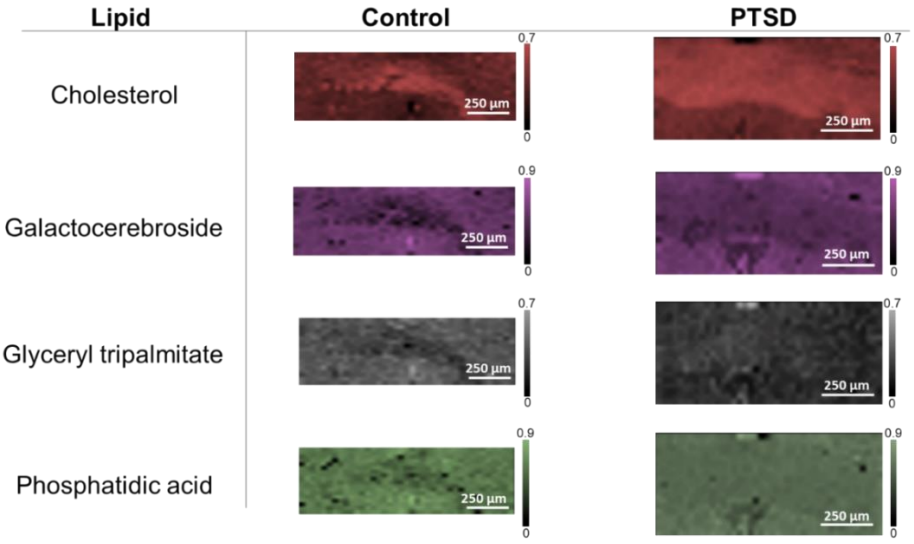

Figure 5.22. Raman maps of cholesterol, galactocerebroside, glyceryl tripalmitate and phosphatidic acid in PVT region of the rat brain. The bars beside each image indicate the value of correlation coefficient between the corresponding lipid and brain spectra.

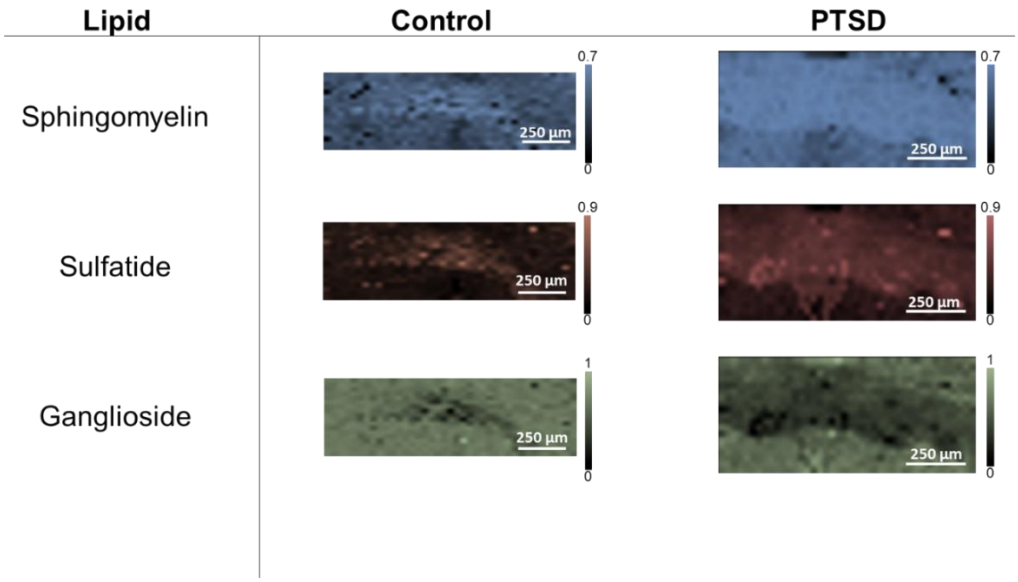

Figure 5.23. Raman maps of sphingomyelin, sulfatide and ganglioside in PVT region of the rat brain. The bars beside each image indicate the value of correlation coefficient between the corresponding lipid and brain spectra.

After plotting the respective maps for each lipid, ImageJ software was used to analyze the relative concentration and distribution of lipids. To this end, the intensity value of brightness in each pixel and also distribution of pixels is needed. The intensity values give the relative concentration change of each lipid. The distribution of pixel intensity describes the distribution of lipids in the PVT region. For a tangible example, comparative Raman maps of cholesterol, galactocerebroside, sulfatide and ganglioside are demonstrated in Figure 5.24a-5.24f.

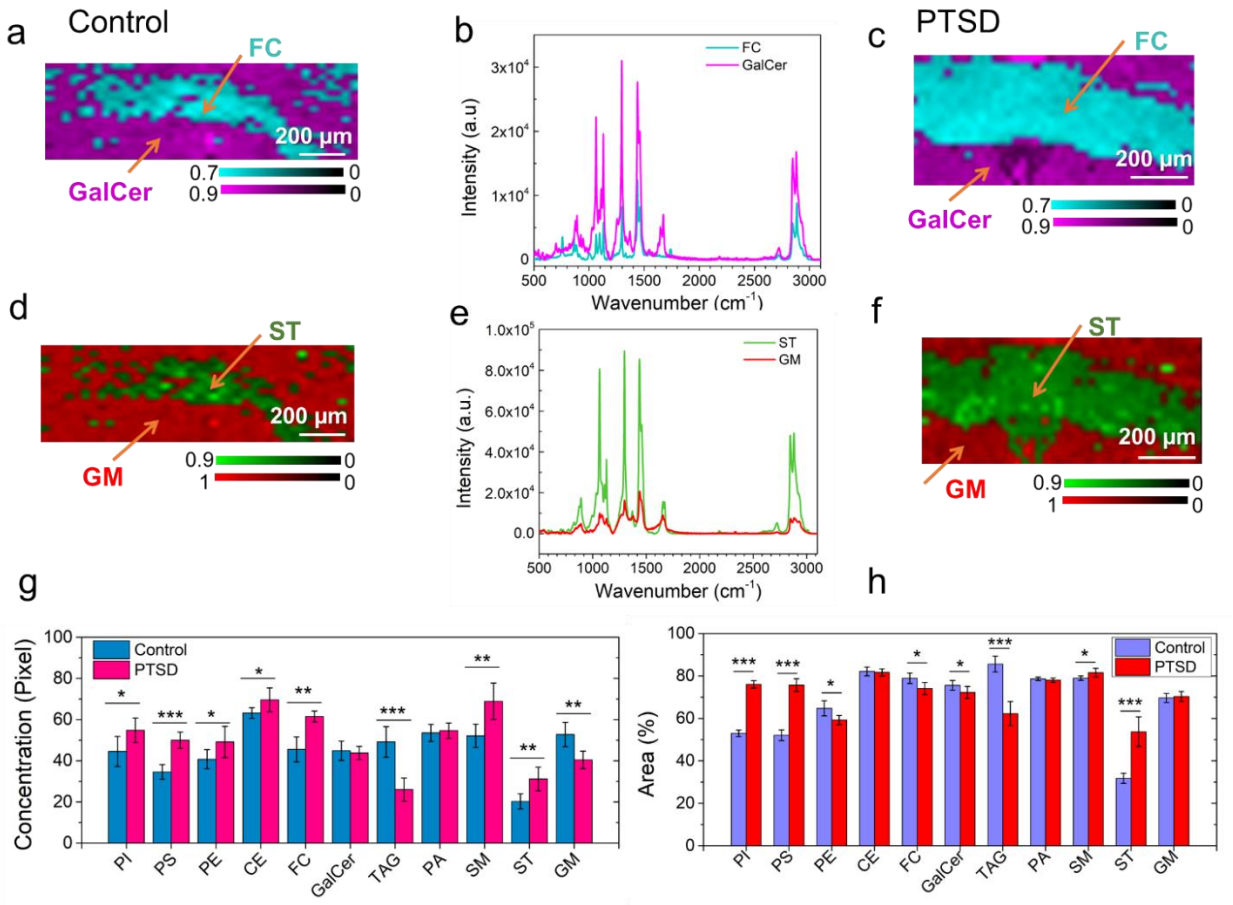

Figure 5.24. Comparison of DCLS Raman spectroscopy images of the lipids from the respective PVT region. DCLS Raman heat maps of cholesterol (FC) and galactocerebroside (GalCer) plotted from the signature Raman spectra for (a) Control, (c) PTSD brain sample. The Raman spectra are shown in (b); (d-e) Raman heat maps and Raman spectra of sulfatide (ST) and ganglioside (GM); Average of relative concentration of lipids within PVT region calculated from the (g) pixel intensity, (h) areal distribution of the Raman images. Statistical significance were calculated using Student's paired t-test, with a two-tailed distribution. *P < 0.05, **P < 0.01, ***P < 0.001, n = 5 per group.

As can be seen, the relative concentration of cholesterol and sulfatide is greater in the PTSD sample compared to the control. In order to quantify the relative concentration values, we used pixel value which is a number between 0-255. The value 0 indicates the minimum brightness and 255 indicates the maximum brightness of a pixel. These values were obtained from 8-bit images by means of ImageJ software. Figure 5.25 shows the pixel value distributions of different lipids in control and PTSD samples. The relative shifts of the peaks to the right (higher pixel values), indicates an increase in the relative concentration of lipids. Therefore, we can acquire the weighted

mean value for each lipid from this diagram that directly indicates the concentration changes of different lipids.

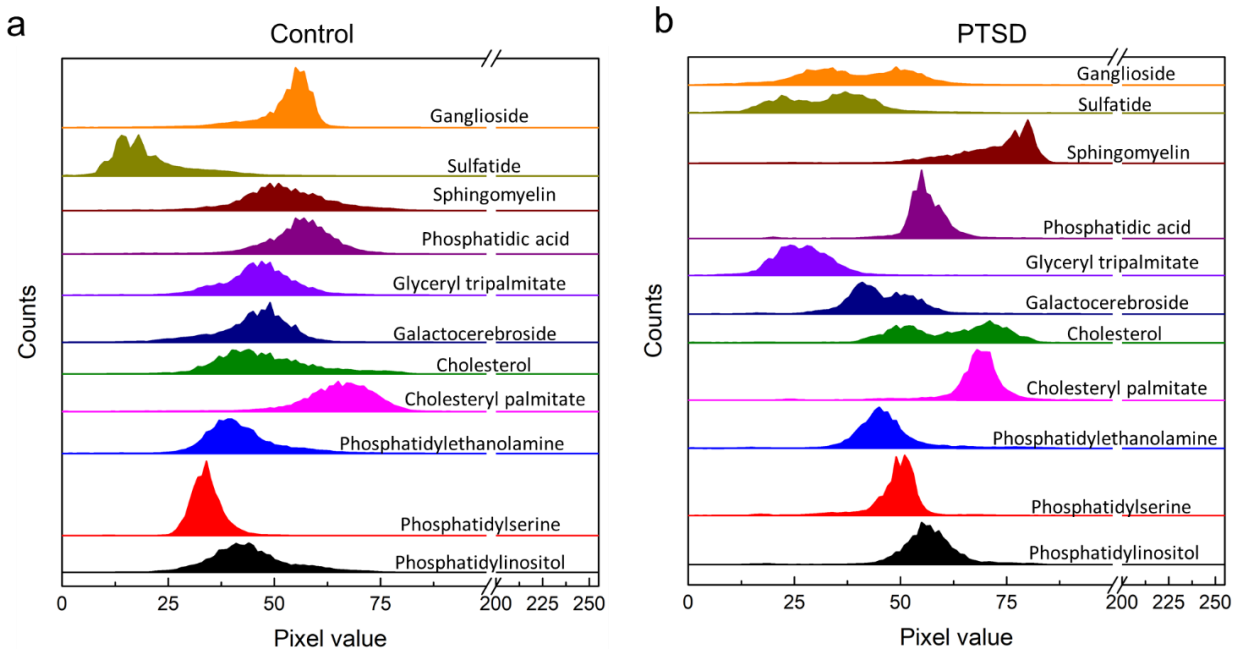

Figure 5.25. Pixel value distributions of different lipids in control and PTSD samples. Relative shifts of the peaks to the right (higher pixel values), indicates an increase in the relative concentration of lipids. Weighted mean value is obtained for each lipid from this diagram. This value directly indicates the concentration changes of different lipids.

Figure 5.24g demonstrates the acquired weighted mean values for different lipids in PTSD and control samples. Accordingly, the relative concentration of phosphatidylinositol, phosphatidylserine, phosphatidylethanolamine, cholesteryl palmitate, cholesterol, sphingomyelin and sulfatide experienced an increase by 23%, 44.6%, 20.6%, 10.2%, 35%, 32.2%, 54% in PTSD sample, respectively. On the other hand, relative concentration of glyceryl tripalmitate and ganglioside decreased by 47.1% and 23.3%, respectively, relative to control tissue. Meanwhile, galactocerebroside and phosphatidic acid did not change noticeably. Stress response is followed by the release of corticosterone.(Oliveira, Chan et al. 2015) This hormone, which is derived from cholesterol, mediates the pathologic responses of severe stress by binding to intercellular receptors. It is believed that the concentration of neutral lipids (cholesteryl palmitate and cholesterol) in brain

is correlated with the level of corticosterone.(Danan and Cohen 2018) Therefore, higher concentration of cholesterol indicates the higher level of corticosterone in brain. Accordingly, the changes in lipid concentration have numerous impacts on physiological mechanisms of stress-related disorders. Changes in the concentration of phospholipids (phosphatidylinositol, phosphatidylserine and phosphatidylethanolamine) and sphingolipids (sphingomyelin, ganglioside, glyceryl tripalmitate and sulfatide) also reveal the alteration of phospholipase A2 (PLA2) which is associated with inflammatory processes in brain.(Noponen, Sanfilipo et al. 1993, Oliveira, Chan et al. 2015)

Apart from the relative concentration of lipids, we have also analyzed the areal distribution of lipids in PVT region. The areal distribution is given as the percentage of occupied areal by each lipid in PVT region (Figure 5.24h). By comparing the results from Figures 5.24g and 5.24h, it can be observed that for some lipids (e.g. cholesterol and ganglioside), the distribution percentage of lipid does not follow the trend of relative concentration. For example, for cholesterol, the lipid areal distribution decreases slightly despite the increase in relative concentration of the lipid. Similarly, for ganglioside the distribution percentage is almost constant while the relative concentration is lower. The reason for the differences is due to the fact that we are not taking into account the pixel intensity values while calculating the areal distribution percentage. In other words, we are using a binary logic for distribution percentage to choose whether a pixel is ON (particular lipid is present) or OFF (lipid is absent). Therefore, relative concentration and areal distribution should be utilized side by side in order to achieve a fair judgment of lipidome alterations in the brain tissues.

5.3.5. MALDI-MS Imaging of Brain Tissue

To validate the Raman imaging results, we utilized MALDI mass spectrometry imaging (MALDI-MSI) as a conventional lipidomic studies method to elucidate the role of lipids in PTSD. The obtained lipidome profile is affected by the choice of ionization mode.(Nygren, Seppänen-Laakso et al. 2011, Ottestad, Hassani et al. 2012, Tan, Lou et al. 2012, Zhu, Dane et al. 2012, Bang and Moon 2013, Cajka and Fiehn 2014) Since wide range of lipids can be ionized in positive mode, its widely used for lipidomics.(Cajka and Fiehn 2014) However, phospholipids such as PI, PS, and PA yield better results in negative ionization mode.(Nygren, Pöhö et al. 2013) Although we used both modes, only the MALDI images obtained in positive mode are shown here. The MALDI-MS spectra obtained in the positive ion mode from the PVT region of the control and PTSD brain tissue sample are shown in Figure 5.26a. The MS spectra display both low molecular weight (400 – 650 Da) and high molecular weight (700 – 1200 Da) lipid species.

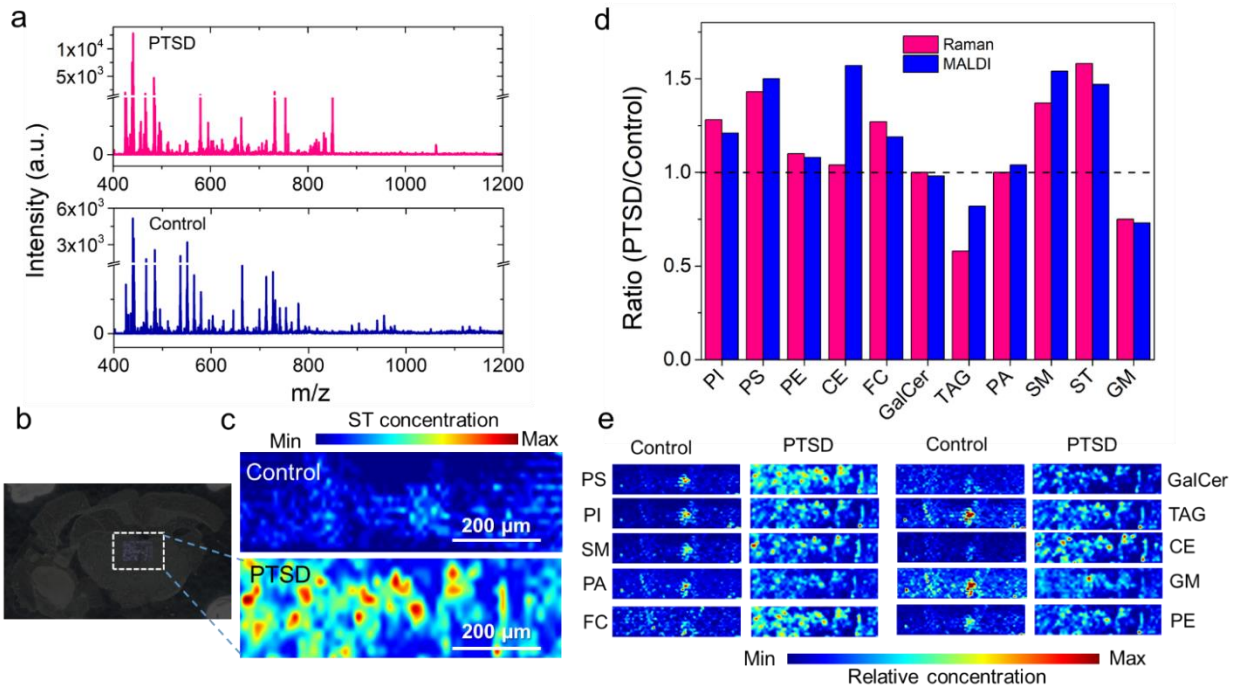

Figure 5.26. Mass spectra and MALDI images obtained from the PVT region of the brain using the positive ion mode.

Positive ion mode also allowed observation of low molecular weight lipids in the control brain tissue such as lysophosphatidylcholines (LPC O-15:1, *m/z* 466.3), which are generally masked by the signal from the matrix.(Kaya, Michno et al. 2017) Intense signal at *m/z* 663.4 for the control brain sample corresponds to PA 30:3;O3. Other observed species were phosphatidylglycerols (PG 28:2, *m/z* 663.4). For the PTSD sample, the intense mass peaks correspond to fatty acyls such as N-acyl taurines (NAT 20:4;O, *m/z* 466.2), glycerophospholipids (PA 39:8, PG 33:3, PA 37:5, PG 31:0, PA O-38:5, PG O-31:1, PG 30:1, *m/z* 731.5; PC O-42:5, PC 41:5, PE 44:5, PC O-40:2, *m/z* 850.7), glycerolipids such as di(acyl|alkyl)glycerols (DG 42:8, *m/z* 731.5; DG 44:3, *m/z* 753.6), tri(acyl|alkyl)glycerols (TAG 43:3, *m/z* 753.6), and sphingolipids such as hexosyl ceramides (HexCer 42:1;O3, *m/z* 850.7).

Figure 5.26b shows the bright field optical image of the MALDI-MS sample. The distribution of each lipid is shown in Figure 5.26c and 5.26e (also see Figure 5.27). We are able to observe the pathological lipid changes in the PVT region of the brain due to PTSD. For example, the positive ion image of sulfatides (ST 38:1, *m/z* 890.5; Figure 5.26c) showed an accumulation of sulfatides near the PVT of the PTSD rat. A similar elevated level of ST after traumatic brain injury was observed in an earlier study.(Pick 2010) Figure 5.26d compares the Raman and MALDI image analysis results.

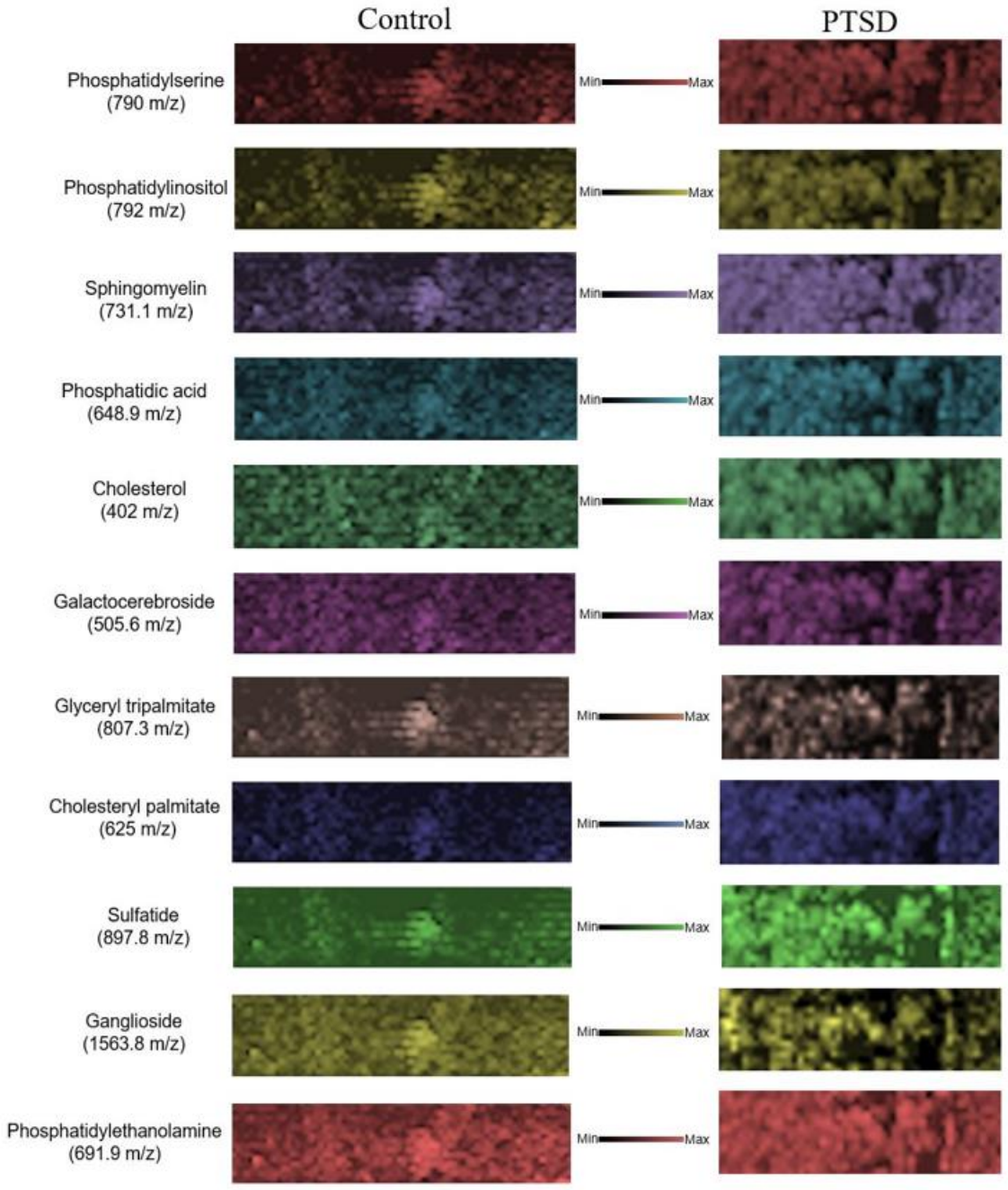

Figure 5.27. MALDI images acquired from PVT region of rat brain for control and PTSD. The corresponding mass value used for plotting the images is showed beside each lipid name. In all the Images, brightness of the pixels shows the relative concentration of the lipid (brighter: higher concentration; darker: lower concentration).

Figure 5.26d shows the ratio of PTSD to control calculated from the Raman images using the mean value of pixel intensity (pink bars) for different lipids. The corresponding PTSD to control ratio calculated from each MALDI-MS image (blue bars) is also compared with the Raman

ratio. The ratio, R = 1 indicates no change, R > 1 indicates increase, and R < 1 indicates decrease of specific lipids in PTSD samples compared to the control samples. Accordingly, an increase in the relative concentration value of phosphatidylinositol (PI), phosphatidylserine (PS), phosphatidylethanolamine (PE), cholesterol (FC), sphingomyelin (SM) and sulfatide (ST) is observed by both Raman and MALDI imaging methods in the PTSD sample compared to the control. Moreover, the decrease in the ganglioside (GM) and glyceryl tripalmitate (TAG) in the PTSD sample was also confirmed by the MALDI images. No significant change was observed for galactocerebroside (GalCer) and phosphatidic acid (PA) by any of the methods. Only cholesteryl palmitate and glyceryl tripalmitate displayed a difference in its relative concentration between MALDI detection and Raman detection. Therefore, the majority of the detected signals in MALDI are in agreement with the Raman imaging analysis.

Figure 5.26e shows representative MALDI-MS images of selected lipid species in control and PTSD brain samples. The images were constructed using the following mass peaks: phosphatidylserine (PS 34:2, *m/z* 760.5; PS 39:0, *m/z* 834.6; PS 39:7, *m/z* 842.5; PS 40:1, *m/z* 868.6; PS 43:4, *m/z* 882.6), phosphatidylinositol (PI 31:3, *m/z* 829.4; PI O-35:2, *m/z* 857.6; PI O-37:3, *m/z* 883.6; PI O-37:2, *m/z* 885.6), sphingomyelin (SM 34:2-O2, *m/z* 723.5; SM 33:0-O2, *m/z* 729.5; SM 34:1-O2, *m/z* 741.5; SM 36:2-O2, *m/z* 767.5), phosphatidic acid (PA O-31:0, *m/z* 643.5; PA O-33:1 & PA 32:1, *m/z* 647.5; PA O-35:3, *m/z* 671.5; PA 35:5, *m/z* 719.4), cholesterol (FC 24:5, *m/z* 401.2; FC 27:1-O, *m/z* 409.3; FC 26:2-O3, *m/z* 425.3; ST 27:1-O, *m/z* 425.3), galactocerebroside (GalCer 34:1-O2, *m/z* 722.5; GalCer 40:2-O2, *m/z* 804.6; GalCer 40:1-O2, *m/z* 806.6; GalCer 41:2-O2, *m/z* 834.6), triacylglyceride (TAG 50:9, *m/z* 817.6; TAG 52:9, *m/z* 845.7; TAG 50:2, *m/z* 869.7; TAG 52:3, *m/z* 895.7; TAG 58:13, *m/z* 921.7), cholesterol ester (CE 18:3, *m/z* 669.6; CE 20:5 & CE 18:2, *m/z* 671.6; CE 22:0, *m/z* 731.7; CE 24:1, *m/z* 757.7),

ganglioside (GM or Hex(3)-HexNAc-KDN-Cer 36:1-O2, *m/z* 1543.8; GM 36:1-O2, *m/z* 1562.9; GM or Hex(4)-HexNAc-Fuc-Cer 36:1-O2, *m/z* 1563.9), phosphatidylethanolamine (PE 36:6, *m/z* 736.5; PE O-36:6, *m/z* 744.5; PE O-37:1, *m/z* 746.6; PE 37:6, *m/z* 750.5; PE 38:7, *m/z* 762.5; PE O-36:3, *m/z* 766.5; PE O-37:1, *m/z* 768.6; PE 40:7, *m/z* 790.5; PE 39:0, *m/z* 790.6; PE 40:6, *m/z* 792.6; PE 37:3, *m/z* 794.5; PE O-39:2, *m/z* 794.6).

The membrane lipid PI plays an important role in the signal transduction.(Jackson, Wang et al. 2005) Although experiments performed in a different region of the brain (prefrontal cortex, PFC, and hippocampus), Oliveira et al. also reported an increase of PI in the rate brain due to chronic stress.(Oliveira, Chan et al. 2016) The increase of other phospholipids such as PE and PS reported in our study are supported by other literature observations using neurodegenerative disease models.(Davidson, Jonas et al. 1998, Harper, Jensen et al. 2014, Mesa-Herrera, Taoro-González et al. 2019) In addition to cholesterol and phospholipids, sphingolipids are the most common membrane lipids in the brain.(Jackson, Wang et al. 2005, Jackson, Wang et al. 2007, Jain, Ngoy et al. 2014) Sphingolipids such as gangliosides are implicated in brain development, memory formation as well as synaptic transmission.(Sonnino and Chigorno 2000) Our results show a decrease in the gangliosides concentration in PTSD samples, which is supported by the observations from Martin et al. and Kracun et al. using the brain tissue of human subjects.(Kracun, Rosner et al. 1992, Martín, Fabelo et al. 2010) Further study by Oliveira et al. showed that the alteration in lipid levels in the brain is area dependent. They observed an increase of the PI in the hippocampus and a decrease in PE in the PFC, but no changes in the phospholipid levels in the amygdala or cerebellum.(Oliveira, Chan et al. 2016) These findings suggest that lipidome analysis should be performed in specific areas of the brain for meaningful comparisons. Although the lipid distribution in the brain is dynamic and complex, it is suggested to play some role in depression

and anxiety disorders.(Müller, Reichel et al. 2015) The knowledge gained from this study may provide lipid-based targets for disease prevention and treatment.

5.4. Conclusion

In this study, we have evaluated the application of Raman spectroscopy and imaging for the quantitative analysis of lipid concentrations in paraventricular thalamic nucleus (PVT) of post-traumatic stress disorder (PTSD), and control brain tissue. Raman spectroscopy provided a new tool to non-invasively monitor the lipid changes in the brain tissue. Combining with histology and MALDI mass spectrometry imaging, we have performed a parallel study with Raman imaging and multivariate data analysis to validate the distinguishing of different lipids in brain tissue. Further, we used a direct classical least squares analysis approach for rendering Raman maps and imaging the lipid concentration in the PVT region. By means of this technique and various image processing methods, we have demonstrated the relative alteration of lipids in PVT region before and after inducing PTSD. Our results show a relative increase in the concentration of phosphatidylinositol (28%), phosphatidylserine (43%), phosphatidylethanolamine (11%), cholesteryl palmitate (4%), cholesterol (27%), sphingomyelin (37%) and sulfatide (58%) in the PTSD sample. Meanwhile, a relative decrease in the concentration of glyceryl tripalmitate (71%) and ganglioside (32%) was observed. However, the relative concentration of galactocerebroside and phosphatidic acid did not change noticeably in the PTSD samples compared to the control. The higher relative concentration of cholesterol and cholesteryl palmitate are directly related to the level of corticosterone.

Changes in the concentration of phospholipids and sphingolipids are associated with inflammatory processes in the brain by changing the level of phospholipase A2 (PLA2). Similar Raman imaging methods can be applied to other regions of brain and other types of brain disorders.

The Raman scattering-based label-free method could open new way to perform lipidomic studies on cells and tissue with high spatial resolution for fast and non-destructive analysis.

Appendix. Reprint Permissions

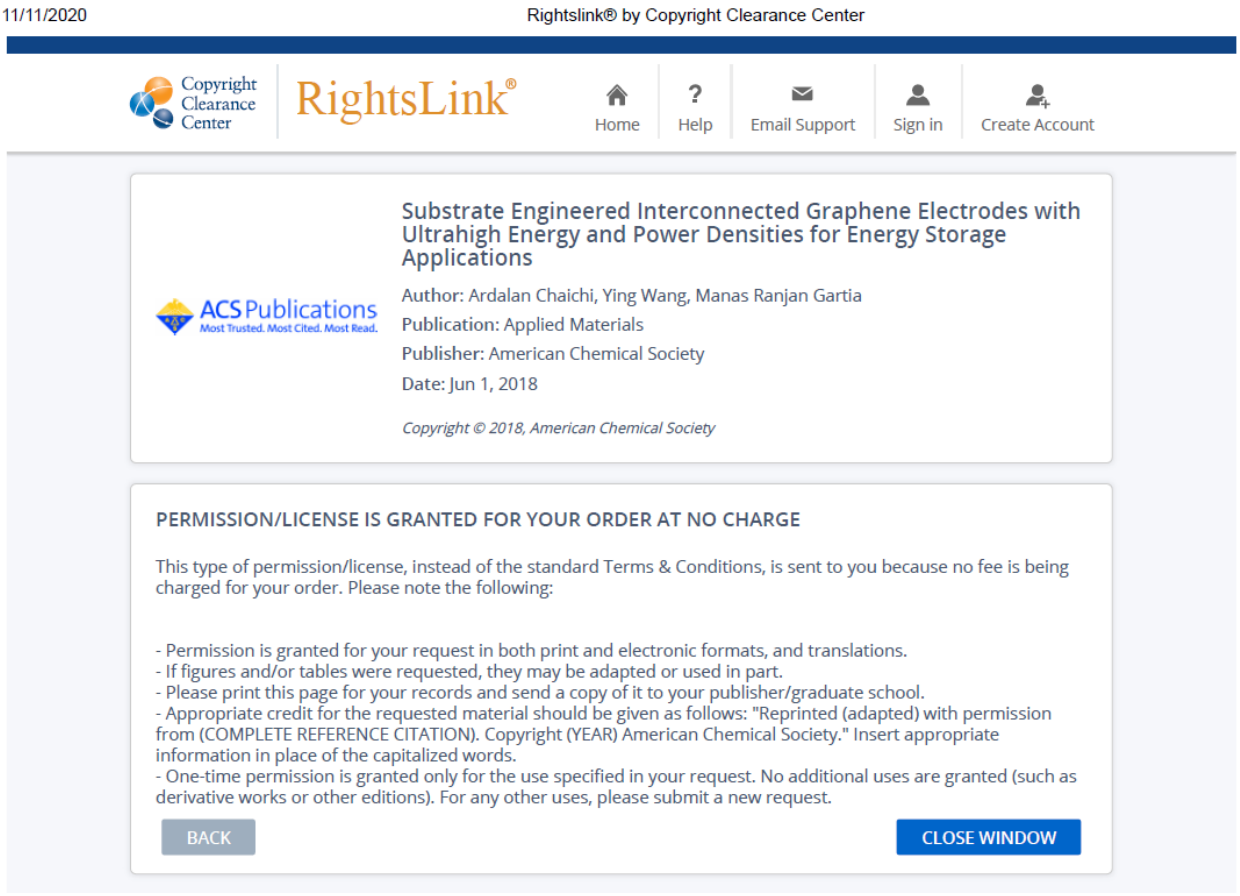

A.1. Reprint permission from the publisher for chapter 2.

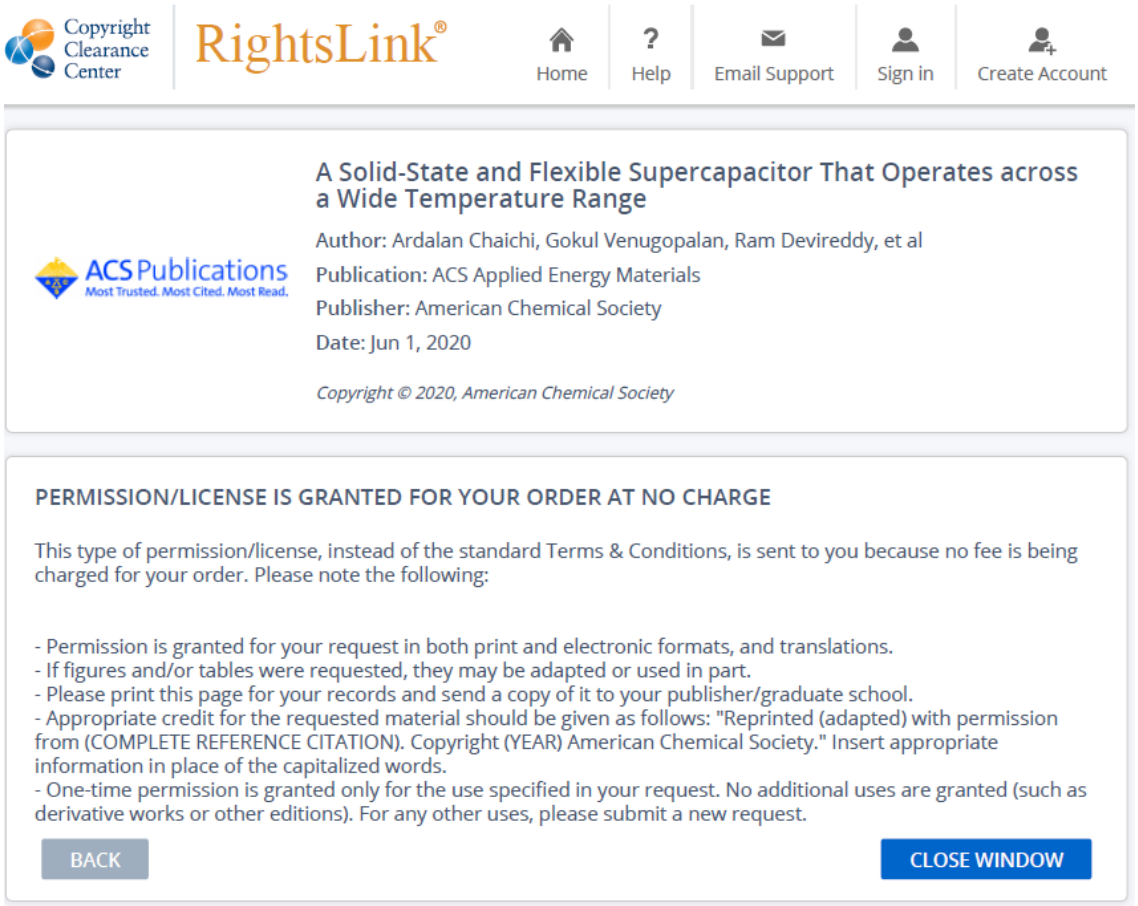

A.2. Reprint permission from the publisher for chapter 3.

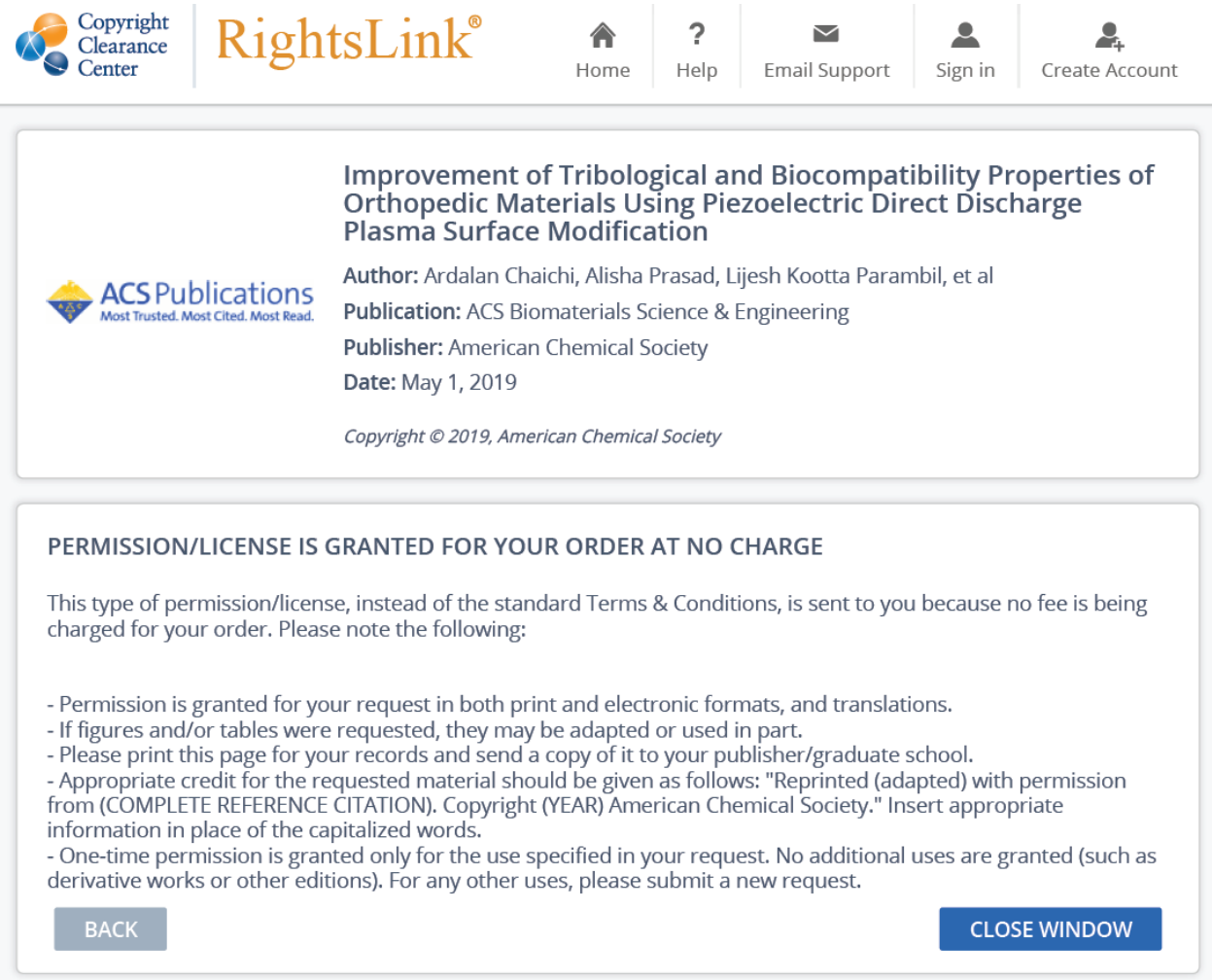

A.3. Reprint permission from the publisher for chapter 4.

Author reusing their own work published by the Royal Society of Chemistry

You do not need to request permission to reuse your own figures, diagrams, etc, that were originally published in a Royal Society of Chemistry publication. However, permission should be requested for use of the whole article or chapter except if reusing it in a thesis. If you are including an article or book chapter published by us in your thesis please ensure that your co-authors are aware of this.

Reuse of material that was published originally by the Royal Society of Chemistry must be accompanied by the appropriate acknowledgement of the publication. The form of the acknowledgement is dependent on the journal in which it was published originally, as detailed in 'Acknowledgements'.

A.4. Reprint permission from the publisher for chapter 5.

List of References

Affatato, S. (2012). Wear of orthopaedic implants and artificial joints, Elsevier.

Andwari, A. M., A. Pesiridis, S. Rajoo, R. Martinez-Botas and V. Esfahanian (2017). "A review of Battery Electric Vehicle technology and readiness levels." Renewable and Sustainable Energy Reviews **78**: 414-430.

Arges, C. G., J. Parrondo, G. Johnson, A. Nadhan and V. Ramani (2012). "Assessing the influence of different cation chemistries on ionic conductivity and alkaline stability of anion exchange membranes." Journal of Materials Chemistry **22**(9): 3733-3744.

Arges, C. G. and L. Zhang (2018). "Anion exchange membranes' evolution toward high hydroxide ion conductivity and alkaline resiliency." ACS Applied Energy Materials **1**(7): 2991-3012.

Armand, M., F. Endres, D. R. MacFarlane, H. Ohno and B. Scrosati (2011). Ionic-liquid materials for the electrochemical challenges of the future. Materials For Sustainable Energy: A Collection of Peer-Reviewed Research and Review Articles from Nature Publishing Group, World Scientific**:** 129-137.

Asbani, B., C. Douard, T. Brousse and J. Le Bideau (2019). "High temperature solid-state supercapacitor designed with ionogel electrolyte." Energy Storage Materials **21**: 439-445.

Ataee, A., Y. Li, D. Fraser, G. Song and C. Wen (2018). "Anisotropic Ti-6Al-4V gyroid scaffolds manufactured by electron beam melting (EBM) for bone implant applications." Materials & Design **137**: 345-354.

Bang, D. Y. and M. H. Moon (2013). "On-line two-dimensional capillary strong anion exchange/reversed phase liquid chromatography–tandem mass spectrometry for comprehensive lipid analysis." Journal of Chromatography A **1310**: 82-90.

Bashash, S., S. J. Moura, J. C. Forman and H. K. Fathy (2011). "Plug-in hybrid electric vehicle charge pattern optimization for energy cost and battery longevity." Journal of power sources **196**(1): 541-549.

Basnayaka, P. A. and M. K. Ram (2017). A Review of Supercapacitor Energy Storage Using Nanohybrid Conducting Polymers and Carbon Electrode Materials. Conducting Polymer Hybrids, Springer**:** 165-192.

Beidaghi, M. and C. Wang (2012). "Micro-supercapacitors based on interdigital electrodes of reduced graphene oxide and carbon nanotube composites with ultrahigh power handling performance." Advanced Functional Materials **22**(21): 4501-4510.

Ben Mabrouk, K., T. H. Kauffmann, H. Aroui and M. D. Fontana (2013). "Raman study of cation effect on sulfate vibration modes in solid state and in aqueous solutions." Journal of Raman Spectroscopy **44**(11): 1603-1608.

Bohndiek, S. E., A. Wagadarikar, C. L. Zavaleta, D. Van de Sompel, E. Garai, J. V. Jokerst, S. Yazdanfar and S. S. Gambhir (2013). "A small animal Raman instrument for rapid, wide-area, spectroscopic imaging." Proceedings of the National Academy of Sciences **110**(30): 12408-12413.

Bokhart, M. T., M. Nazari, K. P. Garrard and D. C. Muddiman (2017). "MSiReader v1. 0: evolving open-source mass spectrometry imaging software for targeted and untargeted analyses." Journal of The American Society for Mass Spectrometry **29**(1): 8-16.

Bovin, M. J., B. P. Marx, F. W. Weathers, M. W. Gallagher, P. Rodriguez, P. P. Schnurr and T. M. Keane (2016). "Psychometric properties of the PTSD checklist for diagnostic and statistical manual of mental disorders–fifth edition (PCL-5) in veterans." Psychological Assessment **28**(11): 1379.

Browne, M. and P. Gregson (1994). "Surface modification of titanium alloy implants." Biomaterials **15**(11): 894-898.

Brügger, B. (2014). "Lipidomics: analysis of the lipid composition of cells and subcellular organelles by electrospray ionization mass spectrometry." Annual review of biochemistry **83**: 79-98.

Buchsteiner, A., A. Lerf and J. Pieper (2006). "Water dynamics in graphite oxide investigated with neutron scattering." The Journal of Physical Chemistry B **110**(45): 22328-22338.

Cajka, T. and O. Fiehn (2014). "Comprehensive analysis of lipids in biological systems by liquid chromatography-mass spectrometry." TrAC Trends in Analytical Chemistry **61**: 192-206.

Carr, B. C. and T. Goswami (2009). "Knee implants–Review of models and biomechanics." Materials & Design **30**(2): 398-413.

Chaichi, A., A. Prasad and M. Gartia (2018). "Raman Spectroscopy and Microscopy Applications in Cardiovascular Diseases: From Molecules to Organs." Biosensors **8**(4): 107.

Chaichi, A., A. Prasad and M. R. Gartia (2018). "Raman spectroscopy and microscopy applications in cardiovascular diseases: From molecules to organs." Biosensors **8**(4): 107.

Chan, R. B., T. G. Oliveira, E. P. Cortes, L. S. Honig, K. E. Duff, S. A. Small, M. R. Wenk, G. Shui and G. Di Paolo (2012). "Comparative lipidomic analysis of mouse and human brain with Alzheimer disease." Journal of Biological Chemistry **287**(4): 2678-2688.

Chandramohan, P., S. Bhero, B. A. Obadele and P. A. Olubambi (2017). "Laser additive manufactured Ti–6Al–4V alloy: tribology and corrosion studies." The International Journal of Advanced Manufacturing Technology **92**(5-8): 3051-3061.

Chee, W. K., H. N. Lim, Z. Zainal, N. M. Huang, I. Harrison and Y. Andou (2016). "Flexible graphene-based supercapacitors: a review." The Journal of Physical Chemistry C **120**(8): 4153-4172.

Chen, C. R., H. Qin, H. P. Cong and S. H. Yu (2019). "A Highly Stretchable and Real-Time Healable Supercapacitor." Advanced Materials **31**(19): 1900573.

Chen, J., C. Li and G. Shi (2013). "Graphene materials for electrochemical capacitors." The journal of physical chemistry letters **4**(8): 1244-1253.

Chen, T. and L. Dai (2013). "Carbon nanomaterials for high-performance supercapacitors." Materials Today **16**(7): 272-280.

Chen, T., Y. Xue, A. K. Roy and L. Dai (2013). "Transparent and stretchable high-performance supercapacitors based on wrinkled graphene electrodes." Acs Nano **8**(1): 1039-1046.

Cheng, D., A. M. Jenner, G. Shui, W. F. Cheong, T. W. Mitchell, J. R. Nealon, W. S. Kim, H. McCann, M. R. Wenk and G. M. Halliday (2011). "Lipid pathway alterations in Parkinson's disease primary visual cortex." PloS one **6**(2).

Cho, E. H., S. G. Lee and J. K. Kim (2005). "Surface modification of UHMWPE with γ-ray radiation for improving interfacial bonding strength with bone cement (II)." Current Applied Physics **5**(5): 475-479.

Claramunt, S., A. Varea, D. López-Díaz, M. M. Velázquez, A. Cornet and A. Cirera (2015). "The importance of interbands on the interpretation of the Raman spectrum of graphene oxide." The Journal of Physical Chemistry C **119**(18): 10123-10129.

Clary, C. and L. Maletsky (2017). Mechanical testing of knee implants. Mechanical Testing of Orthopaedic Implants, Elsevier**:** 207-229.

Cohen, S., M. A. Matar, J. Zohar and H. Cohen (2018). Brain Pathways of Traumatic Memory: Evidence from an Animal Model of PTSD. Sleep and Combat-Related Post Traumatic Stress Disorder, Springer**:** 127-143.

Cote, L. J., R. Cruz-Silva and J. Huang (2009). "Flash reduction and patterning of graphite oxide and its polymer composite." Journal of the American Chemical Society **131**(31): 11027-11032.

Czamara, K., K. Majzner, M. Z. Pacia, K. Kochan, A. Kaczor and M. Baranska (2015). "Raman spectroscopy of lipids: a review." Journal of Raman Spectroscopy **46**(1): 4-20.

Danan, D. and H. Cohen (2018). "P.2.020 - Blunted basal corticosterone pulsatility predicts post-exposure susceptibility to post-traumatic stress disorder phenotype in rats." European Neuropsychopharmacology **28**: S36.

Davidson, W. S., A. Jonas, D. F. Clayton and J. M. George (1998). "Stabilization of α-synuclein secondary structure upon binding to synthetic membranes." Journal of Biological Chemistry **273**(16): 9443-9449.

De Jongh, A., P. A. Resick, L. A. Zoellner, A. Van Minnen, C. W. Lee, C. M. Monson, E. B. Foa, K. Wheeler, E. t. Broeke and N. Feeny (2016). "Critical analysis of the current treatment guidelines for complex PTSD in adults." Depression and Anxiety **33**(5): 359-369.

de Sousa Vieira, E. E., J. A. M. Bispo, A. B. Fernandes and L. Silveira (2016). Biomarkers of chronic kidney disease in the urine of diabetic/hypertensive patients by means of Raman spectroscopy. Biomedical Vibrational Spectroscopy 2016: Advances in Research and Industry, International Society for Optics and Photonics.

Deimede, V., G. Voyiatzis, J. Kallitsis, L. Qingfeng and N. Bjerrum (2000). "Miscibility behavior of polybenzimidazole/sulfonated polysulfone blends for use in fuel cell applications." Macromolecules **33**(20): 7609-7617.

Deslauriers, J., M. Toth, A. Der-Avakian and V. B. Risbrough (2018). "Current status of animal models of posttraumatic stress disorder: behavioral and biological phenotypes, and future challenges in improving translation." Biological psychiatry **83**(10): 895-907.

Desroches, J., M. Jermyn, K. Mok, C. Lemieux-Leduc, J. Mercier, K. St-Arnaud, K. Urmey, M.-C. Guiot, E. Marple and K. Petrecca (2015). "Characterization of a Raman spectroscopy probe system for intraoperative brain tissue classification." Biomedical optics express **6**(7): 2380-2397.

Dikin, D. A., S. Stankovich, E. J. Zimney, R. D. Piner, G. H. Dommett, G. Evmenenko, S. T. Nguyen and R. S. Ruoff (2007). "Preparation and characterization of graphene oxide paper." Nature **448**(7152): 457-460.

Ditta, A., H. Nawaz, T. Mahmood, M. Majeed, M. Tahir, N. Rashid, M. Muddassar, A. Al-Saadi and H. Byrne (2019). "Principal components analysis of Raman spectral data for screening of Hepatitis C infection." Spectrochimica Acta Part A: Molecular and Biomolecular Spectroscopy **221**: 117173.

Draga, R. O., M. C. Grimbergen, P. L. Vijverberg, C. F. v. Swol, T. G. Jonges, J. A. Kummer and J. Ruud Bosch (2010). "In vivo bladder cancer diagnosis by high-volume Raman spectroscopy." Analytical chemistry **82**(14): 5993-5999.

Duke, C. (2003). "The birth and evolution of surface science: Child of the union of science and technology." Proceedings of the National Academy of Sciences **100**(7): 3858-3864.

Durdu, S., M. Usta and A. S. Berkem (2016). "Bioactive coatings on Ti6Al4V alloy formed by plasma electrolytic oxidation." Surface and Coatings Technology **301**: 85-93.

Dybas, J., K. M. Marzec, M. Z. Pacia, K. Kochan, K. Czamara, K. Chrabaszcz, E. Staniszewska-Slezak, K. Malek, M. Baranska and A. Kaczor (2016). "Raman spectroscopy as a sensitive probe of soft tissue composition–Imaging of cross-sections of various organs vs. single spectra of tissue homogenates." TrAC Trends in Analytical Chemistry **85**: 117-127.

Ebenezer, P. J., C. B. Wilson, L. D. Wilson, A. R. Nair and J. Francis (2016). "The anti-inflammatory effects of blueberries in an animal model of post-traumatic stress disorder (PTSD)." PloS one **11**(9): e0160923.

El-Kady, M. F. and R. B. Kaner (2013). "Scalable fabrication of high-power graphene micro-supercapacitors for flexible and on-chip energy storage." Nature communications **4**: 1475.

El-Kady, M. F., V. Strong, S. Dubin and R. B. Kaner (2012). "Laser scribing of high-performance and flexible graphene-based electrochemical capacitors." Science **335**(6074): 1326-1330.

Enqvist, E., D. Ramanenka, P. A. Marques, J. Gracio and N. Emami (2016). "The effect of ball milling time and rotational speed on ultra high molecular weight polyethylene reinforced with multiwalled carbon nanotubes." Polymer Composites **37**(4): 1128-1136.

Faggioli, E., P. Rena, V. Danel, X. Andrieu, R. Mallant and H. Kahlen (1999). "Supercapacitors for the energy management of electric vehicles." Journal of Power Sources **84**(2): 261-269.

Fan, Z., K. Wang, T. Wei, J. Yan, L. Song and B. Shao (2010). "An environmentally friendly and efficient route for the reduction of graphene oxide by aluminum powder." Carbon **48**(5): 1686-1689.

Fang, S., D. Huang, R. Lv, Y. Bai, Z.-H. Huang, J. Gu and F. Kang (2017). "Three-dimensional reduced graphene oxide powder for efficient microwave absorption in the S-band (2–4 GHz)." RSC Advances **7**(41): 25773-25779.

Fazel, M., H. Salimijazi and M. Golozar (2015). "A comparison of corrosion, tribocorrosion and electrochemical impedance properties of pure Ti and Ti6Al4V alloy treated by micro-arc oxidation process." Applied Surface Science **324**: 751-756.

Frost, R. L., M. L. Weier, K. L. Erickson, O. Carmody and S. J. Mills (2004). "Raman spectroscopy of phosphates of the variscite mineral group." Journal of Raman Spectroscopy **35**(12): 1047-1055.

Gallardo-Moreno, A. M., M. A. Pacha-Olivenza, L. Saldaña, C. Pérez-Giraldo, J. M. Bruque, N. Vilaboa and M. L. González-Martín (2009). "In vitro biocompatibility and bacterial adhesion of physico-chemically modified Ti6Al4V surface by means of UV irradiation." Acta Biomaterialia **5**(1): 181-192.

Ghosh, P. (2009). Colloid and interface science, PHI Learning Pvt. Ltd.

Gibson, L., E. N. Wilman and W. F. Laurance (2017). "How green is 'green'energy?" Trends in ecology & evolution **32**(12): 922-935.

Gilman, A., M. Piskarev, A. Kuznetsov and A. Ozerin (2017). "Modification of ultrahigh-molecular-weight polyethylene by low-temperature plasma." High Energy Chemistry **51**(2): 136-144.

Goh, M. S. and M. Pumera (2010). "Multilayer graphene nanoribbons exhibit larger capacitance than their few-layer and single-layer graphene counterparts." Electrochemistry Communications **12**(10): 1375-1377.

Gordon, K. C. and C. M. McGoverin (2011). "Raman mapping of pharmaceuticals." International journal of pharmaceutics **417**(1-2): 151-162.

Graetzel, M., R. A. Janssen, D. B. Mitzi and E. H. Sargent (2012). "Materials interface engineering for solution-processed photovoltaics." Nature **488**(7411): 304-312.

Gu, W. and G. Yushin (2014). "Review of nanostructured carbon materials for electrochemical capacitor applications: advantages and limitations of activated carbon, carbide-derived carbon, zeolite-templated carbon, carbon aerogels, carbon nanotubes, onion-like carbon, and graphene." Wiley Interdisciplinary Reviews: Energy and Environment **3**(5): 424-473.

Guo, J., K. Huang and J. Wang (2015). "Bactericidal effect of various non-thermal plasma agents and the influence of experimental conditions in microbial inactivation: A review." Food Control **50**: 482-490.

Haddad, A., M. Ramadan, M. Khaled, H. S. Ramadan and M. Becherif (2019). "Triple hybrid system coupling fuel cell with wind turbine and thermal solar system." International Journal of Hydrogen Energy.

Haifler, M., I. Pence, Y. Sun, A. Kutikov, R. G. Uzzo, A. Mahadevan-Jansen and C. A. Patil (2018). "Discrimination of malignant and normal kidney tissue with short wave infrared dispersive Raman spectroscopy." Journal of biophotonics **11**(6): e201700188.

Haka, A. S., K. E. Shafer-Peltier, M. Fitzmaurice, J. Crowe, R. R. Dasari and M. S. Feld (2005). "Diagnosing breast cancer by using Raman spectroscopy." Proceedings of the National Academy of Sciences **102**(35): 12371-12376.

Hamilton, J. A., C. J. Hillard, A. A. Spector and P. A. Watkins (2007). "Brain uptake and utilization of fatty acids, lipids and lipoproteins: application to neurological disorders." Journal of Molecular Neuroscience **33**(1): 2-11.

Han, S., D. Wu, S. Li, F. Zhang and X. Feng (2014). "Porous graphene materials for advanced electrochemical energy storage and conversion devices." Advanced Materials **26**(6): 849-864.

Han, W., M. J. Demkowicz, N. A. Mara, E. Fu, S. Sinha, A. D. Rollett, Y. Wang, J. S. Carpenter, I. J. Beyerlein and A. Misra (2013). "Design of radiation tolerant materials via interface engineering." Advanced materials **25**(48): 6975-6979.

Harper, D. G., J. E. Jensen, C. Ravichandran, Y. Sivrioglu, M. Silveri, D. V. Iosifescu, P. F. Renshaw and B. P. Forester (2014). "Tissue-specific differences in brain phosphodiesters

in late-life major depression." The American Journal of Geriatric Psychiatry **22**(5): 499-509.

Herman, J. P. and J. G. Tasker (2016). "Paraventricular hypothalamic mechanisms of chronic stress adaptation." Frontiers in endocrinology **7**: 137.

Hibino, T., K. Kobayashi, M. Nagao and S. Kawasaki (2015). "High-temperature supercapacitor with a proton-conducting metal pyrophosphate electrolyte." Scientific reports **5**: 7903.

Homenick, C. M., R. James, G. P. Lopinski, J. Dunford, J. Sun, H. Park, Y. Jung, G. Cho and P. R. Malenfant (2016). "Fully printed and encapsulated SWCNT-based thin film transistors via a combination of R2R gravure and inkjet printing." ACS applied materials & interfaces **8**(41): 27900-27910.

Horn, M., B. Gupta, J. MacLeod, J. Liu and N. Motta (2019). "Graphene-based supercapacitor electrodes: addressing challenges in mechanisms and materials." Current Opinion in Green and Sustainable Chemistry.

Hsu, D. T., G. J. Kirouac, J.-K. Zubieta and S. Bhatnagar (2014). "Contributions of the paraventricular thalamic nucleus in the regulation of stress, motivation, and mood." Frontiers in behavioral neuroscience **8**: 73.

Huang, N., M. Short, J. Zhao, H. Wang, H. Lui, M. Korbelik and H. Zeng (2011). "Full range characterization of the Raman spectra of organs in a murine model." Optics express **19**(23): 22892-22909.

Huang, S., R. Pandey, I. Barman, J. Kong and M. Dresselhaus (2018). "Raman enhancement of blood constituent proteins using graphene." ACS Photonics **5**(8): 2978-2982.

Huang, S., L. Wang, W. Chen, S. Feng, J. Lin, Z. Huang, G. Chen, B. Li and R. Chen (2014). "Potential of non-invasive esophagus cancer detection based on urine surface-enhanced Raman spectroscopy." Laser Physics Letters **11**(11): 115604.

Huang, X., Z. Zeng, Z. Fan, J. Liu and H. Zhang (2012). "Graphene-based electrodes." Advanced Materials **24**(45): 5979-6004.

Huang, Z., A. McWilliams, H. Lui, D. I. McLean, S. Lam and H. Zeng (2003). "Near-infrared Raman spectroscopy for optical diagnosis of lung cancer." International journal of cancer **107**(6): 1047-1052.

Hunt, B. J. and T. J. Joyce (2016). "A tribological assessment of ultra high molecular weight polyethylene types GUR 1020 and GUR 1050 for orthopedic applications." Lubricants **4**(3): 25.

In, H. J., S. Kumar, Y. Shao-Horn and G. Barbastathis (2006). "Origami fabrication of nanostructured, three-dimensional devices: Electrochemical capacitors with carbon electrodes." Applied Physics Letters **88**(8): 083104.

Iqbal, S., H. Khatoon, A. H. Pandit and S. Ahmad (2019). "Recent development of carbon based materials for energy storage devices." Materials Science for Energy Technologies **2**(3): 417-428.

Jackson, S. N., H.-Y. J. Wang and A. S. Woods (2005). "Direct profiling of lipid distribution in brain tissue using MALDI-TOFMS." Analytical chemistry **77**(14): 4523-4527.

Jackson, S. N., H.-Y. J. Wang and A. S. Woods (2007). "In situ structural characterization of glycerophospholipids and sulfatides in brain tissue using MALDI-MS/MS." Journal of the American Society for Mass Spectrometry **18**(1): 17-26.

Jain, I. and G. Agarwal (2011). "Ion beam induced surface and interface engineering." Surface Science Reports **66**(3-4): 77-172.

Jain, M., S. Ngoy, S. A. Sheth, R. A. Swanson, E. P. Rhee, R. Liao, C. B. Clish, V. K. Mootha and R. Nilsson (2014). "A systematic survey of lipids across mouse tissues." American Journal of Physiology-Endocrinology and Metabolism **306**(8): E854-E868.

Jang, I., S. Kim, C. Kim, H. Lee, H. Yoon, T. Song and U. Paik (2019). "Interface engineering of yttrium stabilized zirconia/gadolinium doped ceria bi-layer electrolyte solid oxide fuel cell for boosting electrochemical performance." Journal of Power Sources **435**: 226776.

Jermyn, M., K. Mok, J. Mercier, J. Desroches, J. Pichette, K. Saint-Arnaud, L. Bernstein, M.-C. Guiot, K. Petrecca and F. Leblond (2015). "Intraoperative brain cancer detection with Raman spectroscopy in humans." Science translational medicine **7**(274): 274ra219-274ra219.

John, A. A., S. K. Jaganathan, E. Supriyanto and A. Manikandan (2016). "Surface modification of titanium and its alloys for the enhancement of osseointegration in orthopaedics." Curr. Sci. **111**(6).

Johra, F. T., J.-W. Lee and W.-G. Jung (2014). "Facile and safe graphene preparation on solution based platform." Journal of Industrial and Engineering Chemistry **20**(5): 2883-2887.

Kalin, M. and J. Vižintin (2000). "Use of equations for wear volume determination in fretting experiments." Wear **237**(1): 39-48.

Kaniyoor, A. and S. Ramaprabhu (2012). "A Raman spectroscopic investigation of graphite oxide derived graphene." Aip Advances **2**(3): 032183.

Kar, S., M. S. Molla, D. R. Katti and K. S. Katti (2019). "Tissue-engineered nanoclay-based 3D in vitro breast cancer model for studying breast cancer metastasis to bone." Journal of tissue engineering and regenerative medicine **13**(2): 119-130.

Karas, M., H. Ehring, E. Nordhoff, B. Stahl, K. Strupat, F. Hillenkamp, M. Grehl and B. Krebs (1993). "Matrix-assisted laser desorption/ionization mass spectrometry with additives to 2, 5-dihydroxybenzoic acid." Organic Mass Spectrometry **28**(12): 1476-1481.

Kasemo, B. (2002). "Biological surface science." Surface science **500**(1-3): 656-677.

Kaya, I., W. Michno, D. Brinet, Y. Iacone, G. Zanni, K. Blennow, H. Zetterberg and J. r. Hanrieder (2017). "Histology-compatible MALDI mass spectrometry based imaging of neuronal lipids for subsequent immunofluorescent staining." Analytical chemistry **89**(8): 4685-4694.

Ke, Q. and J. Wang (2016). "Graphene-based materials for supercapacitor electrodes–A review." Journal of Materiomics **2**(1): 37-54.

Kim, S.-K., H. J. Kim, J.-C. Lee, P. V. Braun and H. S. Park (2015). "Extremely durable, flexible supercapacitors with greatly improved performance at high temperatures." ACS nano **9**(8): 8569-8577.

Kim, T., G. Jung, S. Yoo, K. S. Suh and R. S. Ruoff (2013). "Activated graphene-based carbons as supercapacitor electrodes with macro-and mesopores." Acs Nano **7**(8): 6899-6905.

Kirouac, G. J. (2015). "Placing the paraventricular nucleus of the thalamus within the brain circuits that control behavior." Neuroscience & Biobehavioral Reviews **56**: 315-329.

Kochan, K., E. Maslak, C. Krafft, R. Kostogrys, S. Chlopicki and M. Baranska (2015). "Raman spectroscopy analysis of lipid droplets content, distribution and saturation level in Non-Alcoholic Fatty Liver Disease in mice." Journal of biophotonics **8**(7): 597-609.

Kostov, K. G., T. M. C. Nishime, A. H. R. Castro, A. Toth and L. R. d. O. Hein (2014). "Surface modification of polymeric materials by cold atmospheric plasma jet." Applied Surface Science **314**: 367-375.

Kracun, I., H. Rosner, V. Drnovsek, Z. Vukelic, C. Cosovic, M. Trbojevic-Cepe and M. Kubat (1992). "Gangliosides in the human brain development and aging." Neurochemistry international **20**(3): 421-431.

Krafft, C., L. Neudert, T. Simat and R. Salzer (2005). "Near infrared Raman spectra of human brain lipids." Spectrochimica Acta Part A: Molecular and Biomolecular Spectroscopy **61**(7): 1529-1535.

Krishnamoorthy, K., M. Veerapandian, R. Mohan and S.-J. Kim (2012). "Investigation of Raman and photoluminescence studies of reduced graphene oxide sheets." Applied Physics A **106**(3): 501-506.

Kubinova, S., K. Zaviskova, L. Uherkova, V. Zablotskii, O. Churpita, O. Lunov and A. Dejneka (2017). "Non-thermal air plasma promotes the healing of acute skin wounds in rats." Scientific reports **7**: 45183.

Kulkarni, M., A. Mazare, P. Schmuki and A. Iglič (2014). "Biomaterial surface modification of titanium and titanium alloys for medical applications." Nanomedicine **111**: 111.

Kumar, K. S., N. Choudhary, Y. Jung and J. Thomas (2018). "Recent advances in two-dimensional nanomaterials for supercapacitor electrode applications." ACS Energy Letters **3**(2): 482-495.

Kunčická, L., R. Kocich and T. C. Lowe (2017). "Advances in metals and alloys for joint replacement." Progress in Materials Science **88**: 232-280.

Kusoglu, A. and A. Z. Weber (2017). "New insights into perfluorinated sulfonic-acid ionomers." Chemical reviews **117**(3): 987-1104.

Kyerematen, N. A., T. Brousse and D. Pech (2017). "Microsupercapacitors as miniaturized energy-storage components for on-chip electronics." Nature Nanotechnology **12**(1): 7-15.

LaCour, M., R. Komistek, B. Meccia and A. Sharma (2016). FORWARD SOLUTION MODEL: FUTURE METHOD FOR PREDICTING KNEE & HIP IMPLANT LONGEVITY. Orthopaedic Proceedings, The British Editorial Society of Bone & Joint Surgery.

Lee, A. S., Y.-K. Choe, I. Matanovic and Y. S. Kim (2019). "The energetics of phosphoric acid interactions reveals a new acid loss mechanism." Journal of Materials Chemistry A **7**(16): 9867-9876.

Lee, J. H., N. Park, B. G. Kim, D. S. Jung, K. Im, J. Hur and J. W. Choi (2013). "Restacking-inhibited 3D reduced graphene oxide for high performance supercapacitor electrodes." ACS nano **7**(10): 9366-9374.

Lee, K.-S., S. Maurya, Y. S. Kim, C. R. Kreller, M. S. Wilson, D. Larsen, S. E. Elangovan and R. Mukundan (2018). "Intermediate temperature fuel cells via an ion-pair coordinated polymer electrolyte." Energy & Environmental Science **11**(4): 979-987.

Lee, K.-S., J. S. Spendelow, Y.-K. Choe, C. Fujimoto and Y. S. Kim (2016). "An operationally flexible fuel cell based on quaternary ammonium-biphosphate ion pairs." Nature energy **1**(9): 16120.

Lerf, A., A. Buchsteiner, J. Pieper, S. Schöttl, I. Dekany, T. Szabo and H. Boehm (2006). "Hydration behavior and dynamics of water molecules in graphite oxide." Journal of Physics and Chemistry of Solids **67**(5): 1106-1110.

Levkovitz, Y., D. Fenchel, Z. Kaplan, J. Zohar and H. Cohen (2015). "Early post-stressor intervention with minocycline, a second-generation tetracycline, attenuates post-traumatic stress response in an animal model of PTSD." European Neuropsychopharmacology **25**(1): 124-132.

Li, C. and G. Shi (2012). "Three-dimensional graphene architectures." Nanoscale **4**(18): 5549-5563.

Li, J., F. Zanata, J. L. Curley, E. C. Martin, X. Wu, M. Dietrich, R. V. Devireddy, J. W. Wade and J. M. Gimble (2016). "The relative functionality of freshly isolated and cryopreserved human adipose-derived stromal/stem cells." Cells Tissues Organs **201**(6): 436-444.

Li, P., F. Long, W. Chen, J. Chen, P. K. Chu and H. Wang (2020). "Fundamentals and applications of surface-enhanced Raman spectroscopy–based biosensors." Current Opinion in Biomedical Engineering **13**: 51-59.

Li, Q., J. O. Jensen, R. F. Savinell and N. J. Bjerrum (2009). "High temperature proton exchange membranes based on polybenzimidazoles for fuel cells." Progress in polymer science **34**(5): 449-477.

Li, Y., Y. Zhao, Q. Chen, Y. Yang, Y. Liu, Z. Hong, Z. Liu, Y.-T. Hsieh, L. Meng and Y. Li (2015). "Multifunctional fullerene derivative for interface engineering in perovskite solar cells." Journal of the American Chemical Society **137**(49): 15540-15547.

Lin, H., X. Yu, M. Li, J. Duo, Y. Guo and T. Deng (2019). "Synthesis of Polyporous Ion-Sieve and Its Application for Selective Recovery of Lithium from Geothermal Water." ACS applied materials & interfaces **11**(29): 26364-26372.

Lin, J., C. Zhang, Z. Yan, Y. Zhu, Z. Peng, R. H. Hauge, D. Natelson and J. M. Tour (2012). "3-dimensional graphene carbon nanotube carpet-based microsupercapacitors with high electrochemical performance." Nano letters **13**(1): 72-78.

Liu, C., Z. Yu, D. Neff, A. Zhamu and B. Z. Jang (2010). "Graphene-based supercapacitor with an ultrahigh energy density." Nano letters **10**(12): 4863-4868.

Liu, J. (2014). "Charging graphene for energy." Nature nanotechnology **9**(10): 739-741.

Liu, M., H. Zhao, S. Chen, H. Yu and X. Quan (2012). "Interface engineering catalytic graphene for smart colorimetric biosensing." ACS nano **6**(4): 3142-3151.

Liu, Z., S. Liu, R. Dong, S. Yang, H. Lu, A. Narita, X. Feng and K. Müllen (2017). "High Power In-Plane Micro-Supercapacitors Based on Mesoporous Polyaniline Patterned Graphene." Small **13**(14).

Livak, K. J. and T. D. Schmittgen (2001). "Analysis of relative gene expression data using real-time quantitative PCR and the 2− ΔΔCT method." methods **25**(4): 402-408.

Lu, W., S. Liu, X. Qin, L. Wang, J. Tian, Y. Luo, A. M. Asiri, A. O. Al-Youbi and X. Sun (2012). "High-yield, large-scale production of few-layer graphene flakes within seconds: using chlorosulfonic acid and H 2 O 2 as exfoliating agents." Journal of Materials Chemistry **22**(18): 8775-8777.

Lui, H., J. Zhao, D. McLean and H. Zeng (2012). "Real-time Raman spectroscopy for in vivo skin cancer diagnosis." Cancer research **72**(10): 2491-2500.

Lunov, O., V. Zablotskii, O. Churpita, A. Jäger, L. Polívka, E. Syková, A. Dejneka and Š. Kubinová (2016). "The interplay between biological and physical scenarios of bacterial death induced by non-thermal plasma." Biomaterials **82**: 71-83.

Luo, J., H. D. Jang and J. Huang (2013). "Effect of sheet morphology on the scalability of graphene-based ultracapacitors." Acs Nano **7**(2): 1464-1471.

Lv, T., M. Liu, D. Zhu, L. Gan and T. Chen (2018). "Nanocarbon-Based Materials for Flexible All-Solid-State Supercapacitors." Advanced Materials **30**(17): 1705489.

Macala, L., R. Yu and S. Ando (1983). "Analysis of brain lipids by high performance thin-layer chromatography and densitometry." Journal of lipid research **24**(9): 1243-1250.

Manjoch, H., E. Vainer, M. Matar, G. Ifergane, J. Zohar, Z. Kaplan and H. Cohen (2016). "Predator-scent stress, ethanol consumption and the opioid system in an animal model of PTSD." Behavioural brain research **306**: 91-105.

Martín, V., N. Fabelo, G. Santpere, B. Puig, R. Marín, I. Ferrer and M. Díaz (2010). "Lipid alterations in lipid rafts from Alzheimer's disease human brain cortex." Journal of Alzheimer's Disease **19**(2): 489-502.

Marzi, J., E. M. Brauchle, K. Schenke-Layland and M. W. Rolle (2019). "Non-invasive functional molecular phenotyping of human smooth muscle cells utilized in cardiovascular tissue engineering." Acta biomaterialia **89**: 193-205.

Masarapu, C., H. F. Zeng, K. H. Hung and B. Wei (2009). "Effect of temperature on the capacitance of carbon nanotube supercapacitors." ACS nano **3**(8): 2199-2206.

Matouskova, L., M. Ackermann, J. Horakova, L. Capek, P. Henys and J. Safka (2018). "How does the surface treatment change the cytocompatibility of implants made by selective laser melting?" Expert review of medical devices **15**(4): 313-321.

McEwen, H., P. Barnett, C. Bell, R. Farrar, D. Auger, M. Stone and J. Fisher (2005). "The influence of design, materials and kinematics on the in vitro wear of total knee replacements." Journal of biomechanics **38**(2): 357-365.

Meng, Y., Y. Zhao, C. Hu, H. Cheng, Y. Hu, Z. Zhang, G. Shi and L. Qu (2013). "All-graphene core-sheath microfibers for all-solid-state, stretchable fibriform supercapacitors and wearable electronic textiles." Advanced materials **25**(16): 2326-2331.

Mensah-Darkwa, K., C. Zequine, P. K. Kahol and R. K. Gupta (2019). "Supercapacitor energy storage device using biowastes: a sustainable approach to green energy." Sustainability **11**(2): 414.

Mesa-Herrera, F., L. Taoro-González, C. Valdés-Baizabal, M. Diaz and R. Marín (2019). "Lipid and Lipid Raft Alteration in Aging and Neurodegenerative Diseases: A Window for the Development of New Biomarkers." International journal of molecular sciences **20**(15): 3810.

Millan, E. Z., Z. Ong and G. P. McNally (2017). Chapter 5 - Paraventricular thalamus: Gateway to feeding, appetitive motivation, and drug addiction. Progress in Brain Research. T. Calvey and W. M. U. Daniels, Elsevier. **235:** 113-137.

Mimaroglu, A. and H. Unal (2015). "Investigation of the water lubricated tribological behavior of medical grade UHMWPE." Advances in Materials and Processing Technologies **1**(1-2): 109-114.

Mishra, S. K., S. N. Tripathi, V. Choudhary and B. D. Gupta (2014). "SPR based fibre optic ammonia gas sensor utilizing nanocomposite film of PMMA/reduced graphene oxide prepared by in situ polymerization." Sensors and Actuators B: Chemical **199**: 190-200.

Molinari, A., G. Straffelini, B. Tesi and T. Bacci (1997). "Dry sliding wear mechanisms of the Ti6Al4V alloy." Wear **208**(1-2): 105-112.

Molony, C., J. McIntyre, A. Maguire, R. Hakimjavadi, D. Burtenshaw, G. Casey, M. Di Luca, B. Hennelly, H. J. Byrne and P. A. Cahill (2018). "Label-free discrimination analysis of de-differentiated vascular smooth muscle cells, mesenchymal stem cells and their vascular and osteogenic progeny using vibrational spectroscopy." Biochimica et Biophysica Acta (BBA)-Molecular Cell Research **1865**(2): 343-353.

Morey, R. A., C. C. Haswell, S. R. Hooper and M. D. De Bellis (2016). "Amygdala, hippocampus, and ventral medial prefrontal cortex volumes differ in maltreated youth with and without chronic posttraumatic stress disorder." Neuropsychopharmacology **41**(3): 791.

Movasaghi, Z., S. Rehman and I. U. Rehman (2007). "Raman spectroscopy of biological tissues." Applied Spectroscopy Reviews **42**(5): 493-541.

Müller, C. P., M. Reichel, C. Mühle, C. Rhein, E. Gulbins and J. Kornhuber (2015). "Brain membrane lipids in major depression and anxiety disorders." Biochimica et Biophysica Acta (BBA) - Molecular and Cell Biology of Lipids **1851**(8): 1052-1065.

Munsch, M. (2017). Laser additive manufacturing of customized prosthetics and implants for biomedical applications. Laser Additive Manufacturing, Elsevier**:** 399-420.

Musib, M. K. (2011). "A review of the history and role of UHMWPE as a component in total joint replacements." International Journal of Biological Engineering **1**(1): 6-10.

Nagasubramanian, G., R. Jungst and D. Doughty (1999). "Impedance, power, energy, and pulse performance characteristics of small commercial Li-ion cells." Journal of power sources **83**(1): 193-203.

Naudí, A., R. Cabré, M. Jové, V. Ayala, H. Gonzalo, M. Portero-Otín, I. Ferrer and R. Pamplona (2015). Lipidomics of human brain aging and Alzheimer's disease pathology. International review of neurobiology, Elsevier. **122:** 133-189.

Nègre, L., B. Daffos, V. Turq, P.-L. Taberna and P. Simon (2016). "Ionogel-based solid-state supercapacitor operating over a wide range of temperature." Electrochimica Acta **206**: 490-495.

Nelson, M. D. and A. M. Tumpap (2017). "Posttraumatic stress disorder symptom severity is associated with left hippocampal volume reduction: a meta-analytic study." CNS spectrums **22**(4): 363-372.

Newell, R., J. Faure-Vincent, B. Iliev, T. Schubert and D. Aradilla (2018). "A new high performance ionic liquid mixture electrolyte for large temperature range supercapacitor applications (− 70° C to 80° C) operating at 3.5 V cell voltage." Electrochimica Acta **267**: 15-19.

Niu, Z., W. Zhou, X. Chen, J. Chen and S. Xie (2015). "Highly Compressible and All-Solid-State Supercapacitors Based on Nanostructured Composite Sponge." Advanced materials **27**(39): 6002-6008.

Noponen, M., M. Sanfilipo, K. Samanich, H. Ryer, G. Ko, B. Angrist, A. Wolkin, E. Duncan and J. Rotrosen (1993). "Elevated PLA2 activity in schizophrenics and other psychiatric patients." Biological Psychiatry **34**(9): 641-649.

Notingher, I. (2007). "Raman spectroscopy cell-based biosensors." Sensors **7**(8): 1343-1358.

Nygren, H., P. Pöhö, T. Seppänen-Laakso, U. Lahtinen, M. Oresic and T. Hyötyläinen (2013). "Ultrahigh-performance liquid chromatography-mass spectrometry in lipidomics." LC GC Europe **26**(3): 142-148.

Nygren, H., T. Seppänen-Laakso, S. Castillo, T. Hyötyläinen and M. Orešič (2011). Liquid chromatography-mass spectrometry (LC-MS)-based lipidomics for studies of body fluids and tissues. Metabolic Profiling, Springer**:** 247-257.

Ogundele, O. M., P. J. Ebenezer, C. C. Lee and J. Francis (2017). "Stress-altered synaptic plasticity and DAMP signaling in the hippocampus-PFC axis; elucidating the significance of IGF-1/IGF-1R/CaMKIIα expression in neural changes associated with a prolonged exposure therapy." Neuroscience **353**: 147-165.

Ohira, S., H. Tanaka, Y. Harada, T. Minamikawa, Y. Kumamoto, S. Matoba, H. Yaku and T. Takamatsu (2017). "Label-free detection of myocardial ischaemia in the perfused rat heart by spontaneous Raman spectroscopy." Scientific reports **7**: 42401.

Oliveira, T. G., R. B. Chan, F. V. Bravo, A. Miranda, R. R. Silva, B. Zhou, F. Marques, V. Pinto, J. J. Cerqueira and G. Di Paolo (2016). "The impact of chronic stress on the rat brain lipidome." Molecular psychiatry **21**(1): 80.

Oliveira, T. G., R. B. Chan, F. V. Bravo, A. Miranda, R. R. Silva, B. Zhou, F. Marques, V. Pinto, J. J. Cerqueira and G. Di Paolo (2016). "The impact of chronic stress on the rat brain lipidome." Molecular psychiatry **21**(1): 80-88.

Oliveira, T. G., R. B. Chan, F. V. Bravo, A. Miranda, R. R. Silva, B. Zhou, F. Marques, V. Pinto, J. J. Cerqueira, G. Di Paolo and N. Sousa (2015). "The impact of chronic stress on the rat brain lipidome." Molecular Psychiatry **21**: 80.

Oncel, S. S. (2017). "Green energy engineering: Opening a green way for the future." Journal of Cleaner Production **142**: 3095-3100.

Orešič, M., T. Seppänen-Laakso, D. Sun, J. Tang, S. Therman, R. Viehman, U. Mustonen, T. G. Van Erp, T. Hyötyläinen and P. Thompson (2012). "Phospholipids and insulin resistance in psychosis: a lipidomics study of twin pairs discordant for schizophrenia." Genome medicine **4**(1): 1.

Ossonon, B. D. and D. Bélanger (2017). "Synthesis and characterization of sulfophenyl-functionalized reduced graphene oxide sheets." RSC Advances **7**(44): 27224-27234.

Ottestad, I., S. Hassani, G. I. Borge, A. Kohler, G. Vogt, T. Hyötyläinen, M. Orešič, K. W. Brønner, K. B. Holven and S. M. Ulven (2012). "Fish oil supplementation alters the plasma lipidomic profile and increases long-chain PUFAs of phospholipids and triglycerides in healthy subjects." PLoS One **7**(8).

Palakkal, V. M., J. E. Rubio, Y. J. Lin and C. G. Arges (2018). "Low-resistant ion-exchange membranes for energy efficient membrane capacitive deionization." ACS Sustainable Chemistry & Engineering **6**(11): 13778-13786.

Pavlovich, M., T. Ono, C. Galleher, B. Curtis, D. Clark, Z. Machala and D. Graves (2014). "Air spark-like plasma source for antimicrobial NOx generation." Journal of Physics D: Applied Physics **47**(50): 505202.

Pech, D., M. Brunet, H. Durou, P. Huang, V. Mochalin, Y. Gogotsi, P.-L. Taberna and P. Simon (2010). "Ultrahigh-power micrometre-sized supercapacitors based on onion-like carbon." Nature nanotechnology **5**(9): 651-654.

Penzo, M. A., V. Robert, J. Tucciarone, D. De Bundel, M. Wang, L. Van Aelst, M. Darvas, L. F. Parada, R. D. Palmiter and M. He (2015). "The paraventricular thalamus controls a central amygdala fear circuit." Nature **519**(7544): 455.

Pham, D. T., T. H. Lee, D. H. Luong, F. Yao, A. Ghosh, V. T. Le, T. H. Kim, B. Li, J. Chang and Y. H. Lee (2015). "Carbon nanotube-bridged graphene 3D building blocks for ultrafast compact supercapacitors." ACS nano **9**(2): 2018-2027.

Pick, C. G. (2010). The Consequences of Exposure to Mission-Related Shock Waves Upon Cognitive Potential, TEL-AVIV UNIV (ISRAEL).

Piomelli, D., G. Astarita and R. Rapaka (2007). "A neuroscientist's guide to lipidomics." Nature Reviews Neuroscience **8**(10): 743-754.

Prasain, J. K., L. Wilson, H. D. Hoang, R. Moore and M. A. Miller (2015). "Comparative lipidomics of Caenorhabditis elegans metabolic disease models by SWATH non-targeted tandem mass spectrometry." Metabolites **5**(4): 677-696.

Qu, L., Y. Zhao, A. M. Khan, C. Han, K. M. Hercule, M. Yan, X. Liu, W. Chen, D. Wang and Z. Cai (2015). "Interwoven Three-Dimensional Architecture of Cobalt Oxide Nanobrush-Graphene@ Ni x Co2 x (OH) 6 x for High-Performance Supercapacitors." Nano letters **15**(3): 2037-2044.

Raccichini, R., A. Varzi, S. Passerini and B. Scrosati (2015). "The role of graphene for electrochemical energy storage." Nature materials **14**(3): 271-279.

Raphel, J., M. Holodniy, S. B. Goodman and S. C. Heilshorn (2016). "Multifunctional coatings to simultaneously promote osseointegration and prevent infection of orthopaedic implants." Biomaterials **84**: 301-314.

Rathod, D., M. Vijay, N. Islam, R. Kannan, U. Kharul, S. Kurungot and V. Pillai (2009). "Design of an “all solid-state” supercapacitor based on phosphoric acid doped polybenzimidazole (PBI) electrolyte." Journal of applied electrochemistry **39**(7): 1097-1103.

Raza, W., F. Ali, N. Raza, Y. Luo, K.-H. Kim, J. Yang, S. Kumar, A. Mehmood and E. E. Kwon (2018). "Recent advancements in supercapacitor technology." Nano Energy **52**: 441-473.

REGULA, C., J. IHDE and S. STEPANOV (2017). "Atmospheric Pressure Plasma Jets for Surface Activation Prior to Bonding and Painting." Journal of the Japan Society of Colour Material **90**(8): 282-287.

Ren, J., X.-B. Liu, X.-L. Lu, P.-C. Yu, G.-X. Zhu, Y. Chen and D. Xu (2017). "Microstructure and tribological properties of self-lubricating antiwear composite coating on Ti6Al4V alloy." Surface Engineering **33**(1): 20-26.

Réus, G. Z., H. M. Abelaira, A. L. Maciel, M. A. B. dos Santos, A. S. Carlessi, A. V. Steckert, G. K. Ferreira, S. D. De Prá, E. L. Streck, D. S. Macêdo and J. Quevedo (2015). "Minocycline protects against oxidative damage and alters energy metabolism parameters in the brain of rats subjected to chronic mild stress." Metabolic Brain Disease **30**(2): 545-553.

Robichaud, G., K. P. Garrard, J. A. Barry and D. C. Muddiman (2013). "MSiReader: an open-source interface to view and analyze high resolving power MS imaging files on Matlab platform." Journal of the American Society for Mass Spectrometry **24**(5): 718-721.

Rodrigues, M. M., C. P. Fontoura, C. S. C. Garcia, S. T. Martins, J. A. P. Henriques, C. A. Figueroa, M. Roesch-Ely and C. Aguzzoli (2019). "Investigation of plasma treatment on UHMWPE surfaces: Impact on physicochemical properties, sterilization and fibroblastic adhesion." Materials Science and Engineering: C **102**: 264-275.

Rohner, T. C., D. Staab and M. Stoeckli (2005). "MALDI mass spectrometric imaging of biological tissue sections." Mechanisms of ageing and development **126**(1): 177-185.

Rong, Q., W. Lei, J. Huang and M. Liu (2018). "Low Temperature Tolerant Organohydrogel Electrolytes for Flexible Solid-State Supercapacitors." Advanced Energy Materials **8**(31): 1801967.

Ronzoni, G., A. del Arco, F. Mora and G. Segovia (2016). "Enhanced noradrenergic activity in the amygdala contributes to hyperarousal in an animal model of PTSD." Psychoneuroendocrinology **70**: 1-9.

Rosli, R., A. B. Sulong, W. R. W. Daud, M. A. Zulkifley, T. Husaini, M. I. Rosli, E. Majlan and M. Haque (2017). "A review of high-temperature proton exchange membrane fuel cell (HT-PEMFC) system." International Journal of Hydrogen Energy **42**(14): 9293-9314.

Ruipérez, V., F. Darios and B. Davletov (2010). "Alpha-synuclein, lipids and Parkinson's disease." Progress in lipid research **49**(4): 420-428.

Rygula, A., K. Majzner, K. M. Marzec, A. Kaczor, M. Pilarczyk and M. Baranska (2013). "Raman spectroscopy of proteins: a review." Journal of Raman Spectroscopy **44**(8): 1061-1076.

Saatkamp, C. J., M. L. de Almeida, J. A. M. Bispo, A. L. B. Pinheiro, A. B. Fernandes and L. Silveira (2016). "Quantifying creatinine and urea in human urine through Raman spectroscopy aiming at diagnosis of kidney disease." Journal of biomedical optics **21**(3): 037001.

Samms, S., S. Wasmus and R. Savinell (1996). "Thermal stability of proton conducting acid doped polybenzimidazole in simulated fuel cell environments." Journal of the Electrochemical Society **143**(4): 1225-1232.

Santos, I. s. P., P. J. Caspers, T. C. Bakker Schut, R. van Doorn, V. Noordhoek Hegt, S. Koljenović and G. J. Puppels (2016). "Raman spectroscopic characterization of melanoma and benign melanocytic lesions suspected of melanoma using high-wavenumber Raman spectroscopy." Analytical chemistry **88**(15): 7683-7688.

Schechter, A., R. F. Savinell, J. Wainright and D. Ray (2009). "# 2# 1 and# 2# 1 NMR Study of Phosphoric Acid–Doped Polybenzimidazole under Controlled Water Activity." Journal of the electrochemical society **156**(2): B283-B290.

Schrader, B. (1989). Raman, infrared atlas of organic compounds, VCH-Verlag-Ges.

Seeley, E. H. and R. M. Caprioli (2011). "MALDI imaging mass spectrometry of human tissue: method challenges and clinical perspectives." Trends in biotechnology **29**(3): 136-143.

Seetharaman, S., M. Fleshner, C. R. Park and D. M. Diamond (2016). "Influence of daily social stimulation on behavioral and physiological outcomes in an animal model of PTSD." Brain and behavior **6**(5): e00458.

Shaik, S., X. Wu, J. Gimble and R. Devireddy (2018). "Effects of decade long freezing storage on adipose derived stem cells functionality." Scientific reports **8**(1): 8162.

Shao, Y., M. F. El-Kady, L. J. Wang, Q. Zhang, Y. Li, H. Wang, M. F. Mousavi and R. B. Kaner (2015). "Graphene-based materials for flexible supercapacitors." Chemical Society Reviews **44**(11): 3639-3665.

Share, K., A. Westover, M. Li and C. L. Pint (2016). "Surface engineering of nanomaterials for improved energy storage–A review." Chemical Engineering Science **154**: 3-19.

Sharkey, P. F., W. J. Hozack, R. H. Rothman, S. Shastri and S. M. Jacoby (2002). "Why are total knee arthroplasties failing today?" Clin. Orthop. Relat. Res. **404**: 7-13.

Sharma, N., V. Sharma, Y. Jain, M. Kumari, R. Gupta, S. Sharma and K. Sachdev (2017). Synthesis and characterization of graphene oxide (GO) and reduced graphene oxide (rGO) for gas sensing application. Macromolecular Symposia, Wiley Online Library.

Shin, L. M., S. L. Rauch and R. K. Pitman (2006). "Amygdala, medial prefrontal cortex, and hippocampal function in PTSD." Annals of the New York Academy of Sciences **1071**(1): 67-79.

Simon, P. and Y. Gogotsi (2008). "Materials for electrochemical capacitors." Nature materials **7**(11): 845-854.

Singh, S., C. Prakash, H. Wang, X.-f. Yu and S. Ramakrishna (2019). "Plasma treatment of polyether-ether-ketone: A means of obtaining desirable biomedical characteristics." European Polymer Journal.

Soavi, F., L. G. Bettini, P. Piseri, P. Milani, C. Santoro, P. Atanassov and C. Arbizzani (2016). "Miniaturized supercapacitors: key materials and structures towards autonomous and sustainable devices and systems." Journal of power sources **326**: 717-725.

Sobieraj, M. and C. Rimnac (2009). "Ultra high molecular weight polyethylene: mechanics, morphology, and clinical behavior." Journal of the mechanical behavior of biomedical materials **2**(5): 433-443.

Soltwisch, J., H. Kettling, S. Vens-Cappell, M. Wiegelmann, J. Müthing and K. Dreisewerd (2015). "Mass spectrometry imaging with laser-induced postionization." Science **348**(6231): 211-215.

Somayajula, D. A. (2008). Biocompatibility of Osteoblast Cells on Titanium Implants.

Sonnino, S. and V. Chigorno (2000). "Ganglioside molecular species containing C18-and C20-sphingosine in mammalian nervous tissues and neuronal cell cultures." Biochimica et Biophysica Acta (BBA)-Reviews on Biomembranes **1469**(2): 63-77.

Spiers, R. M., J. Marzi, E. M. Brauchle, S. E. Cross, R. H. Vaughan, P. A. Bateman, S. J. Hughes, K. Schenke-Layland and P. R. Johnson (2019). "Donor age significantly influences the Raman spectroscopic biomolecular fingerprint of human pancreatic extracellular matrix proteins following collagenase-based digestion." Acta biomaterialia **99**: 269-283.

Staiti, P. and F. Lufrano (2016). "Nafion® and Fumapem® polymer electrolytes for the development of advanced solid-state supercapacitors." Electrochimica Acta **206**: 432-439.

Stewart, S., R. J. Priore, M. P. Nelson and P. J. Treado (2012). "Raman imaging." Annual Review of Analytical Chemistry **5**: 337-360.

Stoller, M. D., S. Park, Y. Zhu, J. An and R. S. Ruoff (2008). "Graphene-based ultracapacitors." Nano letters **8**(10): 3498-3502.

Strauss, V., K. Marsh, M. D. Kowal, M. El-Kady and R. B. Kaner (2018). "A simple route to porous graphene from carbon nanodots for supercapacitor applications." Advanced Materials **30**(8): 1704449.

Sun, H., L. Mei, J. Liang, Z. Zhao, C. Lee, H. Fei, M. Ding, J. Lau, M. Li and C. Wang (2017). "Three-dimensional holey-graphene/niobia composite architectures for ultrahigh-rate energy storage." Science **356**(6338): 599-604.

Surmacki, J. M., L. Ansel-Bollepalli, F. Pischiutta, E. R. Zanier, A. Ercole and S. E. Bohndiek (2017). "Label-free monitoring of tissue biochemistry following traumatic brain injury using Raman spectroscopy." Analyst **142**(1): 132-139.

Taberna, P., P. Simon and J.-F. Fauvarque (2003). "Electrochemical characteristics and impedance spectroscopy studies of carbon-carbon supercapacitors." Journal of The Electrochemical Society **150**(3): A292-A300.

Tajima, Y., M. Ishikawa, K. Maekawa, M. Murayama, Y. Senoo, T. Nishimaki-Mogami, H. Nakanishi, K. Ikeda, M. Arita and R. Taguchi (2013). "Lipidomic analysis of brain tissues and plasma in a mouse model expressing mutated human amyloid precursor protein/tau for Alzheimer's disease." Lipids in health and disease **12**(1): 68.

Talari, A. C. S., Z. Movasaghi, S. Rehman and I. U. Rehman (2015). "Raman spectroscopy of biological tissues." Applied spectroscopy reviews **50**(1): 46-111.

Tan, G., Z. Lou, W. Liao, X. Dong, Z. Zhu, W. Li and Y. Chai (2012). "Hydrophilic interaction and reversed-phase ultraperformance liquid chromatography TOF-MS for serum metabonomic analysis of myocardial infarction in rats and its applications." Molecular BioSystems **8**(2): 548-556.

Teran, A. A., M. H. Tang, S. A. Mullin and N. P. Balsara (2011). "Effect of molecular weight on conductivity of polymer electrolytes." Solid State Ionics **203**(1): 18-21.

Timchenko, E., P. Timchenko, L. Volova, S. Pershutkina and P. Y. Shalkovskaya (2018). "Using Raman spectroscopy for the evaluation of extracellular matrices based on heart valves." Journal of Optical Technology **85**(2): 73-76.

Tiruye, G. A., D. Muñoz-Torrero, J. Palma, M. Anderson and R. Marcilla (2016). "Performance of solid state supercapacitors based on polymer electrolytes containing different ionic liquids." Journal of Power Sources **326**: 560-568.

Tu, A. T. and A. Tu (1982). "Raman spectroscopy in biology: principles and applications."

Tuma, R. (2005). "Raman spectroscopy of proteins: from peptides to large assemblies." Journal of Raman Spectroscopy **36**(4): 307-319.

Tung, V. C., M. J. Allen, Y. Yang and R. B. Kaner (2009). "High-throughput solution processing of large-scale graphene." Nature nanotechnology **4**(1): 25-29.

Utzschneider, S., N. Harrasser, C. Schroeder, F. Mazoochian and V. Jansson (2009). "Wear of contemporary total knee replacements–a knee simulator study of six current designs." Clinical Biomechanics **24**(7): 583-588.

Vaithilingam, J., R. D. Goodridge, R. J. Hague, S. D. Christie and S. Edmondson (2016). "The effect of laser remelting on the surface chemistry of Ti6al4V components fabricated by selective laser melting." Journal of Materials Processing Technology **232**: 1-8.

Van Rooij, S., M. Kennis, R. Sjouwerman, M. Van Den Heuvel, R. Kahn and E. Geuze (2015). "Smaller hippocampal volume as a vulnerability factor for the persistence of post-traumatic stress disorder." Psychological medicine **45**(13): 2737-2746.

van Rooij, S. J., J. S. Stevens, T. D. Ely, R. Hinrichs, V. Michopoulos, S. J. Winters, Y. E. Ogbonmwan, J. Shin, N. R. Nugent and L. A. Hudak (2018). "The role of the hippocampus in predicting future posttraumatic stress disorder symptoms in recently traumatized civilians." Biological psychiatry **84**(2): 106-115.

Vellacheri, R., A. Al-Haddad, H. Zhao, W. Wang, C. Wang and Y. Lei (2014). "High performance supercapacitor for efficient energy storage under extreme environmental temperatures." Nano Energy **8**: 231-237.

Venugopalan, G., K. Chang, J. D. Nijoka, S. Livingston, G. M. Geise and C. G. Arges (2019). "Stable and highly conductive polycation-polybenzimidazole membrane blends for intermediate temperature polymer electrolyte membrane fuel cells." ACS Applied Energy Materials **3**(1): 573-585.

Visco, A., L. Torrisi, N. Campo and A. Picciotto (2010). "Comparison of surface modifications induced by ion implantation in UHMWPE." International Journal of Polymer Analysis and Characterization **15**(2): 73-86.

Vollebregt, S., R. Ishihara, F. Tichelaar, Y. Hou and C. Beenakker (2012). "Influence of the growth temperature on the first and second-order Raman band ratios and widths of carbon nanotubes and fibers." Carbon **50**(10): 3542-3554.

Wan, Z., S. Wang, B. Haylock, J. Kaur, P. Tanner, D. Thiel, R. Sang, I. S. Cole, X. Li and M. Lobino (2019). "Tuning the sub-processes in laser reduction of graphene oxide by adjusting the power and scanning speed of laser." Carbon **141**: 83-91.

Wang, C.-C., J. Liang, Y.-H. Liao and S.-Y. Lu (2017). "3D porous graphene nanostructure from a simple, fast, scalable process for high performance flexible gel-type supercapacitors." ACS Sustainable Chemistry & Engineering **5**(5): 4457-4467.

Wang, H., H. Yi, X. Chen and X. Wang (2014). "Asymmetric supercapacitors based on nano-architectured nickel oxide/graphene foam and hierarchical porous nitrogen-doped carbon nanotubes with ultrahigh-rate performance." Journal of Materials Chemistry A **2**(9): 3223-3230.

Wang, K., D. Xiong, Y. Deng and Y. Niu (2017). "Ultra-lubricated surface of Ti6Al4V fabricated with combination of porous TiO2 layer, ultra-high molecular weight polyethylene film and hydrophilic polymer brushes." Materials & Design **114**: 18-24.

Wang, K. X., X. H. Li and J. S. Chen (2015). "Surface and interface engineering of electrode materials for lithium-ion batteries." Advanced Materials **27**(3): 527-545.

Wang, R., X. He, Y. Gao, X. Zhang, X. Yao and B. Tang (2017). "Antimicrobial property, cytocompatibility and corrosion resistance of Zn-doped ZrO2/TiO2 coatings on Ti6Al4V implants." Materials Science and Engineering: C **75**: 7-15.

Wang, Y., Z. Shi, Y. Huang, Y. Ma, C. Wang, M. Chen and Y. Chen (2009). "Supercapacitor devices based on graphene materials." The Journal of Physical Chemistry C **113**(30): 13103-13107.

Ward, K. R., R. W. Barbee, P. S. Reynolds, I. P. Torres Filho, M. H. Tiba, L. Torres, R. N. Pittman and J. Terner (2007). "Oxygenation monitoring of tissue vasculature by resonance Raman spectroscopy." Analytical chemistry **79**(4): 1514-1518.

Wei, Y., M. Wang, N. Xu, L. Peng, J. Mao, Q. Gong and J. Qiao (2018). "Alkaline Exchange Polymer Membrane Electrolyte for High Performance of All-Solid-State Electrochemical Devices." ACS applied materials & interfaces **10**(35): 29593-29598.

Wells, M. A. and J. C. Dittmer (1967). "A comprehensive study of the postnatal changes in the concentration of the lipids of developing rat brain." Biochemistry **6**(10): 3169-3175.

Wen, F., C. Hao, J. Xiang, L. Wang, H. Hou, Z. Su, W. Hu and Z. Liu (2014). "Enhanced laser scribed flexible graphene-based micro-supercapacitor performance with reduction of carbon nanotubes diameter." Carbon **75**: 236-243.

Wilson, C. B., P. J. Ebenezer, L. D. McLaughlin and J. Francis (2014). "Predator exposure/psychosocial stress animal model of post-traumatic stress disorder modulates neurotransmitters in the rat hippocampus and prefrontal cortex." PLoS One **9**(2): e89104.

Wilson, C. B., L. D. McLaughlin, P. J. Ebenezer, A. R. Nair, R. Dange, J. G. Harre, T. L. Shaak, D. M. Diamond and J. Francis (2014). "Differential effects of sertraline in a predator exposure animal model of post-traumatic stress disorder." Frontiers in behavioral neuroscience **8**: 256.

Wood, P. L., M. D. Filiou, D. M. Otte, A. Zimmer and C. W. Turck (2014). "Lipidomics reveals dysfunctional glycosynapses in schizophrenia and the G72/G30 transgenic mouse." Schizophrenia research **159**(2-3): 365-369.

Woodruff, D. P. (2016). Modern techniques of surface science, Cambridge university press.

Wu, G., P. Li, H. Feng, X. Zhang and P. K. Chu (2015). "Engineering and functionalization of biomaterials via surface modification." Journal of Materials Chemistry B **3**(10): 2024-2042.

Wu, H., J. V. Volponi, A. E. Oliver, A. N. Parikh, B. A. Simmons and S. Singh (2011). "In vivo lipidomics using single-cell Raman spectroscopy." Proceedings of the National Academy of Sciences **108**(9): 3809-3814.

Wu, Z.-S., X. Feng and H.-M. Cheng (2014). "Recent advances in graphene-based planar micro-supercapacitors for on-chip energy storage." National Science Review **1**(2): 277-292.

Wu, Z. S., K. Parvez, X. Feng and K. Müllen (2013). "Graphene-based in-plane micro-supercapacitors with high power and energy densities." Nature communications **4**.

Wu, Z. S., K. Parvez, S. Li, S. Yang, Z. Liu, S. Liu, X. Feng and K. Müllen (2015). "Alternating Stacked Graphene-Conducting Polymer Compact Films with Ultrahigh Areal and Volumetric Capacitances for High-Energy Micro-Supercapacitors." Advanced Materials **27**(27): 4054-4061.

Xia, J., F. Chen, J. Li and N. Tao (2009). "Measurement of the quantum capacitance of graphene." Nature nanotechnology **4**(8): 505-509.

Xiao, N., H. Tan, J. Zhu, L. Tan, X. Rui, X. Dong and Q. Yan (2013). "High-performance supercapacitor electrodes based on graphene achieved by thermal treatment with the aid of nitric acid." ACS applied materials & interfaces **5**(19): 9656-9662.

Xie, B., C. Yang, Z. Zhang, P. Zou, Z. Lin, G. Shi, Q. Yang, F. Kang and C.-P. Wong (2015). "Shape-tailorable graphene-based ultra-high-rate supercapacitor for wearable electronics." ACS nano **9**(6): 5636-5645.

Xie, Y., Y. Liu, Y. Zhao, Y. H. Tsang, S. P. Lau, H. Huang and Y. Chai (2014). "Stretchable all-solid-state supercapacitor with wavy shaped polyaniline/graphene electrode." Journal of Materials Chemistry A **2**(24): 9142-9149.

Xiong, G., C. Meng, R. G. Reifenberger, P. P. Irazoqui and T. S. Fisher (2014). "A review of graphene-based electrochemical microsupercapacitors." Electroanalysis **26**(1): 30-51.

Xu, J., N. Yuan, J. M. Razal, Y. Zheng, X. Zhou, J. Ding, K. Cho, S. Ge, R. Zhang and Y. Gogotsi (2019). "Temperature-independent capacitance of carbon-based supercapacitor from− 100 to 60° C." Energy Storage Materials **22**: 323-329.

Xu, Y., Z. Lin, X. Zhong, X. Huang, N. O. Weiss, Y. Huang and X. Duan (2014). "Holey graphene frameworks for highly efficient capacitive energy storage." Nature communications **5**: 4554.

Xu, Z., Z. Li, C. M. Holt, X. Tan, H. Wang, B. S. Amirkhiz, T. Stephenson and D. Mitlin (2012). "Electrochemical supercapacitor electrodes from sponge-like graphene nanoarchitectures with ultrahigh power density." The journal of physical chemistry letters **3**(20): 2928-2933.

Xu, Z., J. Shen, C. Cheng, S. Hu, Y. Lan and P. K. Chu (2017). "In vitro antimicrobial effects and mechanism of atmospheric-pressure He/O2 plasma jet on Staphylococcus aureus biofilm." Journal of Physics D: Applied Physics **50**(10): 105201.

Yadroitsev, I., P. Krakhmalev and I. Yadroitsava (2014). "Selective laser melting of Ti6Al4V alloy for biomedical applications: Temperature monitoring and microstructural evolution." Journal of Alloys and Compounds **583**: 404-409.

Yan, J., Z. Fan, T. Wei, W. Qian, M. Zhang and F. Wei (2010). "Fast and reversible surface redox reaction of graphene–MnO 2 composites as supercapacitor electrodes." Carbon **48**(13): 3825-3833.

Yang, D. and C. Bock (2017). "Laser reduced graphene for supercapacitor applications." Journal of Power Sources **337**: 73-81.

Yang, G., C. Wang, H. Lei, X. Zheng, P. Qin, L. Xiong, X. Zhao, Y. Yan and G. Fang (2017). "Interface engineering in planar perovskite solar cells: energy level alignment, perovskite morphology control and high performance achievement." Journal of Materials Chemistry A **5**(4): 1658-1666.

Yang, H., C. Zhao, R. Li, C. Shen, X. Cai, L. Sun, C. Luo and Y. Yin (2018). "Noninvasive and prospective diagnosis of coronary heart disease with urine using surface-enhanced Raman spectroscopy." Analyst **143**(10): 2235-2242.

Yang, Y., S. W. Ng, D. Chen, J. Chang, D. Wang, J. Shang, Q. Huang, Y. Deng and Z. Zheng (2019). "Freestanding Lamellar Porous Carbon Stacks for Low-Temperature-Foldable Supercapacitors." Small: 1902071.

Yoon, Y., K. Lee, S. Kwon, S. Seo, H. Yoo, S. Kim, Y. Shin, Y. Park, D. Kim and J.-Y. Choi (2014). "Vertical alignments of graphene sheets spatially and densely piled for fast ion diffusion in compact supercapacitors." ACS nano **8**(5): 4580-4590.

Yu, D., K. Goh, H. Wang, L. Wei, W. Jiang, Q. Zhang, L. Dai and Y. Chen (2014). "Scalable synthesis of hierarchically structured carbon nanotube-graphene fibres for capacitive energy storage." Nature nanotechnology **9**(7): 555-562.

Zang, X., R. Zhang, Z. Zhen, W. Lai, C. Yang, F. Kang and H. Zhu (2017). "Flexible, temperature-tolerant supercapacitor based on hybrid carbon film electrodes." Nano Energy **40**: 224-232.

Zeiger, M., N. Jäckel, V. N. Mochalin and V. Presser (2016). "carbon onions for electrochemical energy storage." Journal of Materials Chemistry A **4**(9): 3172-3196.

Zeis, R. (2015). "Materials and characterization techniques for high-temperature polymer electrolyte membrane fuel cells." Beilstein journal of nanotechnology **6**(1): 68-83.

Zequine, C., C. Ranaweera, Z. Wang, S. Singh, P. Tripathi, O. Srivastava, B. K. Gupta, K. Ramasamy, P. Kahol and P. Dvornic (2016). "High per formance and flexible supercapacitors based on carbonized bamboo fibers for wide temperature applications." Scientific reports **6**: 31704.

Zhang, H., J. Yang, H. Hou, S. Chen and H. Yao (2017). "Nitrogen-doped carbon paper with 3D porous structure as a flexible free-standing anode for lithium-ion batteries." Scientific reports **7**(1): 7769.

Zhang, L., M. J. Henson and S. S. Sekulic (2005). "Multivariate data analysis for Raman imaging of a model pharmaceutical tablet." Analytica Chimica Acta **545**(2): 262-278.

Zhang, L., F. Zhang, X. Yang, G. Long, Y. Wu, T. Zhang, K. Leng, Y. Huang, Y. Ma and A. Yu (2013). "Porous 3D graphene-based bulk materials with exceptional high surface area and excellent conductivity for supercapacitors." Scientific reports **3**: 1408.

Zhang, L. L. and X. Zhao (2009). "Carbon-based materials as supercapacitor electrodes." Chemical Society Reviews **38**(9): 2520-2531.

Zhao, H., L. Liu, R. Vellacheri and Y. Lei (2017). "Recent Advances in Designing and Fabricating Self-Supported Nanoelectrodes for Supercapacitors." Advanced Science.

Zheng, H., G. Yang, S. Chen and Y. Jia (2017). "Hydrothermal Synthesis of 3D Porous Structure Bi2WO6/Reduced Graphene Oxide Hydrogels for Enhancing Supercapacitor Performance." ChemElectroChem **4**(3): 577-584.

Zhou, K. and Y. Zhu (2019). "The paraventricular thalamic nucleus: A key hub of neural circuits underlying drug addiction." Pharmacological Research **142**: 70-76.

Zhu, C., A. Dane, G. Spijksma, M. Wang, J. Van der Greef, G. Luo, T. Hankemeier and R. J. Vreeken (2012). "An efficient hydrophilic interaction liquid chromatography separation of 7 phospholipid classes based on a diol column." Journal of Chromatography A **1220**: 26-34.

Zhu, C., P. Yang, D. Chao, X. Wang, X. Zhang, S. Chen, B. K. Tay, H. Huang, H. Zhang and W. Mai (2015). "All metal nitrides solid-state asymmetric supercapacitors." Advanced Materials **27**(31): 4566-4571.

Zhu, Y., L. Li, C. Zhang, G. Casillas, Z. Sun, Z. Yan, G. Ruan, Z. Peng, A.-R. O. Raji and C. Kittrell (2012). "A seamless three-dimensional carbon nanotube graphene hybrid material." Nature communications **3**: 1225.

Zhu, Y., S. Murali, W. Cai, X. Li, J. W. Suk, J. R. Potts and R. S. Ruoff (2010). "Graphene and graphene oxide: synthesis, properties, and applications." Advanced materials **22**(35): 3906-3924.

Zhu, Y., S. Murali, M. D. Stoller, K. Ganesh, W. Cai, P. J. Ferreira, A. Pirkle, R. M. Wallace, K. A. Cychosz and M. Thommes (2011). "Carbon-based supercapacitors produced by activation of graphene." science **332**(6037): 1537-1541.

Zoladz, P. R., M. Fleshner and D. M. Diamond (2012). "Psychosocial animal model of PTSD produces a long-lasting traumatic memory, an increase in general anxiety and PTSD-like glucocorticoid abnormalities." Psychoneuroendocrinology **37**(9): 1531-1545.

Zuo, W., R. Li, C. Zhou, Y. Li, J. Xia and J. Liu (2017). "Battery-supercapacitor hybrid devices: recent progress and future prospects." Advanced Science **4**(7): 1600539.

Vita

Ardalan Chaichi was born in Mashhad, Razavi Khorasan, Iran in 1992. In Spring 2014, he graduated from Ferdowsi University of Mashhad and received his Bachelor of Science in Metallurgical and Materials Engineering. He received his Master's degree in Nanotechnology Engineering (Nanomaterials) in Spring of 2016 from Sharif University of Technology. He enrolled in the Graduate School at Louisiana State University under the supervision of Dr. Manas Ranjan Gartia to pursue his PhD of Mechanical Engineering (Materials Science and Engineering) in Fall 2016.